NONLINEAR DYNAMICS OF HYSTERETIC OSCILLATORS

A Thesis

by

ASHIVNI SHEKHAWAT

Submitted to the Office of Graduate Studies of
Texas A&M University
in partial fulfillment of the requirements for the degree of

MASTER OF SCIENCE

August 2008

Major Subject: Aerospace Engineering

NONLINEAR DYNAMICS OF HYSTERETIC OSCILLATORS

A Thesis

by

ASHIVNI SHEKHAWAT

Submitted to the Office of Graduate Studies of
Texas A&M University
in partial fulfillment of the requirements for the degree of

MASTER OF SCIENCE

Approved by:

Chair of Committee,	Tamás Kalmár-Nagy
Committee Members,	Dimitris C. Lagoudas
	John E. Hurtado
	Thomas Strganac
	Darbha Swaroop
Head of Department,	Helen Reed

August 2008

Major Subject: Aerospace Engineering

ABSTRACT

Nonlinear Dynamics of Hysteretic Oscillators.

(August 2008)

Ashivni Shekhawat, B.Tech., Indian Institute of Technology Kanpur

Chair of Advisory Committee: Dr. Tamás Kalmár-Nagy

The dynamic response and bifurcations of a harmonic oscillator with a hysteretic restoring force and sinusoidal excitation are investigated. A multilinear model of hysteresis is presented. A hybrid system approach is used to formulate and study the problem. A novel method for obtaining exact transient and steady state response of the system is discussed. Simple periodic orbits of the system are analyzed using the KBM method and an analytic criterion for existence of bound and unbound resonance is derived. Results of KBM analysis are compared with those from numerical simulations. Stability and bifurcations of higher period orbits are studied using Poincaré maps. The Poincaré map for the system is constructed by composing the corresponding maps for the individual subsystems of the hybrid system. The novelty of this work lies in a.) the study of a multilinear model of hysteresis, and, b.) developing a methodology for obtaining the exact transient and steady state response of the system.

To my parents, and Preetha

ACKNOWLEDGMENTS

I take pleasure in thanking my advisor Dr. Tamás Kalmár-Nagy, whose guidance and encouragement have been invaluable in shaping this work and my graduate studies. He has been an excellent mentor and a guide who has helped me make the best of my time as a graduate student. I would also like to express my gratitude to the members of my advisor committee, namely, Dr. Dimitris C. Lagoudas, Dr. John E. Hurtado, Dr. Thomas Strganac and Dr. Darbha Swaroop for their critical comments and many insightful discussions. I am immeasurably indebted to Dr. Dimitris C. Lagoudas, Dr. John E. Hurtado and Dr. Raktim Bhattacharya who have been never ending sources of inspiration and my role models. I am deeply touched by their compassion, open-mindedness, and their insatiable desire to educate and to make their students better. I revere the unfathomable knowledge of all my teachers and thank them for sharing it with me.

I would like thank my good friends Roshmik, Jayitha, Mrinal and Justin for making my stay at Texas A&M a memorable and pleasant experience. Without their goodwill and camaraderie things would not have been the same. No mention of me can be complete without a mention of Preetha, my love, who has been a wonderful companion to me through the ups and downs of my life. Above all, I thank my parents for their selfless love, guidance and encouragement at every step of my life.

TABLE OF CONTENTS

CHAPTER Page

CHAPTER Page

LIST OF TABLES

TABLE Page

LIST OF FIGURES

FIGURE Page

FIGURE Page

FIGURE Page

FIGURE Page

FIGURE Page

FIGURE Page

FIGURE Page

CHAPTER I

INTRODUCTION

In this chapter we present a survey of major past and ongoing research related to mathematical modeling of hysteresis. We describe the mathematically simpler models of hysteresis in some detail while giving references to the more complicated models. Even so, not all simple or important models of hysteresis are covered here. The interested reader is referred to Ref. [1] for a more complete treatment of the subject.

A. Hysteresis

Hysteresis plays an important part in many natural phenomena such as shape-memory effect [2], pseudo-plasticity, magnetism [3], sleep-wake cycles [4], friction [5], economics [6, 7], and many more. In a broad sense hysteresis refers to a class of strongly nonlinear phenomena. We emphasize the word 'strongly' because it means that local linearization is not possible for hysteretic systems. In more formal language hysteresis refers to operators with *rate-independent memory*. Even though hysteresis is often associated with hysteresis loops, they are not essential features of hysteresis. It is possible to construct hysteretic systems without loops (Ref. [1], pp. 6). Hysteresis is also associated with dissipation. For periodic phenomena the energy dissipated is proportional to the area of the hysteresis loop.

Mechanical systems with hysteresis often posses attractive damping properties [8]. Several attempts have been made in the literature to utilize these properties for vibration isolation and damping. Lagoudas and Machado [9] investigated the use of SMA components for passive vibration damping, while others have considered hys-

---

The journal model is *IEEE Transactions on Automatic Control*.

teretic elements for seismic vibration isolation [10, 11]. SMAs or other smart material have also been used for active control [2, 12, 13]. Many scholarly texts are devoted solely to the study of hysteretic phenomena [14, 15, 16, 3, 17]. However, despite the enormous literature, the phenomenon of hysteresis is not fully understood. Some of the reasons to this effect are the hitherto (more or less) limited computational resources, success of linear theory in modeling most phenomena to certain satisfaction, and limited theoretical understanding of nonlinear systems in general.

1. Prominent Models of Hysteresis

Mathematical modeling hysteresis is a significant challenge. Many researchers have made considerable effort to come up with theoretical models for hysteresis. The most prominent amongst these are the Preisach model [18], the Prandtl-Ishlinskii model [19, 15], the model of Masing [20], the model of Duhem [21], and the Bouc-Wen model [22, 23]. The bilinear model of hysteresis studied by Caughey [24, 25] can be considered to be a generalization of the Prandtl-Ishlinskii model. The constitutive models for shape memory alloys inherently contain models for hysteresis. Prominent amongst these are the models proposed by Liang and Rogers [26], Boyd and Lagoudas [27], and, Raniecki, Lexcellent and Tanaka [28]

2. Response of Mechanical Systems with Hysteresis

Response of mechanical systems with hysteresis is the subject of this thesis, thus we feel its important to dwell on the developments made on the topic so far. For most mechanical systems hysteresis manifests itself in the form of a hysteretic restoring force or generalized restoring potential. Many of these systems can be modeled by a forced harmonic oscillator with a hysteretic restoring force. Caughey used the Krylov-Bogoliubov-Mitropolsky (KBM) method to study the steady state response

of a bilinear hysteretic oscillator subject to sinusoidal excitation [24]. He derived analytical expressions for frequency response of the system and compared them with simulations using an analog circuit. He found that the system exhibited a soft resonance with no jumps. In Ref. [25] he extended his analysis to random excitations. Masri [29] found the "exact" solutions for a damped harmonic oscillator with a bilinear hysteretic restoring force. In effect he reduced the system to one nonlinear algebraic equation which was to be solved using numerical methods.

Recently there has been a thrust to study the more complex behavior of mechanical systems with hysteretic systems using the modern tools of nonlinear dynamics. Several researchers have used the Harmonic Balance Method (HBM) and Floquet theory to study the steady state response and stability of oscillators with hysteretic elements [30, 31, 32]. In his 1990 work Capecchi [30] used the HBM to study the response of a hysteretic oscillator with periodic excitation. Based on his findings Capecchi concluded that the higher harmonics play a significant role in the overall dynamics of the oscillator. In Ref. [33] Capecchi and co-workers studied the complex behavior of multiple degree of freedom systems with hysteresis. They used the Masing model of hysteresis and analyzed the system using reduced dimensional Poincaré maps. Pratap and Holmes [34] found that hysteretic systems can exhibit chaos in the form of a Smale horseshoe. In fact, most of the above cited references report some kind of complex behavior. Lacarbonara and Vestroni [8] used Poincaré maps and continuation algorithms to map out the bifurcation sequences of some hysteretic systems using the Masing and Bouc-Wen models. Thus, a significant amount of research has been done to understand the response of systems with hysteresis, however, this field is still in its infancy and much needs to be done.

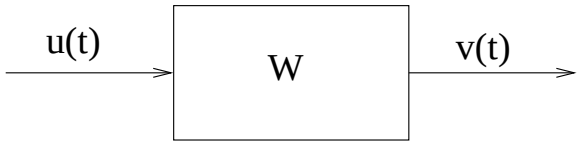

Fig. 1. A hysteretic input-output device.

3. A Historical Note

The word *hysteresis* is of Greek origin (first used around 1795-1805) and literally translates to 'state of being behind or late'. This word was introduced into scientific vocabulary by a physicist named Alfred Ewing in 1895 [35]. Since then the word hysteresis has been used in great many contexts, scientific and otherwise. Examples include its usage in mechanics (plasticity, friction), electrodynamics (ferromagnetism), material science (shape memory effect), electronics (relays) and many more.

In spite of its early discovery, the history mathematical analysis of hysteresis is relatively short (fitting to the name and effect, perhaps). The earliest attempts to model hysteresis were made by Preisach [36] in the 1920's and 30's. However, the first investigation of hysteresis from the point of view of functional analysis was done by R. Bouc in 1966. His work was published in English in 1967 [22]. Bouc modeled hysteresis as a functional operator and studied its properties using analytic methods. Since then several contributions have been made to the literature regarding hysteresis, some details of which can be found in Refs. [15, 1, 14, 37] and the references therein.

B. Mathematical Models of Hysteresis

Consider a system or a device with two state variables $u(t)$ and $v(t)$, where t denotes the time. The variables $u(t)$ and $v(t)$ are the input and output of the system, respec-

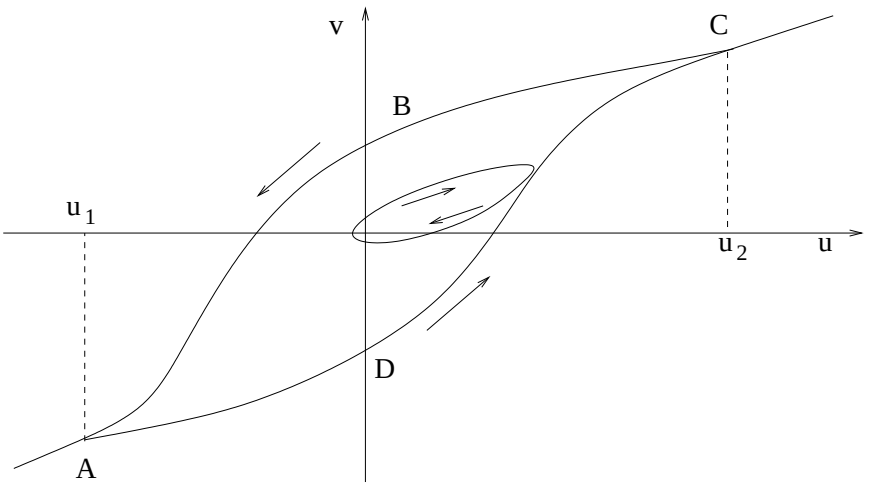

Fig. 2. Hysteresis loops.

tively. It is assumed that both variables are smooth functions of time. If we take a phenomenological point of view and regard the system or the device as a black box then the situation can be represented by figure 1. Mathematically we write

$$v(t) = W(u, v_0)(t), \tag{1.1}$$

where v_0 is the initial value of $v(t)$. Note that the operator $W(., v_0)$ is *not* a function because it depends not only on the present value of $u(t)$, but also on the history of $u(t)$ and the initial value of $v(t)$. The task of mathematical modeling of hysteresis then boils down to finding the operator W.

Figure 2 shows the evolution of the pair (u, v) for one plausible hysteretic operator W over a certain period of time. As shown in the figure, if u is increased monotonically from u_1 to u_2 then the pair (u, v) traces the curve A-D-C. However, if u is decreased monotonically from u_2 to u_1 then the pair (u, v) traces a different curve C-B-A. Also notice that the relation between u and v is single valued (a function) for $u \leq u_1$ or $u \geq u_2$. In such a case the loop A-D-C-B-A is called the major loop of hysteresis.

The region bounded by the major loop is called the region of hysteresis and will be denoted by $\mathcal{L}$. Now suppose that while increasing from u_1, u reverts at some point before reaching u_2. In such a case the pair (u, v) traces a loop similar to the small loop shown in the figure. These loops are called minor loops.

1. Properties of Hysteretic Operators

All hysteretic operators satisfy the following two properties: causality and rate-independence. A third property called reachability is satisfied by most, but not all, hysteretic operators. These properties are discussed next.

a. Causality

It is assumed that the operator $W(., v_0)$ is causal, i.e., the output at a given time is only dependent on the history of the input u and not its future values. Mathematically this can be expressed as follows

$$u_a(t) = u_b(t) \ \forall \ t \in [0, t_1] \Rightarrow W(u_a, v_0)(t_1) = W(u_b, v_0)(t_1), \tag{1.2}$$

even if $u_a(t) \neq u_b(t)$ for some $t \ni [0, t_1]$.

b. Rate-Independence

The property of rate-independence is one of the most important properties of hysteretic operators. Roughly speaking it means that the output at a given instance of time is dependent only on the order of past inputs and not on the rate at which they were attained. It is due to this property that we can draw figures like figure 2 without giving any specific reference to the input rate law. Mathematically one can say that

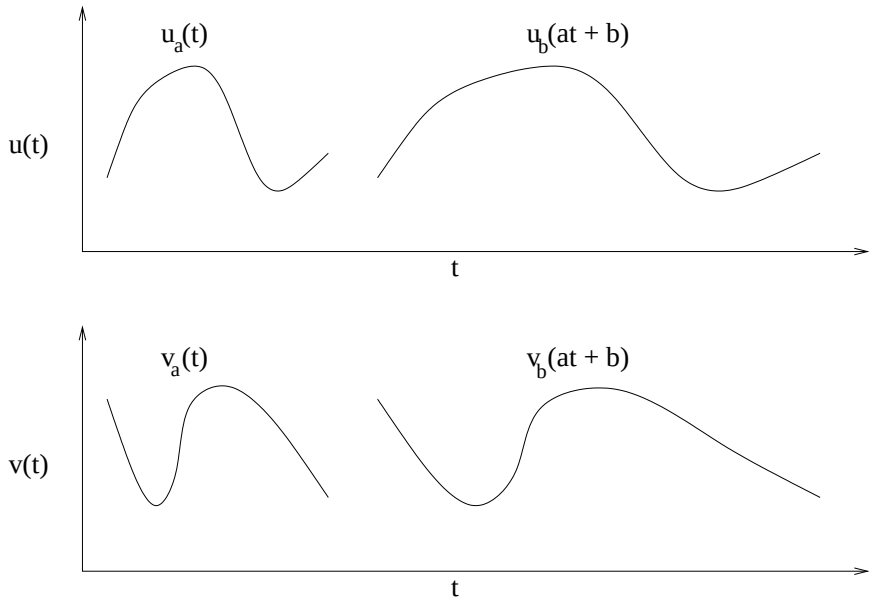

Fig. 3. Rate-independence.

for any increasing diffeomorphism ϕ,

$$u_a(t) = u_b(\phi(t)) \ \forall \ t \in [0, t_1] \Rightarrow W(u_a, v_0)(t) = W(u_b, v_0)(\phi(t)), \ \forall \ t \in [0, t_1]. \quad (1.3)$$

Figure 3 shows an example with $\phi(t) = at + b$.

c. Reachability

Reachability means that starting from any admissible pair (u_a, v_a) it is possible to reach any other pair (u_b, v_b) in the hysteresis region $\mathcal{L}$. In other words, all pairs $(u, v) \in \mathcal{L}$ are admissible and connected by at least one path consisting of admissible loops. Thus, given any admissible pair $(u_a, v_a), \ \exists \ u(t), \ t \in [0, t_1]$ s.t. $W(u, v_a)(t_1) = v_b, \ u(t_1) = u_b, \forall \ (u_b, v_b) \ \in \ \mathcal{L}$. Further, due to rate-independence the actual value of t_1 is immaterial.

Next we present some models of hysteresis that satisfy these properties and are

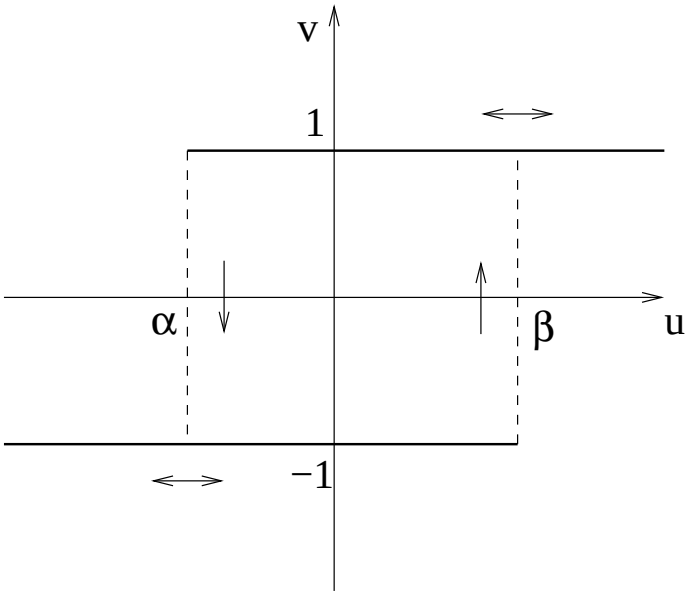

Fig. 4. A nonideal relay.

widely used in the literature.

2. Nonideal Relay

A nonideal relay is one of the simplest models of hysteresis. The nonideal relay operator is parameterized by two parameters α, β with $\alpha < \beta$, and is represented by $R_{\alpha,\beta}$. The operator $R_{\alpha,\beta}$ is bivalued and can take values equal to ± 1 (can be any other arbitrary scalar output values as well). We can write the familiar input-output relation as

$$v(t) = R_{\alpha,\beta}(u, v_0)(t). \tag{1.4}$$

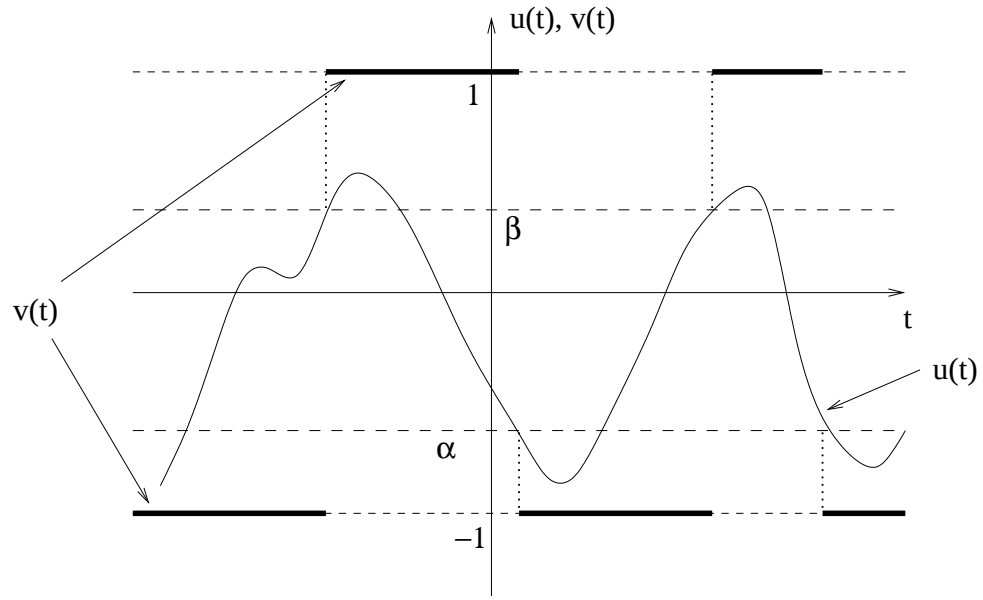

Fig. 5. Input-output for a typical relay.

Figure 4 shows the dynamics of a typical relay. The output of the relay changes only when $u(t) = \alpha$ or $u(t) = \beta$. The output is given by the following explicit formula

$$v(t) = R_{\alpha,\beta}(u, v_0)(t) = \begin{cases} v_0 & \text{if } \alpha < x(\tau) < \beta \ \forall\ \tau \in [0,t]; \\ 1 & \text{if } \exists\ t_1 \in [0,t] \text{ s.t. } u(t_1) \geq \beta,\ x(\tau) > \alpha \ \forall\ \tau \in [t_1,t]; \\ -1 & \text{if } \exists\ t_1 \in [0,t] \text{ s.t. } u(t_1) \leq \alpha,\ x(\tau) < \beta \ \forall\ \tau \in [t_1,t]. \end{cases}$$

The relay operator $R_{\alpha,\beta}$ is obviously causal and rate-independent, thus it is a hysteretic operator. However, notice that the relay does not have a hysteresis loop in the strict sense and does not satisfy the property of reachability. Figure 5 shows the input-output graph for a typical relay.

3. $T(x)$ Model

The $T(x)$ model of hysteresis [38] is a member of the family of models consisting of the Langevin function ($L(x)$) [39], the Brillouin function ($B(x)$) [40], and the $M(x)$ functions [41]. These models are predominantly used in magnetism. The most elementary $T(x)$ function is defined as follows

$$T(x) = \begin{cases} \tanh(x - a_0) + A_0 x + b & \text{for } \dot{x} > 0, \\ \tanh(x + a_0) + A_0 x - b & \text{for } \dot{x} < 0. \end{cases}$$

It is assumed that the hysteresis loop has a magnitude x_m and is symmetric (there are other variants of the model that deal with asymmetric loops, see Ref. [38] for details). The value of b can be found by equating the values of the two branches at $x = x_m$ as

$$b = (\tanh(x_m + a_0) - \tanh(x_m - a_0))/2. \tag{1.5}$$

Figure 6 shows the hysteresis loops for the $T(x)$ model with $a_0 = 1.5, A_0 = 0.05$ and $x_m = 4, 3, 2, 1$.

4. Stop

The model named 'stop' is based on the Prandtl model of elasto-plasticity. This model is also known as the E–P model because it can be considered to be a result of a linear elastic element and a perfectly plastic element connected in series as shown in figure 7. The dynamics of this model are as shown in figure 8. To carry out the analogy with elasto-plasticity u corresponds to strain while v corresponds to stress. When the elastic and plastic elements are connected in series as shown in figure 7 the maximum stress, v, is limited by the available traction, while the strain, u, can increase without bound.

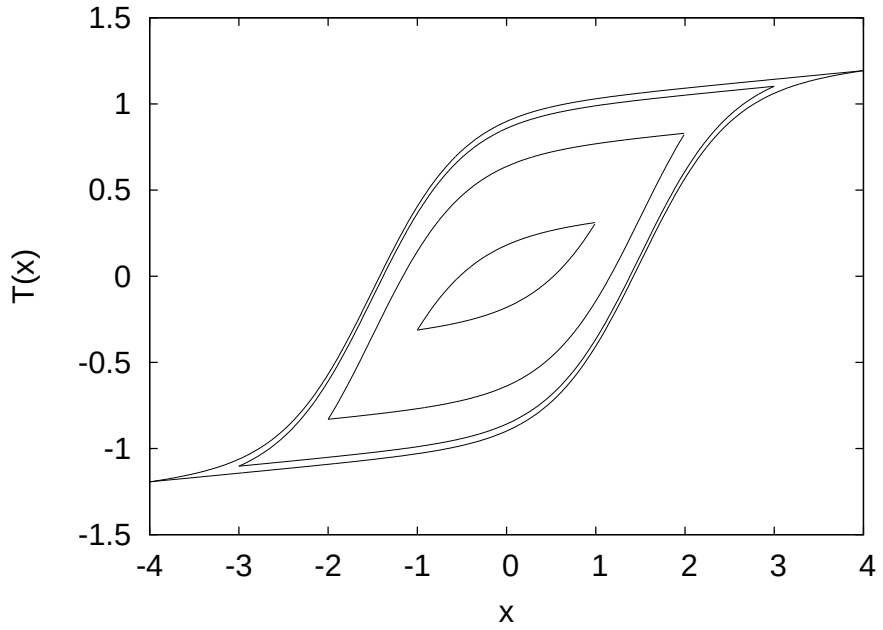

Fig. 6. Hysteresis loops for the $T(x)$ model with $a_0 = 1.5, A_0 = 0.05$.

Fig. 7. An elastic element and a plastic element connected in series.

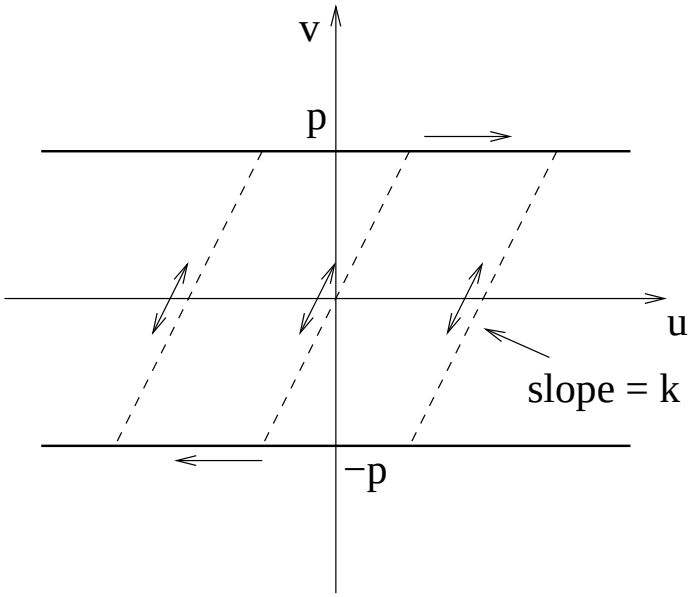

Fig. 8. Dynamics of the stop model.

The model can be represented by the following variational inequalities

$$|v| \leq p, \quad (k\ \mathrm{d}u - \mathrm{d}v)(v - x) \geq 0 \quad \forall\ x, |x| \leq p. \tag{1.6}$$

5. Play

The model 'play' is the dual of the model stop. The play model can be realized by connecting an elastic and a plastic element in parallel as shown in figure 9. The input u can be thought of as the stress while the output v can be thought of as the strain. Obviously, the system shown in figure 9 is capable of sustaining some stress without yielding (equal to the available traction), beyond which the strain grows linearly with the stress. The dynamics of the play model are shown in figure 10.

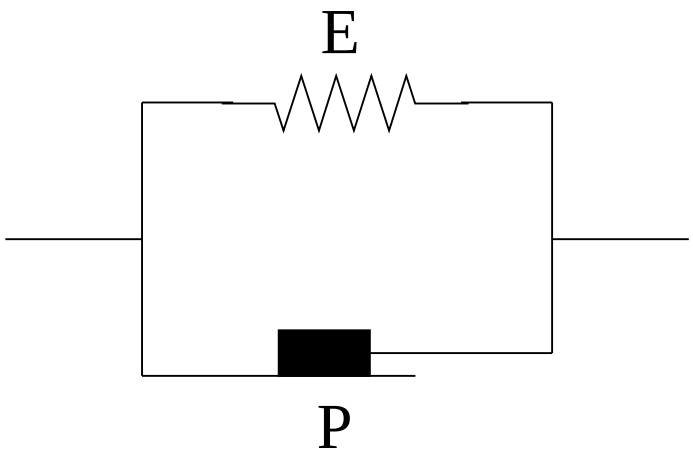

Fig. 9. An elastic element and a plastic element connected in parallel.

The model can be represented by the following variational inequalities

$$|ku - v| \leq p, \quad \mathrm{d}v(ku - v - x) \geq 0 \quad \forall\, x, |x| \leq p. \tag{1.7}$$

6. Bilinear Model

The bilinear model of hysteresis can be considered to be a generalization of the Prandtl models. The dynamics of a harmonic oscillator with bilinear restoring force were studied by Caughey in great detail [25, 24]. The bilinear model can be represented as follows

$$|k_1 u - v| \leq p, \quad (k_2 \mathrm{d}u - \mathrm{d}v)(k_1 u - v - x) \geq 0 \quad \forall\, x, |x| \leq p. \tag{1.8}$$

The dynamics of the bilinear model are depicted in figure 11. Later in the thesis the response of a harmonic oscillator with bilinear restoring force and sinusoidal excitation will be studied in detail. At that point we shall also present an equivalent definition

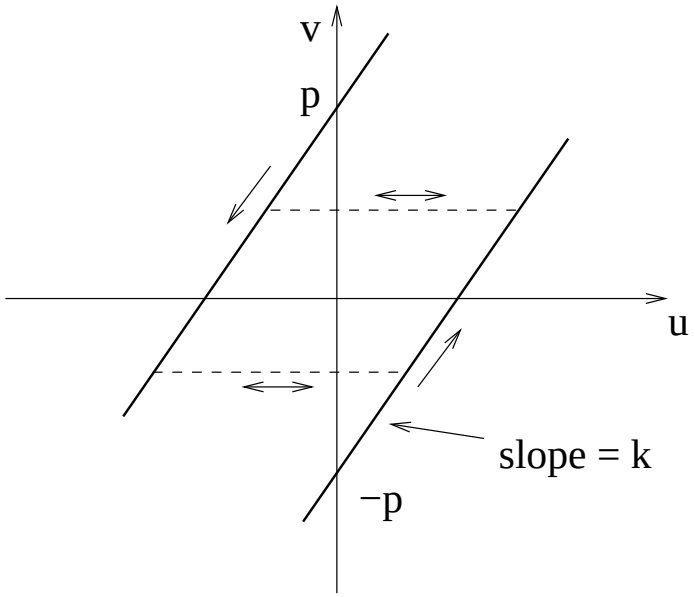

Fig. 10. Dynamics of the play model.

of the model in terms of a hybrid automaton.

7. Multilinear Model

The multilinear model of hysteresis proposed in this thesis is a generalization of the bilinear model. To the best of our knowledge this model has not be studied previously. The motivation for generalizing the bilinear model comes from the fact that for many hysteretic systems the hysteresis loops are not symmetric. However, symmetry of loops is an inherent assumption in the bilinear model. In the multilinear model this shortcoming is remedied by allowing the loading and unloading to take place at curves with two different slopes, viz. k_2, k_3. The dynamics of the multilinear model are shown in figure 12.

The variational formulation of the multilinear model is slightly complicated. It is easy to see that the multilinear model can be thought of as a superposition of two

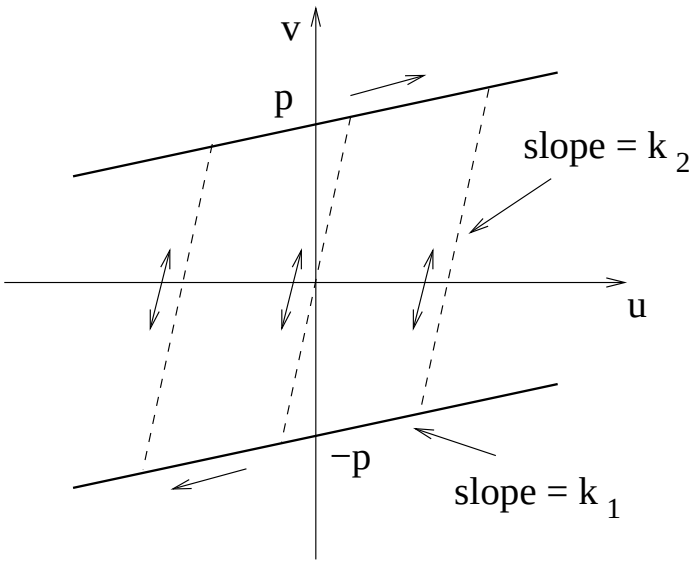

Fig. 11. Dynamics of the bilinear model.

bilinear models. In the multilinear model the evolution of the pair (u, v) along the boundaries of the admissible region is exactly the same as that for the bilinear model. However, the difference is that when the hysteretic region is entered from the top branch ($v = k_1 u + p$), then the evolution takes place along the curves $\mathrm{d}v - k_3 \mathrm{d}u = 0$. Similarly if the hysteretic region is entered from the bottom branch ($v = k_1 u - p$), then the evolution takes place along the curves $\mathrm{d}v - k_2 \mathrm{d}u = 0$.

The variational form of the model can thus be written as follows. At time t_1, if $\exists\ t \in [0, t_1]$ s.t. $v(t) = k_1 u(t) + p,\ v(t_2) \neq k_1 u(t_2) - p\ \forall\ t_2 \in [t, t_1]$ then

$$|k_1 u - v| \leq p, \quad (k_3 \mathrm{d}u - \mathrm{d}v)(k_1 u - v - x) \geq 0 \quad \forall\ x, |x| \leq p. \tag{1.9}$$

Similarly, if $\exists\ t \in [0, t_1]$ s.t. $v(t) = k_1 u(t) - p,\ v(t_2) \neq k_1 u(t_2) + p\ \forall\ t_2 \in [t, t_1]$ then

$$|k_1 u - v| \leq p, \quad (k_2 \mathrm{d}u - \mathrm{d}v)(k_1 u - v - x) \geq 0 \quad \forall\ x, |x| \leq p. \tag{1.10}$$

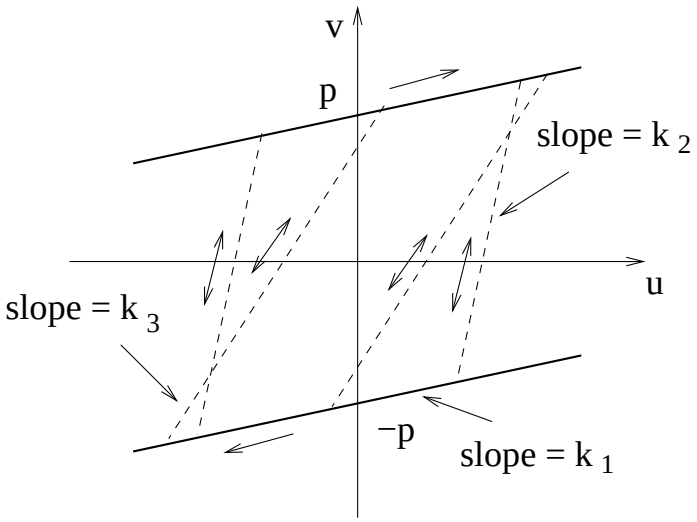

Fig. 12. Dynamics of the multilinear model.

Finally, if $(v - k_1 u + p)(v - k_1 u - p) \neq 0 \ \forall \ t \in [0, t_1]$ then the evolution law is the same as it was at $t = 0$.

8. Preisach Model

The Preisach model of hysteresis is the most long-standing of models of hysteresis. Although this model was proposed in the 1920's it is still a topic of active research. The Preisach model does not correspond to description of any one phenomenon (unlike the $T(x)$ model which is used almost exclusively in magnetism), rather it has the flexibility to be used in several different branches of engineering. The Preisach model is a so-called parameter identification type model, and so are the relay, Prandtl, bilinear, and the multilinear models. Parameter identification type models do not correspond to any one physical phenomenon and thus to make them suitable for use in any phenomenon some parameter identification needs to be done.

The Preisach operator, $P(u, v_0)$, is a superposition of a number of relay operators

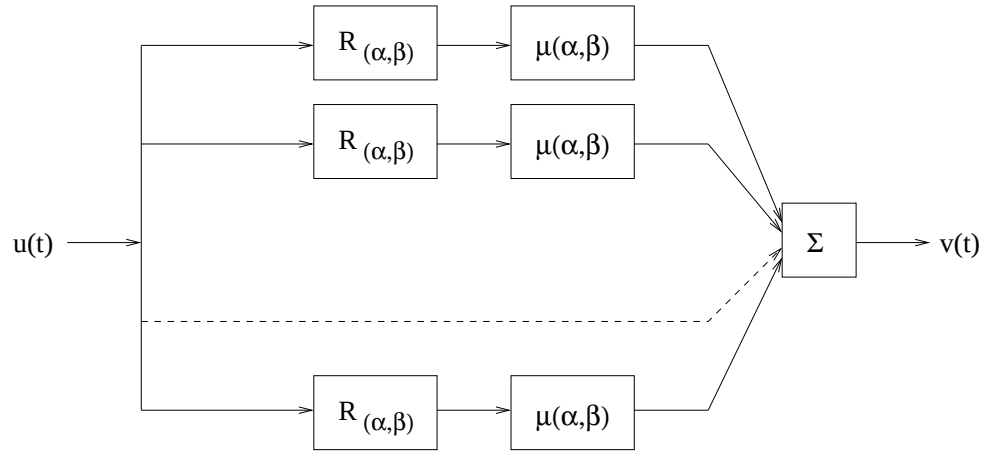

Fig. 13. The discrete Preisach operator.

discussed earlier. The input to the Preisach operator is fed to the individual relay operators and the output is calculated by taking a weighted sum of the individual outputs. The weights for the individual operators can be selected to tune the behavior of the operator. We denote the weight corresponding to the relay $R_{\alpha,\beta}$ by $\mu(\alpha, \beta)$. When the Preisach operator is composed of finitely many relays it is called the discrete Preisach operator. Figure 13 shows a schematic of the discrete Preisach operator. In the limit of infinite number of relays the sum is replaced by an integral and the individual weights are replaced by a distribution. Thus, the input-output relation for the discrete Preisach operator can be written as

$$v(t) = P(u, v_0)(t) = \sum_{\beta>\alpha} \mu(\alpha, \beta) R_{\alpha,\beta}(u, v_0)(t), \tag{1.11}$$

while the equation for the continuous case is

$$v(t) = P(u, v_0)(t) = \int\int_{\beta>\alpha} \mu(\alpha, \beta) R_{\alpha,\beta}(u, v_0)(t) d\alpha d\beta. \tag{1.12}$$

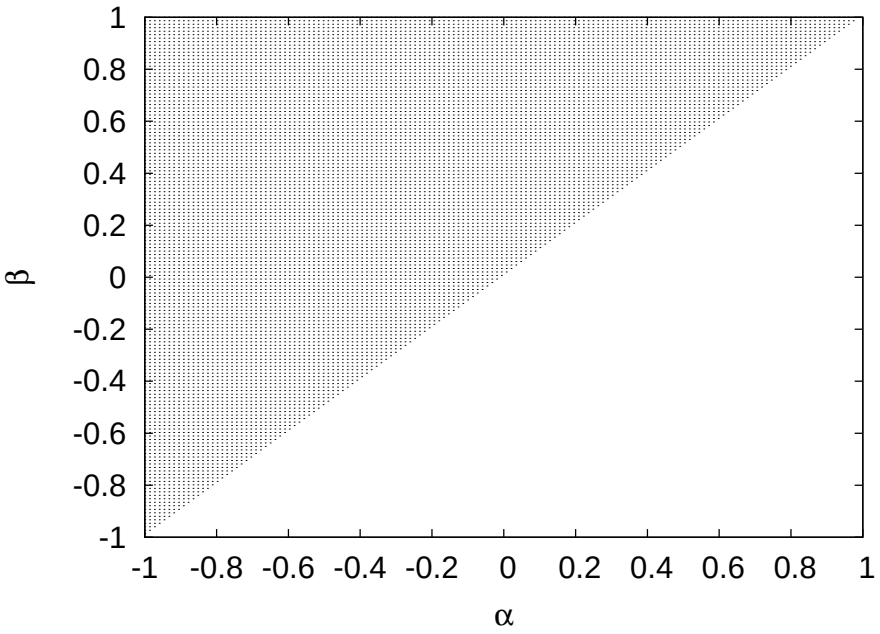

Fig. 14. Discretization of the $\alpha - \beta$ domain with 150 grid points along each axis.

The Preisach model of hysteresis is by far the most versatile model of hysteresis discussed so far. To demonstrate its modeling capability we show some hysteresis loops generate by a discrete Preisach operator. The individual relay operators are obtained by discretising the region $-1 \leq \alpha < \beta \leq 1$ with 150 grid points along α and β axis. The weights are uniform and normalized to set the maximum output of the operator to 1. The typical loops are presented in figure 15. All the graphs in figure 15 have at least one major loop because the input attains values of ± 1 at least once.

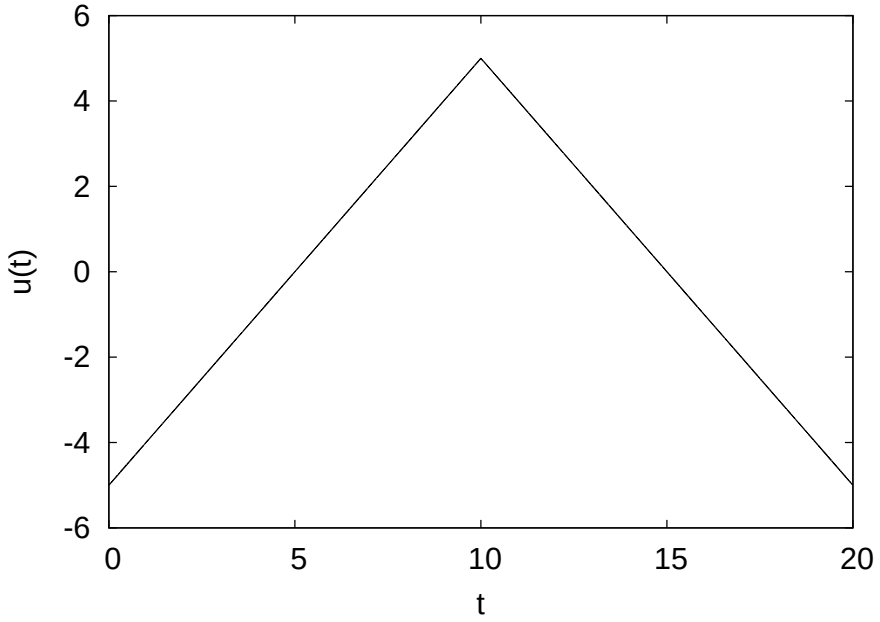

(a) Case I: Input

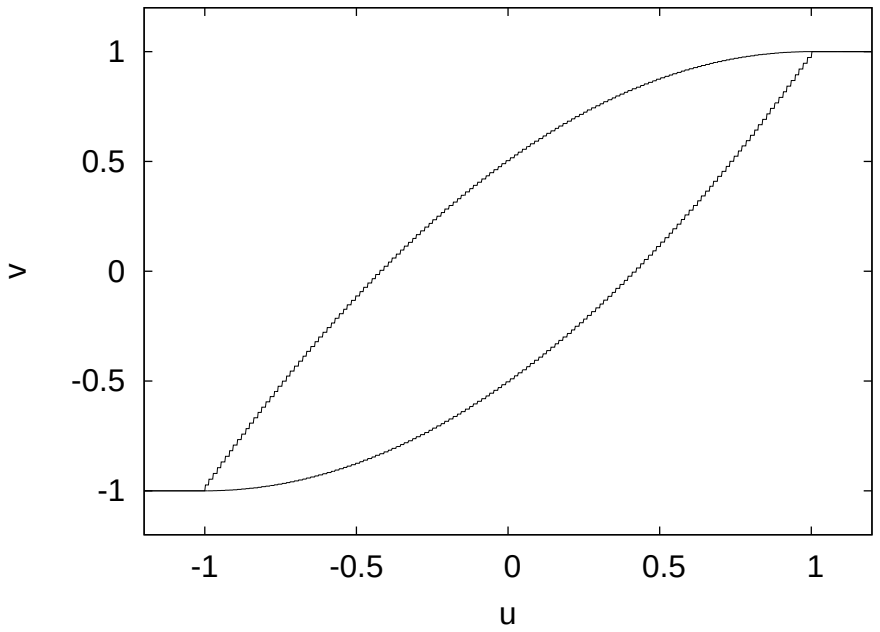

(b) Case I: Output

Fig. 15. Typical hysteresis loops traced by the Preisach operator.

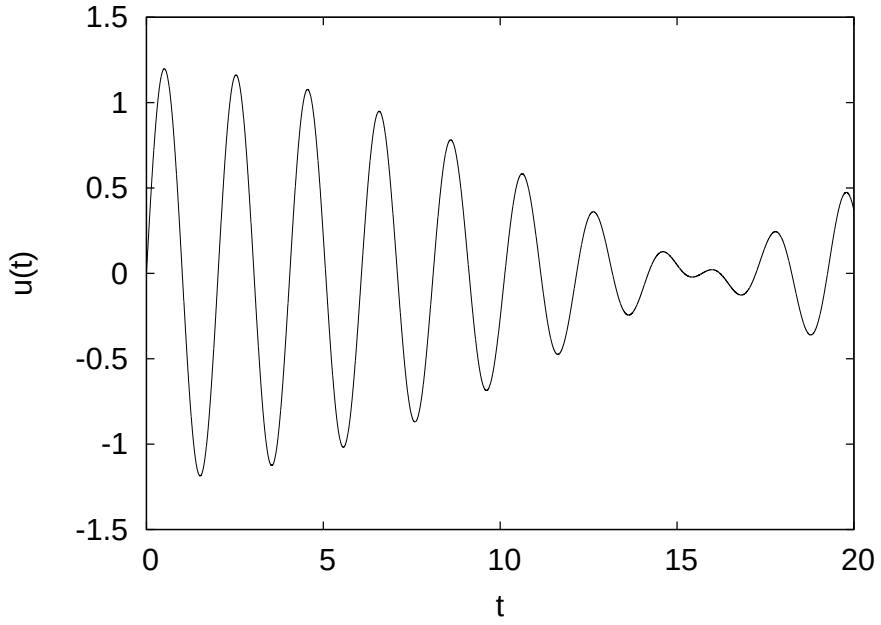

(c) Case II: Input

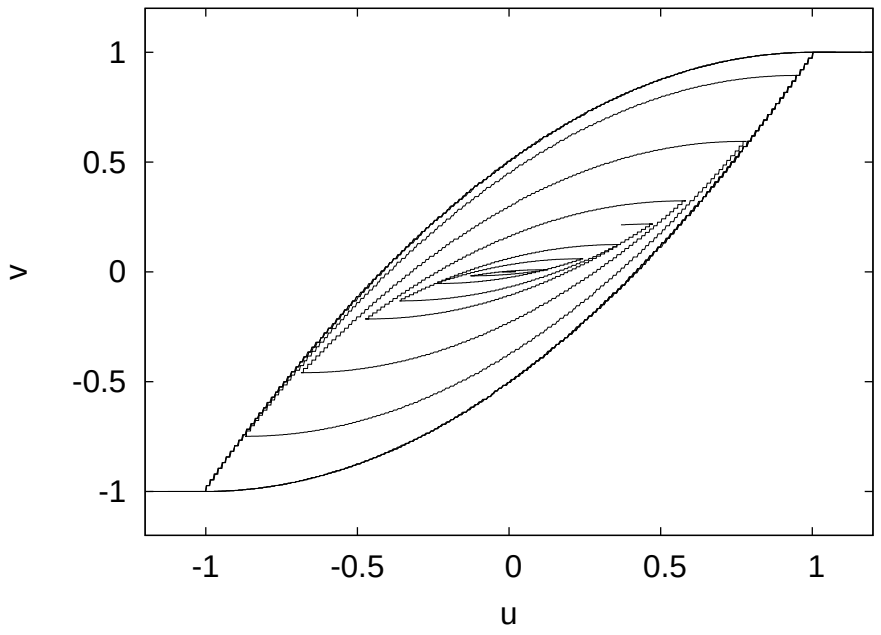

(d) Case II: Output

Fig. 15. Continued ...

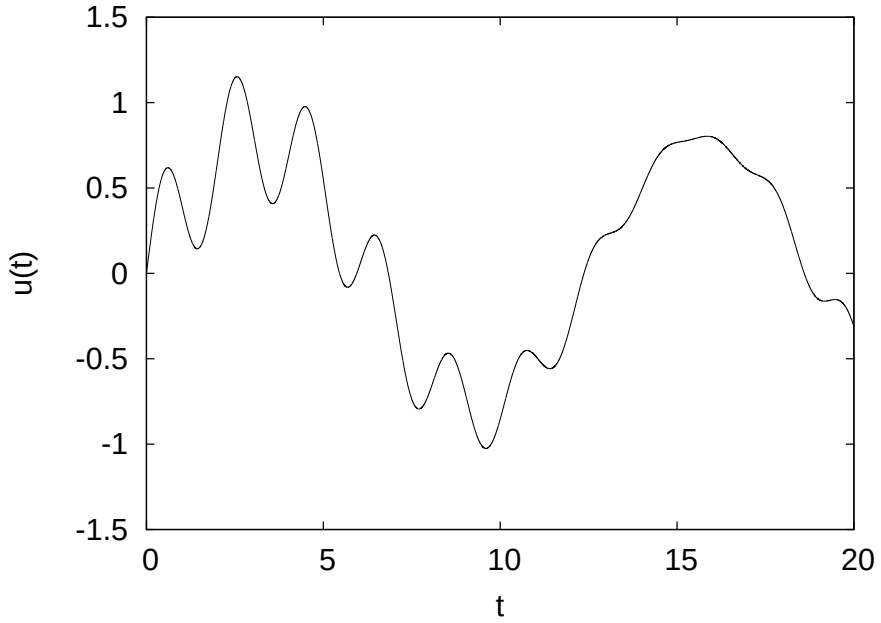

(e) Case III: Input

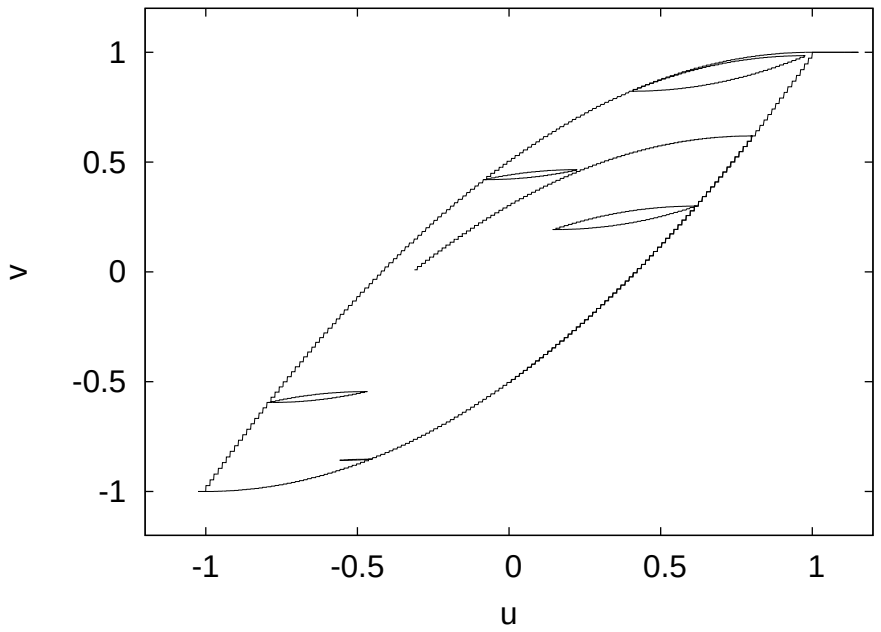

(f) Case III: Output

Fig. 15. Continued ...

CHAPTER II

SHAPE MEMORY ALLOYS AND HYSTERESIS

In this chapter we present a simple description of constitutive relations for Shape Memory Alloys (SMAs) and bring out their relation to hysteresis and hybrid systems. There are many constitutive models for SMAs in the literature. We will mention the prominent models without going into details of any of them. The discussion will be limited to 1-D stress and isothermal loading. We will steer clear of the general thermodynamic theory of SMAs in view of simplicity and present the relevant results without derivations. One of the aims of this chapter is to show the relation between SMAs and the bilinear and multilinear models of hysteresis discussed in chapter I. We will end the chapter with a discussion of hybrid systems and SMAs.

A. Introduction

There is a vast body of literature devoted to the study of shape memory alloys [42, 43, 44]. These materials possess peculiar characteristics like the Shape Memory Effect (SME) and pseudoelasticity. It is envisioned that the special properties of these materials can be exploited to design smart structures and multi-functional materials. For example, Machado and Lagoudas [9] investigated the use of SMA components for passive vibration damping, while Rogers [45] proposed to use SMAs for actively controlling the dynamic response of composites laminates. However, the present understanding of constitutive models as well as dynamic response of SMAs is limited and needs to be improved significantly for this vision to be realized. Naturally, the development of theoretical constitutive models should precede the study of dynamic characteristics of SMAs. In the past few decades there have been considerable advances in modeling of constitutive relations for SMAs. Liang and Rogers [26]

developed a one-dimensional constitutive model (the so-called cosine model) of shape memory alloys. Boyd and Lagoudas [27, 46] developed a phenomenological constitutive model for a general state of stress. Other models like the generalized cosine model [47], the exponential or the R-L model [28], the unified model [48] etc. can also be found in the literature. Thus, there exist some theoretical constitutive models of SMAs on which a study of their dynamic characteristics can be based.

The dynamic response of SMAs is very complicated due to phenomena like martensitic phase transformation and thermomechanical coupling. Much work has been done on simulating the general 3-D response of SMA based structures. The interested reader is referred to Refs. [49, 50] and the references therein for a detailed commentary on the subject. Besides presenting an excellent review of the available literature on the subject Ref. [49] also contains a good discussion of the return mapping algorithm for simulating the dynamic response of SMAs. It has been shown that return mapping based techniques have good stability and convergence properties in general [51].

B. Constitutive Models

In this section we present some constitutive models for SMAs in a cursory manner. The interested reader is referred to Ref. [27] and the references therein for more details of the models.

The unusual properties of SMAs are due to mechanical and thermal stress-induced phase transformations. In general, the SMA can be composed of two phases: martensite and austenite. Martensite and austenite are different crystalline forms of the same material. The relative proportion of martensite and austenite is a function of the thermal and mechanical loading. We assume isothermal conditions, thus elim-

inating the temperature dependence. The relative proportion of the two phases is measured in terms of martensite volume fraction, ξ.

When the material exists as pure martensite or austenite, or a non-transforming mixture, the constitutive relations are the same as that of a general elastic material (law of volumes holds for mixture). However, when a phase transformation takes place, some energy gets used for bringing about the phase transformation and some gets dissipated as heat during the process. Thus, the simple linear stress-strain relations are not valid during phase transformations.

As discussed above, a SMA material can in general be in one of the following phases or modes:

1. Pure austenite,
2. Pure martensite,
3. Non-transforming mixture,
4. Forward transformation (austenite to martensite), and,
5. Reverse transformation (martensite to austenite).

Next we will present the constitutive relations for each of these phases in increasing order of complexity. The symbols used in the ensuing development are defined in table I.

Table I.: Symbols used in constitutive models of SMAs.

Symbol	Definition
α	Second order effective thermal expansion tensor (scalar for 1-D assumption)
σ	Second order stress tensor (scalar for 1-D assumption)
ϵ	Second order strain tensor (scalar of 1-D assumption)
ξ	Martensitic volume fraction
b	Parameter in Boyd-Lagoudas model
ρ	Density
s_0	Effective specific entropy at reference state
a_A, a_M	Material constants associated with temperature induced phase transformation (cosine model)
b_A, b_M	Material constants associated with stress induced phase transformation (cosine model)
S	Fourth order compliance tensor (scalar for 1-D stress)
M_s, M_f	Martensite start and finish temperature at zero stress
A_s, A_f	Austenite start and finish temperature at zero stress
A_a, A_m	Material constants related to A_s, A_f, M_s, M_f
B_a, B_m	Material constants related to A_s, A_f, M_s, M_f
H^{cur}	Maximum transformation strain at current state (scalar for 1-D assumption)
$()^A$	Refers to pure austenitic phase
$()^M$	Refers to pure martensitic phase
ΔS	$S^M - S^A$

1. Pure Austenite or Martensite

We begin by presenting the stress-strain relations for pure martensite and austenite. These are the well known relations from the theory of elasticity. The only difference is the presence of *transformation strain* in pure martensite phase. Eq. 2.1 is the constitutive law for pure austenite phase. The symbols have their usual meanings (S is the compliance tensor, α is the thermal expansion coefficient), and the superscript A refers to austenite.

$$\epsilon = S^A\sigma + \alpha^A(T - T_0). \tag{2.1}$$

Eq. 2.2 is the constitutive law for pure martensite. As indicated earlier the law is different from usual elastic materials because of influence of the transformation strain. The effect of the transformation strain is measured by H^{cur}, which is a 1-D representation of the more general transformational strain tensor.

$$\epsilon = S^M\sigma + \alpha^M(T - T_0) + H^{cur}\mathrm{sgn}(\sigma). \tag{2.2}$$

2. Non-Transforming Mixture

A SMA material can be in a phase where it is a mixture of austenite and martensite and both phases are stable, i.e., the volume fraction ξ is constant with time. The constitutive laws for the mixture can be found using the constitutive laws for the individual materials and the law of mixtures. The law of mixtures yields the following expressions for the equivalent material properties

$$\begin{aligned} S &= S^A + \xi\left(S^M - S^A\right), \\ \alpha &= \alpha^A + \xi\left(\alpha^M - \alpha^A\right). \end{aligned} \tag{2.3}$$

Knowing the equivalent material properties we can write the constitutive law for the mixture as follows

$$\epsilon = S\sigma + \alpha(T - T_0) + H^{cur}\text{sgn}(\sigma)\xi. \tag{2.4}$$

3. Forward Transformation

The constitutive laws that are valid during the phase transformations are discussed next. How and when the phase transformations start and end is left for later discussion. A forward transformation means a transformation that begins with pure austenite ($\xi = 0$) and ends with pure martensite ($\xi = 1$). Similarly a reverse transformation begins with pure martensite ($\xi = 1$) and ends with pure austenite ($\xi = 0$). Obviously, during a phase transformation the volume fraction ξ is not constant. The law for change of the volume fraction is generally found by invoking the principles of thermodynamics along with certain hypothesis on the material behavior. If we assume that the volume fraction is known then we can write the following familiar equations for the constitutive relations

$$\begin{aligned} S &= S^A + \xi\left(S^M - S^A\right), \\ \alpha &= \alpha^A + \xi\left(\alpha^M - \alpha^A\right), \\ \epsilon &= S\sigma + \alpha(T - T_0) + H^{cur}\text{sgn}(\sigma)\xi. \end{aligned} \tag{2.5}$$

The first two equations in the set 2.5 are simple laws of volume-fractions for calculating the equivalent properties of a mixture. Knowing the equivalent material properties, the last equation of the set is the usual elastic constitutive relation with the correction for transformation strain. Thus, the difference between usual elastic constitutive relations and those for a transforming SMA is really embodied by the law for evolution of the volume fraction ξ.

There are many theories as to how the volume fraction evolves with the other

states, namely stress and temperature. Under the hypothesis of isothermal loading Boyd and Lagoudas [27] obtained the following law

$$\xi = \frac{1}{\rho b^M}\left(H^{cur}|\sigma| + \frac{1}{2}\Delta S\sigma^2 + \rho\Delta s_0(T - M_s)\right). \tag{2.6}$$

The other prominent models are the ones studied by Tanaka and co-workers [28], and Liang and Rogers [26]. Tanaka proposed the following exponential law for the evolution of the volume fraction for the forward martensitic transformation

$$\xi = 1 - \exp\left(A_m(T - M_s) + B_m\sigma\right), \tag{2.7}$$

while Liang proposed the so-called cosine model

$$\xi = \frac{1}{2}\left(\cos\left(a_M(T - M_f) + b_M\sigma\right) + 1\right), \tag{2.8}$$

where A_m, B_m, a_M, b_M etc. are related to the material properties. Note that for all the models given the stress, σ and the temperature, T, it is possible to uniquely determine the martensitic volume fraction, ξ, and thus find the strain, ϵ. Also note that the variable ξ can take values between 0 and 1. If for some value of σ the calculated value of ξ turns to be outside this range then it means that for that value of stress the SMA cannot be in a state of transformation (the transformation is already complete or not yet started).

4. Reverse Transformation

The governing equations for the reverse transformation are similar to those for the forward transformation and are summarized below

$$\begin{aligned} S &= S^A + \xi \left(S^M - S^A \right), \\ \alpha &= \alpha^A + \xi \left(\alpha^M - \alpha^A \right), \\ \epsilon &= S\sigma + \alpha(T - T_0) + H^{cur}\mathrm{sgn}(\sigma)\xi. \end{aligned} \tag{2.9}$$

The law for evolution of the volume fraction according to the Boyd-Lagoudas model is

$$\xi = \frac{1}{\rho b^A} \left(H^{cur}|\sigma| + \frac{1}{2}\Delta S\sigma^2 + \rho \Delta s_0 (T - A_f) \right). \tag{2.10}$$

The corresponding expressions for the exponential and the cosine models are

$$\xi = \exp\left(A_a(T - A_s) + B_a\sigma \right), \tag{2.11}$$

and

$$\xi = \frac{1}{2}\left(\cos\left(a_A(T - A_s) + b_A\sigma \right) + 1 \right). \tag{2.12}$$

5. Onset and End of Phase Transformations

The question of when a phase transformation begins and ends will be addressed next. For this discussion we will consider the Boyd-Lagoudas model only. By definition, ξ is 0 at the beginning of the forward transformation and 1 at the end. Thus, the start and end of the forward transformation can be found by substituting $\xi = 0, 1$ in Eq. 2.6. The beginning of forward transformation is given by

$$H^{cur}|\sigma| + \frac{1}{2}\Delta S\sigma^2 + \rho \Delta s_0 (T - M_s) = 0, \tag{2.13}$$

and the end of forward phase transformation is given by

$$H^{cur}|\sigma| + \frac{1}{2}\Delta S\sigma^2 + \rho\Delta s_0(T - M_s) - \rho b^M = 0. \tag{2.14}$$

Similarly, the onset of the reverse transformation is given by

$$H^{cur}|\sigma| + \frac{1}{2}\Delta S\sigma^2 + \rho\Delta s_0(T - A_f) - \rho b^A = 0, \tag{2.15}$$

and the end of the reverse phase transformation is given by

$$H^{cur}|\sigma| + \frac{1}{2}\Delta S\sigma^2 + \rho\Delta s_0(T - A_f) = 0. \tag{2.16}$$

Equations 2.13-2.16 can be used to generate what is called the phase diagram for the material. A phase diagram is basically the locus of points for the onset and end the forward and reverse transformations in the $T - \sigma$ space. Figure 16 shows the phase diagram corresponding to the material properties given in table II. Isothermal loading paths can be constructed by drawing constant temperature contours (vertical lines) on the phase diagram. Figure 17 shows an isothermal path with $T = 308K$. For a given temperature the intersection of the isothermal contour with the curves on the phase diagram gives the values of stress at which the various transformations end and begin. In figure 17, σ^{Ms} and σ^{Mf} are the stress values at the onset and end of the forward martensitic transformation, while σ^{As} and σ^{Af} are the stress values at the onset and end of the forward austenitic transformation.

6. Hysteresis in Stress-Strain Curves

Using Eqs. 2.1-2.16 and values of parameters given in table II the stress-strain curve shown in figure 18 can be obtained. Note that for $\sigma > 0$ (the case $\sigma < 0$ can be handled similarly) the forward transformation begins at $\epsilon = \epsilon^{Ms}$. This point corresponds to $\sigma = \sigma^{Ms}$ on the phase diagram shown in figure 17. It should be pointed out that

Table II. Typical values of material constants.

Quantity	Value
E^A	55 GPa
α^A	22 10^{-6}/K
E^M	46 GPa
α^M	22 10^{-6}/K
M_f	230 K
M_s	245 K
A_f	280 K
A_s	270 K
H^{cur}	0.056
C^A	7.4 MPa/K
C^M	7.4 MPa/K

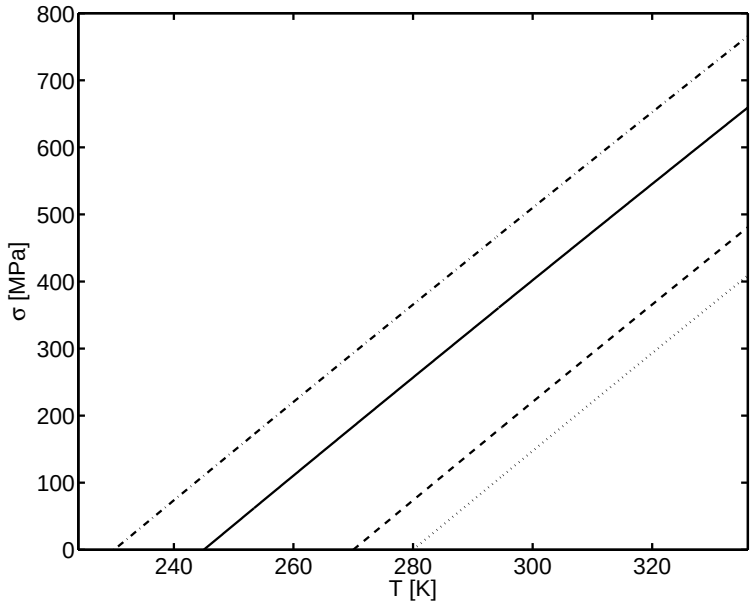

Fig. 16. Phase diagram for a typical SMA.

Eqs. 2.13-2.16 were solved to obtain stress levels at which transformations start or end, however, one can equivalently talk about strain at which the transformations begin or end. Continuing the discussion, the forward transformation ends at $\epsilon = \epsilon^{Mf}$ ($\sigma = \sigma^{Mf}$). Similarly, the reverse transformation begins at $\epsilon = \epsilon^{As}$ etc. Finally, if the system is undergoing a forward transformation, say at $\xi = 0.5$ and the strain is decreased, then the transformation stops and the constitutive relations are given by law of mixtures. This is depicted by the dashed line in figure 18. The transformation starts again when the strain reaches a critical level again, i.e., when the dashed line hits the forward or reverse transformation curve.

The pair (ϵ, σ) can be considered to be a hysteretic input-output pair in the sense in which hysteresis was defined in chapter I. The two lobes in the (ϵ, σ) curve in figure 18 form the major loop of hysteresis. The paths traced by reverting the strain

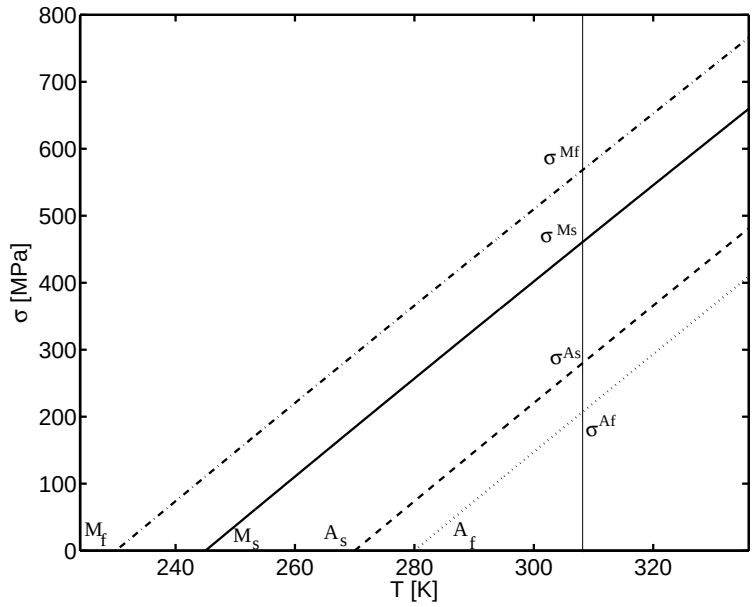

Fig. 17. An isothermal loading path on the phase diagram.

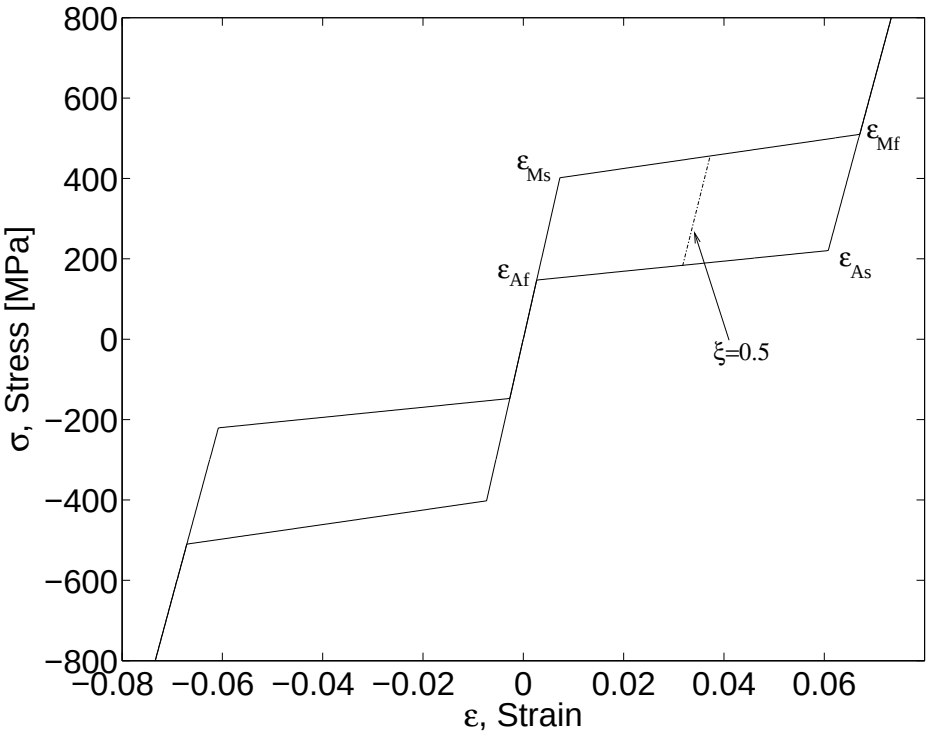

Fig. 18. Stress-strain curve for a typical SMA element.

before completion of the ongoing transformation comprise the minor loops. Note that there are certain similarities in the hysteresis shown in figure 18 and the multilinear model of hysteresis introduced in chapter I. As with the multilinear model, the loading and unloading on the major loop take place along curves of different slopes. The bounding curves of the hysteretic lobes can be approximated by straight lines to a good degree of accuracy. On the other hand, the hysteresis shown by the pair (ϵ, σ) is different from the multilinear model because the region of hysteresis is bounded, and within the region of hysteresis the pair (ϵ, σ) evolves on many different curves as contrast to two for the multilinear model.

C. Hybrid System

In section B it was discussed how a SMA element can be in one of five possible modes and how the transitions between these modes take place. Based on the discussion presented there, a SMA can be represented by a hybrid system as shown in figure 19. As depicted in the figure, the SMA can be in either one of the five states discussed earlier: a). forward transformation, b). reverse transformation, c). pure austenite, d). pure martensite, and e). non-transforming mixture. The dynamic behavior of the SMA is specified by specifying the dynamics for each of these modes and defining consistent rules for transitions amongst modes. Such a description is consistent with that of a hybrid system with various modes and well defined mode transitions.

The transition between the first four modes occurs when stress (or equivalently, strain) hits one of the boundaries defined by Eqs. 2.13-2.16. A transition to a non-transforming mixture takes place when the system is unloaded before completing the transformation. The transition from a non-transforming mixture to a transforming one occurs when the stress becomes equal to that for the forward or reverse trans-

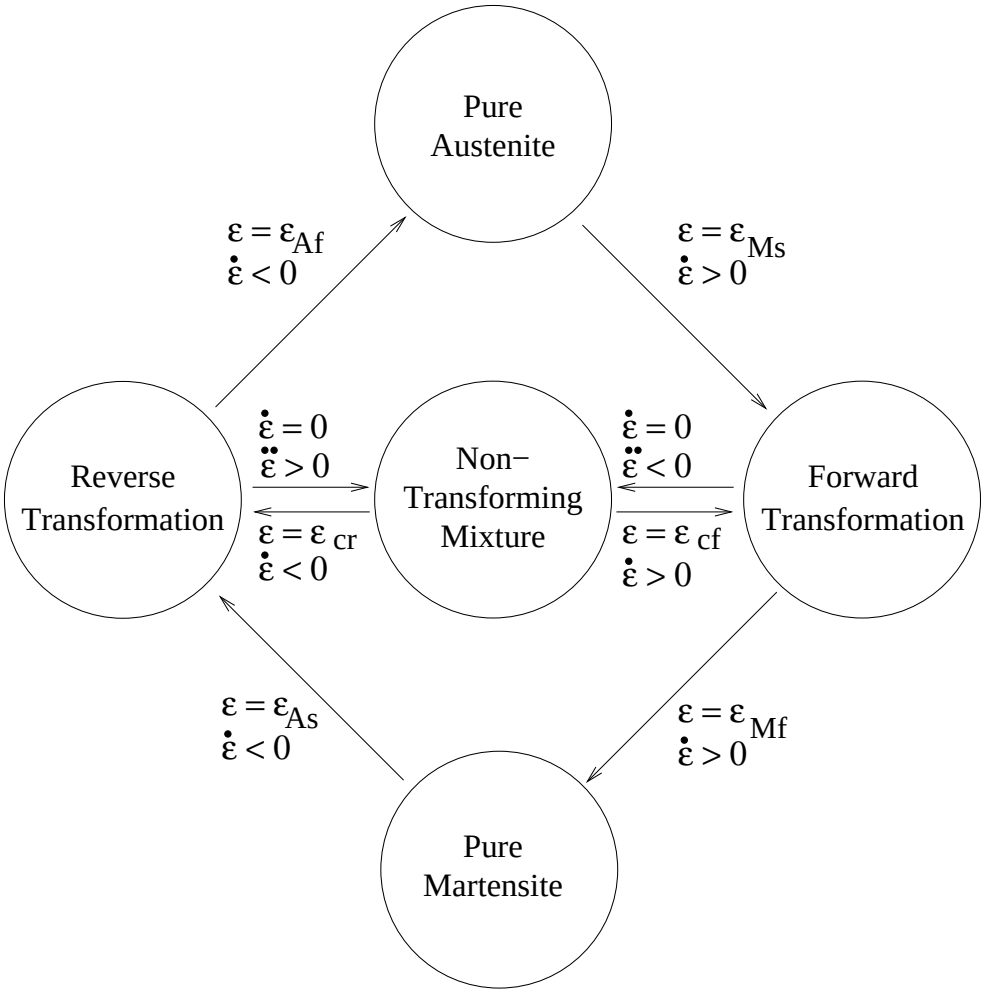

Fig. 19. A hybrid automaton representation of an element SMA.

formation at the given volume fraction. In figure 19 this critical value is denoted by ϵ_{cr} for the reverse transformation and ϵ_{cf} for the forward transformation. Note again that the volume fraction remains constant for a non-transforming mode.

Let us denote the five states of a SMA in 1-D stress as states I, II, III, IV, and V. Namely, state I corresponds to the forward transformation, state II corresponds to the reverse transformation, state III corresponds to pure austenite, state IV corresponds to pure martensite, and state V corresponds to non-transforming mixture. For convenience we define the following functions

$$f_1(\sigma) = H^{cur}|\sigma| + \frac{1}{2}\Delta S\sigma^2 + \rho\Delta s_0(T - M_s), \tag{2.17}$$

$$f_2(\sigma) = H^{cur}|\sigma| + \frac{1}{2}\Delta S\sigma^2 + \rho\Delta s_0(T - M_s) - \rho b^M, \tag{2.18}$$

$$f_3(\sigma) = H^{cur}|\sigma| + \frac{1}{2}\Delta S\sigma^2 + \rho\Delta s_0(T - A_f) - \rho b^A, \tag{2.19}$$

$$f_4(\sigma) = H^{cur}|\sigma| + \frac{1}{2}\Delta S\sigma^2 + \rho\Delta s_0(T - A_f), \tag{2.20}$$

$$f_5(\sigma) = \xi_V - \frac{1}{\rho b^M}\left(H^{cur}|\sigma| + \frac{1}{2}\Delta S\sigma^2 + \rho\Delta s_0(T - M_s)\right), \tag{2.21}$$

$$f_6(\sigma) = \xi_V - \frac{1}{\rho b^A}\left(H^{cur}|\sigma| + \frac{1}{2}\Delta S\sigma^2 + \rho\Delta s_0(T - A_f)\right), \tag{2.22}$$

where ξ_V is the value of the volume fraction at the beginning of state V. The rules for state transitions for the SMA are summarized in table III. Figure 19 provides equivalent rules for the state transitions in terms of ϵ alone. The rules summarized in the figure can be easily deduced from those presented in table III. Having summarized the rules for the transitions, we summarize the constitutive relations for each state.

State I (forward transformation)

$$\epsilon = S\sigma + \alpha(T - T_0) + H^{cur}\mathrm{sgn}(\sigma)\xi, \tag{2.23}$$

$$\xi = \frac{1}{\rho b^M}\left(H^{cur}|\sigma| + \frac{1}{2}\Delta S\sigma^2 + \rho\Delta s_0(T - M_s)\right). \tag{2.24}$$

Table III. Rules for state transitions for SMA materials in 1-D stress.

Transition	Rule
$I \rightarrow IV$	$f_2(\sigma) = 0, \dot{\epsilon} > 0$
$I \rightarrow V$	$\dot{\epsilon} = 0, \ddot{\epsilon} < 0$
$II \rightarrow III$	$f_4(\sigma) = 0, \dot{\epsilon} < 0$
$II \rightarrow V$	$\dot{\epsilon} = 0, \ddot{\epsilon} > 0$
$III \rightarrow I$	$f_1(\sigma) = 0, \dot{\epsilon} > 0$
$IV \rightarrow II$	$f_3(\sigma) = 0, \dot{\epsilon} < 0$
$V \rightarrow I$	$f_5(\sigma) = 0, \dot{\epsilon} > 0$
$V \rightarrow II$	$f_6(\sigma) = 0, \dot{\epsilon} < 0$

State II (reverse transformation)

$$\epsilon = S\sigma + \alpha(T - T_0) + H^{cur}\text{sgn}(\sigma)\xi, \tag{2.25}$$

$$\xi = \frac{1}{\rho b^A}\left(H^{cur}|\sigma| + \frac{1}{2}\Delta S\sigma^2 + \rho\Delta s_0(T - A_f)\right). \tag{2.26}$$

State III (pure austenite)

$$\epsilon = S^A\sigma + \alpha^A(T - T_0). \tag{2.27}$$

State IV (pure martensite)

$$\epsilon = S^M\sigma + \alpha^M(T - T_0) + H^{cur}\text{sgn}(\sigma). \tag{2.28}$$

State V (non-transforming mixture, ξ is constant)

$$\epsilon = S\sigma + \alpha(T - T_0) + H^{cur}\text{sgn}(\sigma)\xi. \tag{2.29}$$

CHAPTER III

PROBLEM FORMULATION

The aim of this chapter is to present the problem that will be studied in rest of this thesis. In a nutshell we aim to study the transient and long-term behavior of an oscillator with hysteretic restoring force and sinusoidal excitation. Figure 20 shows a cartoon of one possible mechanical realization of such a system. In the mechanical system shown in figure 20 $x(t)$ represents the displacement of the cart of unit mass, where t is the time. In general x and t are the dependent and the independent variables, respectively. For the system shown in figure 20 we can write the following equation of motion

$$\ddot{x} = A\cos(\omega t) - F(x, F_0, \rho)(t), \tag{3.1}$$

where $F(x, F_0, \rho)(t)$ is the hysteretic restoring force, F_0 is the initial value of the restoring force, and ρ is a vector of system parameters. As described in chapter I $F(x, F_0, \rho)(t)$ is not a function, rather it is a hysteretic operator that acts on the initial value F_0 and the history of $x(t)$ to output the present value of the restoring force F. We will use the bilinear and multilinear models of hysteresis for modeling the hysteretic restoring force. Instead of using the variational-inequality formulation for

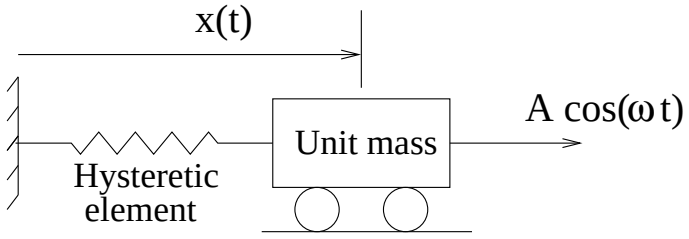

Fig. 20. An oscillator with hysteretic restoring force and sinusoidal excitation.

the bilinear and multilinear models of hysteresis we will present equivalent definitions for these models using a hybrid systems framework. When defined in this manner, these models can also be considered as finite state machines or finite state automata.

A. Bilinear Hysteresis

Recall that we defined the most general bilinear hysteretic operator using variational inequalities in chapter I. In this section we will consider the bilinear hysteretic operator as a finite state automaton (FSA). A FSA has a finite number of states and rules for transitions between states. Each state is characterized by its unique properties. In our case each state will have a unique input-output relation between the pair (x, F). Also, each state can maintain certain memory variables.

1. States or Modes of Bilinear Hysteretic Automaton

We define the bilinear hysteretic operator as having four states (or modes), namely, states I, II, III, and IV. For each of the states the relation between the pair (x, F) is linear. We will first define the input-output relations for each of these states and then discuss the rules for transitions between them. Figure 21 shows the input-output dynamics for the four modes. The relation between pair (x, F) is simple for states II, IV and is given as follows

$$\begin{aligned} F_{II} &= (1-\epsilon)x - \epsilon, \\ F_{IV} &= (1-\epsilon)x + \epsilon, \end{aligned} \tag{3.2}$$

where ϵ is a parameter. We will have more to say about the relevance of the parameter ϵ in section 3. The range of the bilinear hysteretic operator is $(-\infty, \infty)$, and the region of hysteresis is the strip defined by $|F - (1-\epsilon)x| \leq \epsilon$. The states I, III maintain a memory variable which stores the value of the variable x at the time the state is

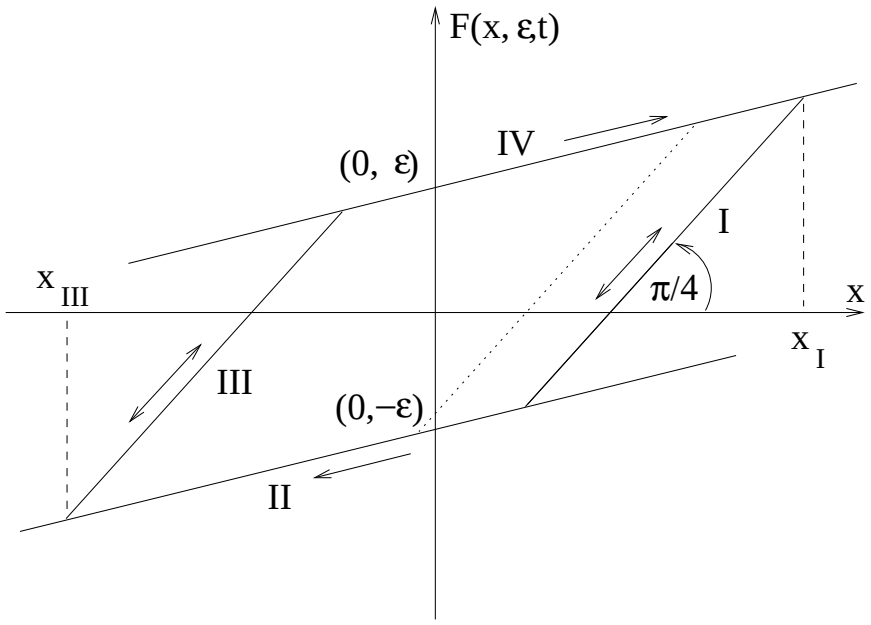

Fig. 21. Four states or modes of the bilinear hysteretic operator.

entered. We represent these variables by x_I and x_{III}, respectively. Thus, if state I is entered at $x = 0.25$ (say) then x_I is set to 0.25 and remains at that value till state I is entered again, at which time it gets set to the corresponding value of x. Knowing x_I and x_{III} the relationship between the pair (x, F) for modes I, III are

$$\begin{aligned} F_I &= x - \epsilon(x_I - 1), \\ F_{III} &= x - \epsilon(x_{III} + 1). \end{aligned} \tag{3.3}$$

2. Mode Transitions

We next define the rules for transitions between the various modes. In the present model there are six permitted transitions: $I \rightarrow II$, $I \rightarrow IV$, $II \rightarrow III$, $III \rightarrow IV$, $III \rightarrow II$, and $IV \rightarrow I$. The rules for these transitions are presented in table IV. These rules are to be interpreted in the following manner. Suppose that the automa-

Table IV. Rules for state transitions in bilinear model.

Transition	Rule
$I \rightarrow II$	$x = x_I - 2,\ \dot{x} < 0$
$I \rightarrow IV$	$x = x_I,\ \dot{x} > 0$
$II \rightarrow III$	$\dot{x} = 0,\ \ddot{x} > 0$
$III \rightarrow IV$	$x = x_{III} + 2,\ \dot{x} > 0$
$III \rightarrow II$	$x = x_{III},\ \dot{x} < 0$
$IV \rightarrow I$	$\dot{x} = 0,\ \ddot{x} < 0$

ton is in state I and suppose that $x_I = 1$. Then, if x decreases and reaches a value of -1 with a negative velocity then all conditions for the rule for transition from state I to II are satisfied and the specified transition will occur. Note that the relationship between the pair (x, F) is defined such that F is continuous with respect to x across transitions.

Finally, we should mention that there certain consistency conditions that need to be satisfied by the automaton. These conditions are listed in table V. The consistency conditions for states I, III are to ensure that the pair (x, F) is within the permitted region of hysteresis at all times. The condition for state II indicates that loading is not possible in state II, i.e., x cannot increase in state II. Similarly, the condition for state IV indicates that unloading is not possible in state IV. It should also be noted that the main role of these conditions is to ensure that the initial conditions are consistent with the description of the automaton. Once proper initialization is done, the consistency conditions are automatically satisfied at all times just by following the proper transition rules and input-output relations. The valid transitions for the bilinear hysteretic automaton and the corresponding rules are shown in a compact

Table V. Consistency conditions for various states in the bilinear model.

State	Consistency Condition
I	$\lvert F-(1-\epsilon)x\rvert \leq \epsilon$
II	$\dot{x} < 0$
III	$\lvert F-(1-\epsilon)x\rvert \leq \epsilon$
IV	$\dot{x} > 0$

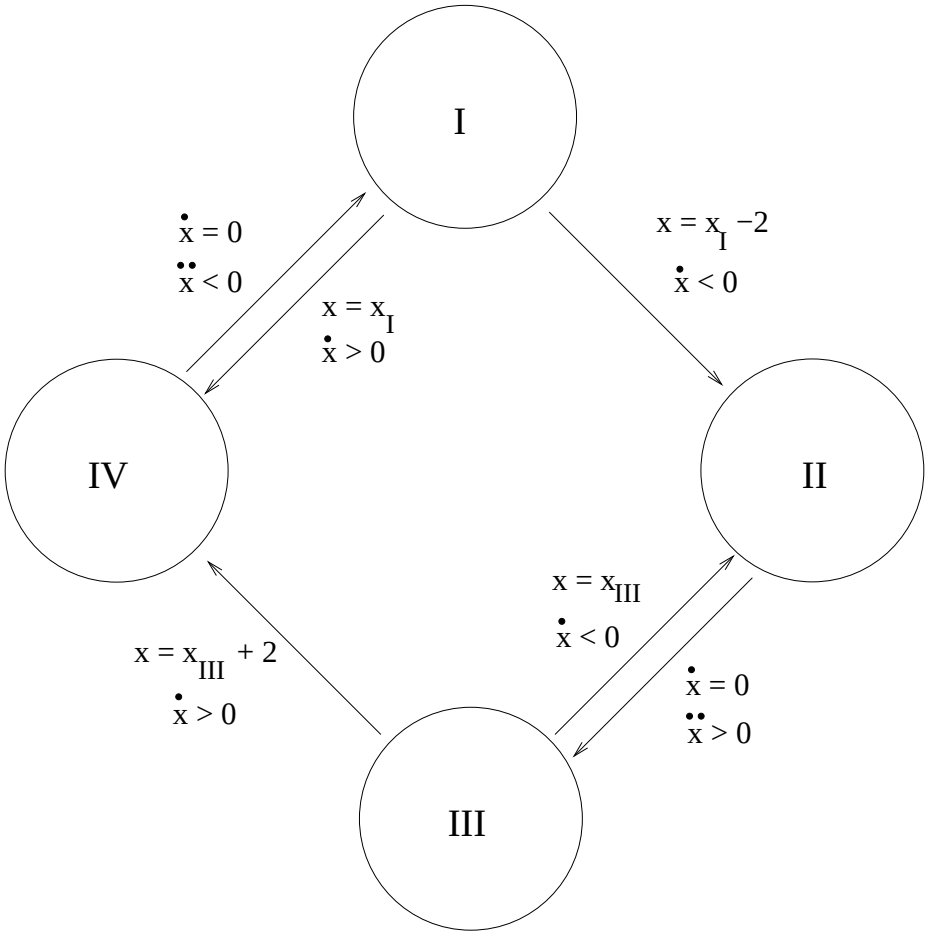

Fig. 22. State transitions for bilinear hysteresis.

manner in figure 22.

3. Role of ϵ

In the previous sections we introduced ϵ as a parameter in the bilinear model of hysteresis. In the later chapters of this thesis we will treat ϵ as a small parameter and carry out perturbation expansions in terms of ϵ. It should be noted that there is a special significance to the case of $\epsilon = 0$. If we set $\epsilon = 0$ in Eqs. 3.2 and 3.3, we get

$$\begin{aligned} F_I &= x, \\ F_{II} &= x, \\ F_{III} &= x, \\ F_{IV} &= x. \end{aligned} \tag{3.4}$$

Thus, for the case of $\epsilon = 0$ the bilinear hysteretic operator reduced to a simple identity function (returns the same value as the input). In context of the system defined by Eq. 3.1 this case corresponds to a simple harmonic oscillator with sinusoidal excitation and natural frequency equal to one. This can be seen by substituting the simplified expressions for F in Eq. 3.1 as follows

$$\ddot{x} + x = A\cos(\omega t). \tag{3.5}$$

Thus, in some sense the norm of ϵ is a measure of strength of hysteresis, and of the nonlinearity in the system.

B. Multilinear Hysteresis

In chapter I we introduced the multilinear hysteretic operator as a generalization of the bilinear hysteretic operator. Thus, it is expected that the automaton description of the multilinear hysteretic operator will not be much different from that of the

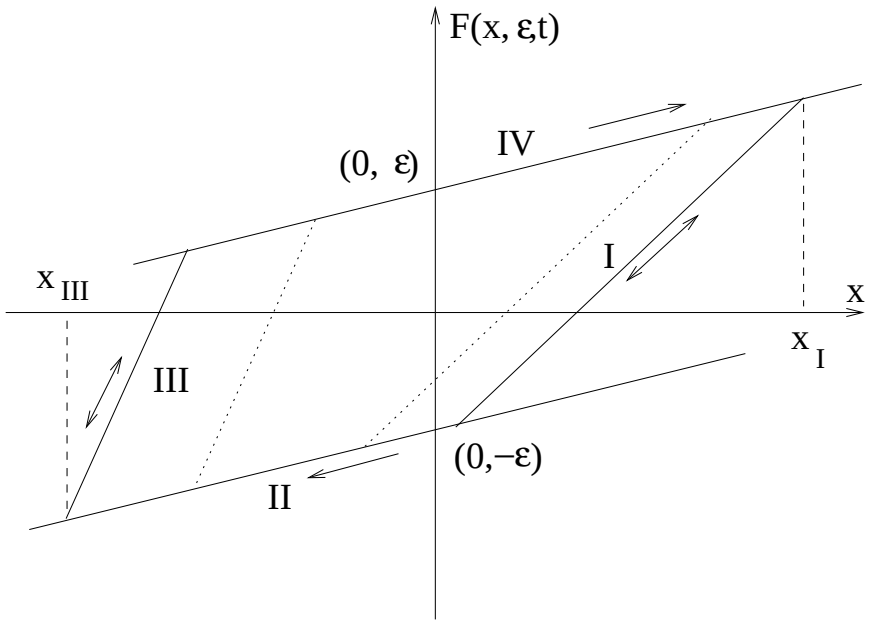

Fig. 23. Four states or modes of the multilinear hysteretic operator.

bilinear one. Without explaining everything afresh, we will take analogies from the bilinear hysteretic automaton to introduce and define its multilinear counterpart.

1. States or Modes of Multilinear Hysteretic Automaton

As with the bilinear case, the multilinear automaton has four states, namely, I, II, III, and IV. The dynamics of these states are shown in figure 23 The relation between pair (x, F) for the four states are given by

$$\begin{aligned} F_I &= (1-\alpha\epsilon)x - x_I\epsilon(1-\alpha) + \epsilon, \\ F_{II} &= (1-\epsilon)x - \epsilon, \\ F_{III} &= (1+\alpha\epsilon)x - x_{III}\epsilon(1+\alpha) - \epsilon, \\ F_{IV} &= (1-\epsilon)x + \epsilon. \end{aligned} \tag{3.6}$$

Table VI. Rules for state transitions in multilinear model.

Transition	Rule
$I \rightarrow II$	$x = x_I - 2/(1-\alpha),\ \dot{x} < 0$
$I \rightarrow IV$	$x = x_I,\ \dot{x} > 0$
$II \rightarrow III$	$\dot{x} = 0,\ \ddot{x} > 0$
$III \rightarrow IV$	$x = x_{III} + 2/(1+\alpha),\ \dot{x} > 0$
$III \rightarrow II$	$x = x_{III},\ \dot{x} < 0$
$IV \rightarrow I$	$\dot{x} = 0,\ \ddot{x} < 0$

Notice that the multilinear model has two parameters, ϵ and α, in contrast to only one parameter for the bilinear case. A discussion about the relevance of these parameters is presented in section 3.

2. Mode Transitions

The automaton representation of multilinear hysteretic operator also has six legal transitions, viz., $I \rightarrow II,\ I \rightarrow IV,\ II \rightarrow III,\ III \rightarrow IV,\ III \rightarrow II$, and $IV \rightarrow I$. Table VI contains the rules for these transitions. The interpretation of the rules is same as that for the bilinear case. Figure 24 shows the valid transitions and the associated rules in a graphical format. The consistency conditions for the multilinear automaton are exactly the same as those for the bilinear one. Nonetheless, they are listed in table VII for the sake of completeness.

3. Role of Parameters ϵ and α

The interpretation that we presented for ϵ as a measure of the nonlinearity in the system for the bilinear case holds for the multilinear case as well. In fact it is easy to

Table VII. Consistency conditions for various states in the multilinear model.

State	Consistency Condition
I	$\lvert F-(1-\epsilon)x\rvert \leq \epsilon$
II	$\dot{x} < 0$
III	$\lvert F-(1-\epsilon)x\rvert \leq \epsilon$
IV	$\dot{x} > 0$

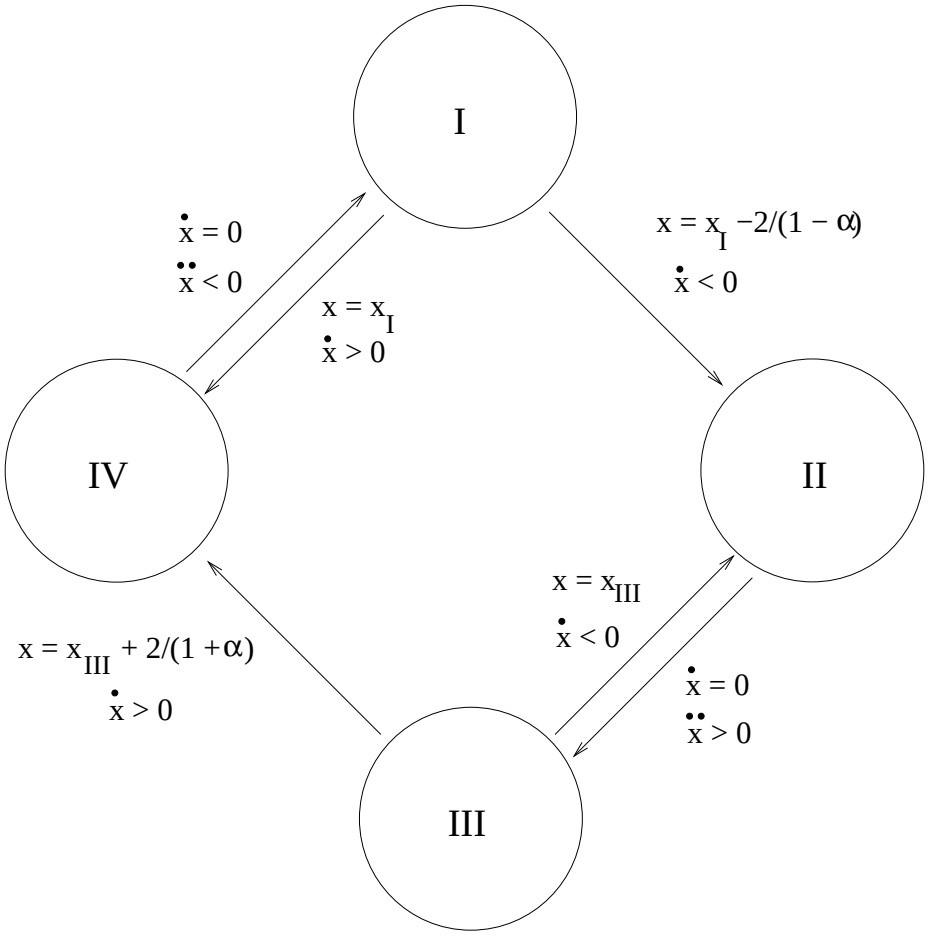

Fig. 24. State transitions for multilinear hysteresis.

see that the set 3.6 reduces to the identity map on substituting $\epsilon = 0$. The interesting fact is that substituting $\alpha = 0$ in the set 3.6 results in the following equations

$$\begin{aligned} F_I &= x - \epsilon(x_I - 1), \\ F_{II} &= (1-\epsilon)x - \epsilon, \\ F_{III} &= x - \epsilon(x_{III} + 1), \\ F_{IV} &= (1-\epsilon)x + \epsilon, \end{aligned} \tag{3.7}$$

which are exactly the same as the sets 3.2 and 3.3. Thus, in the limit of $\alpha \to 0$ the multilinear hysteretic operator reduces to the bilinear hysteretic operator. In this sense α is a measure of the distance between the multilinear hysteretic operator and its bilinear counterpart.

C. Oscillator with Hysteresis

In this section we present the problem that will be the object of investigation in this thesis. Consider the following system

$$\ddot{x} + F(x, F_0, \epsilon, \alpha)(t) = A\cos(\omega t), \tag{3.8}$$

with the following initial conditions

$$x(t_0) = x_0, \dot{x}(t_0) = v_0, F(t_0) = F_0, S(t_0) = S_0, \tag{3.9}$$

where F is the bilinear or the multilinear hysteretic operator, $S_0 \in \{I, II, III, IV\}$ is the initial state of the automaton, and ϵ and α are constants ($\alpha = 0$ for the case of bilinear hysteresis).

We state the following problem: Given the system 3.8 and the initial conditions 3.9 study the transient and the long-term behavior of system.

We will attack this problem using at least three different approaches. On one front we will use perturbation techniques to find asymptotic expansions for the response of the system in terms of the small parameter ϵ. On another front we will define techniques for high-fidelity numerical simulations of the system. This technique will be used to study the transient response of the system. Yet another attack on the problem will be devised by constructing Poincaré maps for study of steady state response of the system. We will use bifurcation and continuation techniques for study of these maps.

It is easy to see that for any given state (I, II, III or IV) of the automaton Eq. 3.8 reduces to the equation of motion of a simple harmonic oscillator with sinusoidal forcing, and thus it can be solved in closed-form. We will conclude this chapter by presenting these closed-form solutions, and demonstrating how these can be patched to form the time response of the system.

1. Closed-form Solutions and State Transitions

The idea behind trying to write the closed-form solutions for individual states is the following. Starting from an initial condition and an initial state, as time progress and the system evolves, the criteria from certain state transitions might get satisfied and the system may switch from one state to other. Given the initial conditions we can write the closed-form solutions for all states, thus we can construct the complete solution for the system if can calculate the time of state transitions. We will soon write down the equations that need to be solved to find these transition times. It turns out that solving these equations is not a trivial task and we will present a methodology for solving them in Appendix B.

We can simplify Eq. 3.8 a bit by noting that the independent variable t occurs explicitly only in the sinusoidal term, thus we can set $t_0 = 0$ without the loss of

Table VIII. Parameters in expression for F for different states.

State	Parameters
I	$\omega_o^2 = 1 - \alpha\epsilon,\ k = x_I\epsilon(1-\alpha) - \epsilon$
II	$\omega_o^2 = 1 - \epsilon,\ k = \epsilon$
III	$\omega_o^2 = 1 + \alpha\epsilon,\ k = x_{III}\epsilon(1+\alpha) + \epsilon$
IV	$\omega_o^2 = 1 - \epsilon,\ k = -\epsilon$

generality if we introduce a phase variable ϕ defined by

$$\phi = \omega t_0 \mod 2\pi. \tag{3.10}$$

Equation 3.8 can then be re-written as

$$\ddot{x} + F(x, F_0, \epsilon, \alpha)(t) = A\cos(\omega t + \phi), \quad t \geq 0, \tag{3.11}$$

with the initial conditions specified at $t = 0$. For any given state the most general form of F can be written as

$$F = \omega_o^2 x - k, \tag{3.12}$$

where the parameters ω_o and k take different values for different states. These values are listed in table VIII. Thus, Eq. 3.11 can be further simplified to become

$$\ddot{x} + \omega_o^2 x = A\cos(\omega t + \phi) + k, \quad t \geq 0, \tag{3.13}$$

where ω_o, k depend on the current state as indicated in table VIII. The general solution to Eq. 3.13 can we written as follows (assuming non-resonant forcing)

$$\begin{aligned} x(t) = &\left(x_0 - \frac{k}{\omega_o^2} - \frac{A\cos\phi}{\omega_o^2 - \omega^2}\right)\cos(\omega_o t) + \frac{1}{\omega_o}\left(v_0 + \frac{A\omega\sin\phi}{\omega_o^2 - \omega^2}\right)\sin(\omega_o t) \\ &+ \frac{A}{\omega_o^2 - \omega^2}\cos(\omega t + \phi) + \frac{k}{\omega_o^2}. \end{aligned} \tag{3.14}$$

The initial conditions x_0, v_0 for different states are found by continuity of solution at state transitions. Thus, if a $I \rightarrow II$ transition occurs at $x = 1.2, \dot{x} = -0.5, t = 2.3$ (say) then the corresponding initial conditions for the solution in state II will be $x_0 = 1.2, v_0 = 0.5, \phi = 2.3\omega \mod 2\pi$ etc. Note that v_0 is always equal to zero for states I, III, $v_0 < 0$ for state II and $v_0 > 0$ for state IV.

2. Some Trajectories

In this section we present some typical trajectories obtained for various values of the system parameters. We show two kinds of trajectories, those corresponding to transient behavior of the system, and those corresponding to to its long-term behavior. The long-term behavior of the system often involves a steady state response. Figure 25 shows the typical transient response of the bilinear oscillator. Note how the continuity of the variables is maintained across state transitions. Figures 26 and 27 show the typical steady state response for bilinear and multilinear oscillator, respectively.

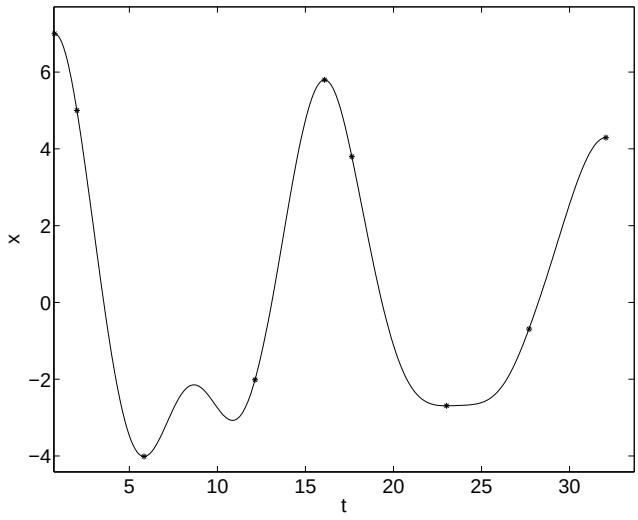

(a) $x(t)$ versus t

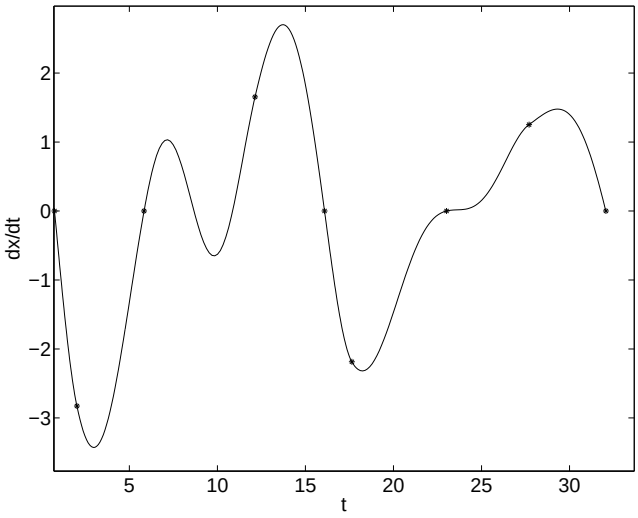

(b) $\dot{x}(t)$ versus t

Fig. 25. Typical transient behavior for the bilinear oscillator. $\epsilon = 0.4, A = 2.0, \omega = 0.4$ $x(0) = 7, \dot{x}(0) = 0, \phi = 0.3$, starting state $= I$. The beginning and the mode transitions are marked by '*'. Transition sequence $I \rightarrow II \rightarrow III \rightarrow IV \rightarrow I \rightarrow II \rightarrow III \rightarrow IV \rightarrow I$.

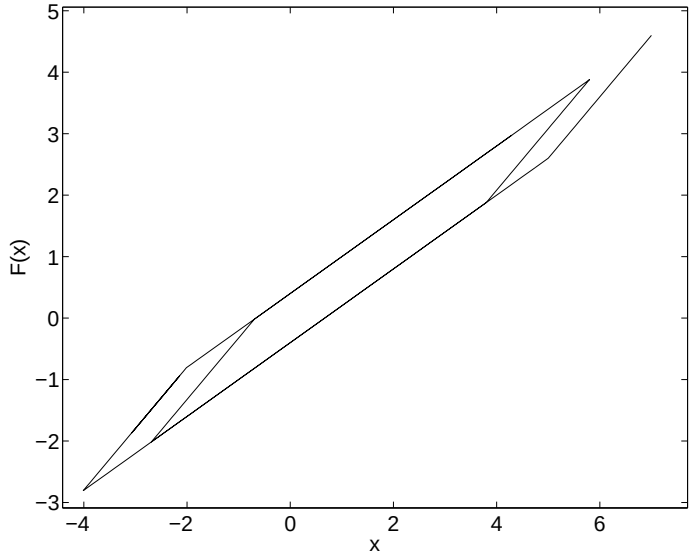

(c) F versus x

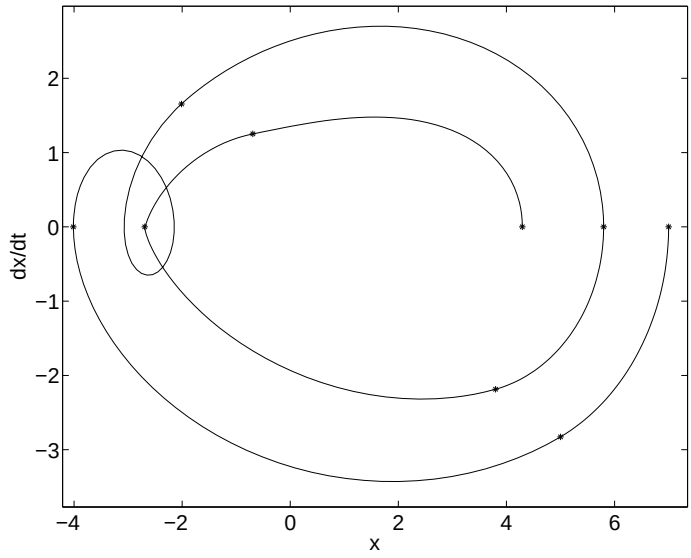

(d) $\dot{x}$ versus x

Fig. 25. Continued ...

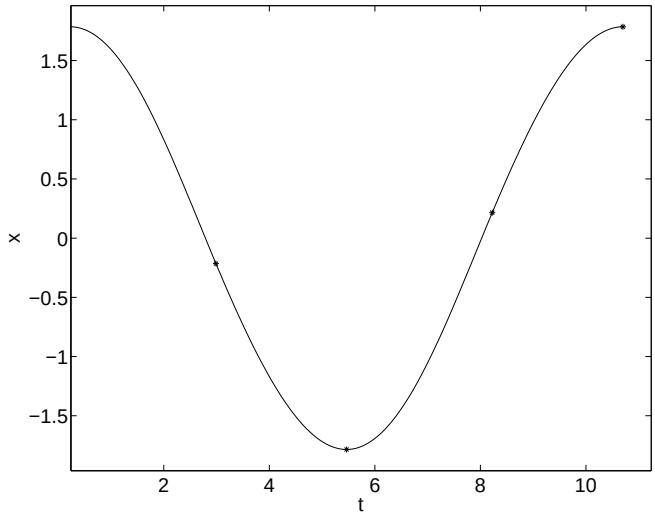

(a) $x(t)$ versus t

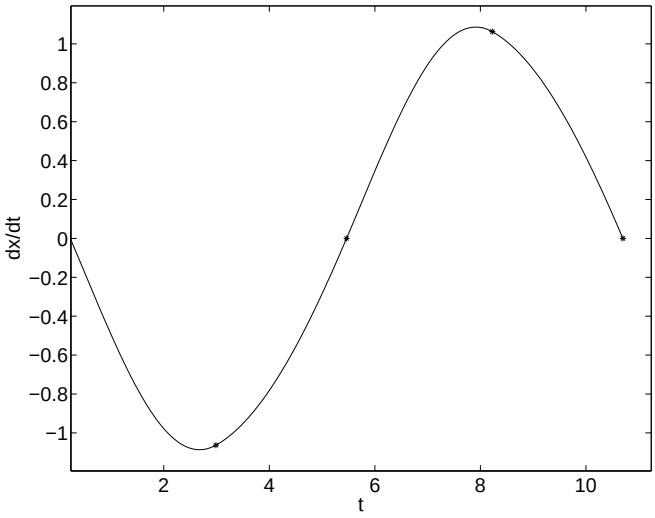

(b) $\dot{x}(t)$ versus t

Fig. 26. Typical steady state response for the bilinear oscillator. $\epsilon = 0.2, A = 1.0, \omega = 0.6$. The beginning and the mode transitions are marked by '*'. Transition sequence $I \rightarrow II \rightarrow III \rightarrow IV \rightarrow I$.

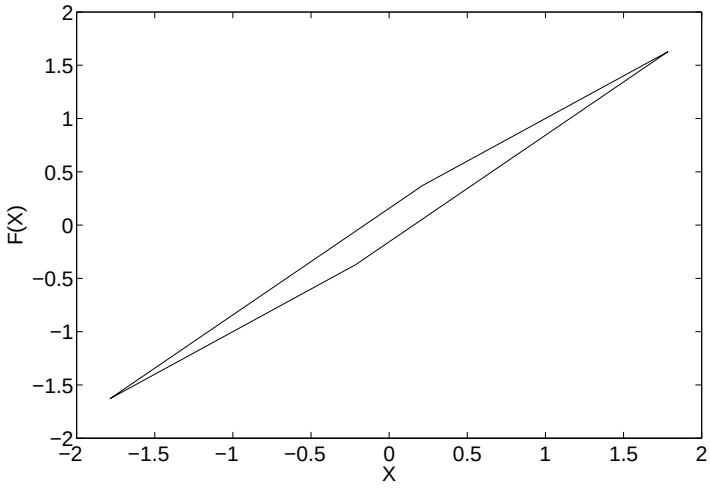

(c) F versus x

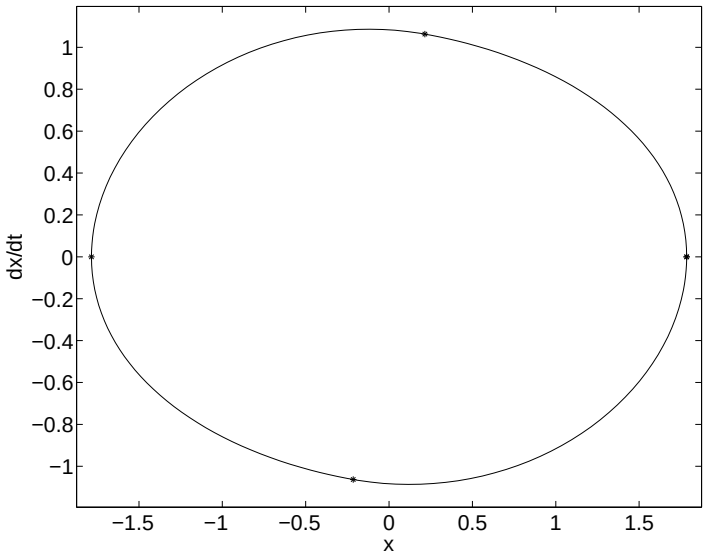

(d) $\dot{x}$ versus x

Fig. 26. Continued ...

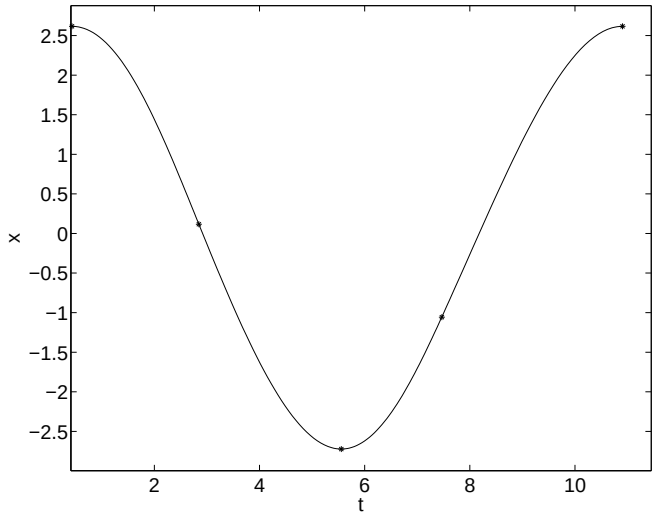

(a) $x(t)$ versus t

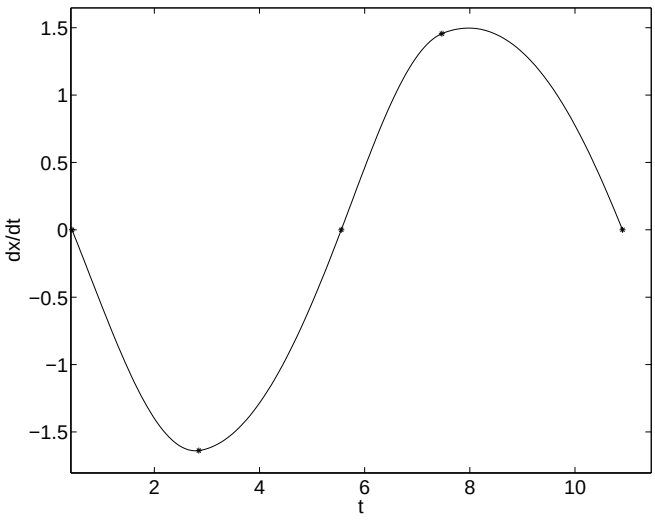

(b) $\dot{x}(t)$ versus t

Fig. 27. Typical steady state response for the multilinear oscillator. $\epsilon = 0.3, \alpha = 0.2, A = 1.2, \omega = 0.6$. The beginning and the mode transitions are marked by '*'. Transition sequence $I \rightarrow II \rightarrow III \rightarrow IV \rightarrow I$.

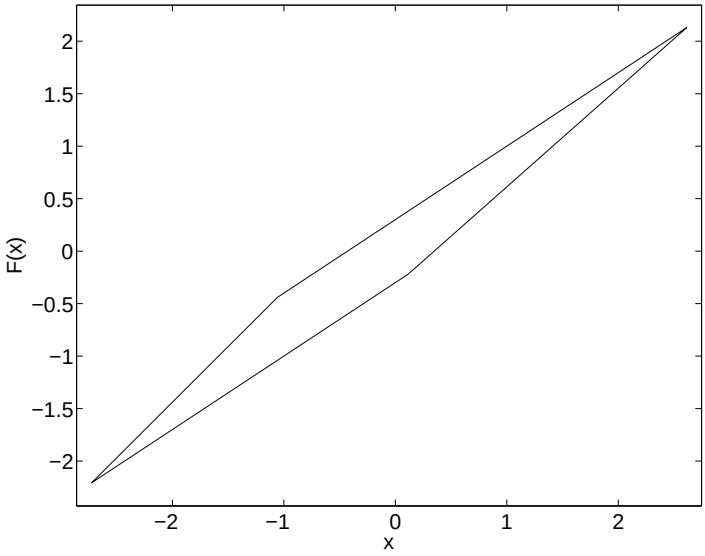

(c) F versus x

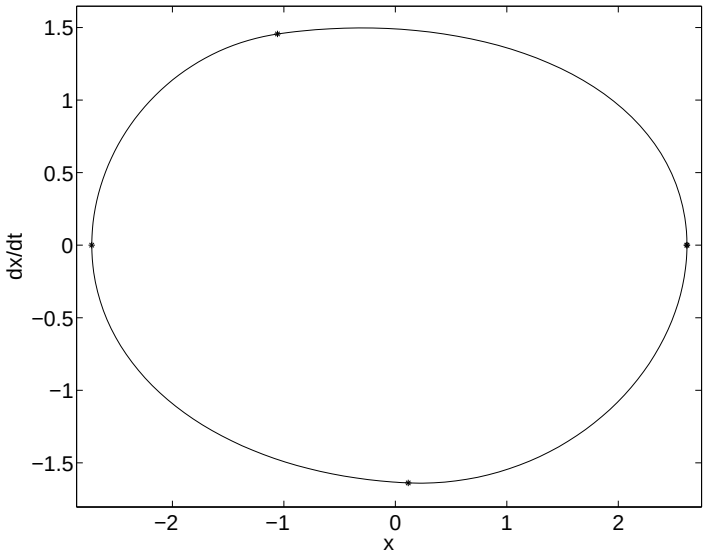

(d) $\dot{x}$ versus x

Fig. 27. Continued ...

CHAPTER IV

OSCILLATORS WITH BILINEAR HYSTERESIS AND SINUSOIDAL EXCITATION

In this chapter we will analyze systems of the form

$$\ddot{x} + F(x, F_0, \epsilon)(t) = A\cos(\omega t), \tag{4.1}$$

where F is the bilinear hysteretic operator discussed in chapter III. Caughey [24] studied similar systems in detail using the KBM method, and the development presented in section A is essentially a reproduction of his work. We include this development for the sake of completeness, and for comparison with the more advanced results to be presented later.

The main focus of this chapter will be on the long-term behavior of the bilinear hysteretic oscillator. The reason for this choice is that due to the dissipation present in the system the transient behavior is relatively short and the effect of initial conditions gets subsided after a few oscillations. We will use two tools for the analysis of the long-term behavior of the system. On one hand we will derive first-order asymptotic expansions for simple steady state response of the system using the KBM method. On the other hand we will define return-maps (or Poincaré maps) for the system, thus reducing the problem of studying the steady state response of the full system to studying the fixed points of this map. The numerical implementation of these maps will use the root-finding methodology discussed in Appendix B. The analysis of these maps will be done using continuation and bifurcation techniques.

A. KBM Analysis of Simple Orbits

Consider again the system

$$\ddot{x} + F(x, F_0, \epsilon)(t) = A\cos(\omega t). \tag{4.2}$$

We will analyze the simple steady state response of Eq. 4.2. By 'simple steady state response' we mean a steady state response with principal period of $2\pi/\omega$ and the following mode transition sequence $\rightarrow I \rightarrow II \rightarrow III \rightarrow IV \rightarrow I \ldots$. Following the KBM method we assume a steady state response with slowly varying amplitude and frequency

$$x(t) = R(t)\cos(\omega t + \phi(t)), \tag{4.3}$$

where

$$\begin{aligned} \dot{R}(t) &\sim \mathcal{O}(\epsilon), \\ \dot{\phi}(t) &\sim \mathcal{O}(\epsilon). \end{aligned} \tag{4.4}$$

Equation 4.4 means that $R(t)$ and $\phi(t)$ are assumed to be slowly varying with time. In the following development the parenthetical t will be dropped for convenience. For the sake of book-keeping we introduce a new variable θ defined as

$$\theta = \omega t + \phi. \tag{4.5}$$

It is clear that $\theta = 0$ at the beginning of state I of the automaton (see chapter III for details about the automaton description). Starting from state I it is easy to see that the automaton will circle over states II, III, and IV as θ goes from 0 to 2π, and the pair (x, F) will trace a loop like the one shown in figure 28. The value of θ at which the various mode transitions occur can be calculated in closed-form. These values are indicated in table IX. Knowing the assumed response we can use Eqs. 3.2,

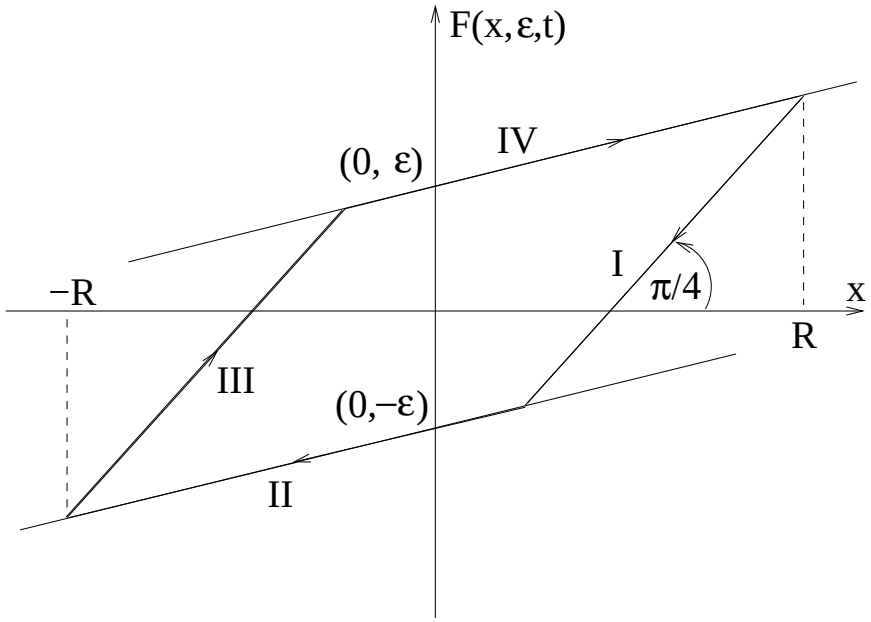

Fig. 28. Bilinear hysteretic restoring force.

Table IX. Value of θ at various mode transitions for simple cycles of the bilinear oscillator.

Transition	θ value
$I \rightarrow II$	$\theta_{I\rightarrow II} = \arccos(1 - 2/R)$
$II \rightarrow III$	$\theta_{II\rightarrow III} = \pi$
$III \rightarrow IV$	$\theta_{III\rightarrow IV} = \pi + \arccos(1 - 2/R)$
$IV \rightarrow I$	$\theta_{IV\rightarrow I} = 2\pi$

3.3 to write the following expressions for the relation between the pair (x, F) for the four states of the automaton

$$\begin{aligned} F_I &= x + (1-R)\epsilon, \\ F_{II} &= (1-\epsilon)x - \epsilon, \\ F_{III} &= x + (R-1)\epsilon, \\ F_{IV} &= (1-\epsilon)x + \epsilon. \end{aligned} \tag{4.6}$$

Differentiating Eq. 4.3 with respect to time,

$$\dot{x} = -\omega R\sin\theta + \dot{R}\cos\theta - \dot{\phi}R\sin\theta. \tag{4.7}$$

Following the KBM method Eq. 4.7 is taken to be correct to order ϵ. Using Eq. 4.4 the $\mathcal{O}(1)$ part of Eq. 4.7 is

$$\dot{x} = -\omega R\sin\theta, \tag{4.8}$$

and the $\mathcal{O}(\epsilon)$ part is

$$\dot{R}\cos\theta - \dot{\phi}R\sin\theta = 0. \tag{4.9}$$

Differentiating Eq. 4.8 w.r.t time

$$\ddot{x} = -\omega^2 R\cos\theta - \omega\dot{R}\sin\theta - \omega R\dot{\phi}\cos\theta. \tag{4.10}$$

Substituting Eq. 4.10 in Eq. 4.2

$$-\omega^2 R\cos\theta - \omega\dot{R}\sin\theta - \omega R\dot{\phi}\cos\theta + F(R\cos\theta, F_0, \epsilon) = A\cos(\theta - \phi), \tag{4.11}$$

where $F_0 = (1-\epsilon)R + \epsilon$. Using Eqs. 4.9 and 4.11 the following relations can be obtained

$$-\omega\dot{R} - \omega^2 R\cos\theta\sin\theta + F(R\cos\theta, F_0, \epsilon)\sin\theta = A\cos(\theta - \phi)\sin\theta, \tag{4.12}$$

$$-\omega R\dot{\phi} - \omega^2 R\cos^2\theta + F(R\cos\theta, F_0, \epsilon)\cos\theta = A\cos(\theta-\phi)\cos\theta. \tag{4.13}$$

Since $R,\ \phi$ are assumed to be slowly varying as compared θ so the above equations can be averaged over one cycle of θ assuming $R,\ \phi$ to be constant over that interval.

$$\dot{R} = \frac{1}{2\pi\omega}\int_0^{2\pi} F(R\cos\theta, F_0, \epsilon)\sin\theta\, d\theta - \frac{A}{2\omega}\sin\phi, \tag{4.14}$$

$$\dot{\phi} = \frac{1}{2\pi R\omega}\int_0^{2\pi} F(R\cos\theta, F_0, \epsilon)\cos\theta\, d\theta - \frac{A}{2R\omega}\cos\phi - \frac{\omega}{2}. \tag{4.15}$$

Eqs. 4.14, 4.15 are sometimes referred to as the *slow-flow* equations. Let

$$C(R) = \frac{1}{\pi}\int_0^{2\pi} F(R\cos\theta, F_0, \epsilon)\cos\theta\, d\theta, \tag{4.16}$$

$$S(R) = \frac{1}{\pi}\int_0^{2\pi} F(R\cos\theta, F_0, \epsilon)\sin\theta\, d\theta. \tag{4.17}$$

The slow-flow equations then become

$$\dot{R} = \frac{S(R)}{2\omega} - \frac{A}{2\omega}\sin\phi, \tag{4.18}$$

$$\dot{\phi} = \frac{C(R)}{2R\omega} - \frac{A}{2R\omega}\cos\phi - \frac{\omega}{2}. \tag{4.19}$$

To evaluate the integral terms in the slow-flow equations notice that

$$\int_0^{2\pi} F(R\cos\theta, F_0, \epsilon)\cos\theta\, d\theta = 2\int_0^{\pi} F(R\cos\theta, F_0, \epsilon)\cos\theta\, d\theta, \tag{4.20}$$

and

$$\int_0^{2\pi} F(R\cos\theta, F_0, \epsilon)\sin\theta\, d\theta = 2\int_0^{\pi} F(R\cos\theta, F_0, \epsilon)\sin\theta\, d\theta. \tag{4.21}$$

From table IX the value of θ at which the transition from F_I to F_{II} occurs is given by

$$\theta_{I\to II} = \arccos(1 - 2/R). \tag{4.22}$$

Thus,

$$S(R) = \frac{2}{\pi}\left(\int_0^{\theta_{I\to II}} F(R\cos\theta, F_0, \epsilon)\sin\theta\, d\theta + \int_{\theta_{I\to II}}^{\pi} F(R\cos\theta, F_0, \epsilon)\sin\theta\, d\theta\right) \tag{4.23}$$

$$= -\frac{\epsilon R}{\pi}\sin^2\theta_{I\to II}, \tag{4.24}$$

and

$$C(R) = \frac{2}{\pi}\left(\int_0^{\theta_{I\to II}} F(R\cos\theta, F_0, \epsilon)\cos\theta\, d\theta + \int_{\theta_{I\to II}}^{\pi} F(R\cos\theta, F_0, \epsilon)\cos\theta\, d\theta\right) \tag{4.25}$$

$$= \frac{R}{\pi}\left(\epsilon\theta_{I\to II} + (1-\epsilon)\pi - \frac{\epsilon}{2}\sin 2\theta_{I\to II}\right). \tag{4.26}$$

To summarize, we took the assumed response to be of the form

$$x(t) = R\cos(\omega t + \phi), \tag{4.27}$$

where

$$\begin{aligned} \dot{R}(t) &\sim \mathcal{O}(\epsilon), \\ \dot{\phi}(t) &\sim \mathcal{O}(\epsilon). \end{aligned} \tag{4.28}$$

Following the KBM method we found the following expressions for the evolution of the variables $R,\ \phi$

$$\begin{aligned} \dot{R} &= \frac{S(R)}{2\omega} - \frac{A}{2\omega}\sin\phi, \\ \dot{\phi} &= \frac{C(R)}{2R\omega} - \frac{A}{2R\omega}\cos\phi - \frac{\omega}{2}, \end{aligned} \tag{4.29}$$

where

$$S(R) = -\frac{\epsilon R}{\pi}\sin^2\theta_{I\to II}, \tag{4.30}$$

$$C(R) = \frac{R}{\pi}\left(\epsilon\theta_{I\to II} + (1-\epsilon)\pi - \frac{\epsilon}{2}\sin 2\theta_{I\to II}\right). \tag{4.31}$$

It should be noted that the above results will not be accurate if used for prediction of transient response of the oscillator. Rather, they should be used for prediction of long-term behavior of the system. Contrast this with the results that are obtained using the KBM method in Appendix A. Those results are valid for the transient as well as the long-term response of the considered systems. The reason for this difference is that the assumed response that we took in the preceding development is periodic with a period equal to the period of the forcing, which is the nature of the long-term behavior of damped systems with external excitation. The method can be modified to capture the short-term behavior of the system as well; however, such an extension is slightly cumbersome and is not carried out in this thesis.

1. Steady State Response

The fixed points of the slow-flow equations correspond to the steady state response of the hysteretic system. Using Eqs. 4.18, 4.19 we get the fixed points of the slow-flow equations as

$$S(R^*) = A\sin\phi^*, \tag{4.32}$$

$$C(R^*) = R\omega^2 + A\cos\phi^*, \tag{4.33}$$

where the superscript * denotes the steady state quantities. Eliminating ϕ^* from the above equations we get

$$\omega^2 = \frac{C(R^*)}{R^*} \pm \left[\left(\frac{A}{R^*}\right)^2 - \left(\frac{S(R^*)}{R^*}\right)^2\right]^{1/2}. \tag{4.34}$$

Similarly we can find ϕ^* as

$$\tan\phi^* = \frac{S(R^*)}{C(R^*) - \omega^2 R^*}. \tag{4.35}$$

Note that Eq. 4.34 is a implicit equation in R^* and will need to be iterated to converge. In principle, given the system parameters $\epsilon,\ A$ and ω we can use Eqs. 4.34 and 4.35 to find the phase and the amplitude of the steady state response of the system. However, in practice it is easier to assume a value of R^* and find the corresponding ω and ϕ^*.

2. Resonance

Resonant frequency of a system is defined as the frequency at which the amplitude of the response is maximum. Therefore, resonance occurs when Eq. 4.34 has a double root, i.e.,

$$\left(\frac{A}{R^*}\right)^2 = \left(\frac{S(R^*)}{R^*}\right)^2. \tag{4.36}$$

Substituting for $S(R^*)$ and $\theta_{I\to II}$ we get

$$R^* = \frac{4\epsilon}{4\epsilon - \pi A}. \tag{4.37}$$

Since R^* is positive by definition, therefore a steady state exists at resonance only if

$$A < \frac{4\epsilon}{\pi}. \tag{4.38}$$

Otherwise, the resonance is unbound.

3. Some Response Curves

In this section we show some typical response curves for the bilinear oscillator as predicted by the KBM method. Essentially, these curves are a plot of R^* versus ω for various values of the system parameters A and ϵ. Figures 29 to 32 show the typical

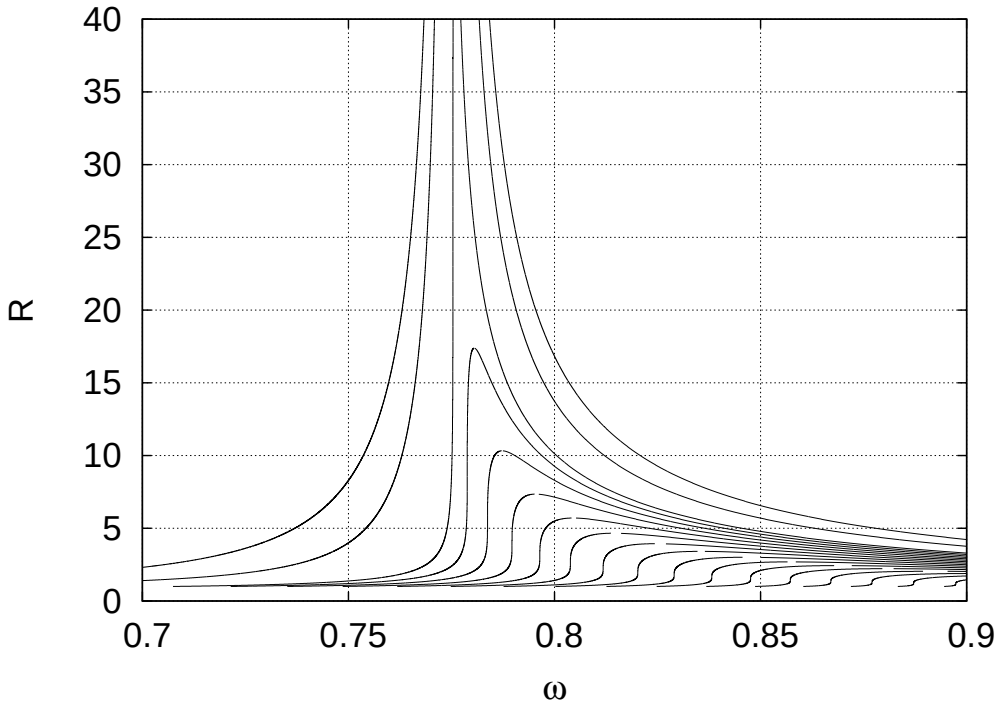

Fig. 29. Frequency response for varying amplitude of excitation. $\epsilon = 0.4$ (fixed), A varied between 0.2 to 0.8.

response with bound and unbound resonance with various values of the parameters ϵ and A.

4. Stability of Response

Having found the steady state response of the system it is instructive to evaluate the stability of the steady state. The single-valued nature of response seen in the previous section indicates that the steady state is always stable. We will verify this intuition with the help of rigorous tools from dynamical systems theory. The stability of the steady state response can be evaluated by studying the stability of the fixed points of the slow-flow equations. The stability of the fixed points of the slow-flow equations will be ascertained by carrying out an eigenvalue analysis. The Jacobian matrix for

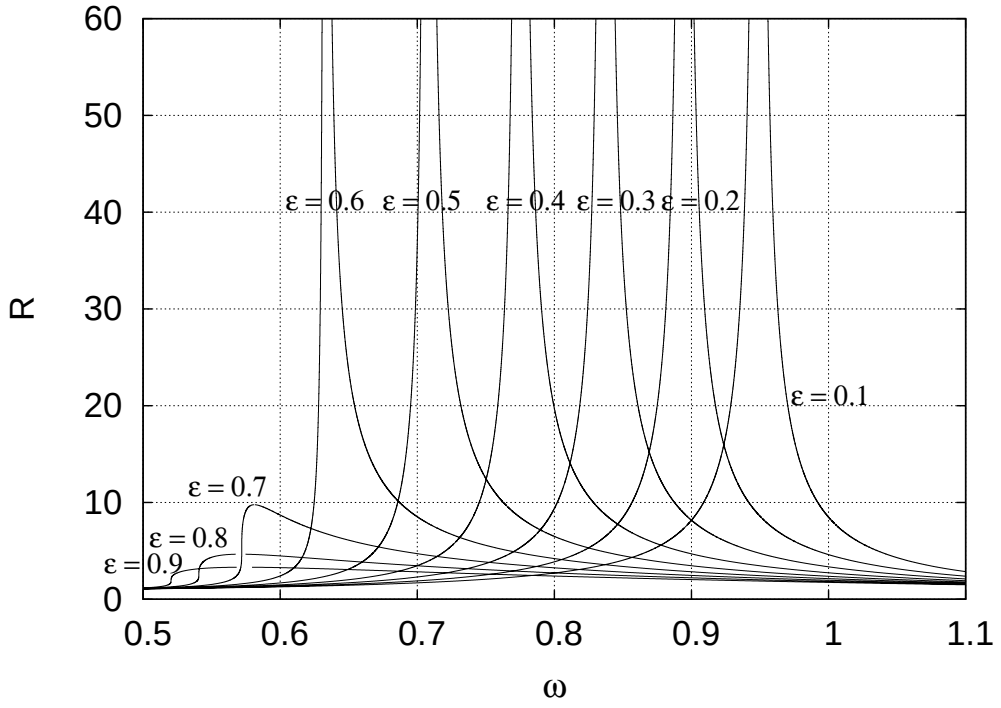

Fig. 30. Frequency response for varying ϵ. ϵ varied between 0.1 and 0.9, $A = 0.8$.

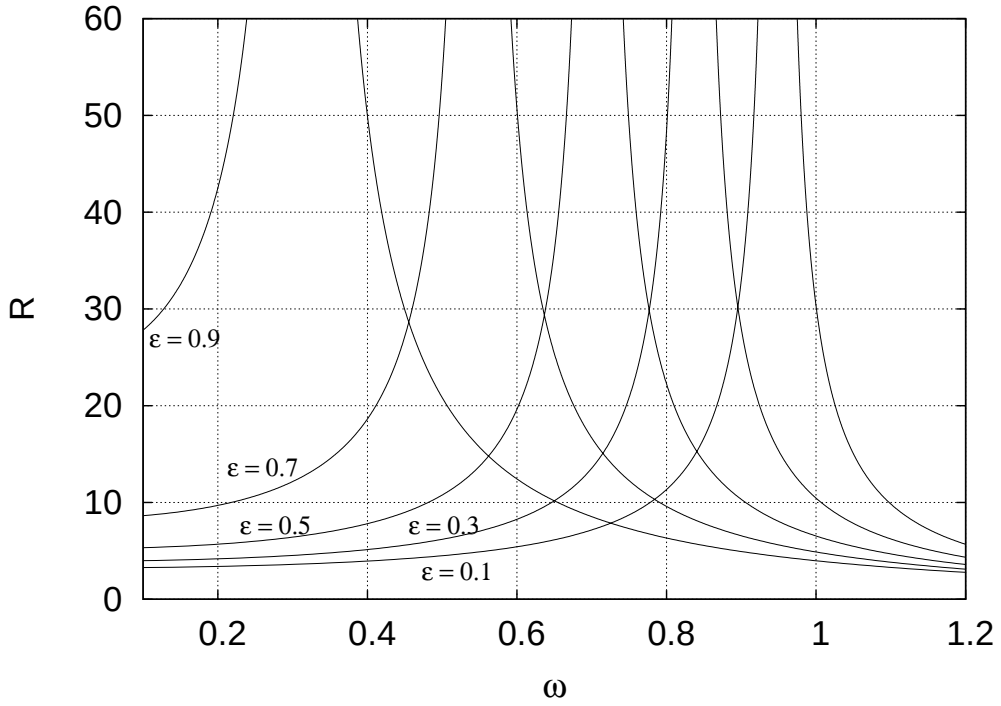

Fig. 31. Frequency response for varying ϵ. ϵ varied between 0.1 and 0.9, $A = 3$.

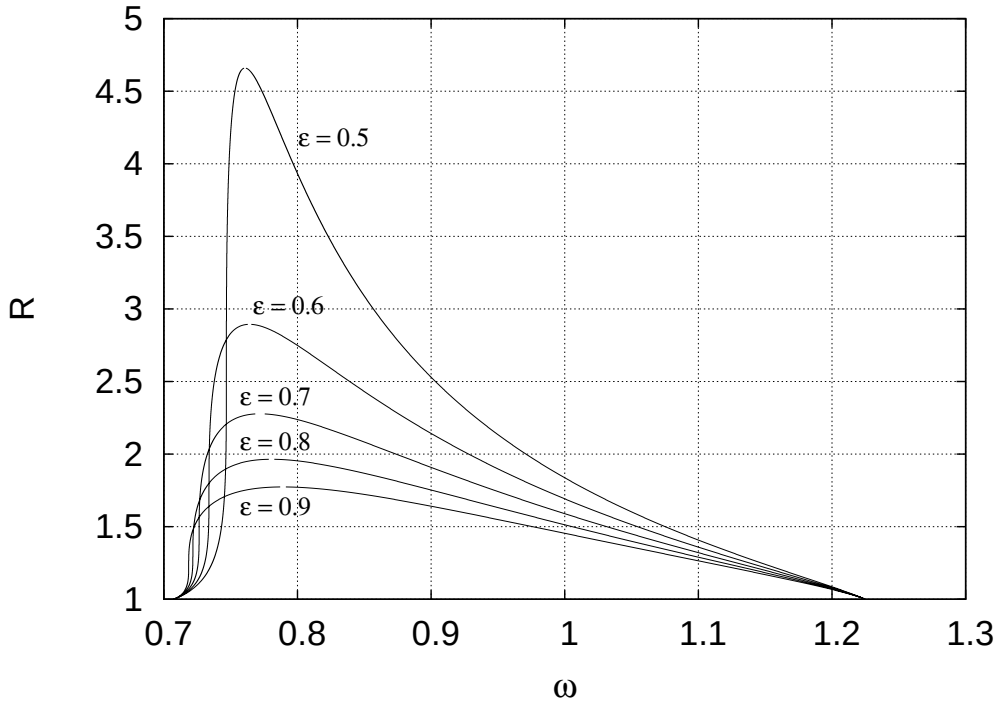

Fig. 32. Frequency response for varying ϵ. ϵ varied between 0.5 and 0.9, $A = 0.5$.

the system 4.18, 4.19 at a general point $R,\ \phi$ is given by

$$\mathbf{J}(R,\phi) = \begin{bmatrix} \frac{1}{2\omega}\frac{\partial S}{\partial R} & -\frac{A\cos\phi}{2\omega} \\ \frac{1}{2\omega}\frac{\partial}{\partial R}\left(\frac{C-A\cos\phi}{R}\right) & \frac{A\sin\phi}{2R\omega} \end{bmatrix}. \tag{4.39}$$

At steady state the Jacobian becomes

$$\mathbf{J}(R^*,\phi^*) = \begin{bmatrix} \frac{1}{2\omega}\frac{\partial S}{\partial R} & \frac{1}{2\omega}\left(R^*\omega^2 - C^*\right) \\ \frac{1}{2R^*\omega}\left(\frac{\partial C}{\partial R} - \omega^2\right) & \frac{S^*}{2R^*\omega} \end{bmatrix}, \tag{4.40}$$

where the partials are evaluated at the fixed point. Since this is a two-dimensional system we do not need to find the eigenvalues of the Jacobian matrix in order to evaluate the stability. Instead, we will use the famous trace-determinant criterion for ascertaining the stability of the response. After some algebra it is possible to obtain the following results

$$\begin{aligned} \text{trace}(J(R^*,\phi^*)) &= \frac{1}{2\omega}\left(\frac{\partial S}{\partial R} + \frac{S^*}{R^*}\right) && (4.41)\\ &= -\frac{\epsilon}{\pi\omega}(1-\cos\theta_1) && (4.42)\\ &< 0, && (4.43) \end{aligned}$$

and

$$\begin{aligned} \det(J(R^*,\phi^*)) &= \frac{1}{4\omega^2}\left[\frac{S}{R}\frac{\partial S}{\partial R} + \left(\frac{C}{R} - \omega^2\right)\left(\frac{\partial C}{\partial R} - \omega^2\right)\right] && (4.44)\\ &= \frac{1}{4\omega^2}\left[\omega^2 - \frac{1}{\pi}\left(\epsilon\theta_1 + (1-\epsilon)\pi - \epsilon\sin\theta_1\right)\right]^2 && (4.45)\\ &> 0. && (4.46) \end{aligned}$$

Since $\text{trace}(J) < 0$ and $\det(J) > 0$ we conclude that the steady state response is always stable.

B. Equivalent Damping Properties

Energy dissipating qualities of hysteretic media are often amongst the most important ones from a vibration damping and vibration isolation point of view. Several researchers have proposed the use of components with hysteretic response, like shape memory alloys, for passive vibration damping. In this section we will investigate the equivalent damping properties of oscillators with bilinear hysteresis. Given the oscillator 4.2 we wish to find the properties $\xi,\ \gamma$ such that the following oscillator has the same steady state response as 4.2

$$\ddot{x} + 2\xi\gamma\dot{x} + \gamma^2 x = A\cos(\omega t). \tag{4.47}$$

We will call the parameter ξ the equivalent damping of the hysteretic oscillator. Let the steady state response of the system 4.47 be

$$x(t) = R_{eq}\cos(\omega t + \phi_{eq}). \tag{4.48}$$

Then, at steady state the work done by dissipative forces in system 4.47 is given by

$$\begin{aligned} W_{\text{dis, equiv}} =& \int_t^{t+2\pi/\omega} 2R_{eq}^2\omega^2\gamma\xi\sin^2(\omega\tau + \phi_{eq})d\tau \\ =& 2\pi R_{eq}^2\omega\gamma\xi. \end{aligned} \tag{4.49}$$

For the hysteretic oscillator with bilinear hysteresis the work done by dissipative forces in one oscillation is equal to the area occupied by the hysteresis loop shown in figure 28. This area can be found to be $4(R-1)\epsilon$. On equating the energy dissipated in one cycle at steady state (assuming same amplitude of response) we get the following expression for the equivalent damping

$$\xi = \frac{2\epsilon}{\pi\omega\gamma}\left(1 - \frac{1}{R}\right)\frac{1}{R}. \tag{4.50}$$

Alternatively, we can derive the above expression as follows. We need the steady state response of the equivalent system 4.47 to match that of the hysteretic system 4.2. We also found the steady state response of the hysteretic system to be of the from $x(t) = R\cos(\omega t + \phi)$, where $R,\ \phi$ are the fixed points of the slow-flow equations. On substituting this expression into Eq. 4.47 we get

$$\begin{aligned} -R\omega^2\cos(\omega t+\phi) - 2\xi R\omega\gamma\sin(\omega t+\phi) + \gamma^2 R\cos(\omega t+\phi) &= A\cos(\omega t) \\ &= A\cos(\phi)\cos(\omega t+\phi) + A\sin(\phi)\sin(\omega t+\phi). \end{aligned} \tag{4.51}$$

Comparing the coefficients of like harmonics in Eq. 4.51 we obtain

$$\begin{aligned} R(\gamma^2-\omega^2) &= A\cos\phi, \\ -2R\xi\omega\gamma &= A\sin\phi. \end{aligned} \tag{4.52}$$

Using Eqs. 4.32 and 4.52

$$\begin{aligned} \xi &= \frac{\epsilon\sin^2\theta_{I\to II}}{2\pi\omega\gamma}, \\ &= \frac{\epsilon}{2\pi\omega\gamma}\left(1-\cos^2\theta_{I\to II}\right), \\ &= \frac{\epsilon}{2\pi\omega\gamma}\left(1-\left(1-\frac{2}{R}\right)^2\right), \\ &= \frac{2\epsilon}{\pi\omega\gamma}\left(1-\frac{1}{R}\right)\frac{1}{R}, \end{aligned} \tag{4.53}$$

which is the same as Eq. 4.50. Finally, we can use Eqs. 4.52, 4.32 and 4.33 to get the following expressions for the equivalent natural frequency and damping in terms of C and S

$$\gamma^2 = \frac{C(R)}{R}, \tag{4.54}$$

$$\xi = \frac{-S(R)}{2R\omega\gamma}. \tag{4.55}$$

Figures 33 and 34 show the variation of the equivalent damping with the fre-

quency of excitation for some typical cases.

C. Poincaré Maps

The use of Poincaré maps for study of periodic and steady state responses is one of the most potent tools of nonlinear dynamics. In case of non-autonomous we can talk of Poincaré maps only in a loose sense because time adds an extra dimension to the problem and the limitcycle in phase-space is not a true limitcycle in the augmented space with time dimension. In such cases it is customary to talk of return-maps instead of Poincaré maps. The essential idea behind construction of return-maps is that if the excitation is periodic with a period T then a steady state response also has to be periodic with a period of nT for some $n \geq 1$. Thus, the time dimension can be removed from the picture by sampling the system at appropriate intervals (necessarily integral multiples of T).

Our problem is more complicated than both of the cases mentioned above. Not only do we have a non-autonomous system, we also have a hybrid one. The general task of defining proper Poincaré sections for such systems is far from trivial. However, in the particular case at hand there is a certain structure to the problem that renders it amenable for analysis. We will first describe this structure and then exploit it to construct Poincaré maps for the analysis of the problem.

Notice that the way in which we have defined the possible transitions of the automaton imposes a certain structure on the possible steady state responses. Due to the oscillatory nature of the solution over each individual state of the automaton the state IV is necessarily followed by I. Thus, if the state IV appears in a steady state response then we can be sure that the next state will be I. Similarly, the state II is necessarily preceded by the state I or III and necessarily followed by state III.

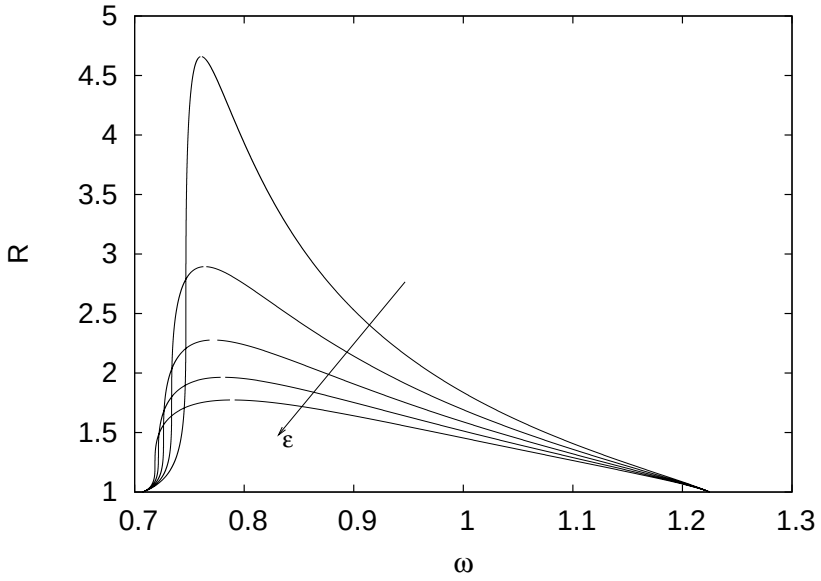

(a) Response versus frequency

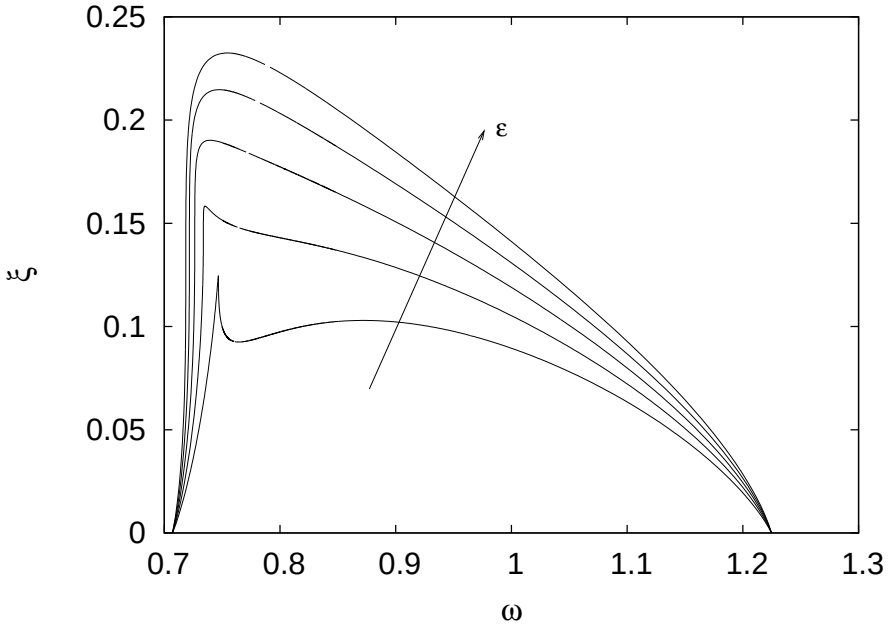

(b) Equivalent damping versus frequency

Fig. 33. Variation of equivalent damping with frequency. $A = 0.5$, ϵ varied between 0.5 and 0.9.

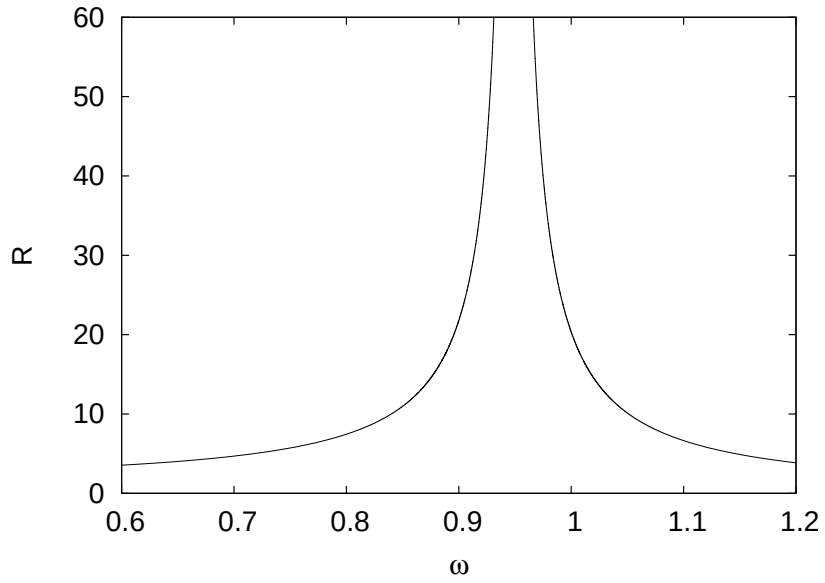

(a) Response versus frequency

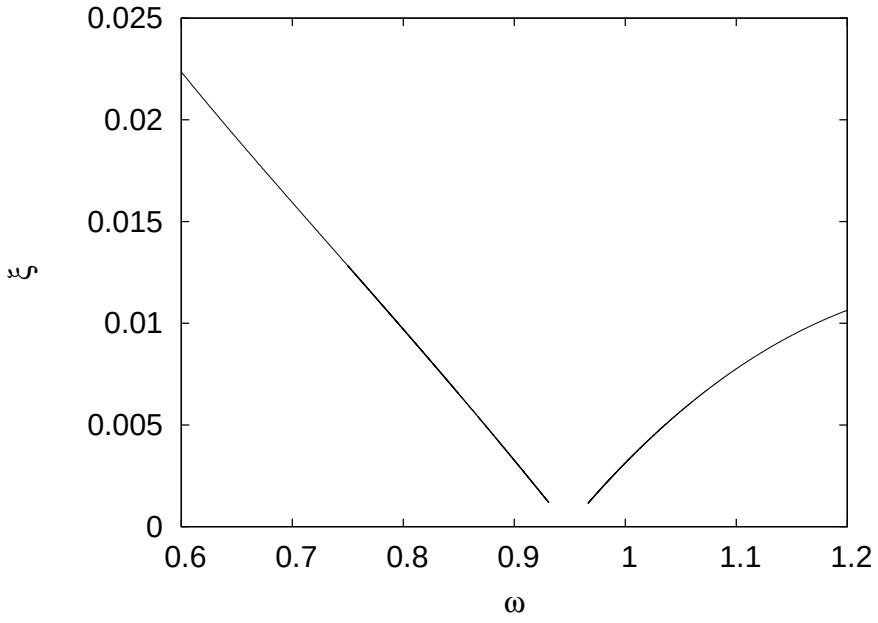

(b) Equivalent damping versus frequency

Fig. 34. Variation of equivalent damping with frequency. $A = 2.0$, $\epsilon = 0.1$.

On the other hand, the state IV is definitely preceded by the state III or I. Putting these building blocks together, we can conclude that any steady state of the system will be of the following general form

$$(\rightarrow (I \rightarrow IV)_{n_i \text{ times}} \rightarrow I \rightarrow II \rightarrow$$
$$\rightarrow (III \rightarrow II)_{m_i \text{ times}} \rightarrow III \rightarrow IV \rightarrow)_{i \text{ such blocks with different } n_i, m_i}.$$

The simplest cycle that we analyzed using the KBM method can be obtained by setting $i = 1,\ n_1 = m_1 = 0$. Choosing these values we get the cycle $I \rightarrow II \rightarrow III \rightarrow IV \rightarrow \ldots$. Also recall that at the beginning of state I, $x = x_I = x_I(0)$ (notation), $\dot{x} = 0$ and the time is reset by introducing the phase variable ϕ. Thus, the starting of state I is characterized by two variables x_I and ϕ. We can construct a Poincaré map as mapping of these variables onto themselves after one complete cycle (whatever the structure of the cycle may be). Each steady state response will correspond to a fixed point of this two-dimensional map. The cycle will stable if the corresponding fixed points of this map are stable. Note that this map can undergo all the classical bifurcations of two-dimensional maps, viz. the Neimark-Sacker, the Hopf and the fold bifurcations etc. However it can have some bifurcations that are not generic to two-dimensional maps. These bifurcations appear due to the fact that this map is not a true Poincaré map and represents the dynamics of a hybrid system. Among others, the map can undergo a bifurcation at which the number $n_i,\ m_i$ or i changes. These will be global bifurcations and will be difficult to detect and follow in general.

In the analysis presented here we will fix the structure of the cycle by fixing $n_i,\ m_i$ and i and then study the classical bifurcations of the resulting map. Using the development presented in chapter III we will write down the analytical conditions for all transitions. However, as we will see, the conditions are too complicated to be of any practical use. In order to calculate the state transitions we will use the root

isolation methodology discussed in Appendix B to numerically calculate the Poincaré map. The numerical analysis of the maps will be carried out using the CL_CONT package of the MATCONT suite.

We introduce the following function

$$\begin{aligned} x_n(t) = &\left(x_0 - \frac{k}{\omega_o^2} - \frac{A\cos\phi}{\omega_o^2 - \omega^2} \right) \cos(\omega_o t) + \frac{1}{\omega_o} \left(v_0 + \frac{A\omega\sin\phi}{\omega_o^2 - \omega^2} \right) \sin(\omega_o t) \\ &+ \frac{A}{\omega_o^2 - \omega^2} \cos(\omega t + \phi) + \frac{k}{\omega_o^2}, \end{aligned} \tag{4.56}$$

where $n \in (I,\ II,\ III,\ IV)$. With appropriate values of parameters $k,\ \omega_o$ and initial conditions $x_0,\ \phi,\ v_0$ the function $x_n(t)$ represents the $x(t)$ for the different states of the automaton. The appropriate values of $k,\ \omega_o$ for each state can be found in table VIII. The appropriate boundary terms for each state are given in table X. Note that the boundary terms depend not only on the present state but also on the last state.

Given the appropriate boundary terms and parameters we can use table IV to write the explicit equations to be solved for each state transition. These equations are listed in table XI.

We use $t^*_{n\to m}$ to denote the time at which the transition from n to m takes place. Note that time is set to zero at the beginning of each state, thus $t^*_{n\to m}$ is measured from the starting of the state n. Figures 35 and 36 show the variation of $t^*_{I\to II}$ with x_I and ϕ_I for some values of $\epsilon,\ A$ and ω. It can be seen in the figures that $t^*_{I\to II}$ is in general a discontinuous function of both x_I and ϕ_I. The reason for this discontinuity is simple to understand. In general we have

$$\begin{aligned} \frac{\partial t^*_{I\to II}}{\partial x_I(0)} &= -\frac{\partial x_I(t)/\partial x_I(0)}{\partial x_I(t)/\partial t}\Big|_{t=t^*_{I\to II}}, \\ \frac{\partial t^*_{I\to II}}{\partial \phi_I} &= -\frac{\partial x_I(t)/\partial \phi_I}{\partial x_I(t)/\partial t}\Big|_{t=t^*_{I\to II}}. \end{aligned} \tag{4.57}$$

Table X. Boundary terms in expression for $x_n(t)$ for different states for the bilinear hysteretic oscillator.

State	Previous State	Boundary terms
I	IV	$x_0 = x_I = x_{IV}(t^*_{IV\to I}), v_0 = \dot{x}_I = 0,$ $\phi_0 = \phi_I = \omega t^*_{IV\to I} \mod 2\pi$
II	I	$x_0 = x_{II} = x_I(t^*_{I\to II}), v_0 = \dot{x}_{II} = \dot{x}_I(t^*_{I\to II}),$ $\phi_0 = \phi_{II} = \omega t^*_{I\to II} \mod 2\pi$
II	III	$x_0 = x_{II} = x_{III}(t^*_{III\to II}), v_0 = \dot{x}_{II} = \dot{x}_{III}(t^*_{III\to II}),$ $\phi_0 = \phi_{III} = \omega t^*_{III\to II} \mod 2\pi$
III	II	$x_0 = x_{III} = x_{II}(t^*_{II\to III}), v_0 = \dot{x}_{III} = 0,$ $\phi_0 = \phi_{III} = \omega t^*_{II\to III} \mod 2\pi$
IV	III	$x_0 = x_{IV} = x_{III}(t^*_{III\to IV}), v_0 = \dot{x}_{IV} = \dot{x}_{III}(t^*_{III\to IV}),$ $\phi_0 = \phi_{IV} = \omega t^*_{III\to IV} \mod 2\pi$
IV	I	$x_0 = x_{IV} = x_I(t^*_{I\to IV}), v_0 = \dot{x}_{IV} = \dot{x}_I(t^*_{I\to IV}),$ $\phi_0 = \phi_{IV} = \omega t^*_{I\to IV} \mod 2\pi$

It is obvious that the RHS of the set 4.57 blows up if

$$\frac{\partial x_I(t)}{\partial t}\Big|_{t=t^*_{I\to II}} = 0. \tag{4.58}$$

Equation 4.58 can be interpreted as a double root of $x_I(t) = x_0 - 2$. At a double root two simple roots of the function $x_I(t) - (x_0 - 2)$ collide and annihilate each other. In this condition a small change in system parameters can make the difference between existence and non-existence of the roots. Thus, there is a discontinuity in the root as a function of the parameters near the double root. This phenomenon is sometimes also known as the *grazing bifurcation*.

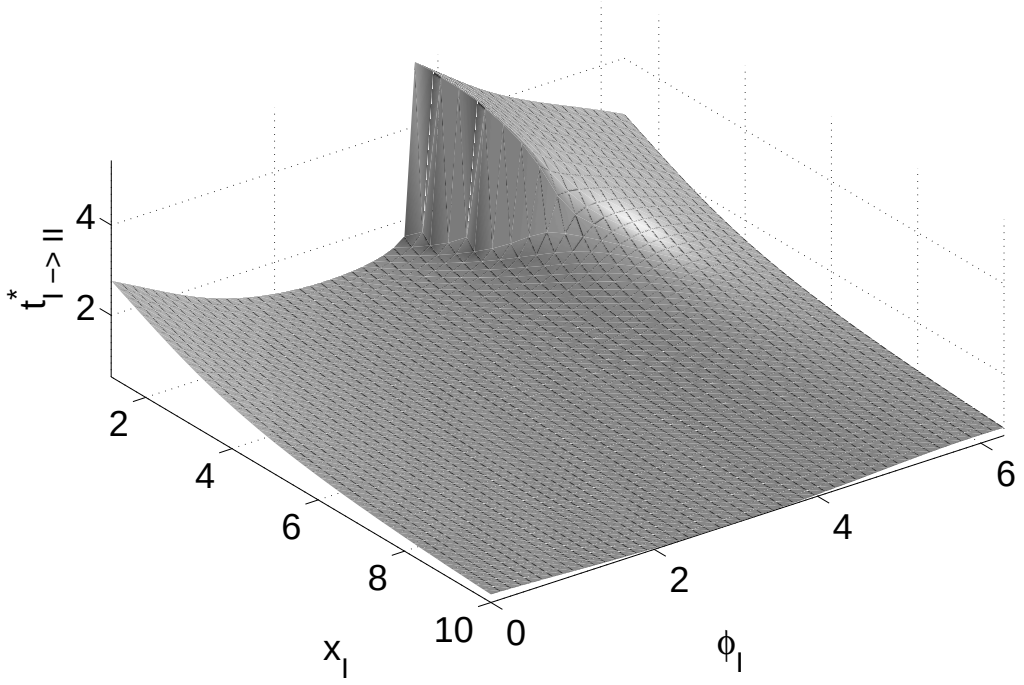

(a) Variation of $t^*_{I\to II}$ with x_I and ϕ_I.

Fig. 35. Variation of $t^*_{I\to II}$ with x_I and ϕ_I. $\epsilon = 0.2,\ A = 2,\ \omega = 1.2$.

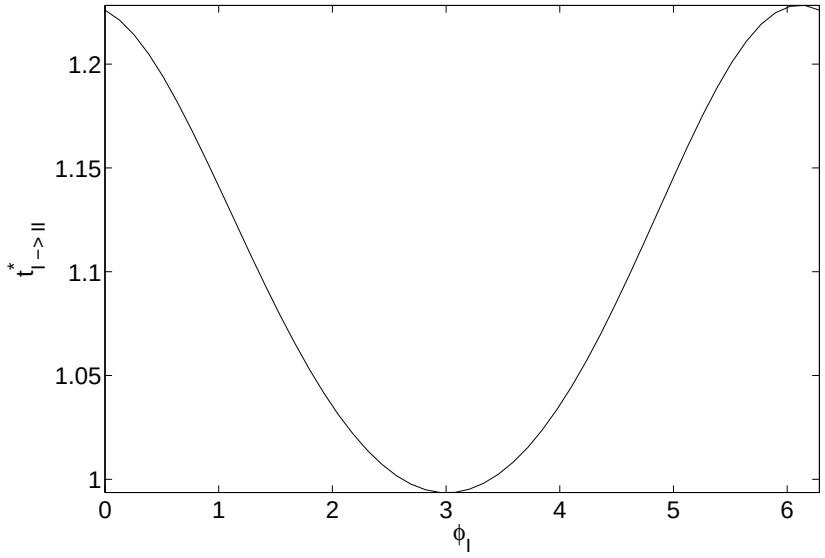

(b) $t^*_{I\to II}$ versus ϕ_I with $x_I = 1.9$.

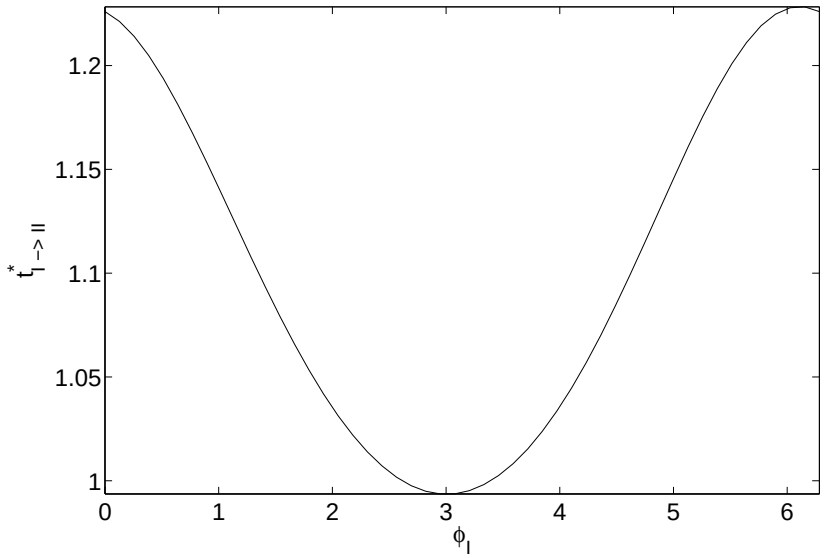

(c) $t^*_{I\to II}$ versus ϕ_I with $x_I = 5.5$.

Fig. 35. Continued ...

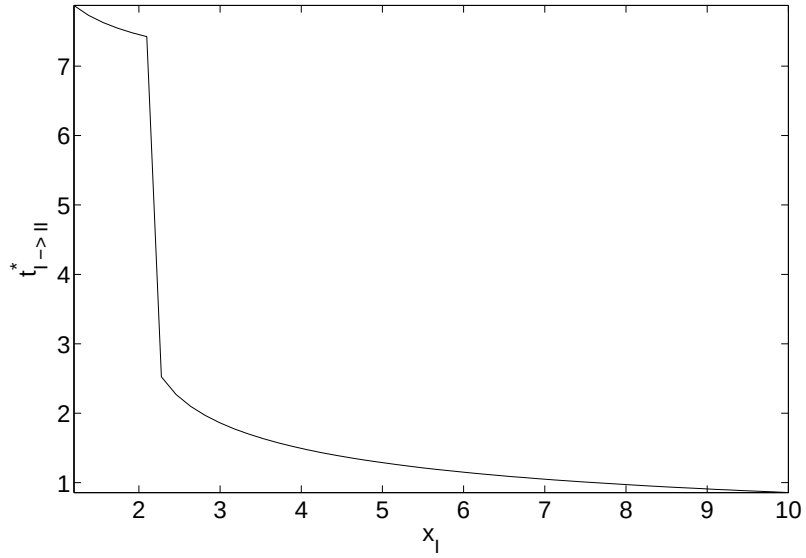

(d) $t^*_{I\to II}$ versus x_I with $\phi_I = 4.1$.

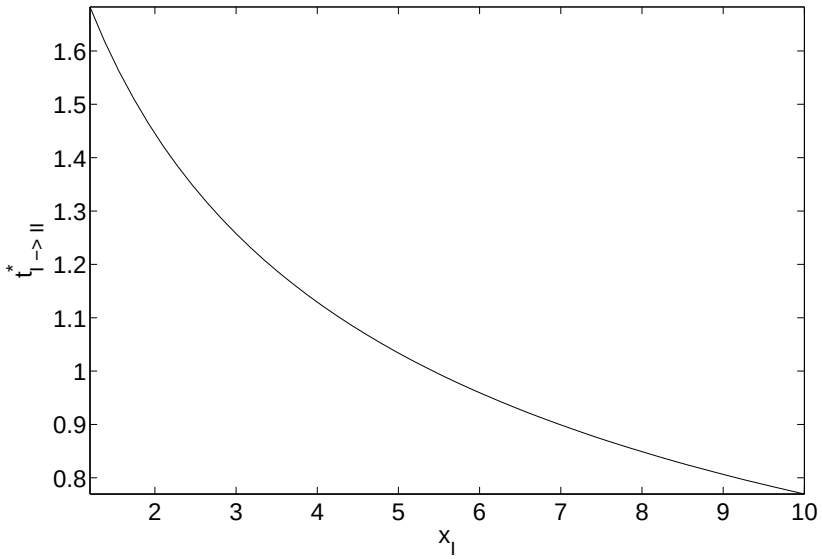

(e) $t^*_{I\to II}$ versus x_I with $\phi_I = 2.4$.

Fig. 35. Continued ...

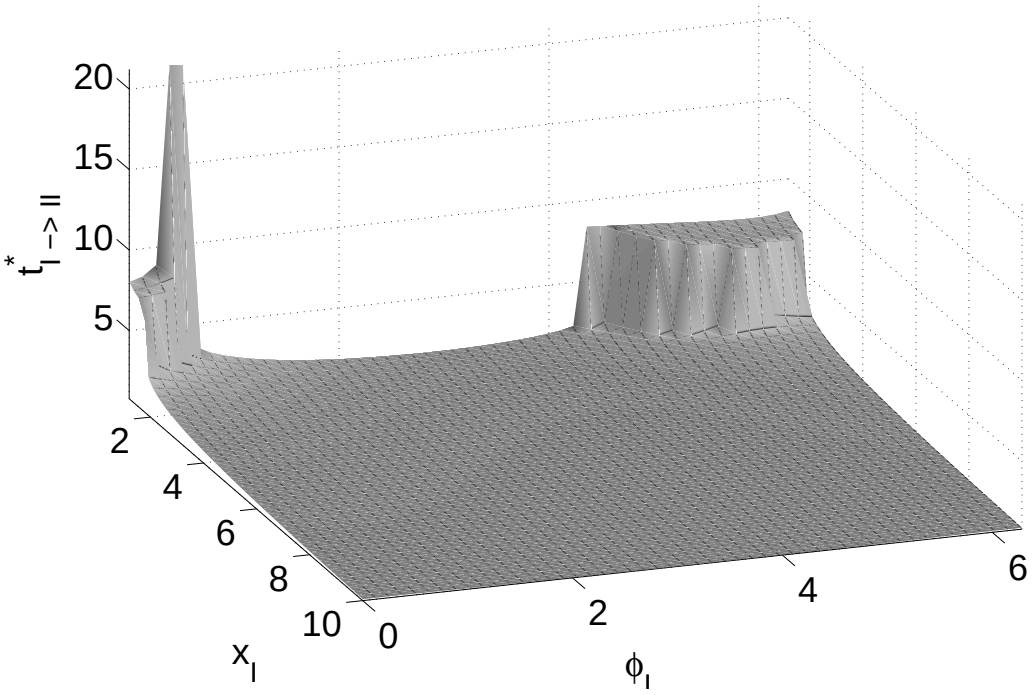

(a) Variation of $t^*_{I\to II}$ with x_I and ϕ_I.

Fig. 36. Variation of $t^*_{I\to II}$ with x_I and ϕ_I. $\epsilon = 0.4,\ A = 0.7,\ \omega = 0.4$.

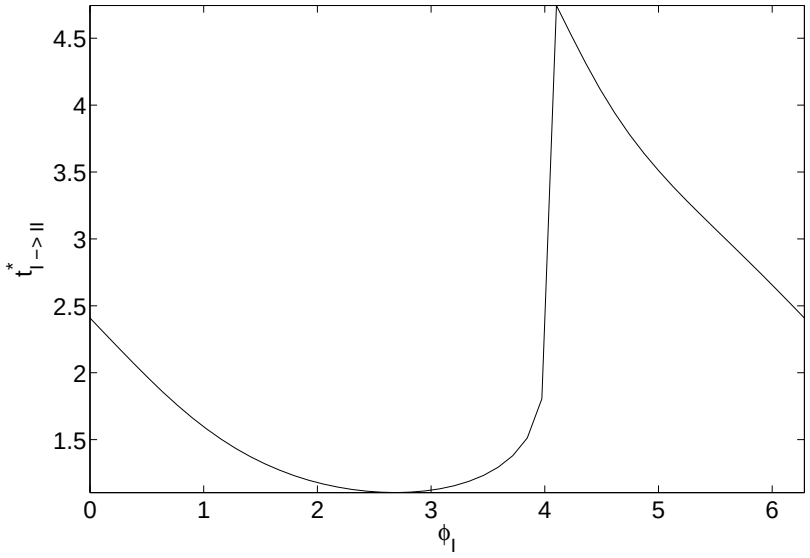

(b) $t^*_{I\to II}$ versus ϕ_I with $x_I = 5.5$.

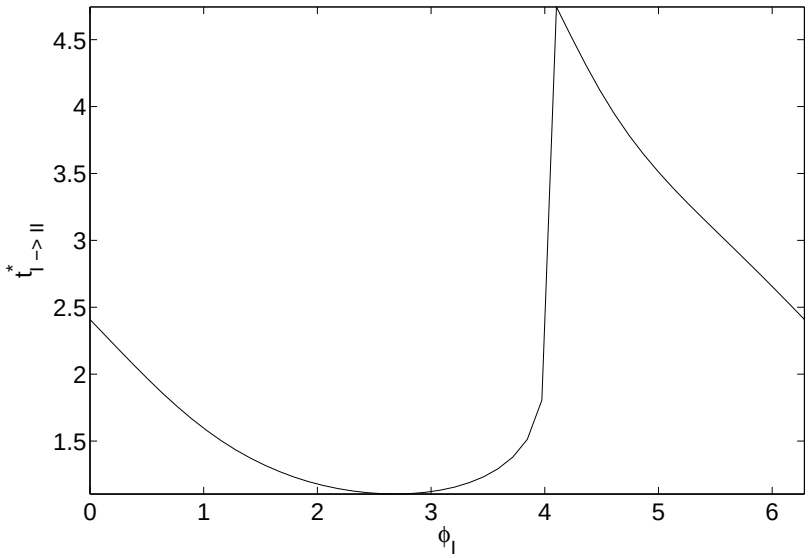

(c) $t^*_{I\to II}$ versus ϕ_I with $x_I = 1.4$.

Fig. 36. Continued ...

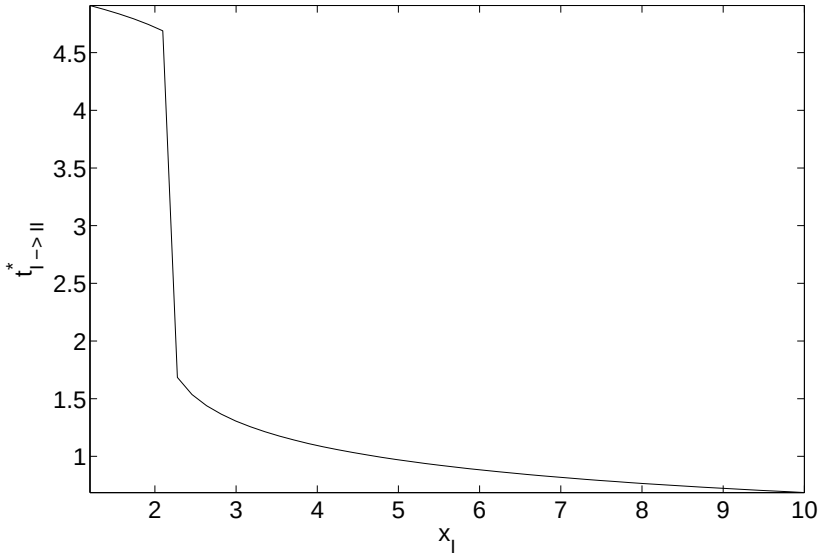

(d) $t^*_{I\to II}$ versus x_I with $\phi_I = 5.6$.

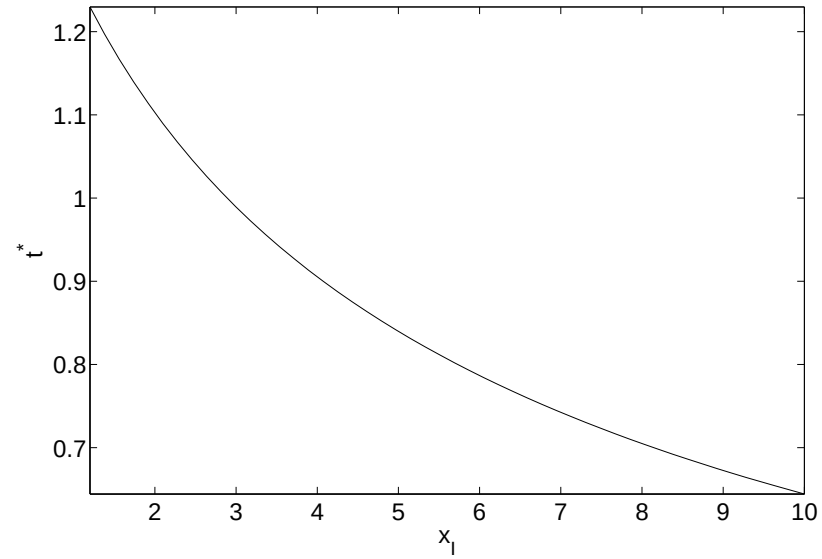

(e) $t^*_{I\to II}$ versus x_I with $\phi_I = 3.0$.

Fig. 36. Continued ...

Table XI. Conditions for mode transitions for the bilinear automaton.

Transition	Condition
$I \rightarrow II$	$x_I(t) = x_0 - 2 = x_I - 2,\ \dot{x}_I(t) < 0$
$I \rightarrow IV$	$x_I(t) = x_0 = x_I,\ \dot{x}_I(t) > 0$
$II \rightarrow III$	$\dot{x}_{II}(t) = 0,\ \ddot{x}_{II}(t) > 0$
$III \rightarrow IV$	$x_{III}(t) = x_0 + 2 = x_{III} + 2,\ \dot{x}_{III}(t) > 0$
$III \rightarrow II$	$x_{III}(t) = x_0 = x_{III},\ \dot{x}_{III}(t) < 0$
$IV \rightarrow I$	$\dot{x}_{IV}(t) = 0,\ \ddot{x}_{IV}(t) < 0$

1. Typical Results

Figure 37 shows the response curves obtained by carrying out a bifurcation analysis of the Poincaré maps using MATCONT. It was observed that for all the cases run (not all of which are presented here) the Poincaré map does not undergo any of the classical bifurcations. For most of the cases the response curves found from the bifurcation analysis match fairly well with those obtained from the KBM analysis, even for values of ϵ comparable to unity. Figure 38 shows the response amplitude calculated using the KBM method. The amplitude response shown in figure 37 matches up well with its counterpart obtained from the KBM analysis. Figure 39 shows a plot of the response obtained from the KBM analysis and the Poincaré maps on the same graph.

On the other hand consider the response curves shown in figure 40. For most values of ω the response curves match the prediction of the KBM method (shown in figure 41). For a better comparison the response curves obtained from the KBM method and the Poincaré maps is plotted on the same graph in figure 42. Notice, the two small bumps between $\omega = 0.5,\ 0$. Figure 43 shows a magnified view of these bumps. These bumbs correspond to the sub-harmoic resonances in the system.

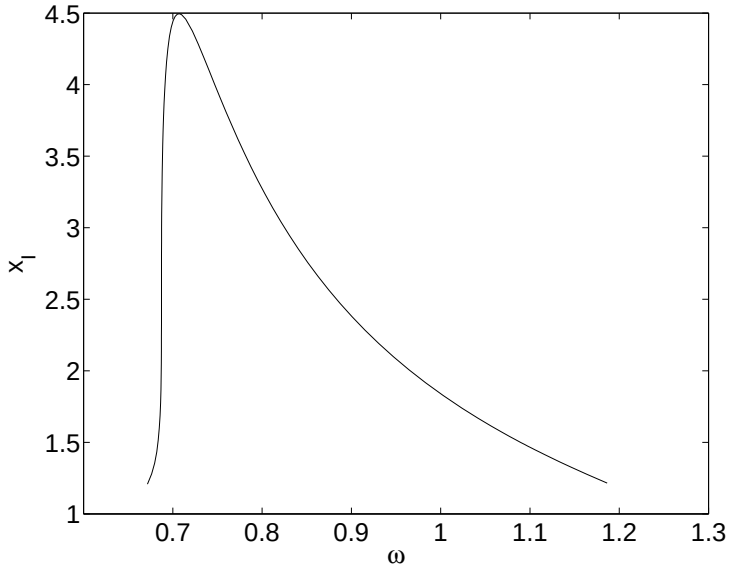

(a) x_I versus ω

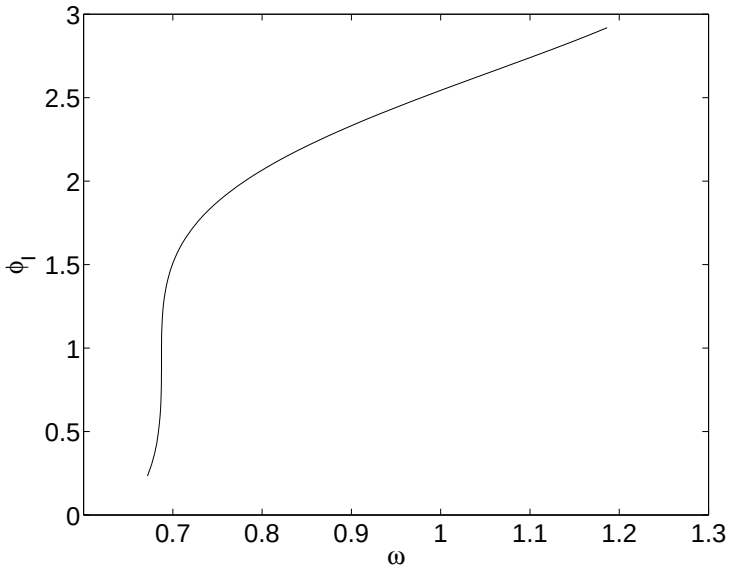

(b) ϕ_I versus ω

Fig. 37. Response curves obtained from Poincaré maps. $\epsilon = 0.6,\ A = 0.6$.

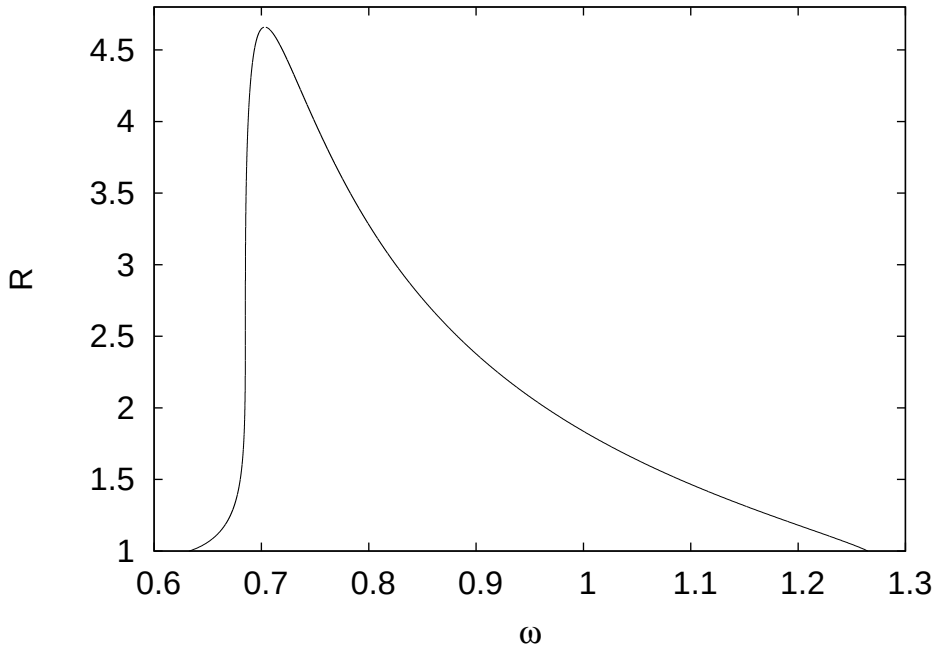

Fig. 38. Response curves obtained from KBM analysis. $\epsilon = 0.6,\ A = 0.6$.

Note that the response curve is not discontinious at these bumps even though the figures show it to be so. This apparent discontinuity appears because the continuation algorithm (MATCONT) was not able to trace the response curves near the bumps. In the region near the bumps the KBM analysis predicts a smooth decline in the amplitude of the response, and does not match well with the results of the bifurcation analysis in this region. The first (larger) bump appears around $\omega = 0.3$. Figure 44 shows a typical steady state response with $\omega = 0.3$ in time domain and phase-space. It is easy to see that the response of the system is no longer 'almost sinusoidal', thus the basic assumption of the KBM method does not hold. Hence the true amplitude of the cycle does not match up with the predictions from the KBM method.

The smaller bump appears for similar reasons. Figure 45 shows a typical cycle from the vicinity of this bump in time-domain and phase-space. Notice again that the nature of the solution does not match the description of being sinusoidal with slowly

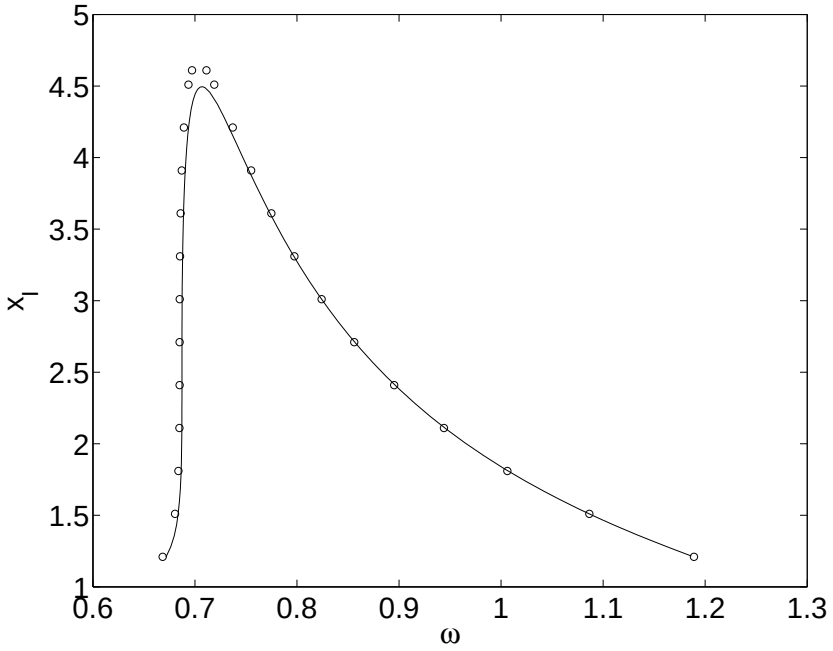

Fig. 39. Comparison of response curves obtained using the KBM method (shown by circles) and the Poincaré maps (shown by solid line). $\epsilon = 0.6,\ A = 0.6$.

varying phase and amplitude. We should also spend some time analyzing the phase response shown in the second graph of figure 40. The graph shows four disconnected branches in the phase response. The two major branches are discontinuous due to the presence unbounded resonance which induces a discontinuous phase change of π. The bigger of the two smaller branches appears discontinuous, but it is indeed connected with the lower major branch due to the fact that ϕ_I is a cyclic variable and the boundaries $\phi_I = 0$ and $\phi_I = 2\pi$ are indeed connected.

In the numerous cases studied it was noted that the simple steady state response with four state transitions is the only long-term response of the system (other than harmonic oscillation on mode I or III). It was further noticed that these orbits do not undergo any of the classical bifurcations and in general the response amplitude is in good agreement with that obtained using the KBM method even for larger values of ϵ.

D. Transient Response

We conclude this chapter by presenting some result showing the typical transient response of the system. It should be noted that even though the steady state response of the system consists of simple periodic orbits in the phase plane, the transient response is typically much more complex. Figures 46 and 47 show some transient trajectories of the system. Note that in the transient response the transition sequence does not necessarily follow the pattern $\rightarrow I \rightarrow II \rightarrow III \rightarrow IV \rightarrow$.

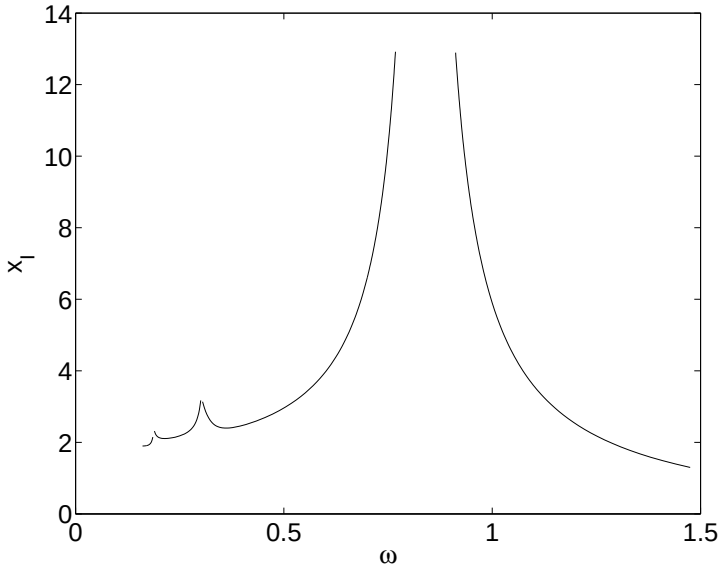

(a) x_I versus ω

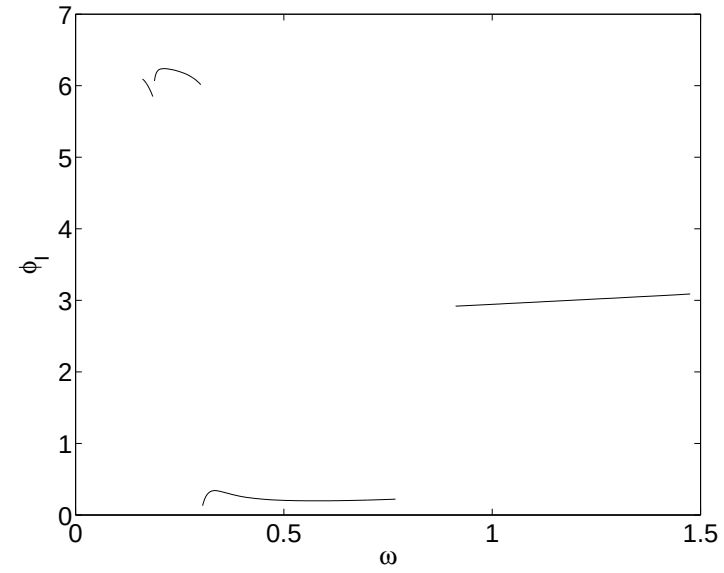

(b) ϕ_I versus ω

Fig. 40. Response curves obtained from Poincaré maps. $\epsilon = 0.3,\ A = 1.6$.

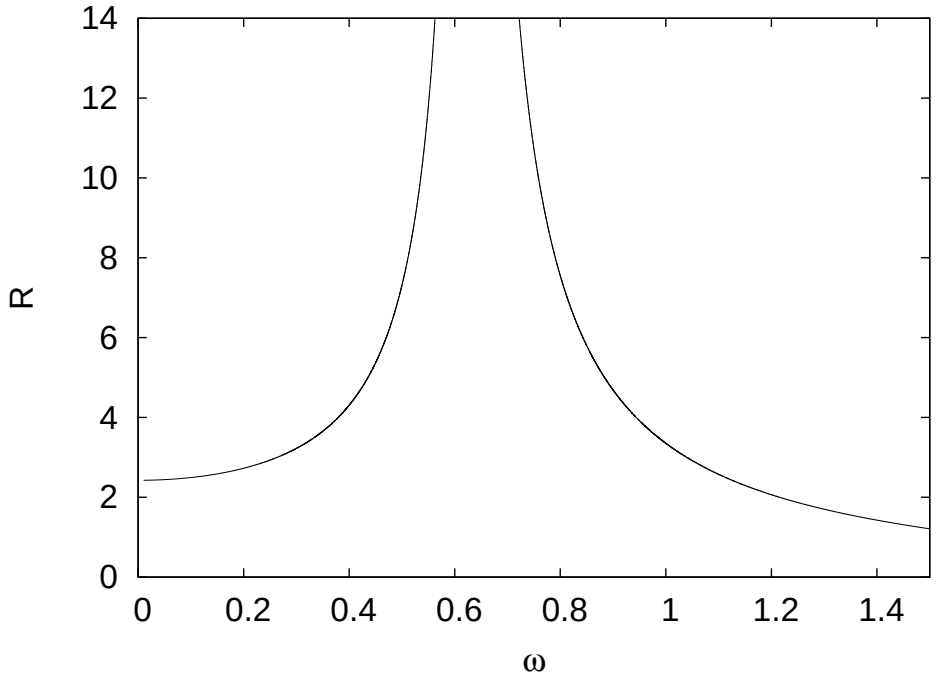

Fig. 41. Response curves obtained from KBM analysis. $\epsilon = 0.3,\ A = 1.6$.

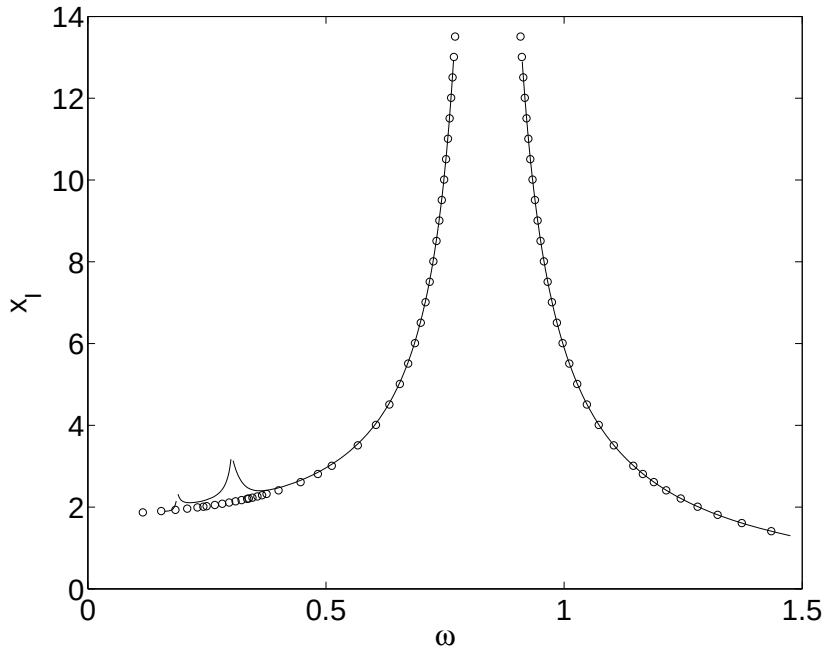

Fig. 42. Comparison of response curves obtained using the KBM method (shown by circles) and the Poincaré maps (shown by solid line). $\epsilon = 0.3,\ A = 1.6$.

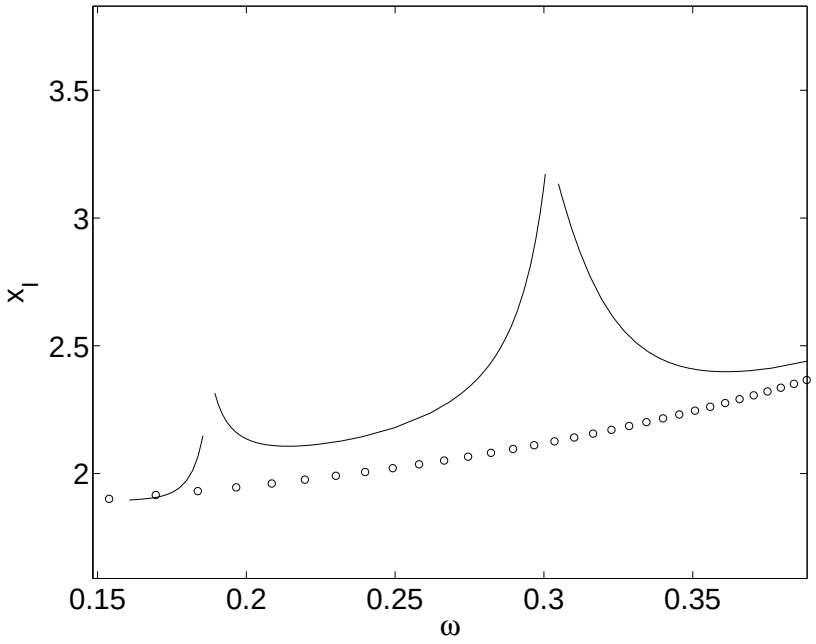

Fig. 43. A magnified view of the sub-harmonic responses. $\epsilon = 0.3,\ A = 1.6$.

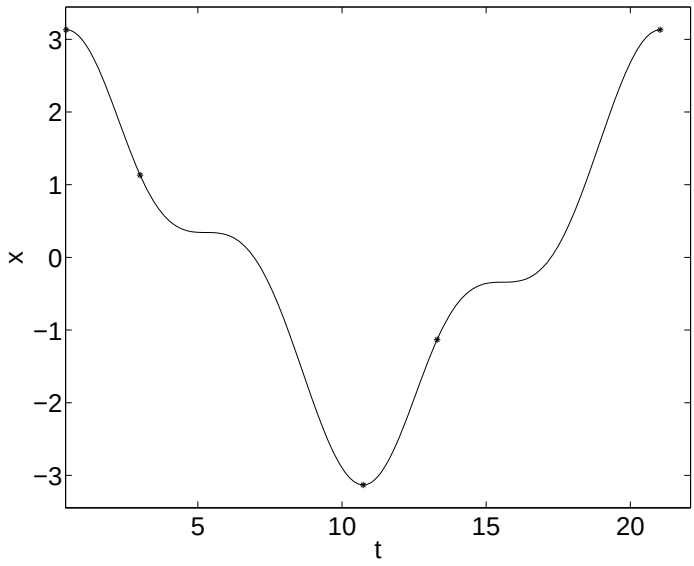

(a) $x(t)$ versus t

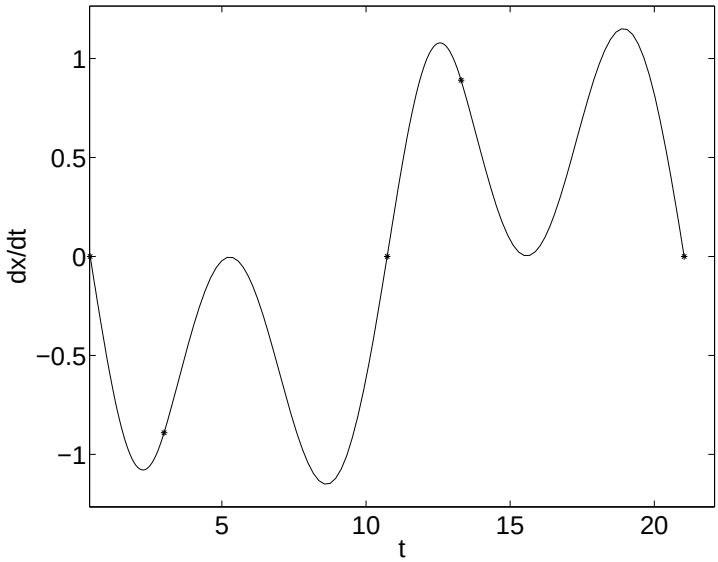

(b) $\dot{x}(t)$ versus t

Fig. 44. Steady state response in time domain. $\epsilon = 0.3, A = 1.6, \omega = 0.3049$. Notice the 'non-sinusoidal' nature of the solution.

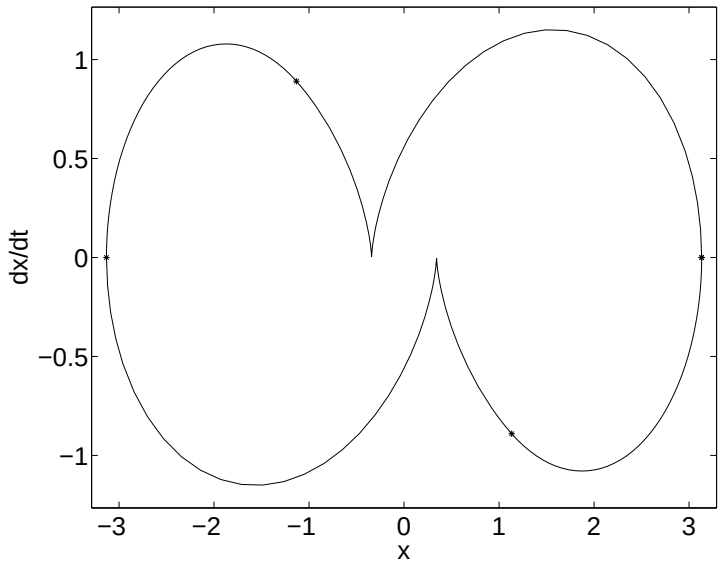

(c) $\dot{x}$ versus x

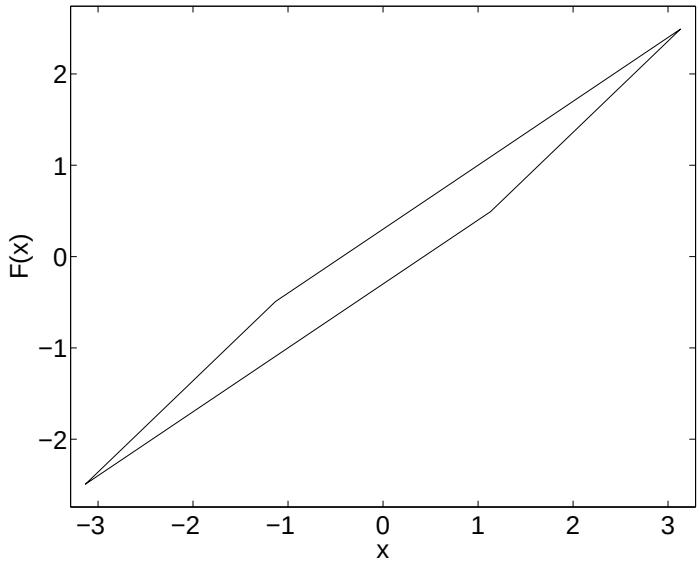

(d) $F(x)$ versus x

Fig. 44. Continued ...

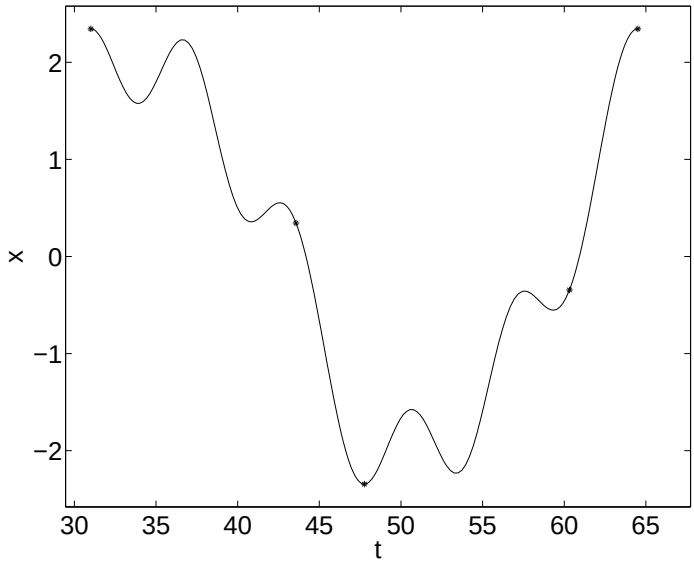

(a) $x(t)$ versus t

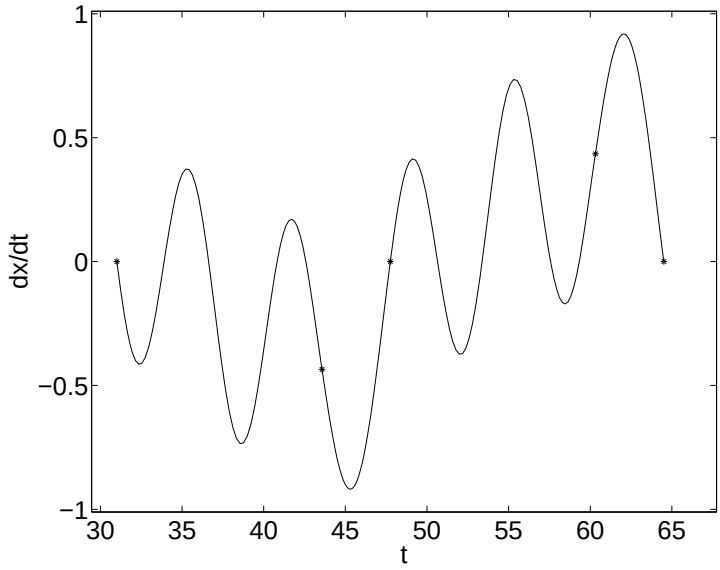

(b) $\dot{x}(t)$ versus t

Fig. 45. Steady state response in time domain. $\epsilon = 0.3, A = 1.6, \omega = 0.187$. Notice the highly 'non-sinusoidal' nature of the solution.

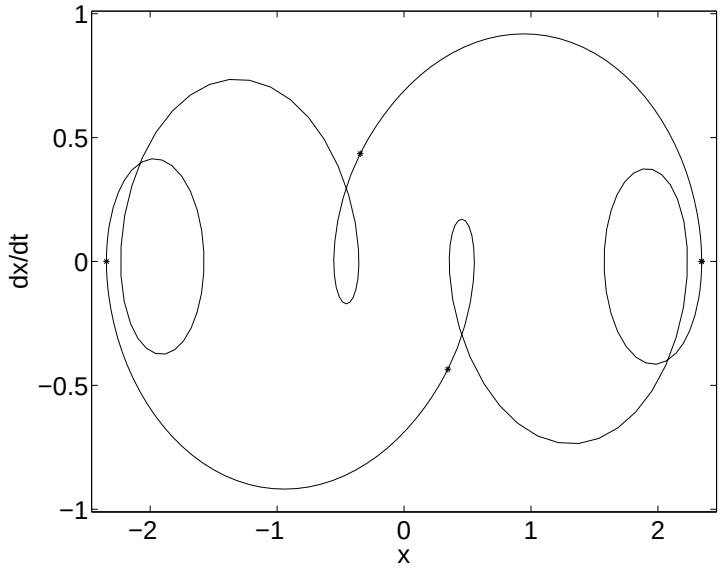

(c) $\dot{x}$ versus x

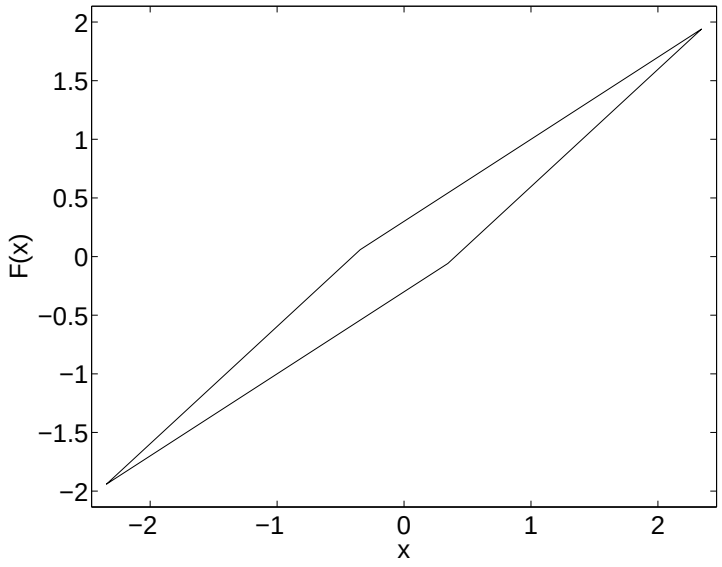

(d) $F(x)$ versus x

Fig. 45. Continued ...

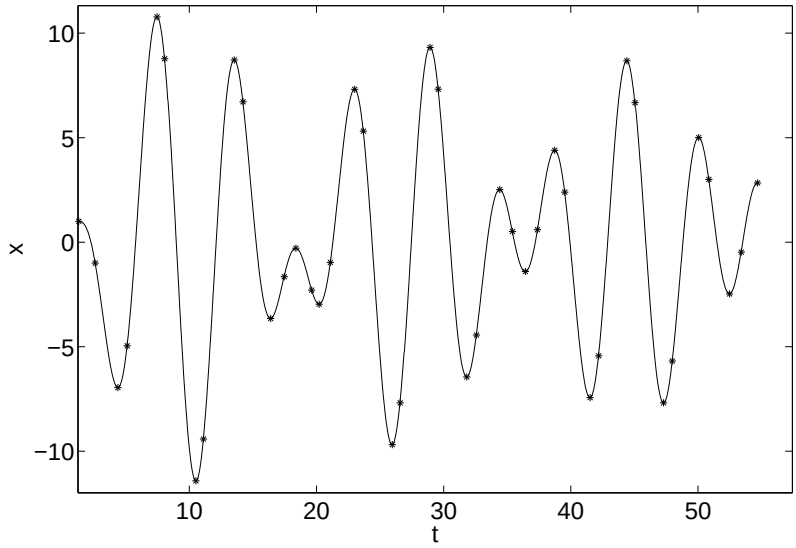

(a) $x(t)$ versus t

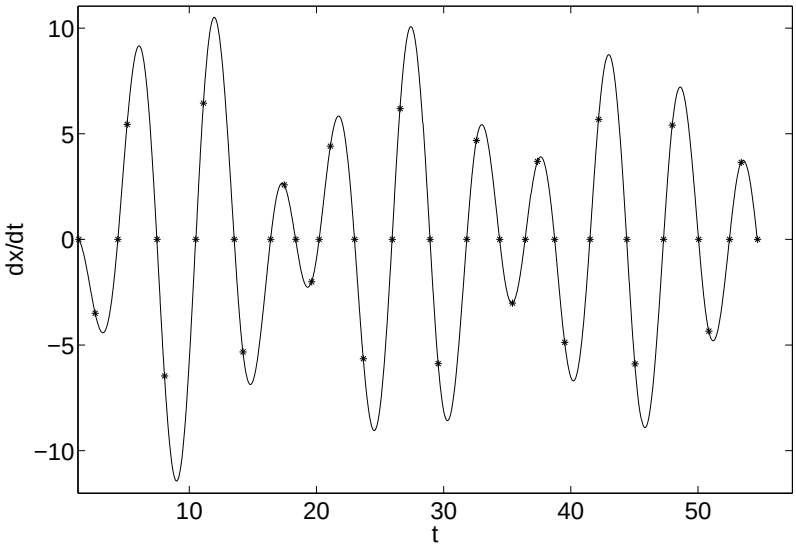

(b) $\dot{x}(t)$ versus t

Fig. 46. Transient response with $\epsilon = 0.3,\ A = 3.65,\ \omega = 1.2$. Initial conditions: $x(t_0) = 1,\ \dot{x}(t_0) = 0,\ t_0 = \pi/2\omega$, starting state $= I$. The first 40 state transitions are shown.

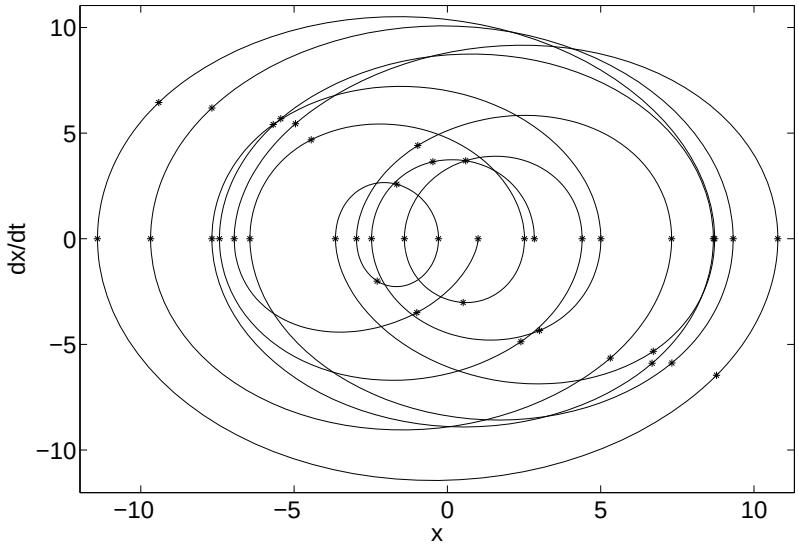

(c) $\dot{x}$ versus x

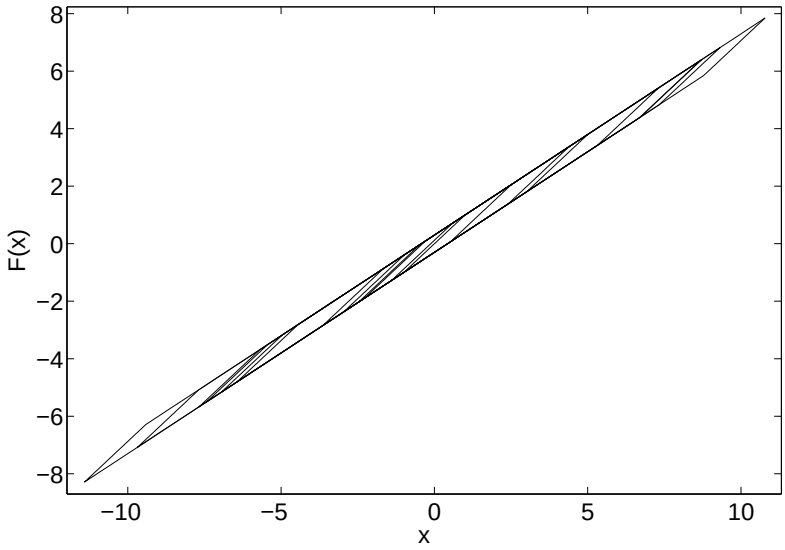

(d) $F(x)$ versus x

Fig. 46. Continued ...

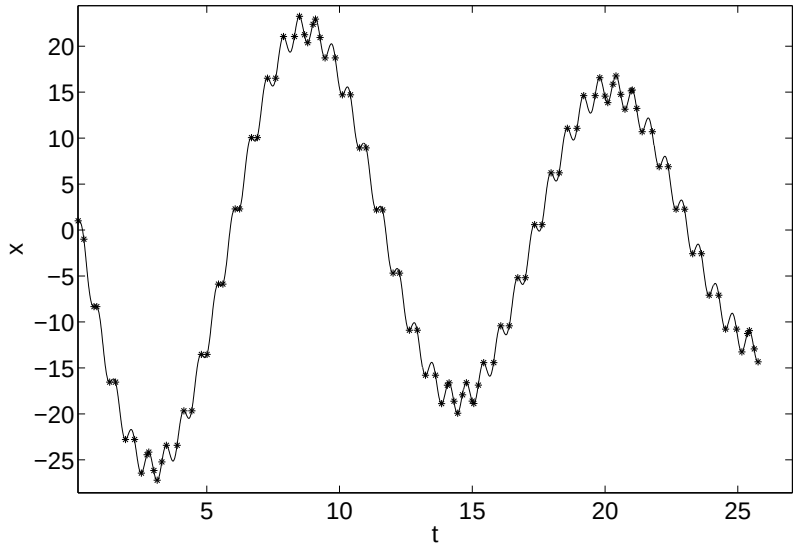

(a) $x(t)$ versus t

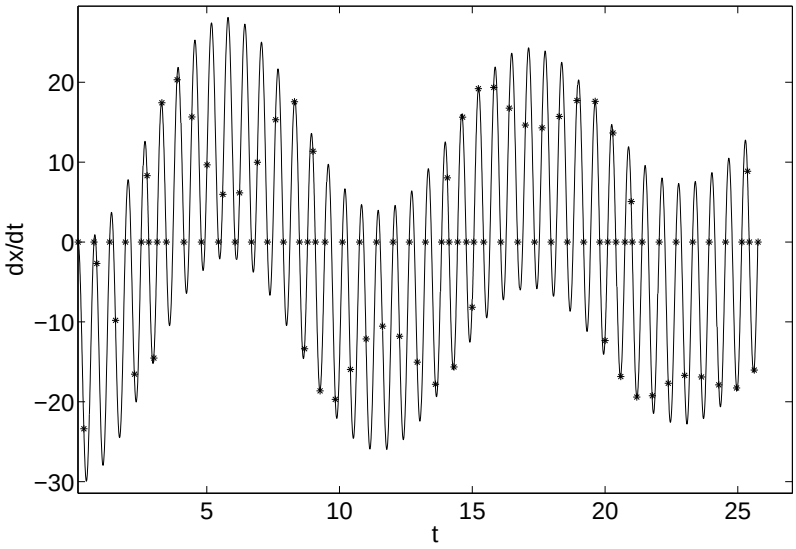

(b) $\dot{x}(t)$ versus t

Fig. 47. Transient response with $\epsilon = 0.7,\ A = 150,\ \omega = 10$. Initial conditions: $x(t_0) = 1,\ \dot{x}(t_0) = 0,\ t_0 = \pi/2\omega$, starting state $= I$. The first 100 state transitions are shown.

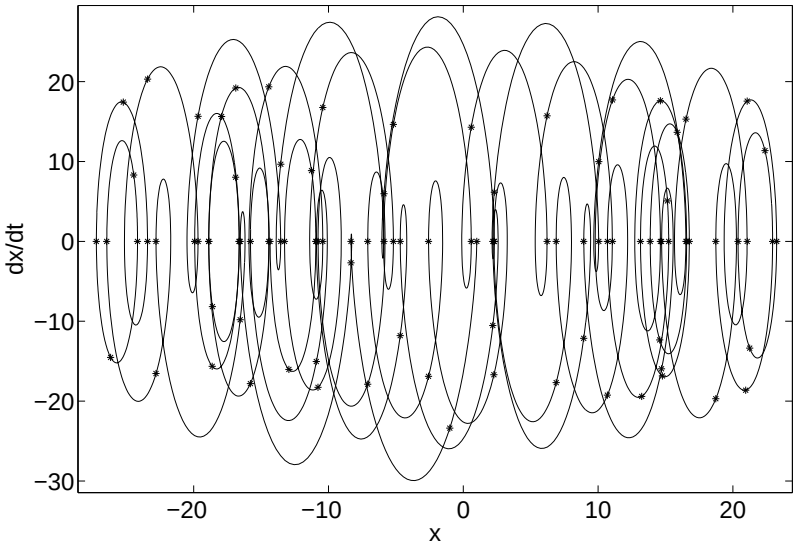

(c) $\dot{x}$ versus x

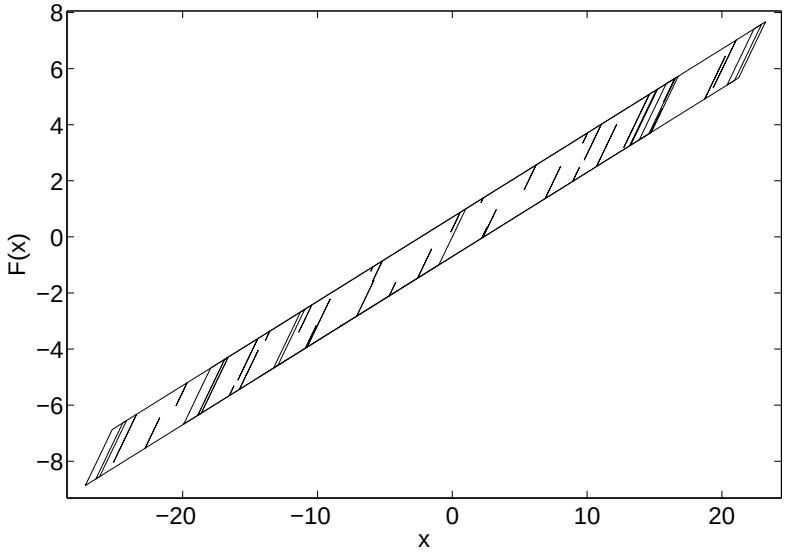

(d) $F(x)$ versus x

Fig. 47. Continued ...

CHAPTER V

OSCILLATORS WITH MULTILINEAR HYSTERESIS AND SINUSOIDAL EXCITATION

In this chapter we will analyze the behavior of oscillators with hysteretic restoring force and sinusoidal excitation where the hysteresis is modeled using the multilinear model of hysteresis. These systems are governed by the following equation

$$\ddot{x} + F(F_0, \epsilon, \alpha)(x(t)) = A\cos(\omega t), \tag{5.1}$$

where F is the multilinear hysteretic operator introduced in chapter I. Note that in the above equation we have loosely used the notation $F(x, F_0, \epsilon, \alpha)$ for the hysteretic restoring force instead of the more formal notation $F(F_0, \epsilon, \alpha)(x)$. This slight abuse of notation saves signification confusion in the later development. As in chapter IV, we will focus on the long-term behavior of the system. The justification focusing on the long-term behavior is that the transient response decays quickly due to the presence of dissipation in the system. This chapter extends chapter IV and the work of Caughey [24] to the analysis of systems with multilinear hysteresis.

The development presented in this chapter follows the layout of chapter IV. We investigate the long-term behavior of Eq. 5.1 using two tools: asymptotic expansions and Poincaré maps. The asymptotic expansions obtained by treating ϵ as a small parameter are seen to provide excellent approximation to the amplitude and frequency of steady state response of the system. To analyze the system more rigorously we construct Poincaré maps (return-maps) and analyze their stability and bifurcations by using tools from nonlinear dynamics. We also calculate the equivalent damping of the hysteretic oscillator for simple steady state response.

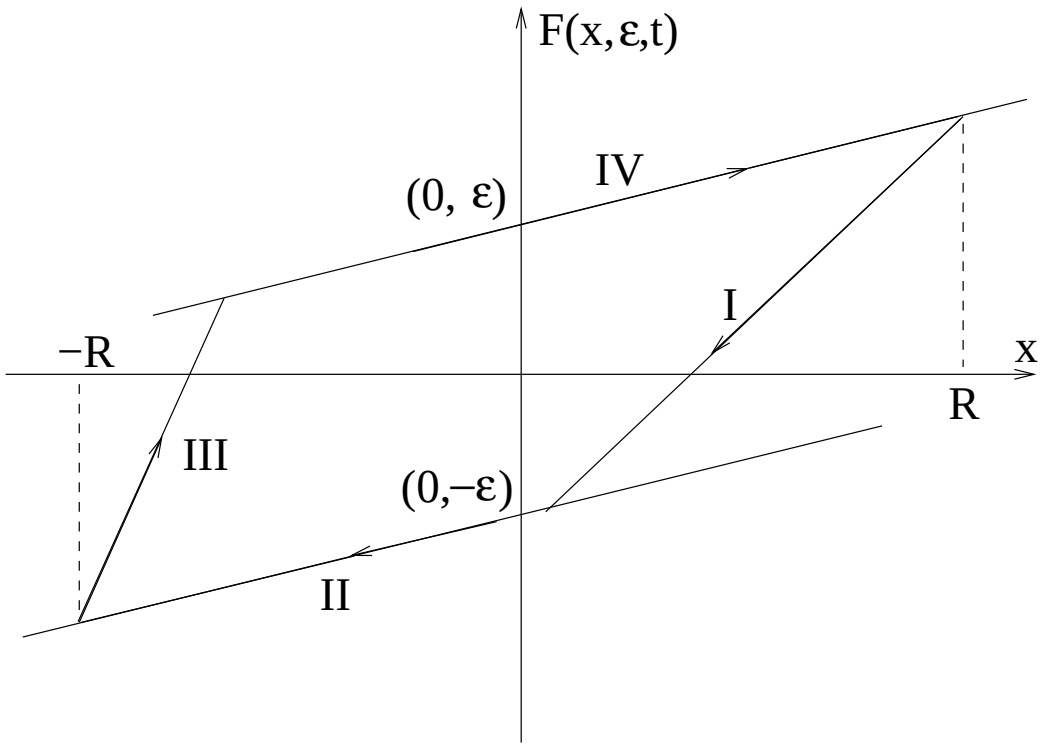

Fig. 48. Multilinear hysteretic restoring force.

A. KBM Analysis of Simple Orbits

In this section we will analyze simple steady state response of Eq. 5.1 for small ϵ using the KBM method. A 'simple steady state response' means a response with principal period of $2\pi/\omega$ the following state transition sequence $\rightarrow I \rightarrow II \rightarrow III \rightarrow IV \rightarrow \ldots$ (see Fig. 48). It should be noted that the KBM method is not limited to analysis of 1-period responses and it can be extended to take into account the higher period response. However, we will focus on the period-1 or the simple steady state response of Eq. 5.1 because it is found to be the dominant response of the system (orbits with other periods are significantly fewer).

As in the bilinear case we assume that the long-term response of Eq. 5.1 is

of sinusoidal character with slowly varying amplitude and frequency. Under this hypothesis we can write

$$x(t) = R(t)\cos\left(\omega t + \phi(t)\right), \tag{5.2}$$

where $R(t)$ and $\phi(t)$ are assumed to be slowly varying with time, i.e.,

$$\begin{aligned} \dot{R}(t) &\sim \mathcal{O}(\epsilon), \\ \dot{\phi}(t) &\sim \mathcal{O}(\epsilon). \end{aligned} \tag{5.3}$$

In the following development the parenthetical t will be dropped for convenience. We introduce a new variable θ defined as follows

$$\theta = \omega t + \phi. \tag{5.4}$$

Obviously x is maximum $(= R)$ at $\theta = 0,\ 2\pi$ and minimum $(= -R)$ at $\theta = \pi$. Thus, if we assume that a simple periodic orbit of the system starts in state I at $\theta = 0$ then it is easy to see that the automaton undergoes transitions $I \to II$, $II \to III$, $III \to IV$ and $IV \to I$ at the following values of x and θ

$$\begin{aligned} x_{I\to II} &= R - \frac{2}{1-\alpha}, \\ \theta_{I\to II} &= \arccos\left(1 - \frac{2}{R(1-\alpha)}\right), \end{aligned} \tag{5.5}$$

$$\begin{aligned} x_{II\to III} &= -R, \\ \theta_{II\to III} &= \pi, \end{aligned} \tag{5.6}$$

$$\begin{aligned} x_{III\to IV} &= -R + \frac{2}{1+\alpha}, \\ \theta_{III\to IV} &= \arccos\left(-1 + \frac{2}{R(1+\alpha)}\right), \end{aligned} \tag{5.7}$$

and

$$\begin{aligned} x_{IV\to I} &= R, \\ \theta_{IV\to I} &= 2\pi. \end{aligned} \tag{5.8}$$

For a period-1 orbit of magnitude R to exist Eqs. 5.5 - 5.8 should have consistent solutions. These requirements impose the following conditions

$$R > x_{I\to II} > -R, \tag{5.9}$$

$$-R < x_{III\to IV} < R. \tag{5.10}$$

The above inequalities have a solution iff

$$|\alpha| < 1. \tag{5.11}$$

Using Eqs. 5.5-5.11 the following relation can be obtained

$$R > \frac{1}{1-|\alpha|}. \tag{5.12}$$

Therefore, a simple period-1 orbit with amplitude R exists only if the condition 5.12 is satisfied. Figure 49 shows the variation of the minimum amplitude of response, R_{min}, required for existence of simple period-1 orbits for various values of α. Note that as $\alpha \to 1$, $R_{min} \to \infty$. For $\alpha = 0$, $R_{min} = 1$, which is expected since for $\alpha = 0$ the multilinear hysteretic operator degenerates to a bilinear hysteretic operator and the minimum amplitude of response required for existence of hysteresis in the bilinear case is 1.

Assuming that necessary conditions for the existence of a period-1 orbit are met we can write the equations for the restoring force for the four branches or modes of

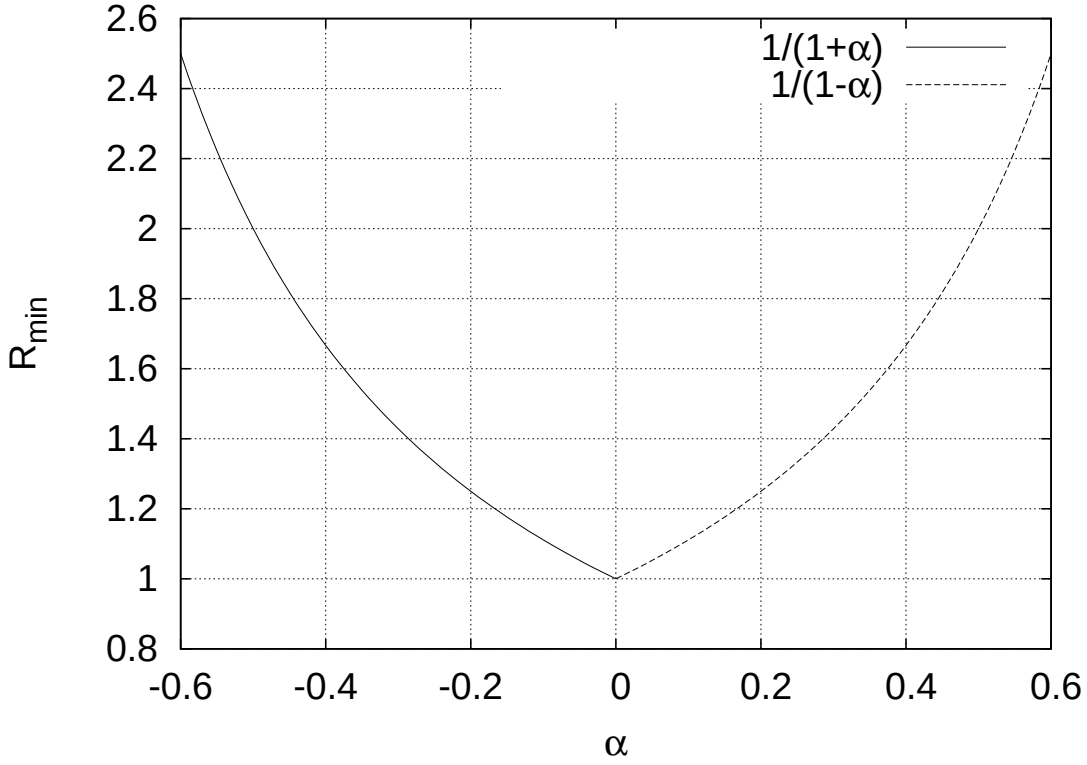

Fig. 49. Minimum amplitude of response required for existence of period-1 orbits for various values of α.

hysteresis as follows

$$\begin{aligned} F_I &= (1-\alpha\epsilon)x + R\epsilon(\alpha-1) + \epsilon, \\ F_{II} &= (1-\epsilon)x - \epsilon, \\ F_{III} &= (1+\alpha\epsilon)x + R\epsilon(\alpha+1) - \epsilon, \\ F_{IV} &= (1-\epsilon)x + \epsilon. \end{aligned} \tag{5.13}$$

As pointed out earlier, in the limit $\epsilon \to 0$, Eq. 5.1 reduces to that of a forced simple harmonic oscillator, and in the limit $\alpha \to 0$, $\epsilon \neq 0$, it reduces to that of a forced harmonic oscillator with bilinear restoring force.

We now proceed to find the steady state response of the system using the KBM method. Differentiating Eq. 5.2 with respect to time and using Eq. 5.4 we get,

$$\dot{x} = -\omega R\sin\theta + \dot{R}\cos\theta - \dot{\phi}R\sin\theta. \tag{5.14}$$

Since $\dot{R},\ \dot{\phi}$ are assumed to be much smaller than ω, the $\mathcal{O}(1)$ part of Eq. 5.14 is given by

$$\dot{x} = -\omega R\sin\theta, \tag{5.15}$$

and the $\mathcal{O}(\epsilon)$ part is

$$\dot{R}\cos\theta - \dot{\phi}R\sin\theta = 0. \tag{5.16}$$

Differentiating Eq. 5.15 with respect to time we get the following relation

$$\ddot{x} = -\omega^2 R\cos\theta - \omega\dot{R}\sin\theta - \omega R\dot{\phi}\cos\theta. \tag{5.17}$$

On substituting Eq. 5.17 in Eq. 5.1 the following can be deduced

$$-\omega^2 R\cos\theta - \omega\dot{R}\sin\theta - \omega R\dot{\phi}\cos\theta + F(R\cos\theta, F_0, \epsilon, \alpha) = A\cos(\theta-\phi). \tag{5.18}$$

Using Eqs. 5.16 and 5.18 the following relations can be obtained

$$-\omega\dot{R} - \omega^2 R\cos\theta\sin\theta + F(R\cos\theta, F_0, \epsilon, \alpha)\sin\theta = A\cos(\theta-\phi)\sin\theta, \tag{5.19}$$

$$-\omega R\dot{\phi} - \omega^2 R\cos^2\theta + F(R\cos\theta, F_0, \epsilon, \alpha)\cos\theta = A\cos(\theta-\phi)\cos\theta. \tag{5.20}$$

Using the fact that $\dot{R},\ \dot{\phi}$ are $\mathcal{O}(\epsilon)$ quantities while $\dot{\theta}$ is $\mathcal{O}(1)$ Eqs. 5.19, 5.20 can be averaged over one period of θ while treating $R,\ \phi$ as constants. Thus, we obtain

$$\dot{R} = \frac{1}{2\pi\omega}\int_0^{2\pi} F(R\cos\theta, F_0, \epsilon, \alpha)\sin\theta\, d\theta - \frac{A}{2\omega}\sin\phi, \tag{5.21}$$

$$\dot{\phi} = \frac{1}{2\pi R\omega}\int_0^{2\pi} F(R\cos\theta, F_0, \epsilon, \alpha)\cos\theta\, d\theta - \frac{A}{2R\omega}\cos\phi - \frac{\omega}{2}. \tag{5.22}$$

Eqs. 5.21, 5.22 are called the *slow-flow* equations. We define

$$C(R) = \frac{1}{\pi}\int_0^{2\pi} F(R\cos\theta, \epsilon, \alpha, t)\cos\theta\, d\theta, \tag{5.23}$$

$$S(R) = \frac{1}{\pi}\int_0^{2\pi} F(R\cos\theta, \epsilon, \alpha, t)\sin\theta\, d\theta. \tag{5.24}$$

Eqs. 5.22, 5.21 can be re-written as

$$\dot{R} = \frac{S(R)}{2\omega} - \frac{A}{2\omega}\sin\phi, \tag{5.25}$$

$$\dot{\phi} = \frac{C(R)}{2R\omega} - \frac{A}{2R\omega}\cos\phi - \frac{\omega}{2}. \tag{5.26}$$

Next we evaluate the integrals $S(R),\ C(R)$. Using Eqs. 5.5-5.8 the integrals $S(R),\ C(R)$

can be evaluated as follows

$$S(R) = \frac{1}{\pi}\left(\int_0^{\theta_1} F(R\cos\theta, F_0, \epsilon, \alpha)\sin\theta\, d\theta + \int_{\theta_1}^{\pi} F(R\cos\theta, F_0, \epsilon, \alpha)\sin\theta\, d\theta\right) \tag{5.27}$$

$$+\frac{1}{\pi}\left(\int_{\pi}^{\theta_2} F(R\cos\theta, F_0, \epsilon, \alpha)\sin\theta\, d\theta + \int_{\theta_2}^{2\pi} F(R\cos\theta, F_0, \epsilon, \alpha)\sin\theta\, d\theta\right) \tag{5.28}$$

$$= -\frac{\epsilon R}{2\pi}\left[(1-\alpha)\sin^2\theta_1 + (1+\alpha)\sin^2\theta_2\right], \tag{5.29}$$

and

$$C(R) = \frac{1}{\pi}\left(\int_0^{\theta_1} F(R\cos\theta, F_0, \epsilon, \alpha)\cos\theta\, d\theta + \int_{\theta_1}^{\pi} F(R\cos\theta, F_0, \epsilon, \alpha)\cos\theta\, d\theta\right) \tag{5.30}$$

$$+\frac{1}{\pi}\left(\int_{\pi}^{\theta_2} F(R\cos\theta, F_0, \epsilon, \alpha)\cos\theta\, d\theta + \int_{\theta_2}^{2\pi} F(R\cos\theta, F_0, \epsilon, \alpha)\cos\theta\, d\theta\right) \tag{5.31}$$

$$= \frac{R}{4\pi}\left[\epsilon(1-\alpha)(2\theta_1 - \sin 2\theta_1) + \epsilon(1+\alpha)(2\theta_2 - \sin 2\theta_2) + 4(1-2\epsilon)\pi\right], \tag{5.32}$$

where

$$\begin{aligned}\theta_1 &= \theta_{I\to II},\\ \theta_2 &= \theta_{III\to IV}.\end{aligned} \tag{5.33}$$

Having evaluated the terms $S(R)$, $C(R)$ it is possible to solve the slow-flow equations. As pointed out in chapter IV the slow-flow equations are not adequate for analyzing the transient behavior of the system (contrary to the results obtained in Appendix A using the KBM method). The reason for this limitation is that the assumed response (Eq. 5.2) has a frequency equal to the frequency of excitation. It is well known that the long-term response of weakly nonlinear systems with damping contains only the frequency of excitation. Thus, the nature of the assumed response is similar to that of the long-term response of a damped system. Hence, the above development does

not adequately capture the transient response of the system.

1. Steady State Response

The steady state response of Eq. 5.1 can be found by evaluating the fixed points of the slow-flow equations. Denoting $R^*,\ \phi^*$ as the fixed points, we can use Eqs. 5.21, 5.22 to get

$$S(R^*) = A\sin\phi^*, \tag{5.34}$$

$$C(R^*) = R\omega^2 + \pi A\cos\phi^*. \tag{5.35}$$

The above equations can be solved for $R^*,\ \phi^*$ as follows

$$\omega^2 = \frac{C(R^*)}{R^*} \pm \left[\left(\frac{A}{R^*}\right)^2 - \left(\frac{S(R^*)}{R^*}\right)^2\right]^{1/2}, \tag{5.36}$$

$$\tan\phi^* = \frac{S(R^*)}{C(R^*) - \omega^2 R^*}. \tag{5.37}$$

Note that even though Eq. 5.36 can be solved for R^* using iterative methods, it is more convenient to specify R^* and solve for the corresponding values of ω. Once the pair $R^*,\ \omega$ is known Eq. 5.37 can be solved to find ϕ^*. From the expressions for $C(R)$ and $S(R)$ and Eq. 5.36 it is obvious that for any given ω the response is single-valued. Thus, according to the KBM analysis the multilinear oscillator does not show the jump phenomena which is characteristic of many nonlinear systems.

2. Resonance

By definition, resonance occurs when Eq. 5.36 has a double root, i.e.,

$$\left(\frac{A}{R^*}\right)^2 = \left(\frac{S(R^*)}{R^*}\right)^2. \tag{5.38}$$

Substituting for $S(R^*)$, θ_1, and θ_2, we obtain (at resonance)

$$R^* = \frac{4\epsilon}{(1-\alpha^2)(4\epsilon - \pi A)}. \tag{5.39}$$

Since R^* is positive by definition and from Eq. 5.11 we have $1-\alpha^2 > 0$, therefore a steady state exists at resonance only if

$$A < \frac{4\epsilon}{\pi}. \tag{5.40}$$

Otherwise, the resonance is unbound. Note that the nature of resonance does not depend on the value of α.

3. Some Response Curves

The response curves for the system can be obtained by using Eqs. 5.36, 5.37. These curves are essentially plots of R^*, ϕ^* versus ω for various values of the system parameters $A,\ \alpha,\ \epsilon$. Figures 50 to 53 show the typical response with bound and unbound resonance for various values of the parameters $A,\ \alpha$ and ϵ. It should be noted that the steady state values found using the KBM method match with those obtained from numerical simulations and Poincaré map based analysis presented later to a good degree even for large ϵ.

4. Stability of Response

The stability of the steady state response can be evaluated by studying the stability of the fixed points of the slow-flow equations. The Jacobian matrix for the system 5.25, 5.26 at a point $R,\ \phi$ is given by

$$\mathbf{J}(R,\phi) = \begin{bmatrix} \frac{1}{2\omega}\frac{\partial S}{\partial R} & -\frac{A\cos\phi}{2\omega} \\ \frac{1}{2\omega}\frac{\partial}{\partial R}\left(\frac{C - A\cos\phi}{R}\right) & \frac{A\sin\phi}{2R\omega} \end{bmatrix}. \tag{5.41}$$

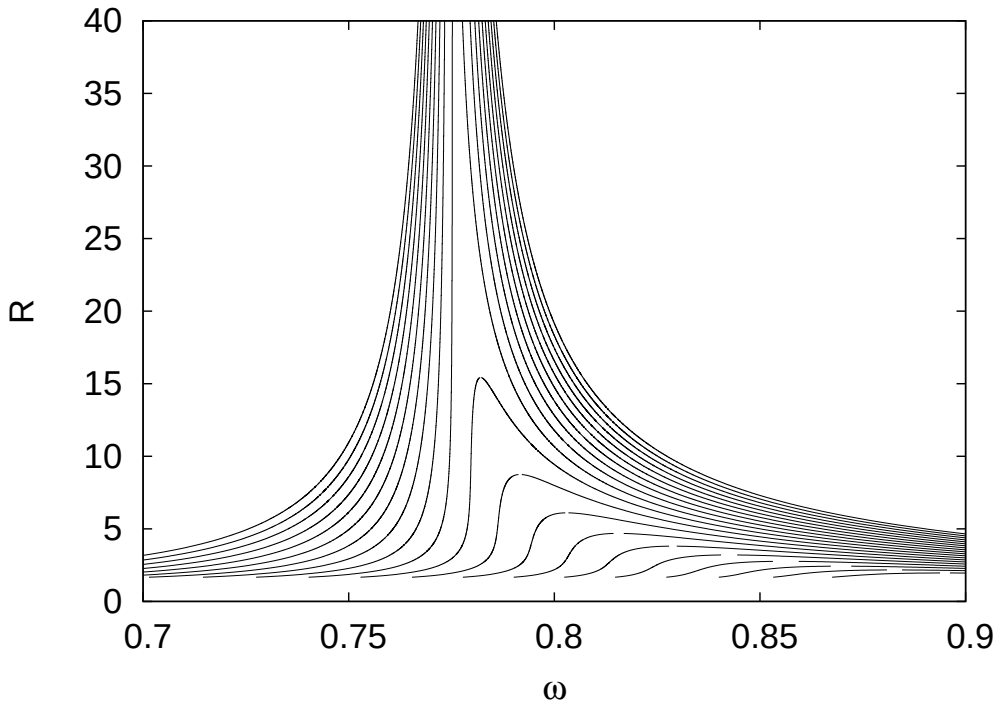

Fig. 50. Frequency response for varying A. $\epsilon = 0.4,\ \alpha = 0.5$, A varies between 0.2 to 0.8.

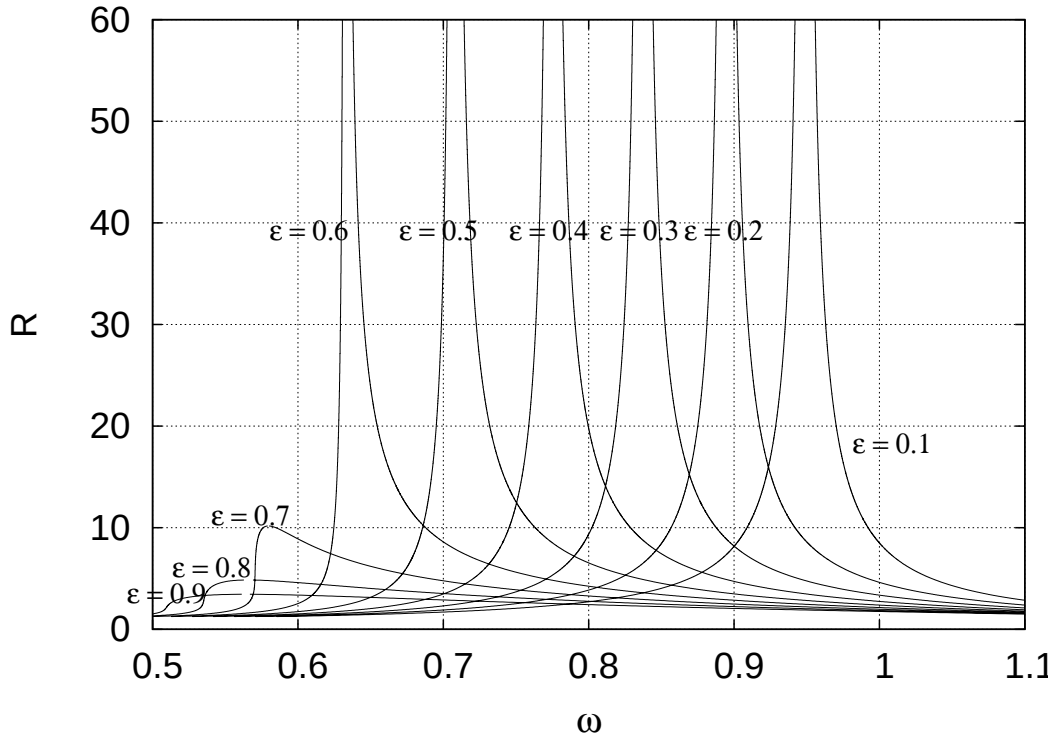

Fig. 51. Frequency response for varying ϵ. $A = 0.8,\ \alpha = 0.2$, ϵ varies between 0.1 and 0.9.

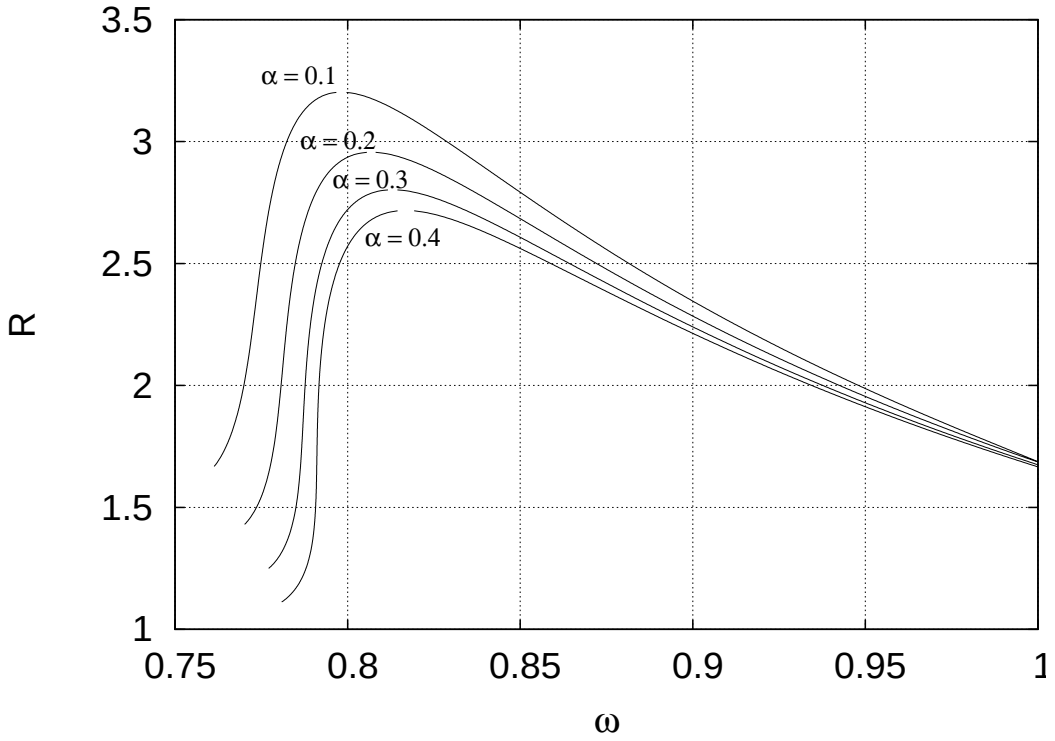

Fig. 52. Frequency response for varying α. $\epsilon = 0.5,\ A = 0.4$, α varies between 0.1 and 0.5.

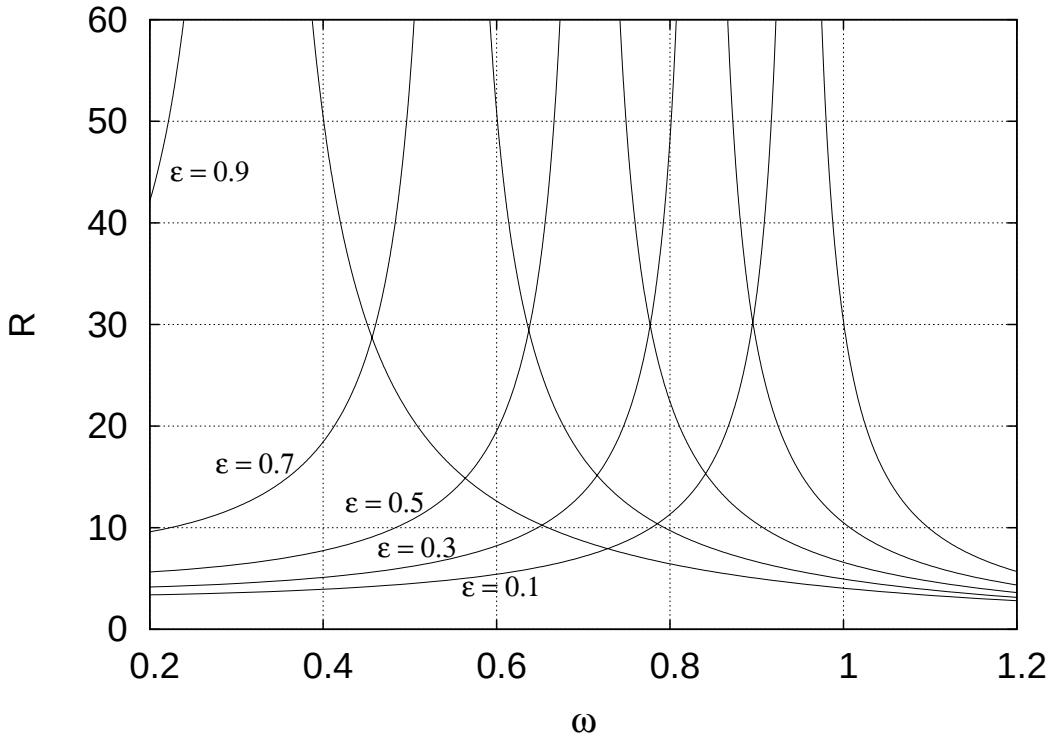

Fig. 53. Frequency response for varying ϵ. $A = 3,\ \alpha = 0.5$, ϵ varies between 0.1 and 0.9.

At steady state the Jacobian can be written as

$$\mathbf{J}(R^*, \phi^*) = \begin{bmatrix} \frac{1}{2\omega}\frac{\partial S}{\partial R} & \frac{1}{2\omega}\left(R^*\omega^2 - C^*\right) \\ \frac{1}{2R^*\omega}\left(\frac{\partial C}{\partial R} - \omega^2\right) & \frac{S^*}{2R^*\omega} \end{bmatrix}, \tag{5.42}$$

with the partial derivatives evaluated at the fixed point. Since we are studying a two-dimensional system we can use the trace-determinant criteria for finding the system stability. The trace of the Jacobian matrix can be evaluated as follows

$$\begin{aligned} \text{trace}(J(R^*, \phi^*)) =& \frac{1}{2\omega}\left(\frac{\partial S}{\partial R} + \frac{S^*}{R^*}\right) \\ =& -\frac{\epsilon}{4\pi\omega}\left[(1-\alpha)(1-\cos\theta_1)^2 + (1+\alpha)(1+\cos\theta_2)^2\right] \\ & -\frac{\epsilon}{4\pi\omega}\left[(1-\alpha)\sin\theta_1^2 + (1+\alpha)\sin\theta_2^2\right] \\ =& -\frac{\epsilon}{2\pi\omega}\left[(1-\alpha)(1-\cos\theta_1) + (1+\alpha)(1+\cos\theta_2)\right] \\ =& -\frac{\epsilon}{\pi R\omega} \\ & < 0. \end{aligned} \tag{5.43}$$

and the determinant can be found to be the following

$$\begin{aligned} \det(J(R^*, \phi^*)) &= \frac{1}{4\omega^2}\left[\frac{S}{R}\frac{\partial S}{\partial R} + \left(\frac{C}{R} - \omega^2\right)\left(\frac{\partial C}{\partial R} - \omega^2\right)\right] \\ &= \frac{1}{4\omega^2}\left[\left(\omega^2 - \frac{1}{2}\left(\frac{C}{R} + \frac{\partial C}{\partial R}\right)\right)^2 + \frac{S}{R}\frac{\partial S}{\partial R} - \frac{1}{4}\left(\frac{C}{R} - \frac{\partial C}{\partial R}\right)^2\right]. \end{aligned} \tag{5.44}$$

It is possible to show that

$$\begin{aligned}\frac{S}{R}\frac{\partial S}{\partial R}-\frac{1}{4}\left(\frac{C}{R}-\frac{\partial C}{\partial R}\right)^2 =&\frac{\epsilon^2}{4\pi^2}\left[(1-\alpha)\sin^2\theta_1+(1+\alpha)\sin^2\theta_2\right]\\ &\left[(1-\alpha)(1-\cos\theta_1)^2+(1+\alpha)(1+\cos\theta_2)^2\right]\\ &-\frac{\epsilon^2}{4\pi^2}\left[(1-\alpha)\sin\theta_1(1-\cos\theta_1)\right.\\ &\left.+(1+\alpha)\sin\theta_2(1+\cos\theta_2)\right]^2\\ =&\frac{\epsilon^2}{4\pi^2}(1-\alpha^2)\left[(1-\alpha)\sin\theta_1+(1+\alpha)\sin\theta_2\right]^2.\end{aligned} \tag{5.45}$$

Therefore,

$$\begin{aligned}\det(J(R^*,\phi^*)) &= \frac{1}{4\omega^2}\left[\left(\omega^2-\frac{1}{2}\left(\frac{C}{R}+\frac{\partial C}{\partial R}\right)\right)^2+\frac{S}{R}\frac{\partial S}{\partial R}-\frac{1}{4}\left(\frac{C}{R}-\frac{\partial C}{\partial R}\right)^2\right]\\ &= \frac{1}{4\omega^2}\left[\left(\omega^2-\frac{1}{2}\left(\frac{C}{R}+\frac{\partial C}{\partial R}\right)\right)^2\right.\\ &\quad\left.+\frac{\epsilon^2}{4\pi^2}(1-\alpha^2)\left[(1-\alpha)\sin\theta_1+(1+\alpha)\sin\theta_2\right]^2\right]\\ &\geq 0.\end{aligned} \tag{5.46}$$

Thus, by the trace-determinant criteria the steady state response of the system is always stable.

B. Equivalent Damping Properties

In this section we will derive expressions for the damping and natural frequency of a linear harmonic oscillator that has the same amplitude and phase response as the hysteretic oscillator when both systems have the same harmonic excitation. We will follow the development presented in chapter IV section B. We aim to find parameters ξ, γ such that the steady state response of the following oscillator matches that of

the hysteretic oscillator discussed in previous sections

$$\ddot{x} + 2\xi\gamma\dot{x} + \gamma^2 x = A\cos(\omega t). \tag{5.47}$$

The parameters ξ and γ can be considered to be the equivalent damping and natural frequency of the hysteretic oscillator. Proceeding as in chapter IV section B we can get the following expressions for γ ξ

$$\gamma^2 = \frac{C(R)}{R}, \tag{5.48}$$

and

$$\xi = \frac{-S}{2R\omega\xi}. \tag{5.49}$$

Figures 54 and 55 show the variation of the equivalent damping with the frequency of excitation for some typical cases.

C. Poincaré Maps

In this section we analyze the steady state response of Eq. 5.1 using Poincaré maps. The development presented here is very similar to that presented in chapter IV section C. Thus, some details are omitted here and can be found in chapter IV section C.

Following the arguments presented in chapter IV we can deduce the following general structure of the periodic orbits of the system

$$(\rightarrow (I \rightarrow IV)_{n_i \text{ times}} \rightarrow I \rightarrow II \rightarrow$$
$$\rightarrow (III \rightarrow II)_{m_i \text{ times}} \rightarrow III \rightarrow IV \rightarrow)_{i \text{ such blocks with different } n_i, m_i}.$$

Thus, every periodic orbit of the system has at least one $IV \rightarrow I$ transition. By definition $\dot{x}_I$ is zero, i.e., the velocity is zero at the beginning of state I. The beginning of state I is then characterized by the value of x and the time t at which the $IV \rightarrow I$

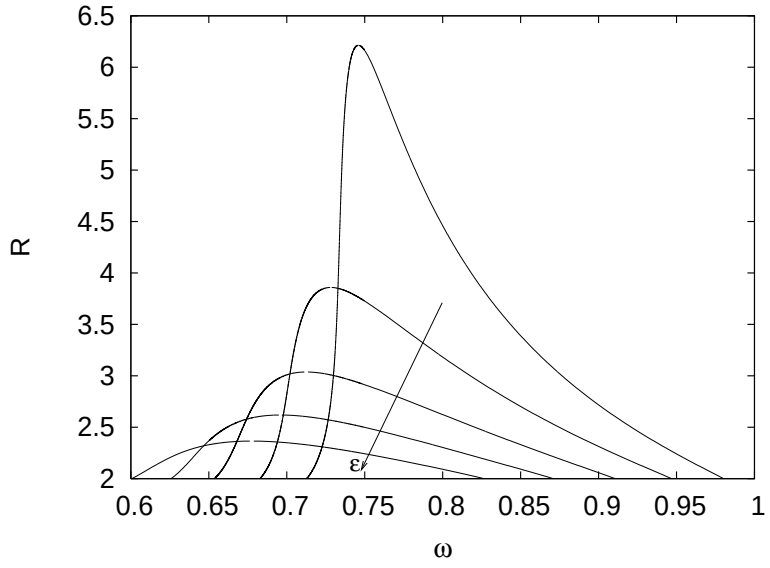

(a) Response versus frequency

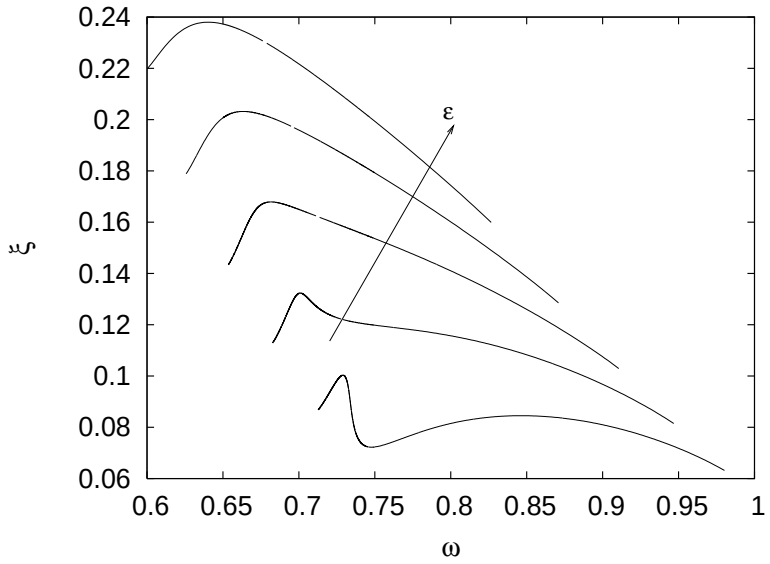

(b) Equivalent damping versus frequency

Fig. 54. Variation of equivalent damping with frequency. $A = 0.5, \alpha = 0.5$, ϵ varied between 0.5 and 0.9.

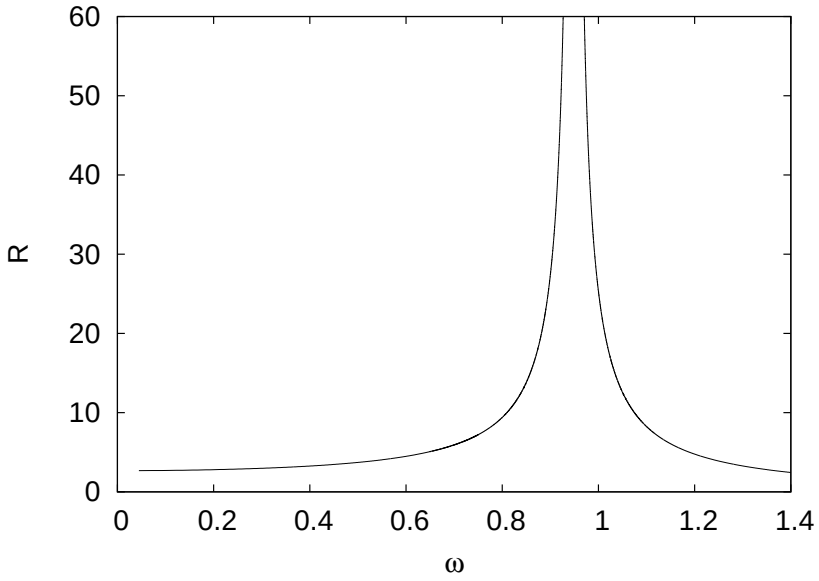

(a) Response versus frequency

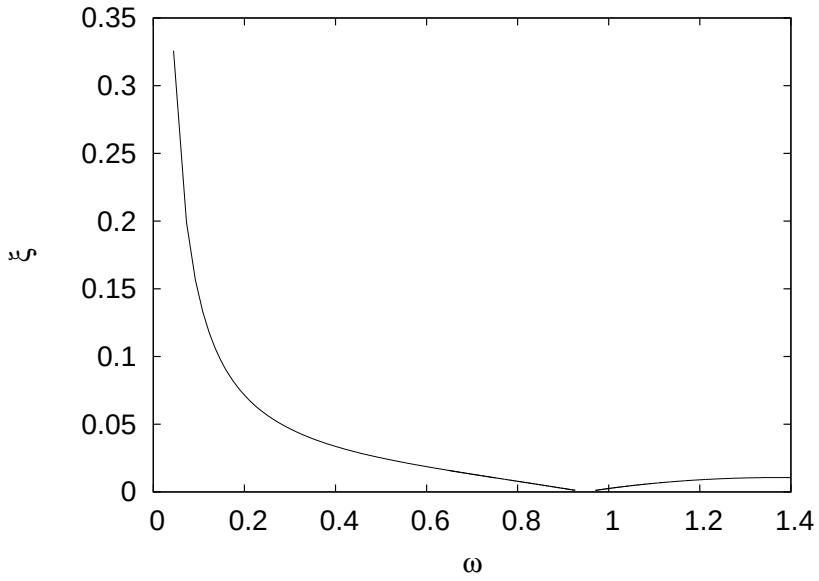

(b) Equivalent damping versus frequency

Fig. 55. Variation of equivalent damping with frequency. $A = 2.5$, $\epsilon = 0.1, \alpha = 0.3$.

transition occurs. We use the symbols x_I and t_I^* to represent these values. The explicit dependence of the system on t is via the forcing term $A\cos(\omega t)$, so we can set $t = 0$ at the beginning of each state provided we introduce an appropriate phase variable $\phi_n,\ n \in \{I,\ II,\ III,\ IV\}$ defined by

$$\phi_n = \omega t_n^* \mod 2\pi, \tag{5.50}$$

and modify the forcing term to become $A\cos(\omega t + \phi_n)$. In particular, for the $IV \to I$ transition we introduce the phase variable ϕ_I defined by

$$\phi_I = \omega t_I^* \mod 2\pi, \tag{5.51}$$

and change the forcing term to $A\cos(\omega t + \phi_I)$. After introducing the variable ϕ we can characterize the beginning of state I by the pair (x_I, ϕ_I). A periodic orbit may have many $IV \to I$ transitions. We can mark any one of these transitions and define a map

$$(x_I, \phi_I)_i \mapsto (x_I, \phi_I)_{i+1}, \tag{5.52}$$

where the subscript i denotes the i^{th} return to the marked state I. At this point there can be some confusion as to what is meant by a 'marked' state I. To clear this confusion consider a periodic orbit that has the following sequence of state transitions

$$\left(\to I \to II \to III \to IV \to \hat{I} \to IV \to\right), \tag{5.53}$$

where $\hat{I}$ denotes the marked state I. Note that the above cycle may be also written as follows

$$\left(\to III \to IV \to \hat{I} \to IV \to I \to II \to\right). \tag{5.54}$$

Even though the start and end of a periodic orbit are arbitrary, the sequence of state transitions is preserved and thus the marked state can be identified irrespective of

which transition we choose to call the beginning of the orbit. Further, each complete orbit should have only one marked state. Considering these arguments the map 5.52 is indeed well defined and can be used to study the periodic orbits of the system in almost the same manner as a usual Poincaré map.

The map 5.52 would be a Poincaré map if the system being considered were an autonomous system, and it would be a return-map if the system were a non-autonomous system with periodic dependence on t. However, since the system that we are studying is a non-smooth hybrid system the map 5.52 is neither a Poincaré map nor a return-map in the exact sense. Nonetheless, we will loosely call it a Poincaré map. The fixed points of the Poincaré map represent closed orbits of the system, and the stability of these fixed points can be used to characterize the stability of the corresponding orbits. The bifurcations of this map have direct correspondence with the bifurcations of the periodic response of Eq. 5.1.

In order construct the map 5.52, given the pair $(x_I,\ \phi_I)_i$ we need to be able to calculate the pair $(x_I,\ \phi_I)_{i+1}$. To calculate this pair we proceed as follows. Since the pair $(x_I,\ \phi_I)$ fully characterizes the system in state I, we can in principle calculate the time of the next transition given $(x_I,\ \phi_I)$. Once the time of the next transition is known, the value of $x,\ \dot{x}$ and ϕ at the beginning of the new state can be found. Continuing this process through the transitions that make the orbit we can find the pair $(x_I, \phi_I)_{i+1}$. The transition criteria for the various transitions were defined in chapter III. Using those criteria we will next write the equations needed to solve for the various transition times. To this end we define a function $x_n(t), n \in \{I,\ II,\ III,\ IV\}$ which plays a central role in determining the state transitions.

$$\begin{aligned} x_n(t) = &\left(x_0 - \frac{k}{\omega_o^2} - \frac{A\cos\phi_0}{\omega_o^2 - \omega^2}\right)\cos(\omega_o t) + \frac{1}{\omega_o}\left(v_0 + \frac{A\omega\sin\phi_0}{\omega_o^2 - \omega^2}\right)\sin(\omega_o t) \\ &+ \frac{A}{\omega_o^2 - \omega^2}\cos(\omega t + \phi_0) + \frac{k}{\omega_o^2}. \end{aligned} \tag{5.55}$$

It is easy to check that for appropriate values of the constants $x_0,\ v_0,\ \phi_0,\ k$, and ω_o the function $x_n(t)$ evaluates to the solution $x(t)$ of Eq. 5.1 for the different states of the automaton. The general structure of $x(t)$ is similar for all the states because the structure of the governing equation (Eq. 5.1) is similar for all the states. The difference in the expression for $x(t)$ for different states comes for two sources: system parameters and initial conditions. The system parameters k and ω_o for the various states are given in table XII, while the initial conditions $x_0,\ v_0,\ \phi_0$ for the different states are given in table XIII. Recall that we use the notation $x_I = x_I(0), x_{II} = x_{II}(0)$ etc.

Table XII. Parameters in expression for $x_n(t)$ for different states.

State	Parameters
I	$\omega_o^2 = 1 - \alpha\epsilon,\ k = x_I\epsilon(1-\alpha) - \epsilon$
II	$\omega_o^2 = 1 - \epsilon,\ k = \epsilon$
III	$\omega_o^2 = 1 + \alpha\epsilon,\ k = x_{III}\epsilon(1+\alpha) + \epsilon$
IV	$\omega_o^2 = 1 - \epsilon,\ k = -\epsilon$

We have summarized the conditions for various mode transitions in table XIV. Using these conditions and the appropriate expressions for $x_n(t)$ we can in principle solve for the transition time for any transition. In practice it is not simple to solve the resulting equations for finding the transition time. A method for solving these equations is presented in Appendix B.

Figures 56 and 57 show the variation of $t^*_{I\to II}$ with x_I and ϕ_I for some values of $\epsilon,\ A$ and ω. As a convention, if for certain parameter values the transition time is greater than certain threshold value then it is set to -1 for plotting purposes. The figures show that $t^*_{I\to II}$ is discontinuous in both x_I and ϕ_I. At the points where the

Table XIII. Initial conditions in expression for $x_n(t)$ for different states for the multi-linear hysteretic oscillator.

State	Previous State	Initial Conditions
I	IV	$x_0 = x_I = x_{IV}(t^*_{IV\to I}), v_0 = \dot{x}_I = 0,$ $\phi_0 = \phi_I = \omega t^*_{IV\to I} \mod 2\pi$
II	I	$x_0 = x_{II} = x_I(t^*_{I\to II}), v_0 = \dot{x}_{II} = \dot{x}_I(t^*_{I\to II}),$ $\phi_0 = \phi_{II} = \omega t^*_{I\to II} \mod 2\pi$
II	III	$x_0 = x_{II} = x_{III}(t^*_{III\to II}), v_0 = \dot{x}_{II} = \dot{x}_{III}(t^*_{III\to II}),$ $\phi_0 = \phi_{III} = \omega t^*_{III\to II} \mod 2\pi$
III	II	$x_0 = x_{III} = x_{II}(t^*_{II\to III}), v_0 = \dot{x}_{III} = 0,$ $\phi_0 = \phi_{III} = \omega t^*_{II\to III} \mod 2\pi$
IV	III	$x_0 = x_{IV} = x_{III}(t^*_{III\to IV}), v_0 = \dot{x}_{IV} = \dot{x}_{III}(t^*_{III\to IV}),$ $\phi_0 = \phi_{IV} = \omega t^*_{III\to IV} \mod 2\pi$
IV	I	$x_0 = x_{IV} = x_I(t^*_{I\to IV}), v_0 = \dot{x}_{IV} = \dot{x}_I(t^*_{I\to IV}),$ $\phi_0 = \phi_{IV} = \omega t^*_{I\to IV} \mod 2\pi$

discontinuity occurs the partial derivatives of $t^*_{I\to II}$ with respect to x_I and ϕ_I are not defined. These partial derivatives can be written as

$$\begin{aligned}\frac{\partial t^*_{I\to II}}{\partial x_I(0)} &= -\frac{\partial x_I(t)/\partial x_I(0)}{\partial x_I(t)/\partial t}\Big|_{t=t^*_{I\to II}},\\ \frac{\partial t^*_{I\to II}}{\partial \phi_I} &= -\frac{\partial x_I(t)/\partial \phi_I}{\partial x_I(t)/\partial t}\Big|_{t=t^*_{I\to II}}.\end{aligned} \tag{5.56}$$

The above partial derivatives are not defined when

$$\frac{\partial x_I(t)}{\partial t}\Big|_{t=t^*_{I\to II}} = 0. \tag{5.57}$$

The condition expressed by Eq. 5.57 implies that $t^*_{I\to II}$ is a root $x_I(t) = x_I(0) -$

Table XIV. Conditions for mode transitions for the multilinear automaton.

Transition	Condition
$I \rightarrow II$	$x_I(t) = x_0 - 2/(1-\alpha) = x_I - 2/(1-\alpha),\ \dot{x}_I(t) < 0$
$I \rightarrow IV$	$x_I(t) = x_0 = x_I,\ \dot{x}_I(t) > 0$
$II \rightarrow III$	$\dot{x}_{II}(t) = 0,\ \ddot{x}_{II}(t) > 0$
$III \rightarrow IV$	$x_{III}(t) = x_0 + 2/(1+\alpha) = x_{III} + 2/(1+\alpha),\ \dot{x}_{III}(t) > 0$
$III \rightarrow II$	$x_{III}(t) = x_0 = x_{III},\ \dot{x}_{III}(t) < 0$
$IV \rightarrow I$	$\dot{x}_{IV}(t) = 0,\ \ddot{x}_{IV}(t) < 0$

$2/(1-\alpha)$ of multiplicity greater than 1. It is shown in chapter III that in general the equations determining the mode transitions cannot have roots of multiplicity higher than 2. Thus, Eq. 5.57 implies the existence of an algebraic saddle-node bifurcation for the equation $x_I(t) = x_I(0) - 2/(1-\alpha)$ (see table XIV). This bifurcation is also know as the grazing bifurcation. Although we have discussed the case of $I \rightarrow II$ transition the other transitions can have grazings as well.

1. Typical Results

In this section we present one set of results obtained from the bifurcation analysis of the Poincaré map defined by Eq. 5.52. Note that since the bilinear hysteretic oscillator is a special case of the multilinear oscillator, the multilinear oscillator shows all phenomena exhibited by the bilinear oscillator. These include "bumps" in the response curve (see chapter IV section C) and non-sinusoidal orbits. With this in mind, in this section we present two phenomena that are exhibited by the multilinear hysteretic oscillator but not by its bilinear counterpart. These phenomena are grazing bifurcation of periodic orbits, and multi-valued frequency response.

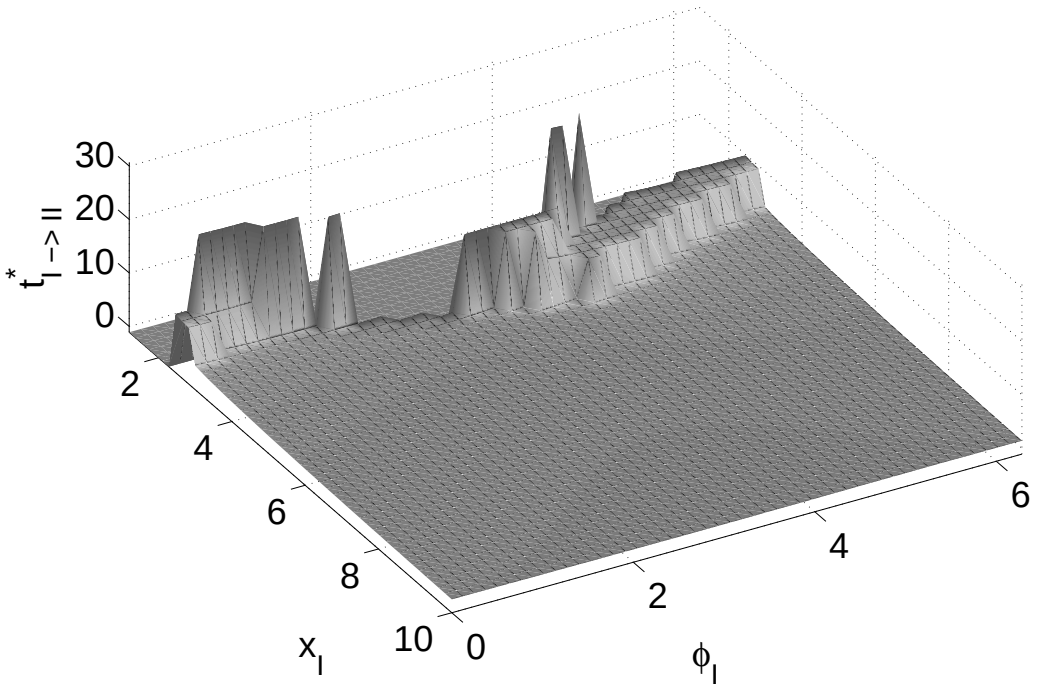

(a) Variation of $t^*_{I\to II}$ with x_I and ϕ_I.

Fig. 56. Variation of $t^*_{I\to II}$ with x_I and ϕ_I. $\epsilon = 0.3,\ \alpha = 0.7,\ A = 0.75,\ \omega = 1.3$.

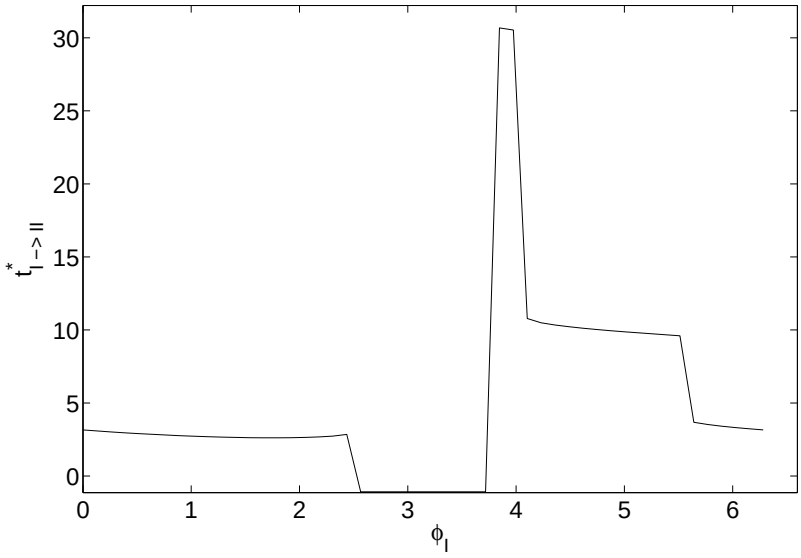

(b) $t^*_{I\to II}$ versus ϕ_I with $x_I = 3.2$.

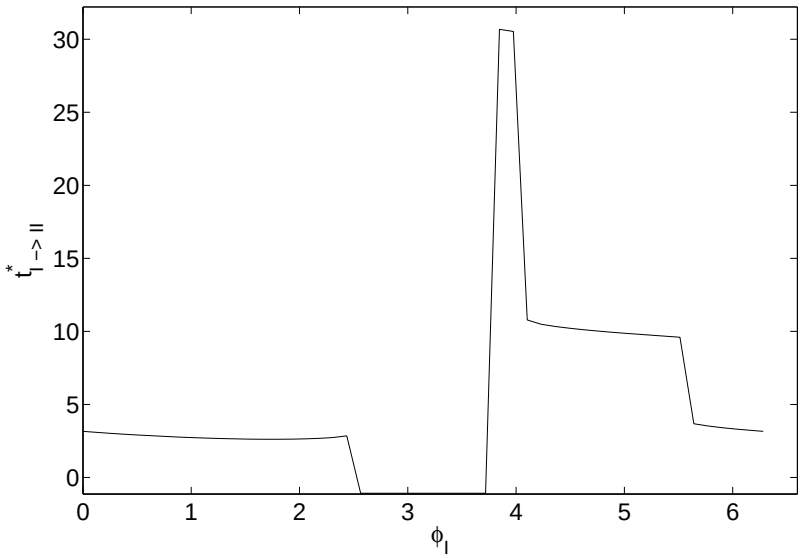

(c) $t^*_{I\to II}$ versus ϕ_I with $x_I = 6.4$.

Fig. 56. Continued ...

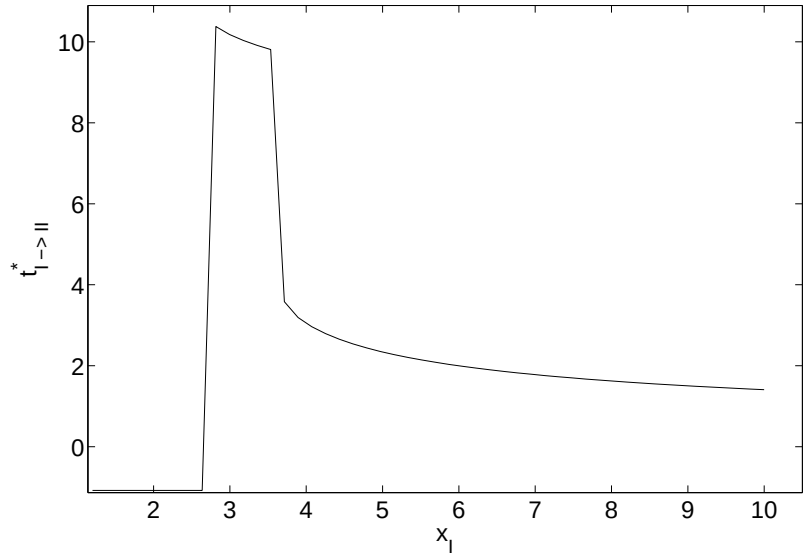

(d) $t^*_{I\to II}$ versus x_I with $\phi_I = 4.7$.

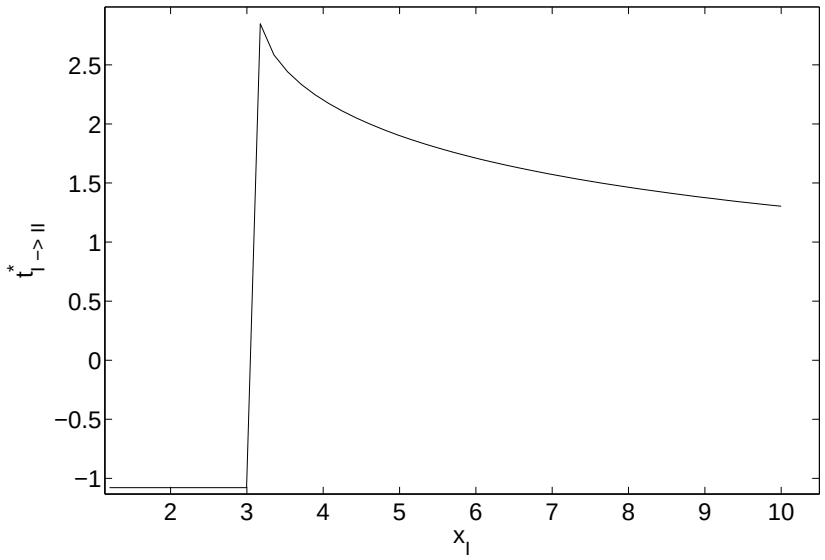

(e) $t^*_{I\to II}$ versus x_I with $\phi_I = 2.4$.

Fig. 56. Continued ...

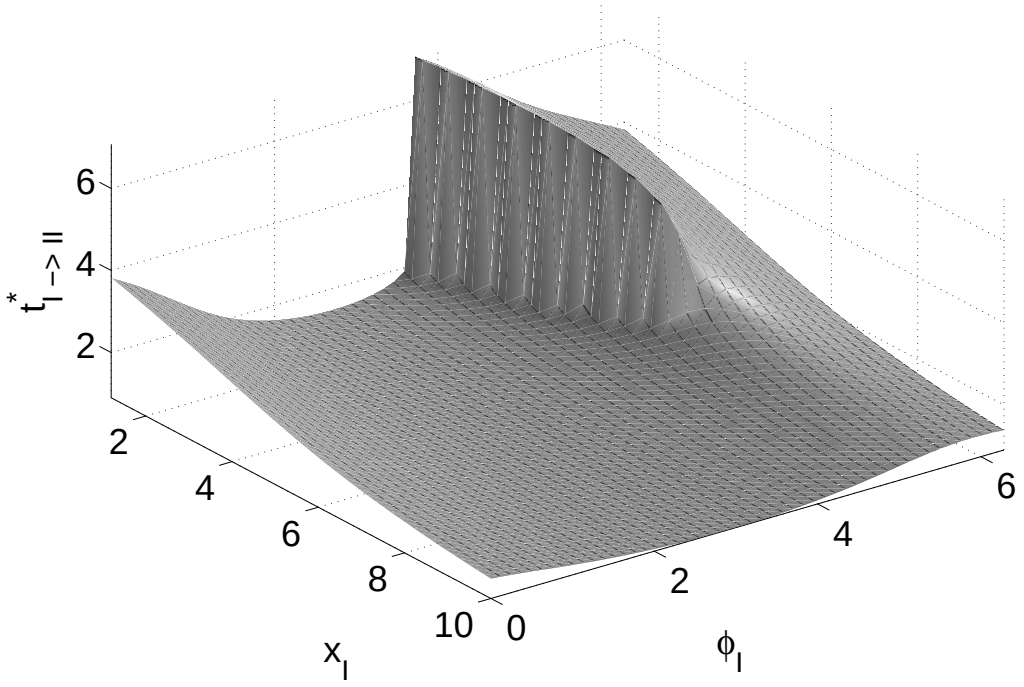

(a) Variation of $t^*_{I\to II}$ with x_I and ϕ_I.

Fig. 57. Variation of $t^*_{I\to II}$ with x_I and ϕ_I. $\epsilon = 0.42,\ \alpha = 0.4,\ A = 2.5,\ \omega = 0.8$.

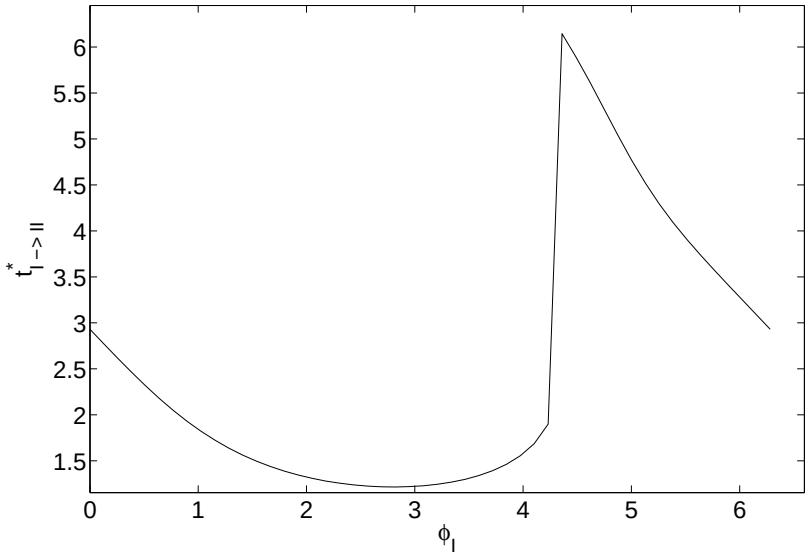

(b) $t^*_{I\to II}$ versus ϕ_I with $x_I = 3.7$.

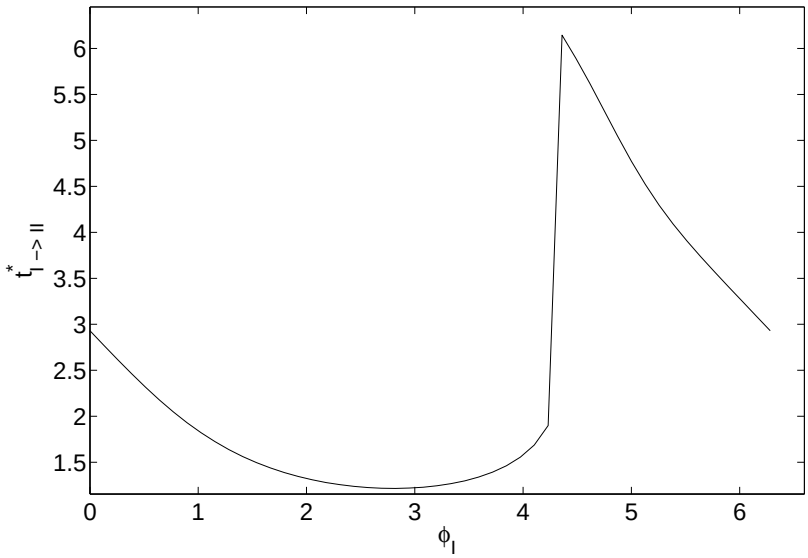

(c) $t^*_{I\to II}$ versus ϕ_I with $x_I = 7.3$.

Fig. 57. Continued ...

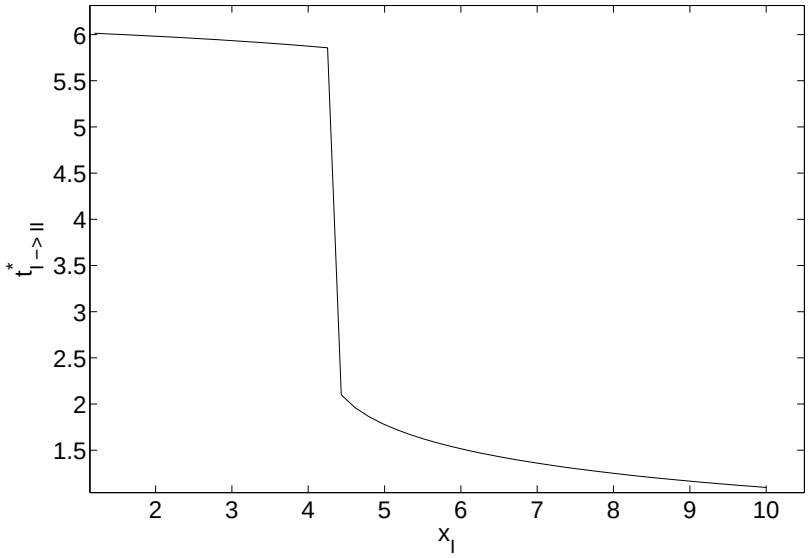

(d) $t^*_{I\to II}$ versus x_I with $\phi_I = 4.48$.

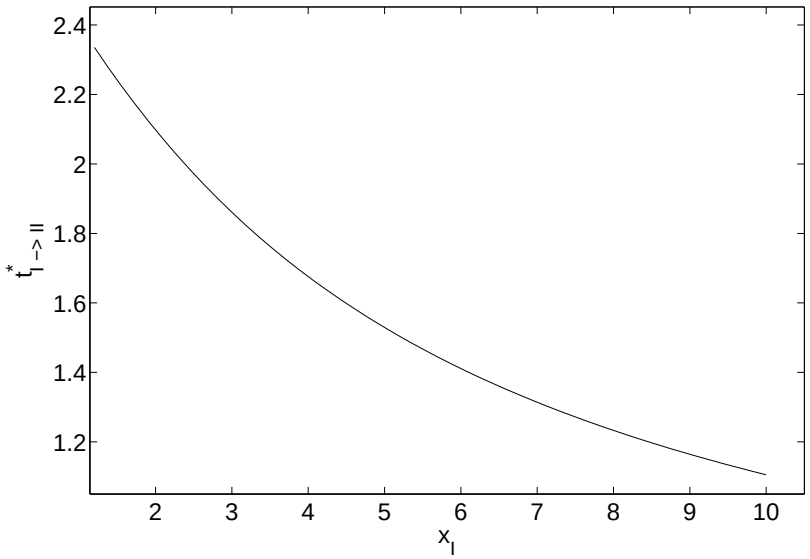

(e) $t^*_{I\to II}$ versus x_I with $\phi_I = 1.15$.

Fig. 57. Continued ...

Figure 58 shows one response curve for the multilinear hysteretic oscillator. The ordinate axis of the graph shows the amplitude of the periodic orbit while the abscissa corresponds to the frequency of excitation. The amplitude of the periodic orbit is defined as the average of the difference of the maximum and the minimum displacement over the orbit. Mathematically this can be expressed as

$$\text{Amplitude} = \lim_{t_0 \to \infty} \frac{\sup_{t \in (t_0, t_0 + 2\pi/\omega]} (x(t)) - \inf_{t \in (t_0, t_0 + 2\pi/\omega]} (x(t))}{2}. \tag{5.58}$$

The above limit exists if and only if the solution $x(t)$ is a periodic orbit or converges to a periodic orbit. Figure 58 shows that for some values of ω there exist two response amplitudes. Further, the figure also shows that there exist orbits with 4, 6, and 8 mode transitions. Note that even though the long-term response of the system can have orbits with more than 4 mode transitions, the orbit with 4 transitions forms the dominant part of the response. Figure 59 shows the response of the amplitude obtained from the KBM method. It can be seen that the amplitude of the dominant orbit matches the prediction of the KBM method to good accuracy even though the value of ϵ is not small as compared to unity.

The multi-valued response shown in figure 58 is due to the appearance of the cycles (orbits) other than the dominant one. We will discuss one mechanism by which these orbits can be born from the dominant 4-cycle (orbit with 4 transitions). Figure 61 shows a sequence of orbits consisting of 4 state transitions that lead to the birth of an orbit with 6 state transitions. Reducing the frequency of excitation leads to a reduction in the amplitude of the response if the frequency is less than the resonance frequency. However, as the amplitude of the response reduces the transition from state I to II comes close to the transition from state II to III. At a certain point these transitions collide and annihilate the 4-cycle. Notice that at this point the velocity at the $I \to II$ transition must be zero, thus this is a grazing bifurcation.

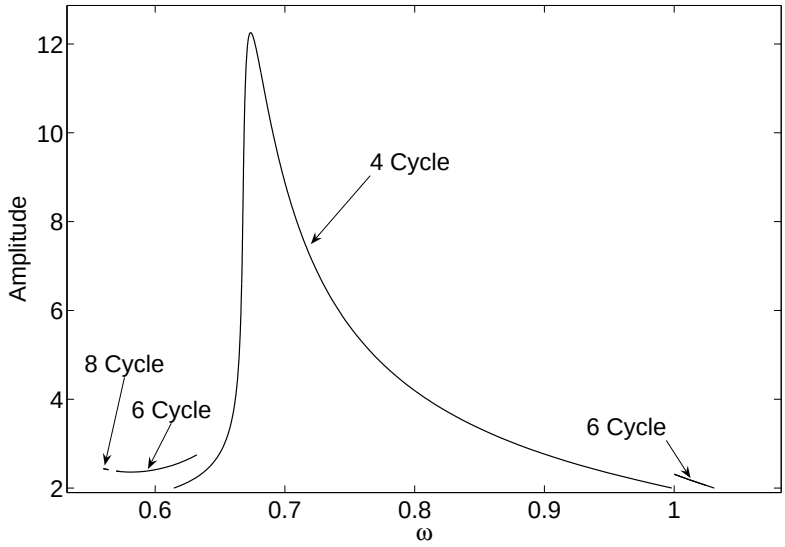

Fig. 58. Response curves obtained from Poincaré maps. $\epsilon = 0.57,\ \alpha = 0.5,\ A = 0.65$.

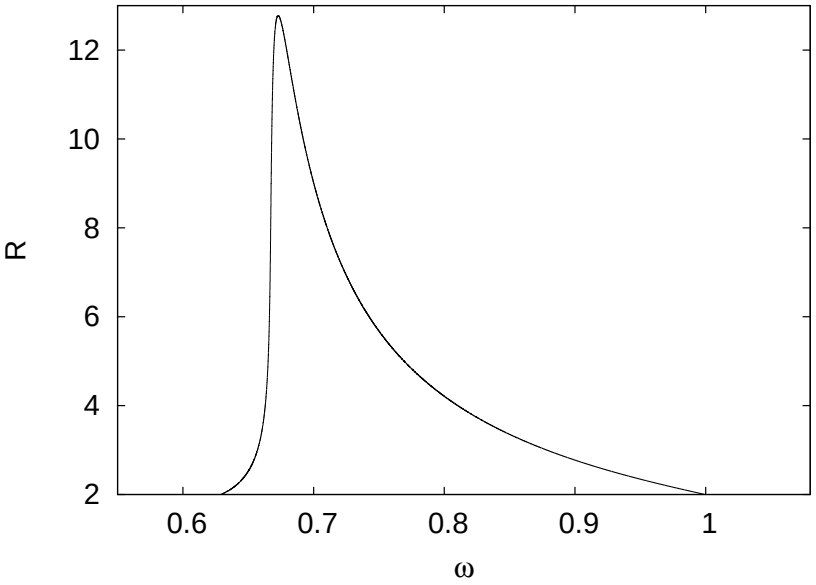

Fig. 59. Response curves obtained from KBM method. $\epsilon = 0.57,\ \alpha = 0.5,\ A = 0.65$.

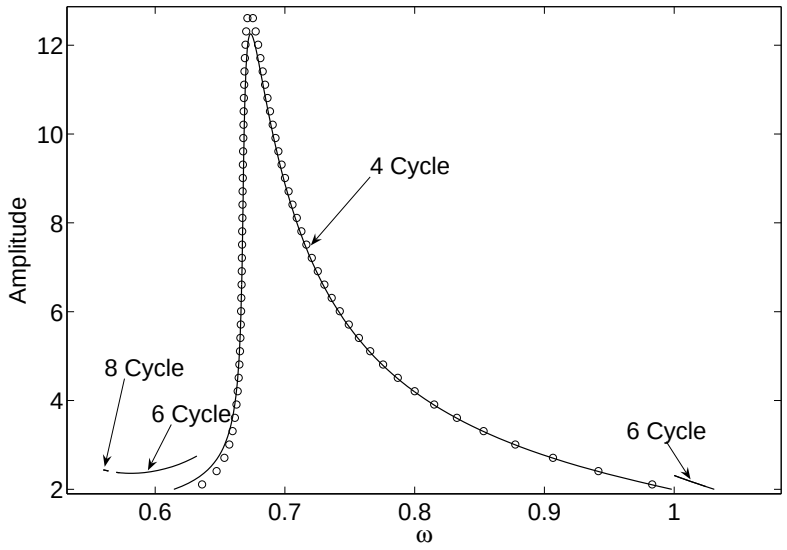

Fig. 60. Comparison of response curves obtained from KBM method (shown by circles) and Poincaré maps (shown by solid line). $\epsilon = 0.57,\ \alpha = 0.5,\ A = 0.65$.

The destruction of the 4-cycle can either result in the creation of a non-dissipative orbit corresponding to oscillations on mode state I or III, or it can result in the creation of a more complex cycle. The non-dissipative orbit will appear only if the steady state amplitude is less than $1/(1+|\alpha|)$. However, this is not true immediately after the destruction of the 4-cycle, since the 4-cycle is destroyed when the steady state amplitude is approximately equal to $1/(1-|\alpha|)$ (see section A and Eq. 5.11). Thus, the destruction of the 4-cycle results in the formation of a cycle with more than 4 state transitions. In the particular case shown in figure 58 the new cycle has 6 transitions. Note that the above mechanism of appearance of orbits with greater number of transitions is not the only possible mechanism. As shown in figure 58 a 8-cycle also exists for some frequency. This 8-cycle is not created by the same mechanism as the 6-cycle. Due to the complicated nature of the system not all the mechanisms of creation and destruction of the cycles are understood at this point.

Figures 62-64 show representative 4, 6 and 8-cycles.

In the various numerical experiments (not reported here) it was observed that simple 4-cycles constituted the dominant response of the system. More complicated behavior like higher period orbits or orbits with greater number of transitions were significantly fewer. In all cases the results from KBM analysis matched the true dominant response with good accuracy. Finally, no aperiodic or chaotic response was observed in the system.

D. Transient Response

To conclude this chapter we present the transient response of the system for some typical parameter values. Figures 65 and 66 show the evolution of relevant quantities in time-domain and the phase space. It should be noticed that the typical transient response of the system is much more complex than its long-term behavior which consists almost exculsively of simple periodic orbits. The sequence of state transitions is richer for the transient response and typically consists of all possible state transitions.

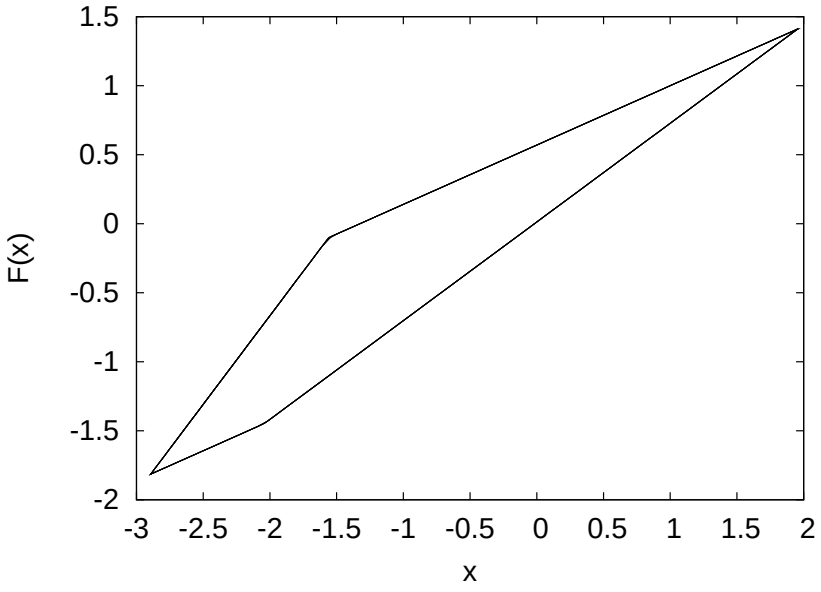

(a) $\omega = 0.64$

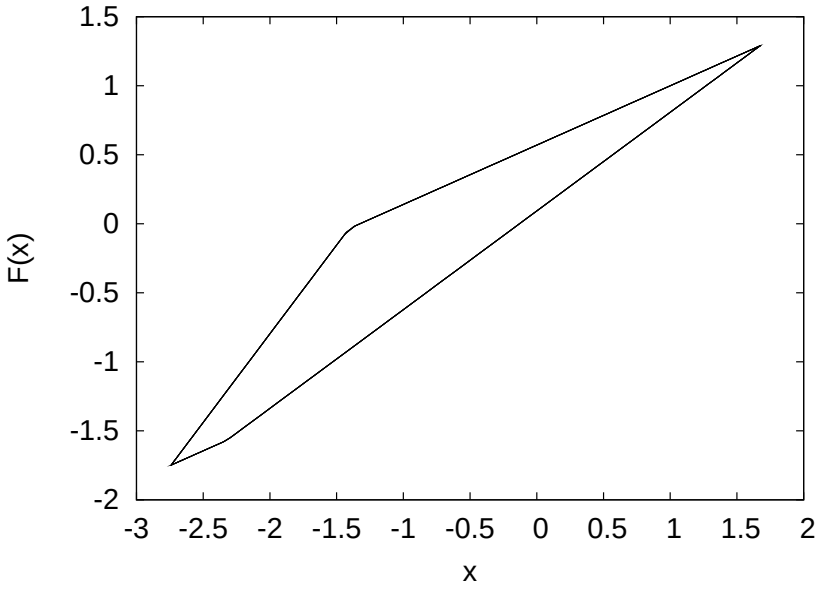

(b) $\omega = 0.63$

Fig. 61. Sequence of orbits leading to bifurcation of a 4-cycle into a 6 cycle. $\epsilon = 0.57,\ \alpha = 0.5,\ A = 0.65.$

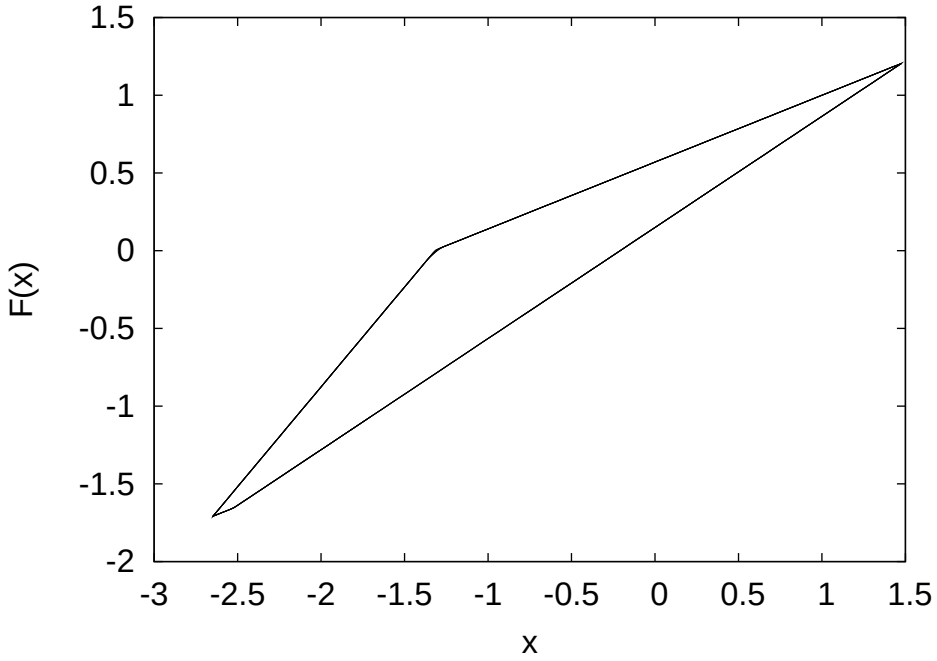

(c) $\omega = 0.62$

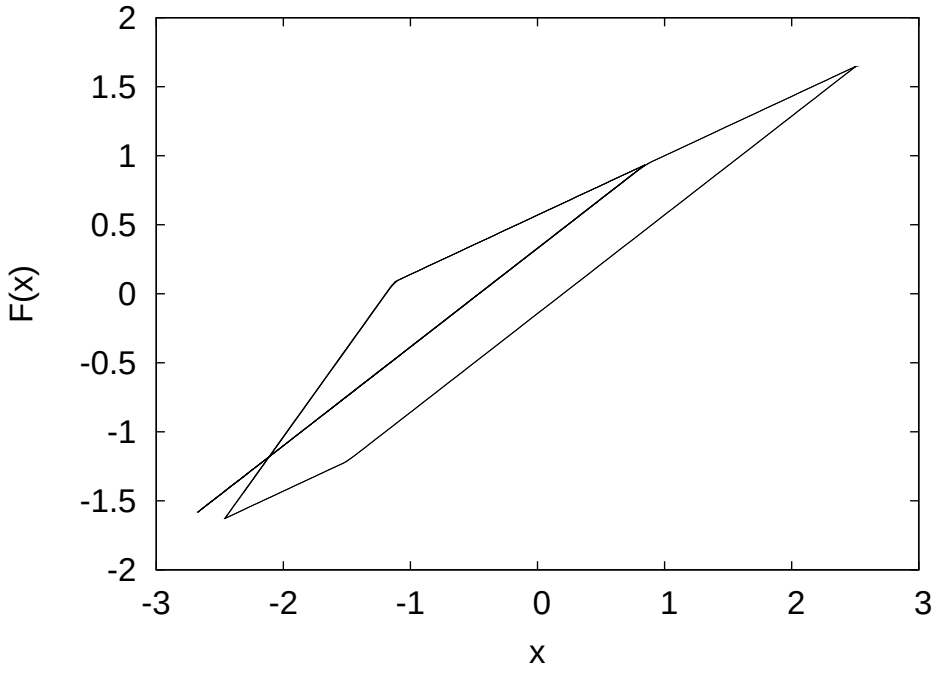

(d) $\omega = 0.61$

Fig. 61. Continued ...

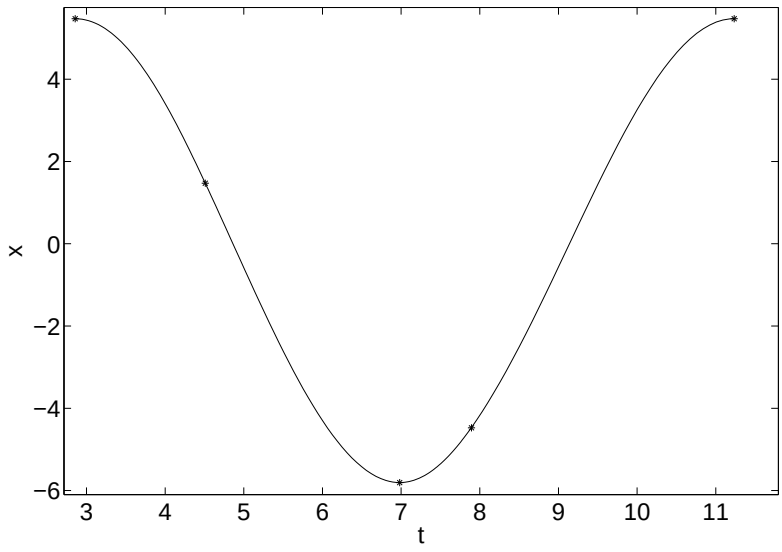

(a) $x(t)$ versus t

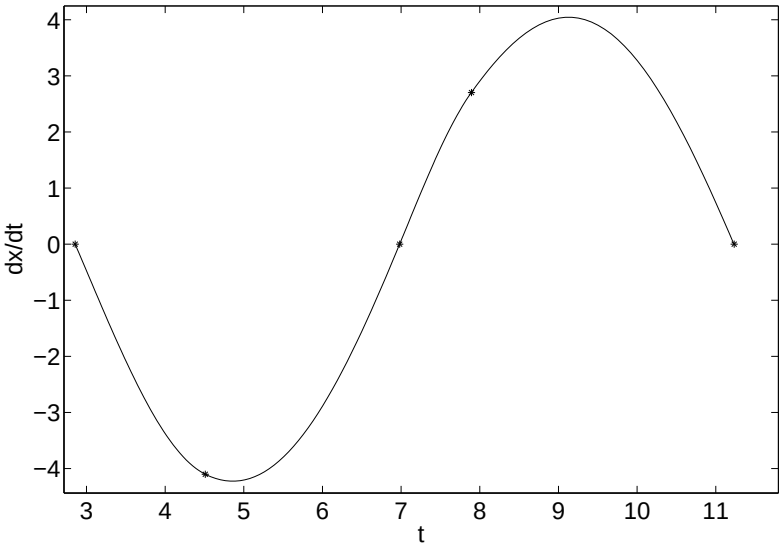

(b) $\dot{x}(t)$ versus t

Fig. 62. A 4-cycle, transition sequence: $\rightarrow$ I $\rightarrow$ II $\rightarrow$ III $\rightarrow$ IV $\rightarrow$. $\epsilon = 0.57,\ \alpha = 0.5,\ A = 0.65,\ \omega = 0.75.$

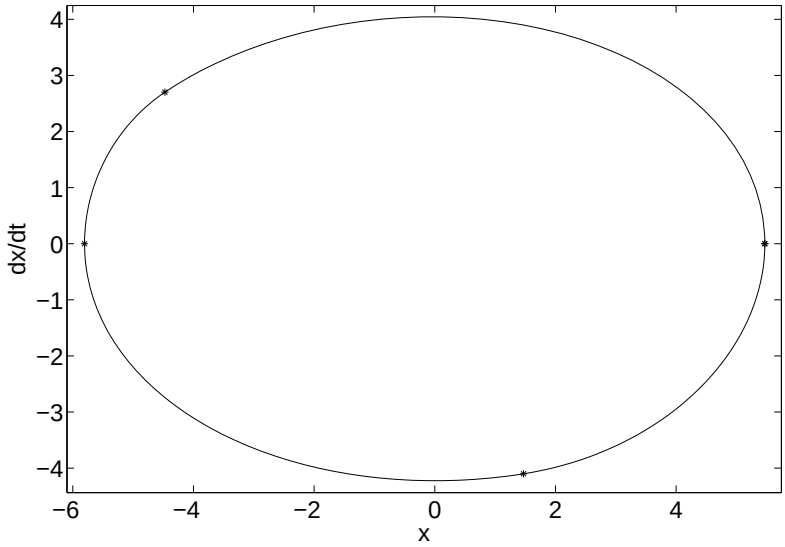

(c) $\dot{x}$ versus x

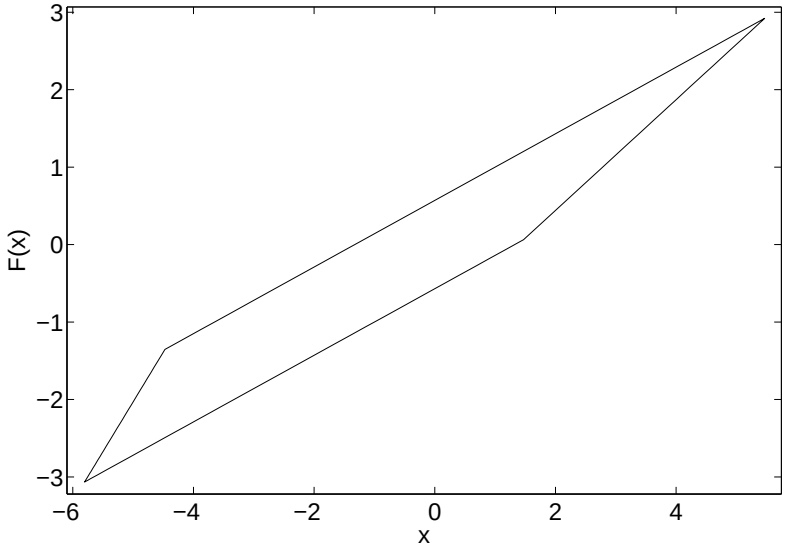

(d) $F(x)$ versus x

Fig. 62. Continued ...

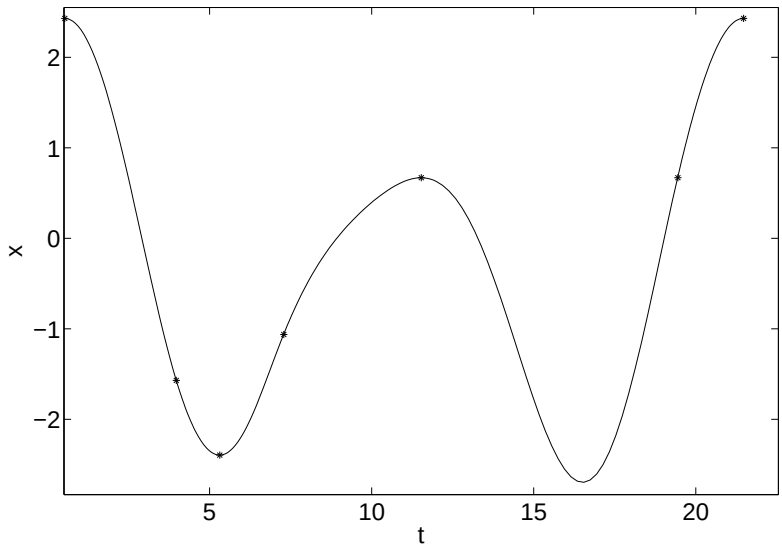

(a) $x(t)$ versus t

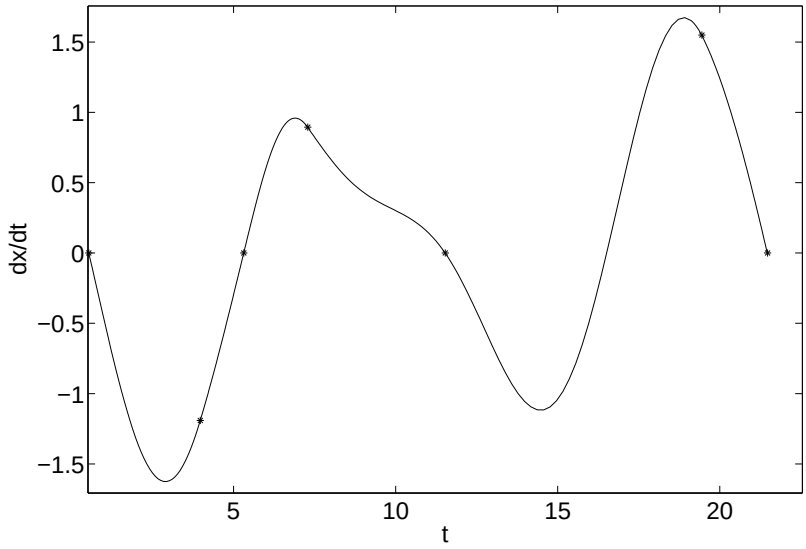

(b) $\dot{x}(t)$ versus t

Fig. 63. A 6-cycle, transition sequence: $\rightarrow I \rightarrow II \rightarrow III \rightarrow IV \rightarrow I \rightarrow IV \rightarrow$. $\epsilon = 0.57,\ \alpha = 0.5,\ A = 0.65,\ \omega = 0.6$.

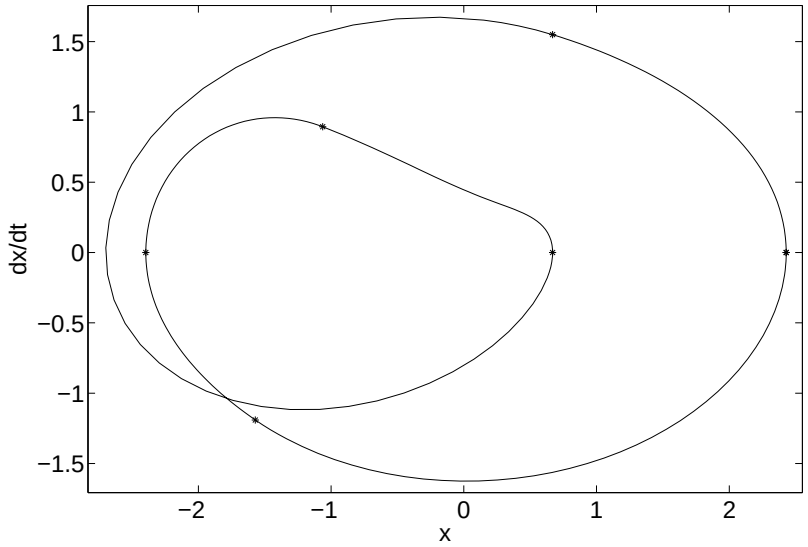

(c) $\dot{x}$ versus x

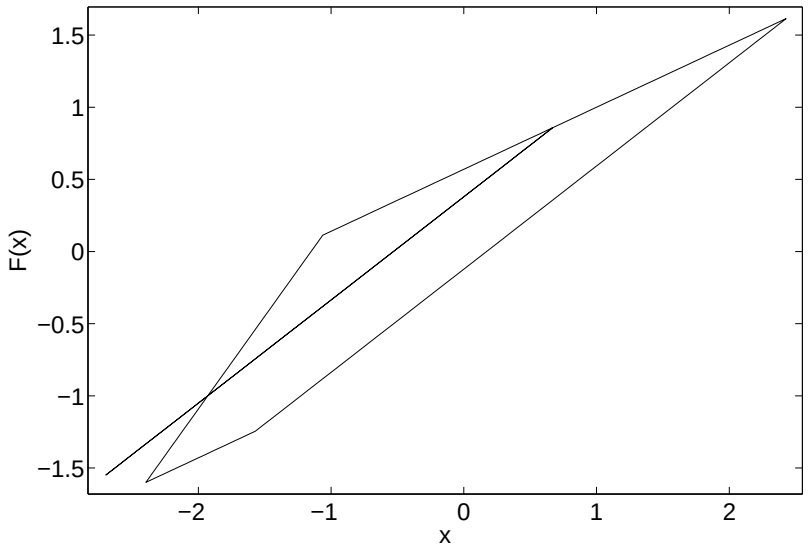

(d) $F(x)$ versus x

Fig. 63. Continued ...

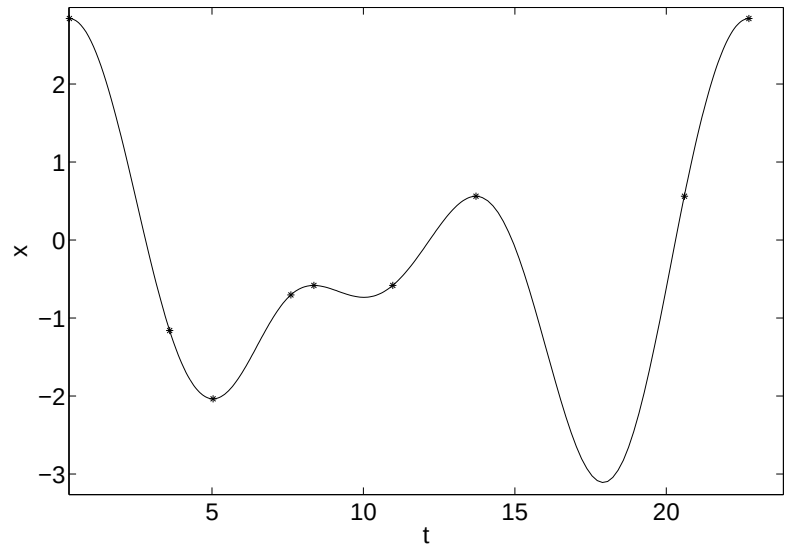

(a) $x(t)$ versus t

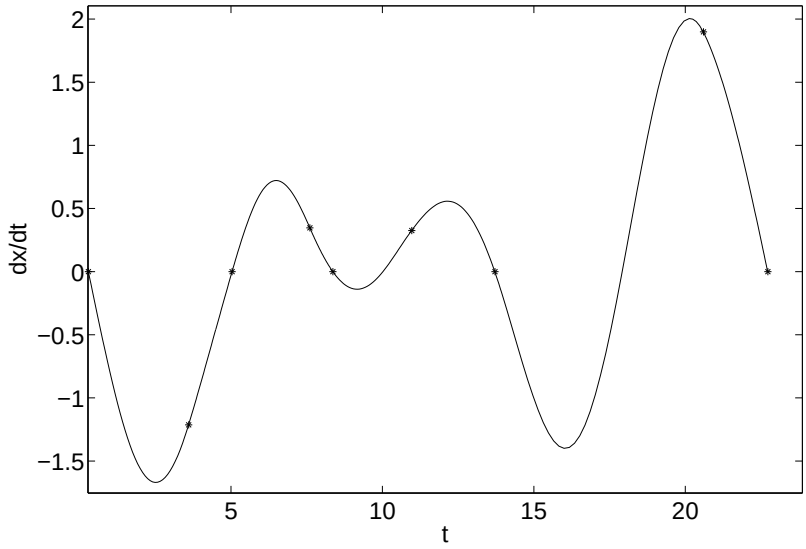

(b) $\dot{x}(t)$ versus t

Fig. 64. A 8-cycle, transition sequence: $\rightarrow I \rightarrow II \rightarrow III \rightarrow IV \rightarrow I \rightarrow IV \rightarrow I \rightarrow IV \rightarrow$. $\epsilon = 0.57,\ \alpha = 0.5,\ A = 0.65,\ \omega = 0.56$.

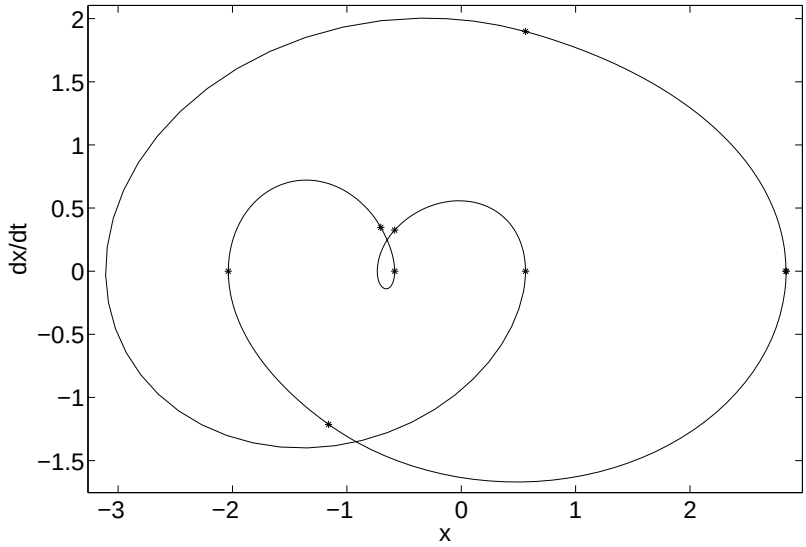

(c) $\dot{x}$ versus x

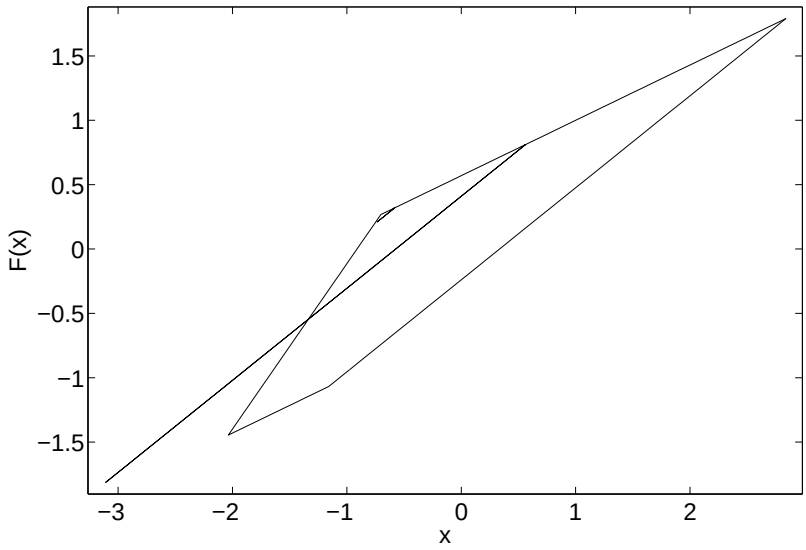

(d) $F(x)$ versus x

Fig. 64. Continued ...

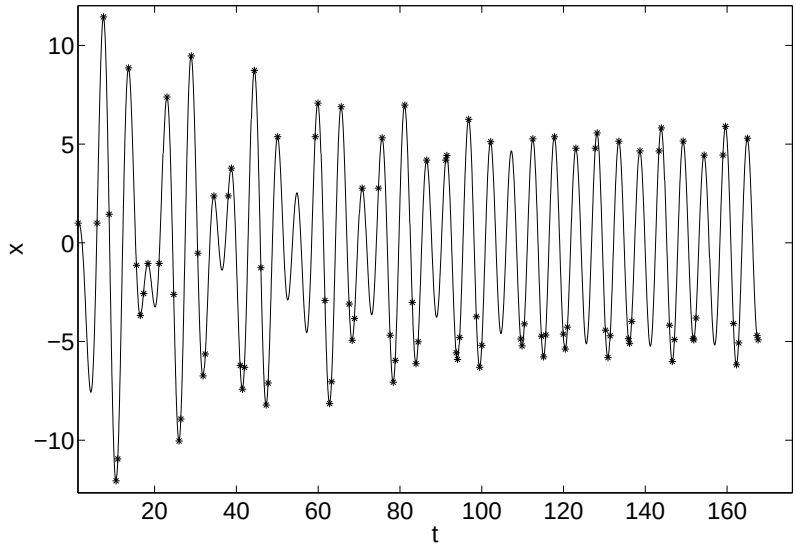

(a) $x(t)$ versus t

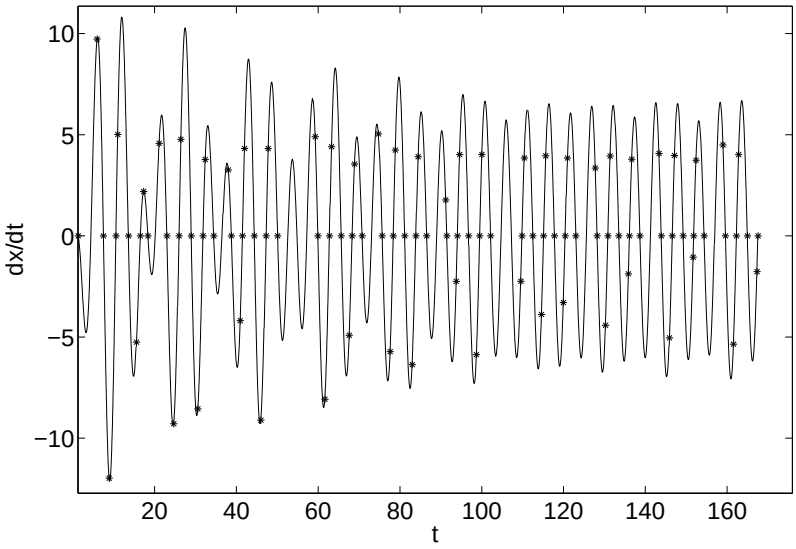

(b) $\dot{x}(t)$ versus t

Fig. 65. Transient response with $\epsilon = 0.3,\ A = 3.65,\ \alpha = 0.8,\ \omega = 1.2$. Initial conditions: $x(t_0) = 1,\ \dot{x}(t_0) = 0,\ t_0 = \pi/2\omega$, starting state $= I$. The first 100 state transitions are shown.

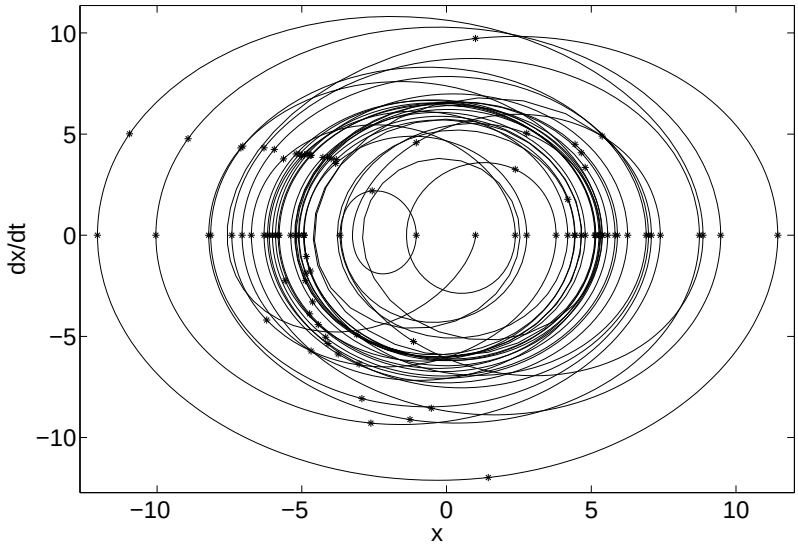

(c) $\dot{x}$ versus x

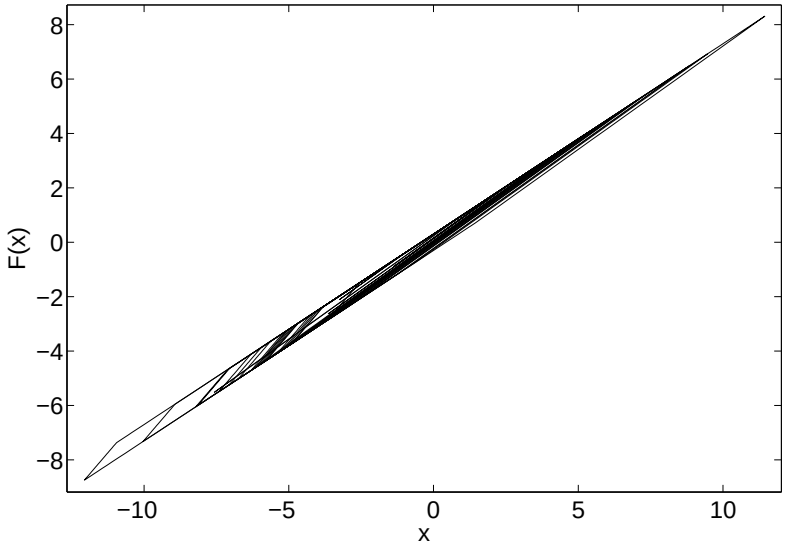

(d) $F(x)$ versus x

Fig. 65. Continued ...

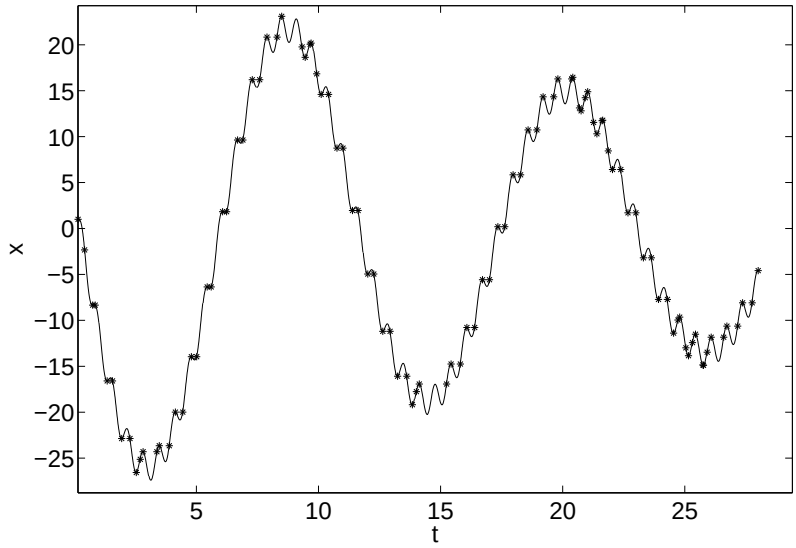

(a) $x(t)$ versus t

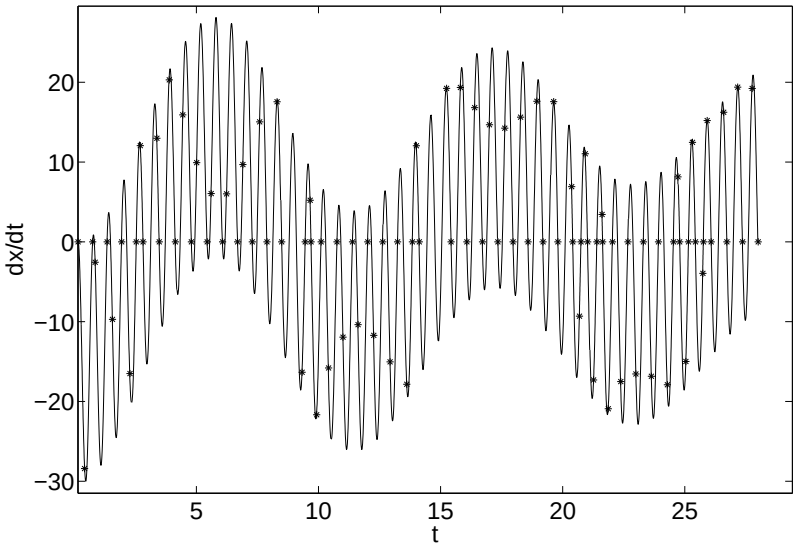

(b) $\dot{x}(t)$ versus t

Fig. 66. Transient response with $\epsilon = 0.7,\ A = 150,\ \alpha = 0.4,\ \omega = 10$. Initial conditions: $x(t_0) = 1,\ \dot{x}(t_0) = 0,\ t_0 = \pi/2\omega$, starting state $= I$. The first 100 state transitions are shown.

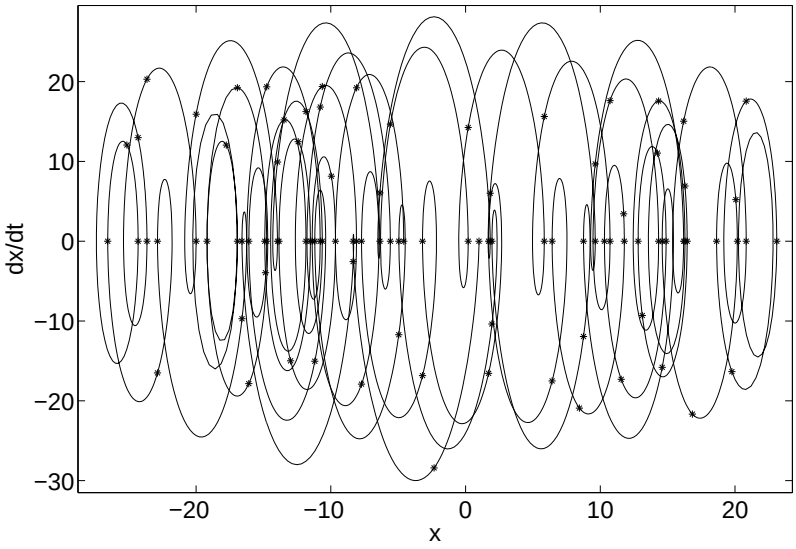

(c) $\dot{x}$ versus x

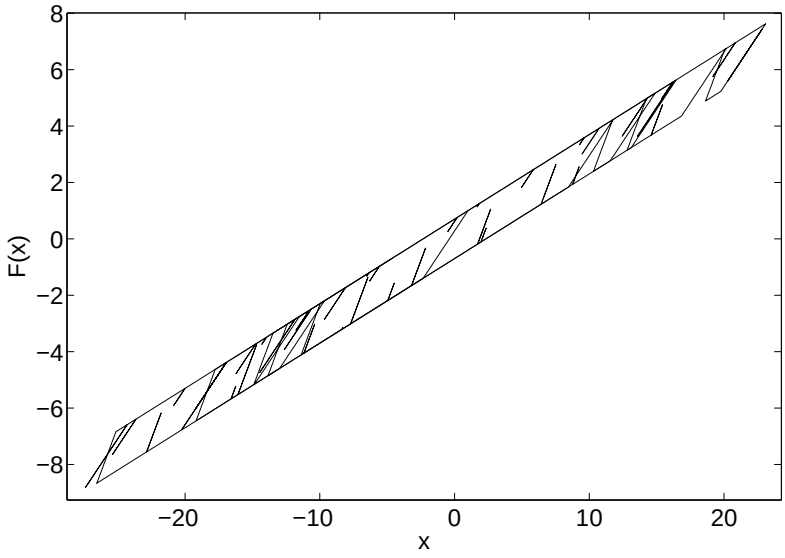

(d) $F(x)$ versus x

Fig. 66. Continued ...

CHAPTER VI

ONE DEGREE OF FREEDOM SMA OSCILLATOR WITH SINUSOIDAL EXCITATION

In this chapter we study the steady state response of an oscillator with a SMA spring and sinusoidal excitation. The Boyd-Lagoudas model is used for SMA modeling (see Chapter II). In order to simplify the analysis the thermo-mechanical coupling is not taken into account. The KBM method is used for steady state analysis of the system. The response curves obtained from the steady state analysis are compared with the experimental data provided in Ref. [52]. The results of the KBM analysis are also compared with those obtained by using a return mapping algorithm based numerical method discussed in Ref. [52]. Since the KBM method and its applications have been discussed in detail in chapters IV and V, and appendix A, so most derivations and details are omitted. Instead, we focus on trying to develop an intuitive understanding of the results.

A. Experimental Setup and Governing Equations

Figure 67 shows the experimental setup used in Ref [52]. The block of mass m can slide in the vertical direction with minimal friction, however, the frame does not permit any motion in the horizontal plane. The block is supported by two pre-strained SMA wires. The wires are pre-strained to avoid slacking. The amount of pre-strain is calculated such that in the static equilibrium both wires have strain equal to 0.04[1]. The entire setup is mounted on a platform capable of producing sinusoidal

[1]Note that static equilibrium is not possible if both wires have exactly equal strains. However, for the given system the two values differ by less than 5%, and are taken to be approximately equal. Also note that the value 0.04 is not arbitrary. It is selected so as to ensure that the static equilibrium corresponds to a certain

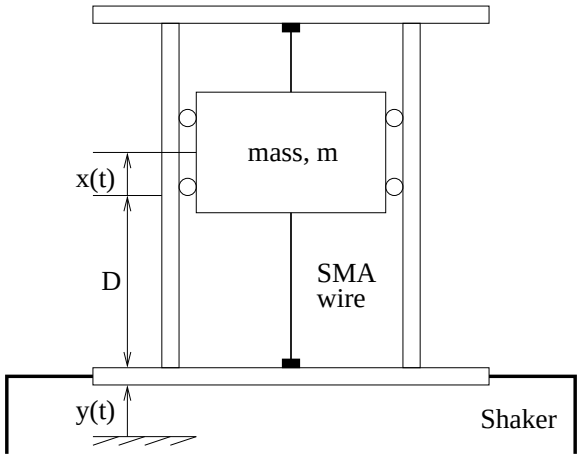

Fig. 67. Schematic of experimental setup used in Ref [52].

excitation. This platform is called the shaker. The setup is equipped with sensors that can measure the acceleration of the shaker and of the block. In the typical experiments the frequency of excitation of the shaker is varied slowly and uniformly over a range while the amplitude of the acceleration of the shaker held constant. The acceleration of the block is measured as an output. This variation of frequency over a range will be referred to as a 'sine sweep'. For convenience the amplitude of the acceleration of the shaker is varied in multiples of g, the acceleration due to gravity. In order to avoid structural vibrations the setup was designed such that the frequencies of the structural modes were sufficiently far from the desired range of excitation. The relevant specifications of the experimental setup are presented in table XV.

1. Equations of Motion

In the following development the gravitational force is neglected in comparison with the elastic force. In fact, we tacitly made this assumption earlier when we assumed

location on the stress-strain curve. See Ref. [52] for details.

Table XV. Specifications of the experimental setup.

Parameter	Value
L, length of unstrained wires	72.6 mm
d, diameter of the wires	0.51 mm
m, mass of the block	0.6 kg
ϵ^o, pre-strain introduced in the wires	0.04

that at static equilibrium the wires have equal strains. Let $x(t)$ be the displacement of the block from its static equilibrium position, and $y(t)$ be the displacement of the platform in the inertial frame (see figure 67). Then the equation of motion of the block can be written as follows

$$m(\ddot{x} + \ddot{y}) = F_u - F_l - F_d, \tag{6.1}$$

where, F_u, F_l are the tensile forces exerted by the upper and the lower wire, respectively, and F_d is the damping force. Note that in Ref. [52] the damping force F_d was not taken into account. We include F_d to account for any small dissipation that might be present due to the friction, viscosity etc. in the setup. Let ng be the peak acceleration of the shaker, where $n \in 1, 2, \ldots$, and g is the acceleration due to gravity, and let ω be the frequency of the oscillations of the shaker. Then Eq. 6.1 can be written as

$$m(\ddot{x} - ng\cos(\omega t)) = F_u - F_l - F_d, \tag{6.2}$$

or

$$\ddot{x} + \frac{F_l - F_u}{m} + \frac{F_d}{m} = ng\cos(\omega t). \tag{6.3}$$

2. Material Response

In order to solve Eq. 6.3 we need to find F_l, F_u, and F_d given $x, \dot{x}$ and perhaps the time history $x(t)$. Let σ_u and σ_l be the stress in the upper and the lower wire, respectively. Then,

$$F_u = \frac{\pi d^2 \sigma_u}{4}, \tag{6.4}$$

and

$$F_l = \frac{\pi d^2 \sigma_l}{4}, \tag{6.5}$$

where d is the diameter of the wires. The stress in the wires can be found if we know the corresponding strain. Let ϵ_u and ϵ_l be the strain in the upper and the lower wire, respectively. Then the following relations hold

$$\epsilon_u = \epsilon^o - \epsilon, \tag{6.6}$$

$$\epsilon_l = \epsilon^o + \epsilon, \tag{6.7}$$

where ϵ is defined as

$$\epsilon \equiv x/L, \tag{6.8}$$

and ϵ^o is the pre-strain. The constitutive model discussed in chapter II can used to deduce the stress-strain relations relating the pairs (σ_u, ϵ_u), and (σ_l, ϵ_l). The values of the relevant material constants can be found in table XVI. Figure 68 shows the stress-strain curve obtained using the Boyd-Lagoudas model. The reader is referred to Ref. [52] for a comparison of the modeled stress-strain curve and the experimental stress-strain curve. The net restoring force, $F_u - F_l$, can now be obtained using the force-displacement relations for the individual wires. Figure 69 shows the plot of $F = F_u - F_l$ versus x. For the curve shown in figure 69 the loading takes place along the upper branch while the unloading takes place along the lower branch. The

Table XVI. Material constants for experimental setup.

Quantity	Value	Quantity	Value
E^A	33 GPa	E^M	14.75 GPa
α^A	22 10^{-6}/K	α^M	10 10^{-6}/K
M_f	227 K	M_s	243 K
A_f	270 K	A_s	261 K
C^A	4.3 MPa/K	C^M	4.3 MPa/K
H^{cur}	0.023		

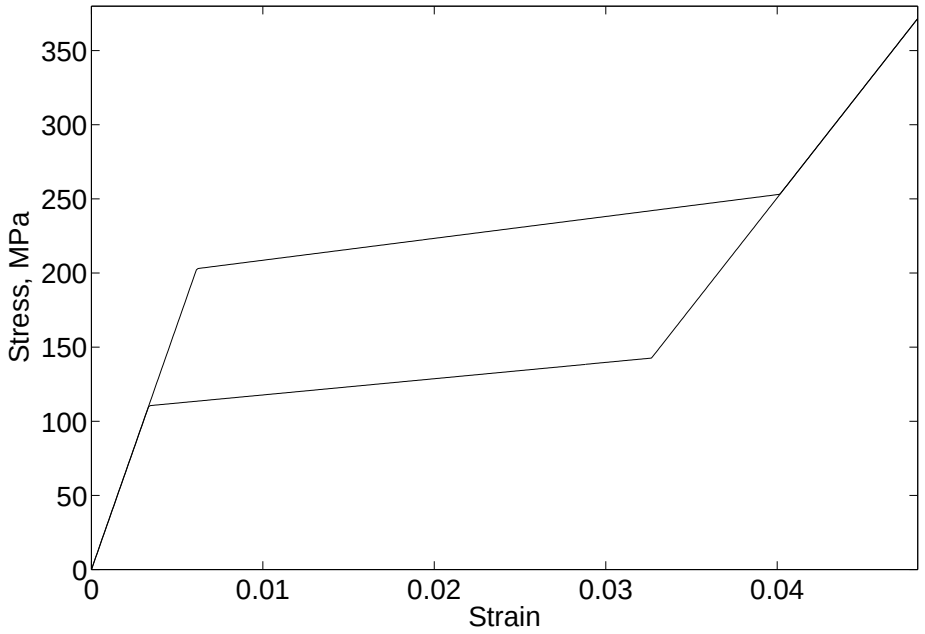

Fig. 68. Stress-strain curve of the material used in experiment. The curve is obtained using the Boyd-Lagoudas model.

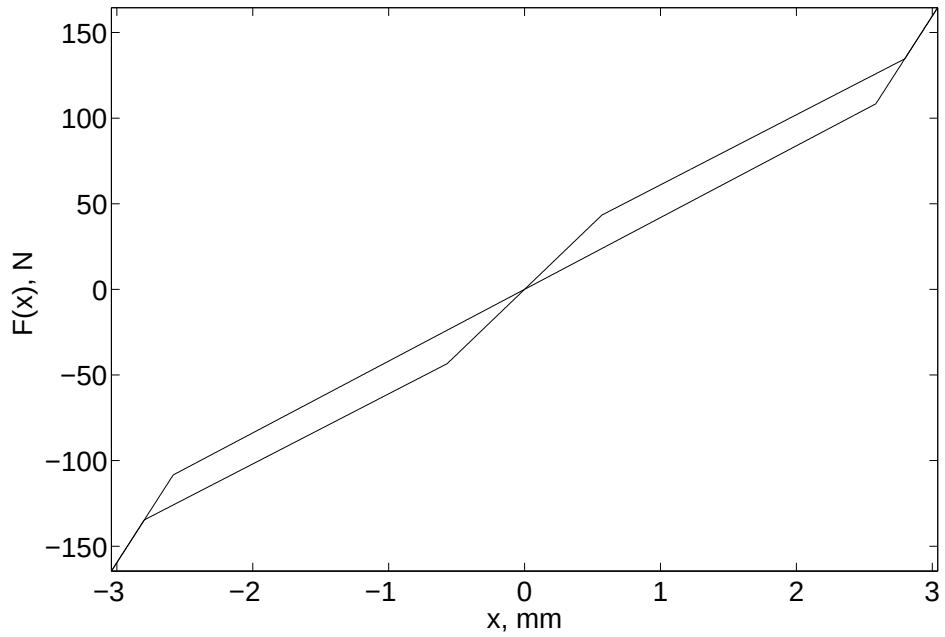

Fig. 69. Net restoring force, $F = F_u - F_l$ versus the displacement x.

viscous force F_d is characterized by a viscosity constant ξ

$$F_d = 2\xi\omega_n\dot{x}, \tag{6.9}$$

where ω_n is the frequency of harmonic oscillations along the first linear portion of the loading branch. The expression for ω_n can be found to be

$$\omega_n = \left[\frac{\pi E^M d^2}{2Lm}\right]^{\frac{1}{2}}. \tag{6.10}$$

We choose $\xi = 0.01$. This value is found by trial and error to get the best match between the experimental and analytical results. We will have more to say about this later.

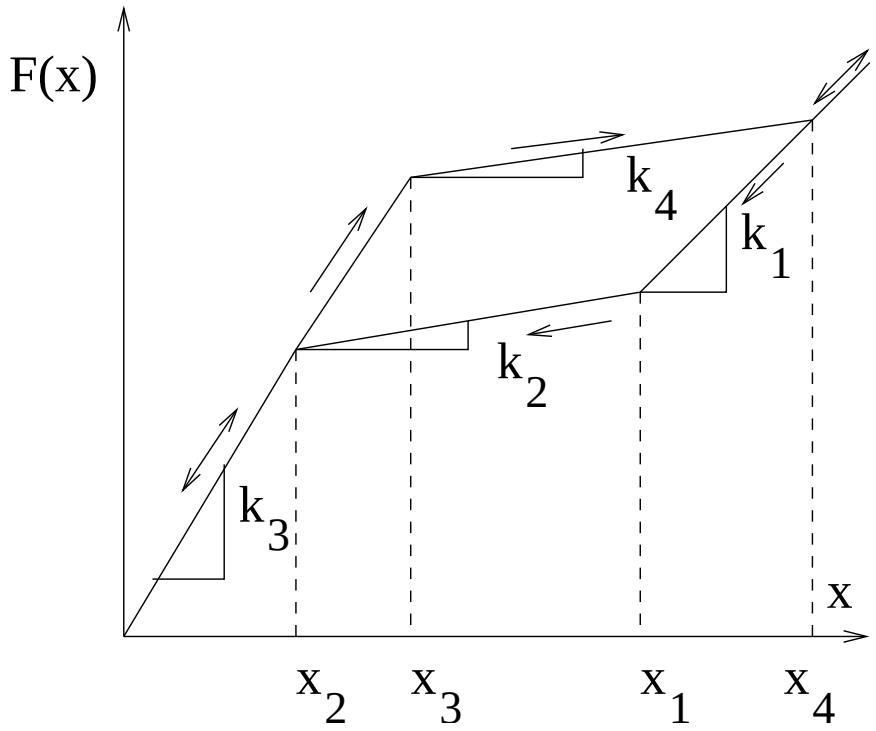

Fig. 70. Hysteretic restoring force.

B. KBM Analysis

The KBM method can be used to study the steady state response of Eq. 6.3 if we can express the restoring force F as $F(x, \delta)$, where the following holds

$$\lim_{\delta \to 0} F(x, \delta) = \mathcal{L}(x) \text{ uniformly in } \delta, \tag{6.11}$$

where $\mathcal{L}(.)$ is an arbitrary linear function. Under this hypothesis the KBM analysis will yield $\mathcal{O}(\delta)$ accurate results. Note that we have loosely taken $F(x, \delta)$ to be a function, while it is indeed a hysteretic operator. Nonetheless, the above arguments can be suitably generalized for the case of hysteretic operators.

Consider the hysteretic $(x, F(x))$ curve shown in figure 70. Only positive values

of x are shown in the figure because the F is assumed to be a odd function. Let the following hold for some sufficiently small δ

$$\frac{k_2}{k_3} = \delta, \tag{6.12}$$

$$k_1 = (1 + \gamma\delta)k_3, \tag{6.13}$$

and

$$x_1 - x_2 = \beta\delta, \tag{6.14}$$

where $\gamma, \beta \sim \mathcal{O}(1)$. Then, it is easy to see that

$$\lim_{\delta \to 0} F(x, \delta) = k_3\delta \text{ uniformly in } \delta. \tag{6.15}$$

One can show that all these requirements are satisfied by the force-displacement curves for the experimental setup, and thus the KBM method can be used to obtain the steady state response curves.

1. The Piecewise Linear Spring

Before analyzing the hysteretic system given by Eq. 6.3 we will present the analysis for a simpler, but closely related system. Consider the piecewise linear restoring force shown in figure 71. This system can be obtained from the hysteretic system shown in figure 70 by setting $x_3 = x_2,\ x_4 = x_1$. The frequency response of this system can be understood easily without getting into undue complications introduced by hysteresis. We wish to study the following system

$$\ddot{x} + c\dot{x} + F_{pw}(x) = A\cos(\omega t). \tag{6.16}$$

The subscript pw is used to indicated that $F_{pw}(x)$ is the piecewise linear restoring force and not the hysteretic one. For this analysis the coefficient of viscosity, c, is

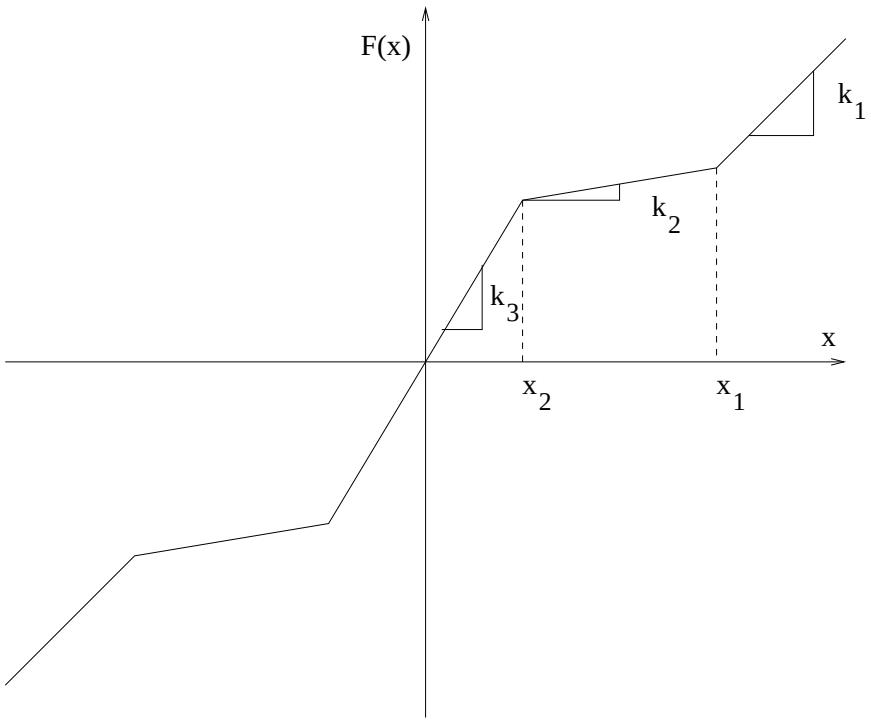

Fig. 71. Piecewise linear restoring force.

taken to be 0.1. Following the KBM we assume a response of the form

$$x(t) = R\cos(\omega t + \phi), \tag{6.17}$$

where

$$\begin{aligned} \dot{R} &\sim \mathcal{O}(\delta), \\ \dot{\phi} &\sim \mathcal{O}(\delta). \end{aligned} \tag{6.18}$$

The development presented in chapters IV, V and appendix A can be used to obtain the following relations for the steady state values of response amplitude and phase

$$S(R^*) = A\sin\phi^*, \tag{6.19}$$

$$C(R^*) = R\omega^2 + \pi A\cos\phi^*, \tag{6.20}$$

where

$$C(R) = \frac{1}{\pi}\int_0^{2\pi} F_{pw}(R\cos\theta)\cos\theta\, d\theta, \tag{6.21}$$

$$S(R) = \frac{1}{\pi}\int_0^{2\pi} (F_{pw}(R\cos\theta) - c\omega R\sin\theta)\sin\theta\, d\theta. \tag{6.22}$$

Eqs. 6.19, 6.20 can be solved to get the familiar relations for the amplitude and phase response of the system

$$\omega^2 = \frac{C(R^*)}{R^*} \pm \left[\left(\frac{A}{R^*}\right)^2 - \left(\frac{S(R^*)}{R^*}\right)^2\right]^{1/2}, \tag{6.23}$$

$$\tan\phi^* = \frac{S(R^*)}{C(R^*) - \omega^2 R^*}. \tag{6.24}$$

Before presenting the response curves obtained from Eqs. 6.23 and 6.24 we will try to understand the behavior of the system in more intuitive terms. The restoring force F_{pw} corresponds to a linear spring followed by a softening followed by a hardening

of the spring. The softening begins at $R = x_2$ and the hardening begins at $R = x_1$. Thus, one should expect that for $0 < R < x_2$ the response curve will be exactly that of a damped harmonic oscillator. In the range $x_2 < R < x_1$ the response would show a softening, thus the amplitude response curves would 'lean left' in the $\omega - R$ plane. Finally, for $R > x_1$ the curves would lean towards the right. The net effect will be that the response curve will look like a skewed 'S'. It is expected that the jump phenomena will be encountered.

The above line of reasoning is confirmed by the analytical results. Figures 72-75 show some response curves along with the corresponding force-displacement characteristics. It can be seen that the general shape of the response curves is similar to a skewed 'S'. As anticipated, the steady state response has two jumps. The amount of tilt in the response curves is proportional to the softening or hardening.

We expect similar response curves for the hysteretic system. However, the maximum response amplitude of the experimental setup is limited by the amount of pre-strain. The maximum response amplitude can be calculated to be 3.04 mm. It can also be seen that the major loop of hysteresis is completed only for response amplitudes greater than 2.78 mm (see figure 69). Thus, instead of expecting skewed 'S' like response curves, we expect to see curves with left leaning spines. Instead of two unstable branches, we expect a single unstable branch.

C. Results

The KBM analysis can be applied to Eq. 6.3 in a manner analogous to the piecewise linear spring. For the experimental setup we get $x_1 = 2.58$ mm, $x_2 = 0$ mm, $x_3 = 0.57$ mm, $x_4 = 2.78$ mm and k_1= 123.4 N/mm, $k_2 = 41.91$ N/mm, $k_3 = 43.4$ N/mm, $k_4 =$ 40.93 N/mm. These constants can be used to find the major loops of the hysteresis

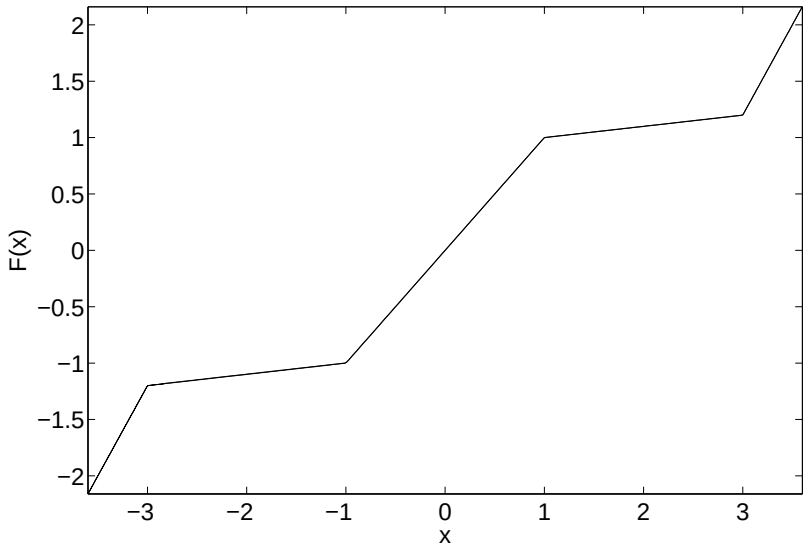

(a) Restoring force versus displacement.

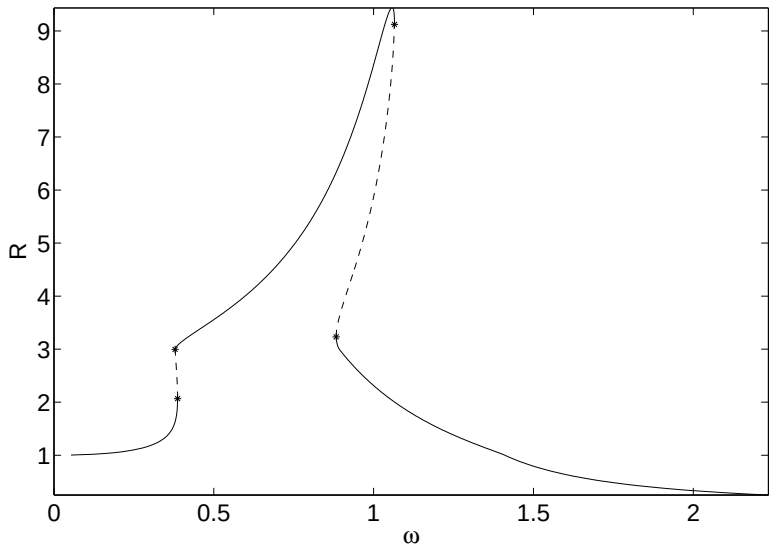

(b) Response versus frequency of excitation.

Fig. 72. Frequency response of the piecewise linear spring. Solid line indicates stable response, dashed line indicates unstable response. The bifurcation points are marked by '*'. $x_1 = 3,\ x_2 = 1,\ k_1 = 1.6,\ k_2 = 0.1,\ k_3 = 1,\ c = 0.1$.

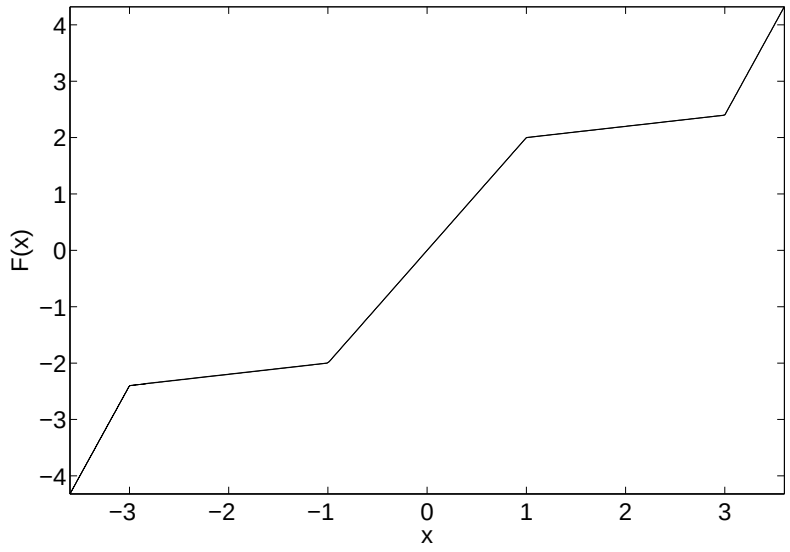

(a) Restoring force versus displacement.

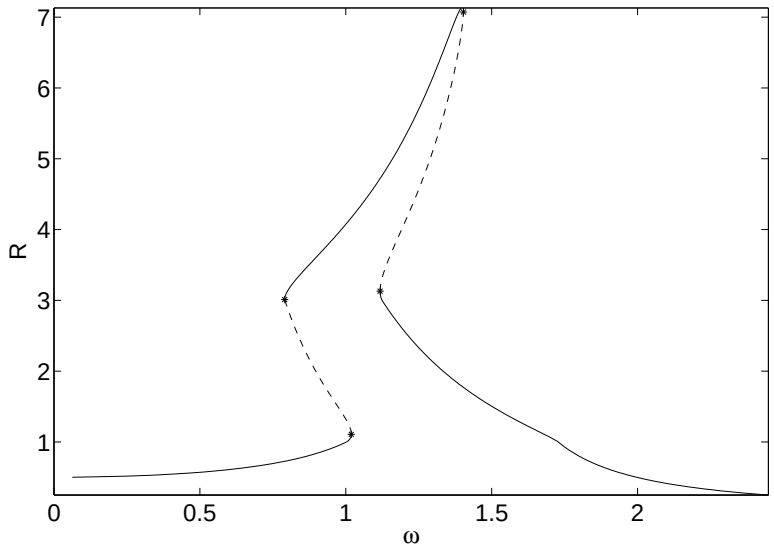

(b) Response versus frequency of excitation.

Fig. 73. Frequency response of the piecewise linear spring. Solid line indicates stable response, dashed line indicates unstable response. The bifurcation points are marked by '*'. $x_1 = 3,\ x_2 = 1,\ k_1 = 3.2,\ k_2 = 0.2,\ k_3 = 2,\ c = 0.1$.

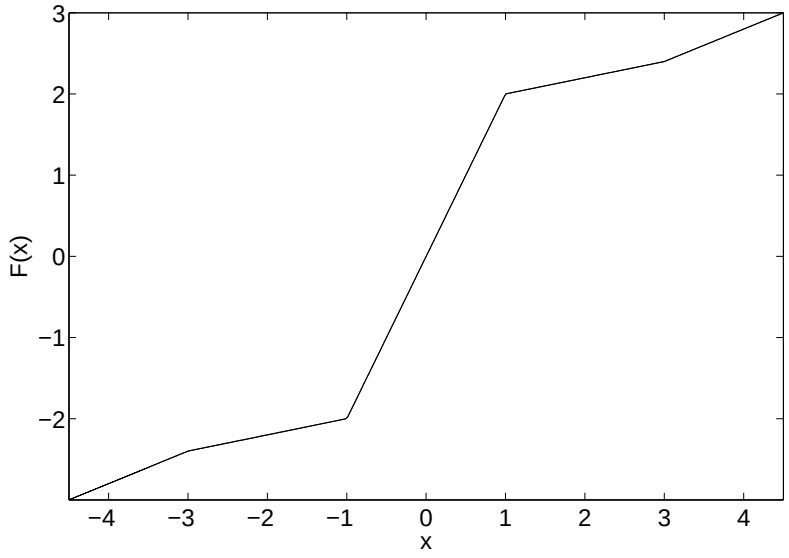

(a) Restoring force versus displacement.

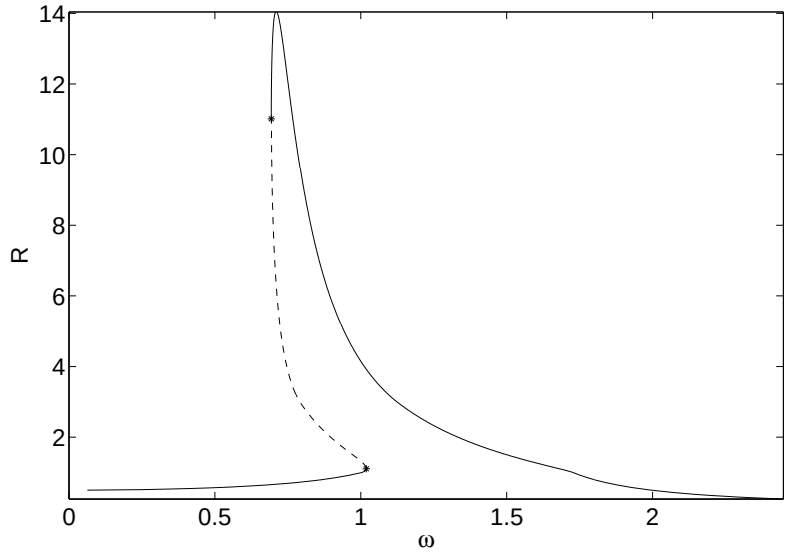

(b) Response versus frequency of excitation.

Fig. 74. Frequency response of the piecewise linear spring. Solid line indicates stable response, dashed line indicates unstable response. The bifurcation points are marked by '*'. $x_1 = 3,\ x_2 = 1,\ k_1 = 0.4,\ k_2 = 0.2,\ k_3 = 2,\ c = 0.1.$

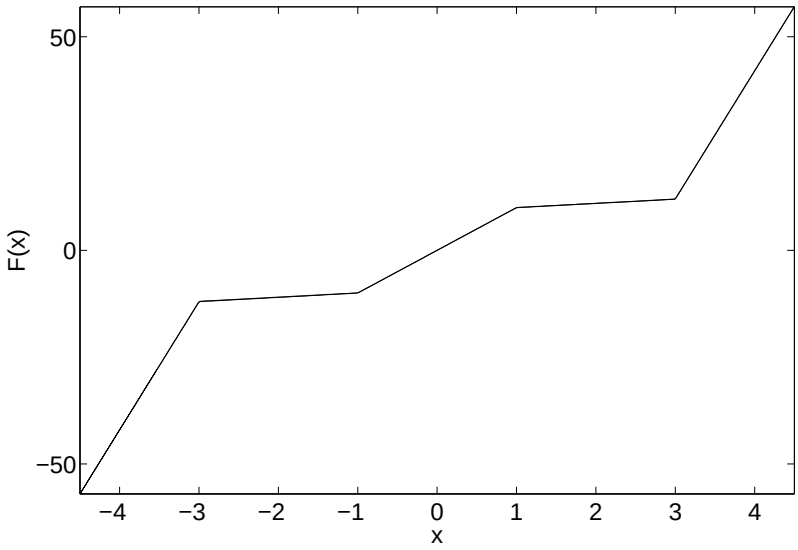

(a) Restoring force versus displacement.

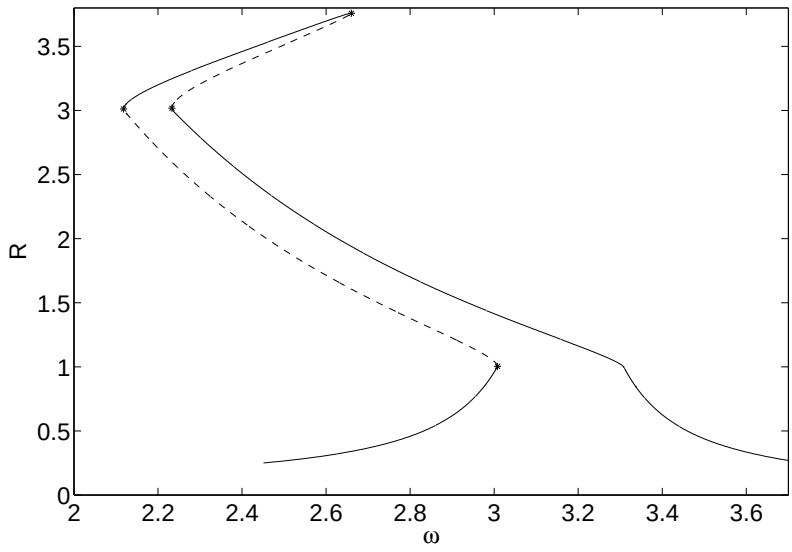

(b) Response versus frequency of excitation.

Fig. 75. Frequency response of the piecewise linear spring. Solid line indicates stable response, dashed line indicates unstable response. The bifurcation points are marked by '*'. $x_1 = 3,\ x_2 = 1,\ k_1 = 30,\ k_2 = 1,\ k_3 = 10,\ c = 0.1$.

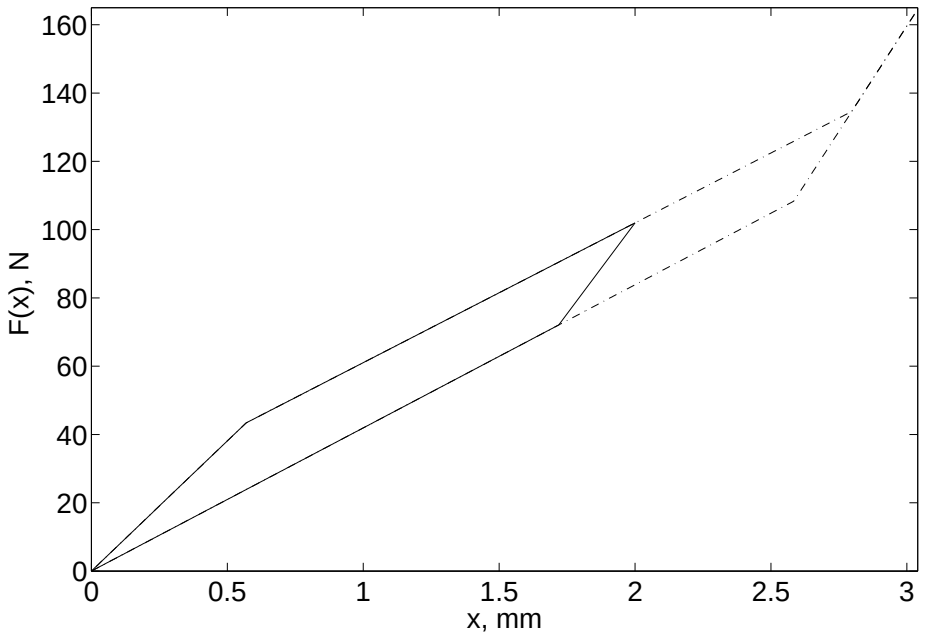

Fig. 76. A minor loop of hysteresis for the pair $(x, F(x))$.

for the system. However, since for most cases the response amplitude is smaller than x_4, therefore, we need to model the minor loops as well. Figure 76 shows a minor loop of amplitude 20 mm for positive x. The slope of the branch of the minor loop that is different from the major loop is assumed to be a linear function of R, i.e. the slope, say, k is given by

$$k = k_3 + \frac{R - x_3}{x_x - x_3}(k_1 - k_3). \tag{6.25}$$

With this the modeling of the system is complete and we move on to present the results of the analysis. As in Ref. [52] we present the results in terms of a transmissibility ratio, TR, defined as the ratio of the maximum inertial acceleration of the block of mass m to the maximum acceleration of the platform. Mathematically, we can define

this ratio as follows

$$TR = \lim_{t_0 \to \infty} \sup_{t \in (t_0, t_0 + 2\pi/\omega)} \left(\frac{\ddot{x} + \ddot{y}}{\ddot{y}} \right). \tag{6.26}$$

The above limit exists iff there exists a steady state response with period $2\pi/\omega$. Under the KBM hypothesis it is possible to show that the above limit converges to the following

$$\begin{aligned} TR &= \sup_t \left(\frac{R\omega^2 \cos(\omega t + \phi) + ng\cos(\omega t)}{ng} \right) \\ &= \frac{[(R\omega^2 \cos\phi + ng)^2 + (R\omega^2 \sin\phi)^2]^{\frac{1}{2}}}{ng} \end{aligned} \tag{6.27}$$

The transmissibility ratio is a measure of the vibration isolation achieved by the SMA wires. If this ratio is zero then perfect isolation is achieved. In Ref. [52] TR was measured experimentally and was also calculated using a return mapping based algorithm. The transmissibility ratio was measured for the case of $n = 1, 2$ using up and down sine sweeps. An up sine sweep means that the frequency of excitation is gradually increased, while a down sine sweeps that the frequency of excitation is gradually decreased. The tests covered frequencies from 32 to 128 Hz.

Figure 77 shows the transmissibility ratio for the $1g$ sweep (a sine sweep with maximum input acceleration of $1g$) obtained using the KBM method. As discussed earlier the response has the general softening character. In the figure the stable response is shown with solid lines while the unstable response is shown with dashed lines. For the $1g$ sweep the unstable branch exists between $f = 51.57$ Hz and $f = 52.76$ Hz, where $f = 2\pi\omega$. The transmissibility ratio for the up and down sweeps is shown in figures 78 and 79 respectively. The jump phenomenon is evident in all the curves. The corresponding results for the $2g$ sweep are shown in figures 80-82. For the $2g$ sweeps the unstable branch exists between $f = 45.53$ Hz and $f = 48.47$ Hz.

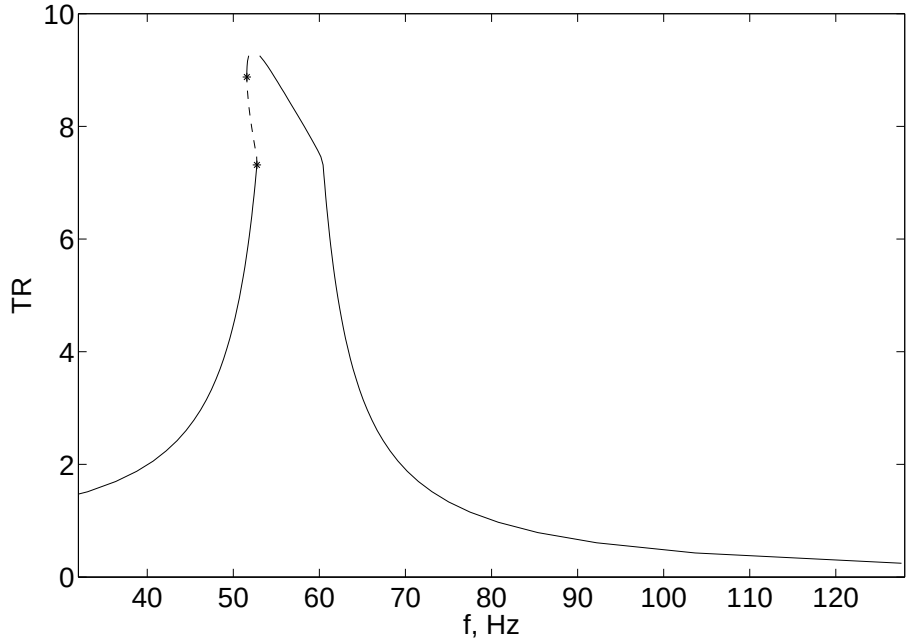

Fig. 77. Transmissibility ratio for $1g$ sweep calculated using the KBM method. Solid line indicates stable response, dashed line indicates unstable response. The bifurcation points are marked by '*'.

It can be seen in all the graphs that the nature of the response resembles that of a softening spring, thus we infer that the variable ϵ is less than 0.04 for the considered cases. Figures 83 and 84 show the steady state amplitude of ϵ versus f. As expected, the peak value of ϵ is less than 0.04 in both cases.

Next we show the comparison of the results obtained from the KBM analysis with the experimental data and the return mapping algorithm based analysis presented in Ref. [52]. The experimental data and the results of return mapping based algorithm are read from graphs presented in the said reference. The numerical values read from the graphs for the $1g$ sine sweep are presented in table XVII. The symbols TR_{up}, TR_{dn}, and TR_{rm} are used for data pertaining to the up sweep, the down

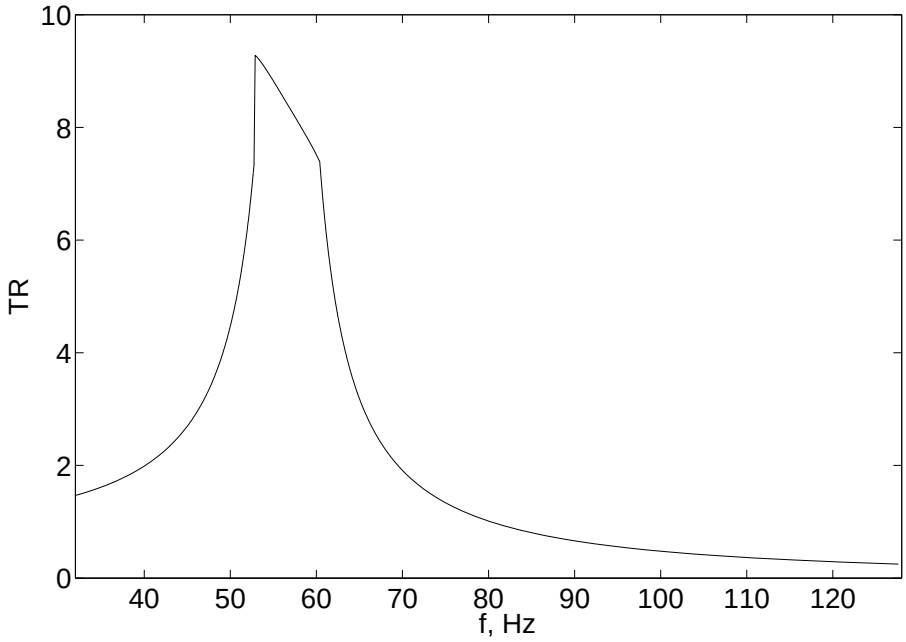

Fig. 78. Transmissibility ratio for $1g$ up sweep calculated using the KBM method.

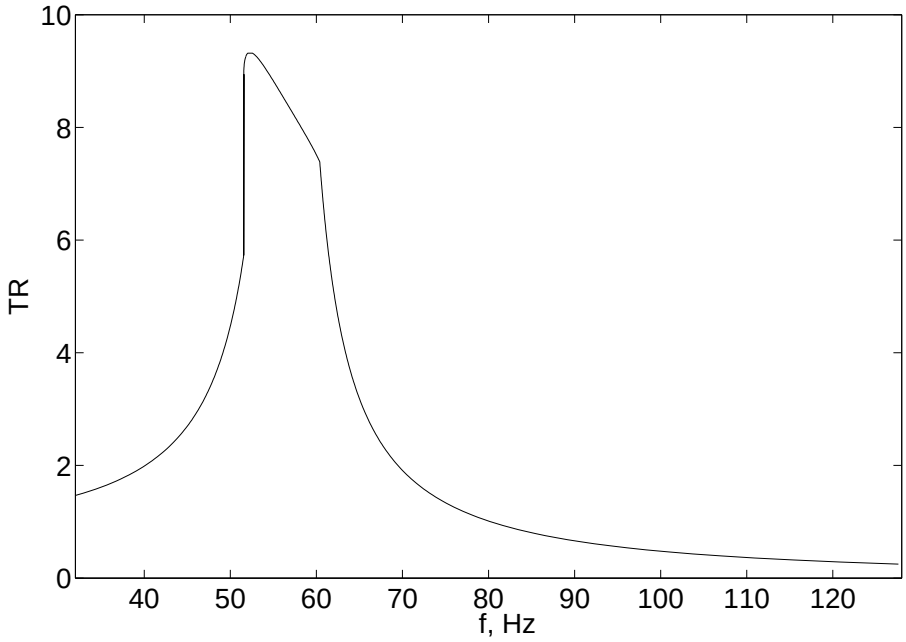

Fig. 79. Transmissibility ratio for $1g$ down sweep calculated using the KBM method.

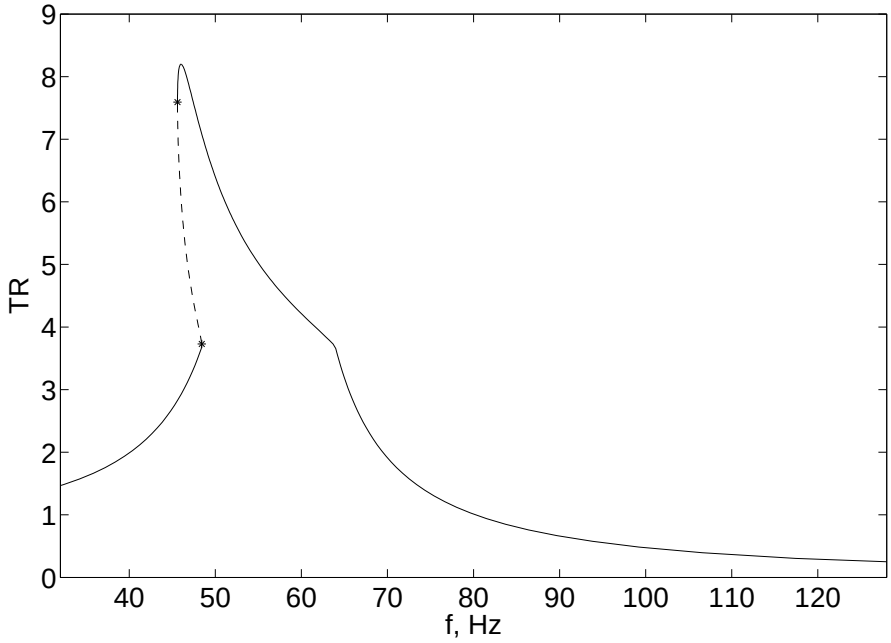

Fig. 80. Transmissibility ratio for $2g$ sweep calculated using the KBM method. Solid line indicates stable response, dashed line indicates unstable response. The bifurcation points are marked by '*'.

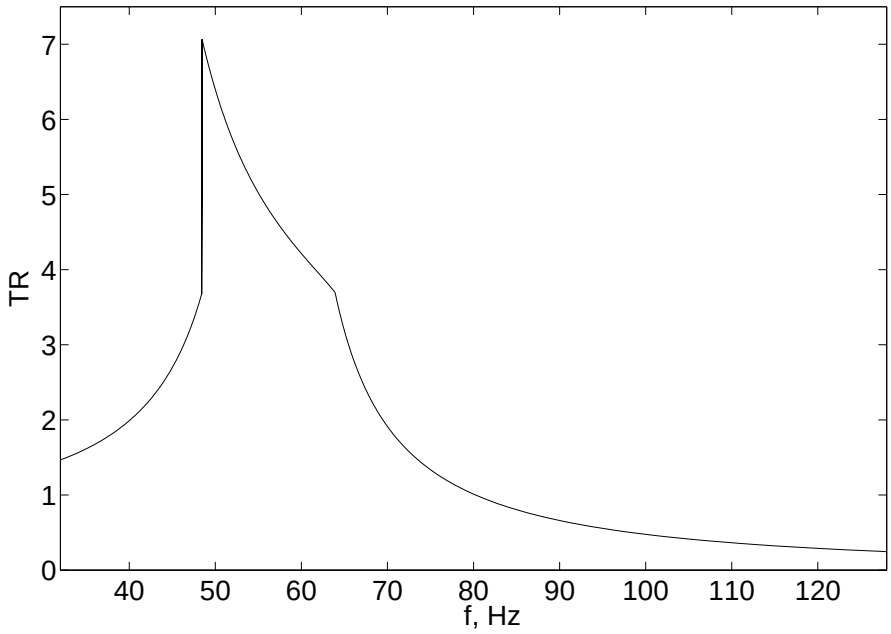

Fig. 81. Transmissibility ratio for $2g$ up sweep calculated using the KBM method.

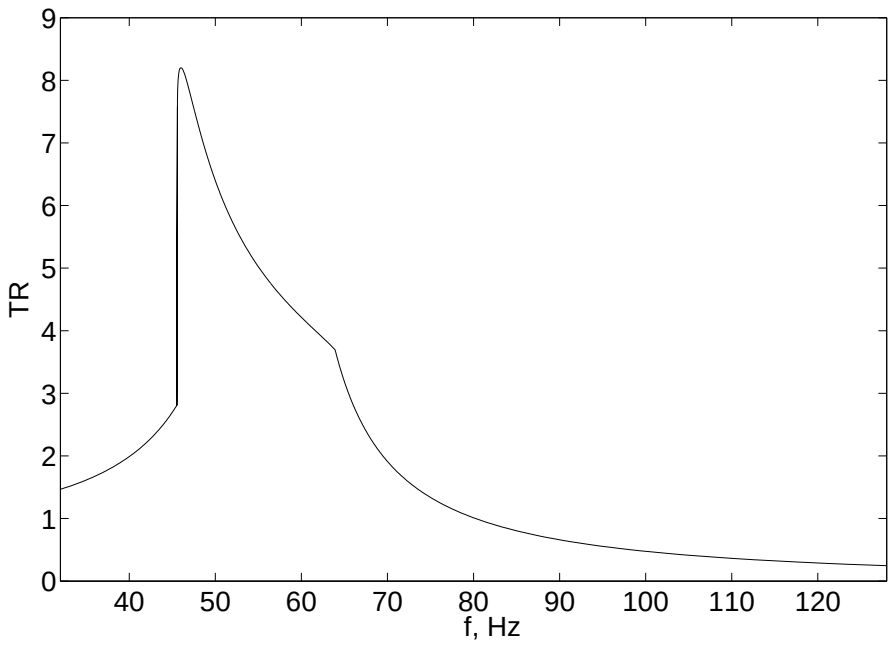

Fig. 82. Transmissibility ratio for $2g$ down sweep calculated using the KBM method.

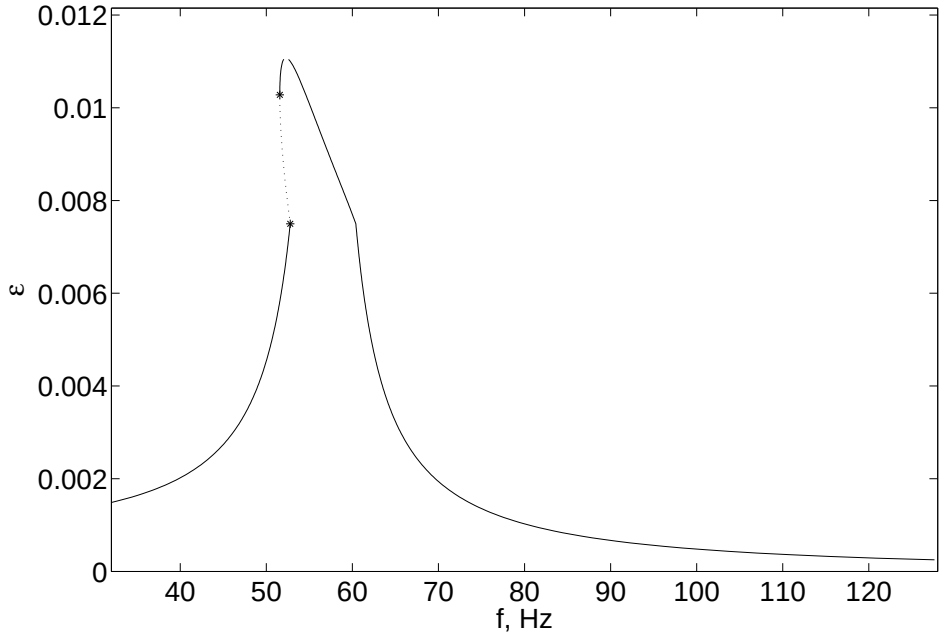

Fig. 83. Steady state amplitude of ϵ for $1g$ sweep calculated using the KBM method. Solid line indicates stable response, dashed line indicates unstable response. The bifurcation points are marked by '*'.

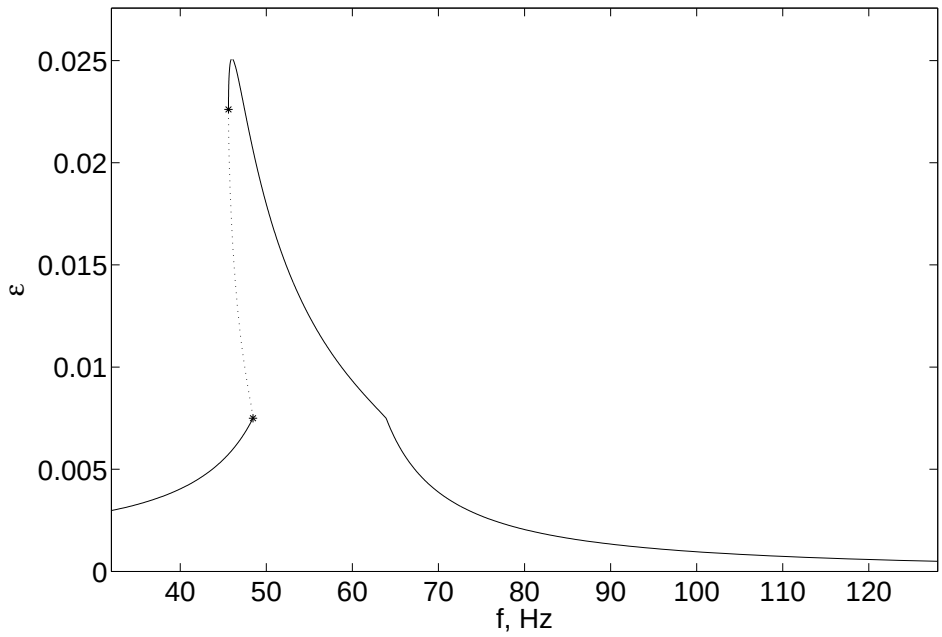

Fig. 84. Steady state amplitude of ϵ for $2g$ sweep calculated using the KBM method. Solid line indicates stable response, dashed line indicates unstable response. The bifurcation points are marked by '*'.

sweep and the return mapping algorithm, respectively. Figures 85 and 86 show the comparison of experimental results with those obtained from the KBM analysis. It can be seen that the two results match to a good degree of accuracy. Figures 87 and 88 show the comparison of the results from the KBM analysis, experiments, and the return mapping algorithm based analysis. Table XVIII and figures 89-92 show the corresponding graphs for the $2g$ sweeps.

1. Discussion of Results

It is seen that the asymptotic methods gives results that are comparable in quality to the much more sophisticated return mapping algorithm based analysis. However, none of the methods give results are entirely agreeable with the experimental data. In the opinion of the author this difference is attributed mostly to the fact that the stress-strain curve predicted by the Boyd-Lagoudas model does not match the experimental data exactly (or with marginal error). Of course, this is a quantitative assessment and one needs to devise qualitative measures of accuracy of the response curves as well as the stress-strain curves. Another major source of discrepancy seems to be the dissipation present in the experimental setup (apart from the dissipation due to the SMA elements). It can be safely said that the amplitude of the response cannot be accurately predicted unless the dissipation effect of the setup is measured and taken into account. It was seen that changing the damping coefficient from 0.01 to say 0.005 had significant effect on the peak amplitude of response. This effect is significantly more pronounced near the resonance because the damping due to SMA wires is least near the resonance. The thermomechanical coupling is ignored in the KBM analysis. The effect of the thermomechanical coupling might be significant since the temperature of the SMA wires varies by 20-30 K in some of the experiments. A more sophisticated analysis where the thermomechanical coupling is taken into

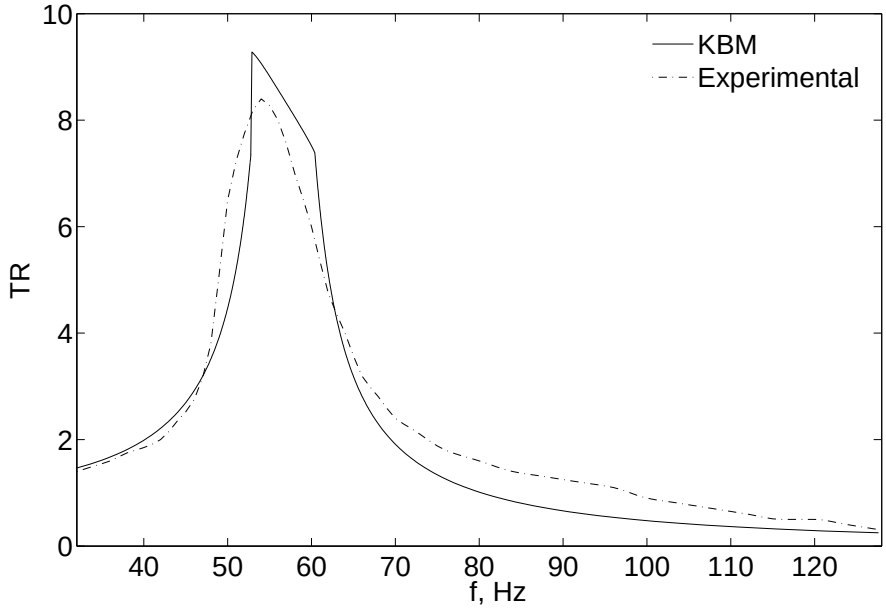

Fig. 85. Comparison of results obtained from the KBM analysis with the experimental data for $1g$ up sweep.

account may lead to significantly better results.

Table XVII. Experimental and numerical data for $1g$ sine sweeps taken from Ref. [52].

f, Hz	TR_{up}	TR_{dn}	TR_{rm}	f, Hz	TR_{up}	TR_{dn}	TR_{rm}
32.00	1.40	1.40	1.60	68.00	2.80	2.60	2.70
34.00	1.50	1.50	1.80	70.00	2.40	2.30	2.30
36.00	1.60	1.60	2.00	72.00	2.20	2.20	1.90
38.00	1.75	1.75	2.20	76.00	1.80	1.80	1.50
40.00	1.85	1.85	2.40	80.00	1.60	1.60	1.20
42.00	2.00	2.00	2.70	84.00	1.40	1.40	1.00
44.00	2.35	2.35	3.10	88.00	1.30	1.30	0.80
46.00	2.75	2.60	3.50	92.00	1.20	1.20	0.75
48.00	3.80	3.20	3.80	96.00	1.10	1.10	0.65
50.00	6.50	4.00	5.00	100.00	0.90	0.90	0.60
52.00	7.75	8.75	7.25	104.00	0.80	0.80	0.50
54.00	8.40	8.25	6.30	108.00	0.70	0.70	0.50
56.00	8.00	6.60	5.70	112.00	0.60	0.60	0.45
58.00	7.00	5.25	5.25	116.00	0.50	0.50	0.40
60.00	6.00	4.50	5.00	120.00	0.50	0.50	0.40
62.00	4.75	3.75	4.50	124.00	0.40	0.40	0.35
64.00	4.00	3.25	3.90	128.00	0.30	0.30	0.30
66.00	3.20	2.90	3.30				

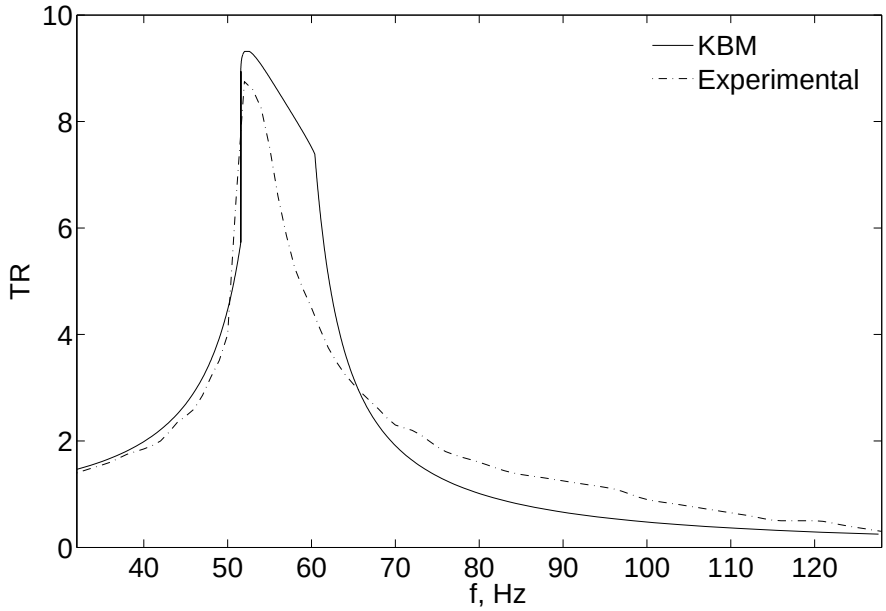

Fig. 86. Comparison of results obtained from the KBM analysis with the experimental data for $1g$ down sweep.

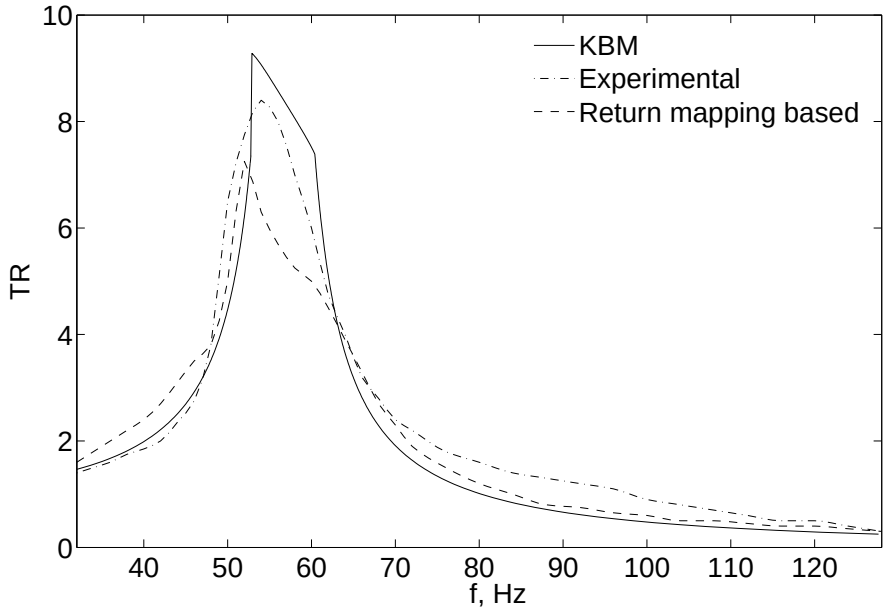

Fig. 87. Comparison of results obtained from the KBM analysis and the return mapping algorithm with the experimental data for $1g$ up sweep.

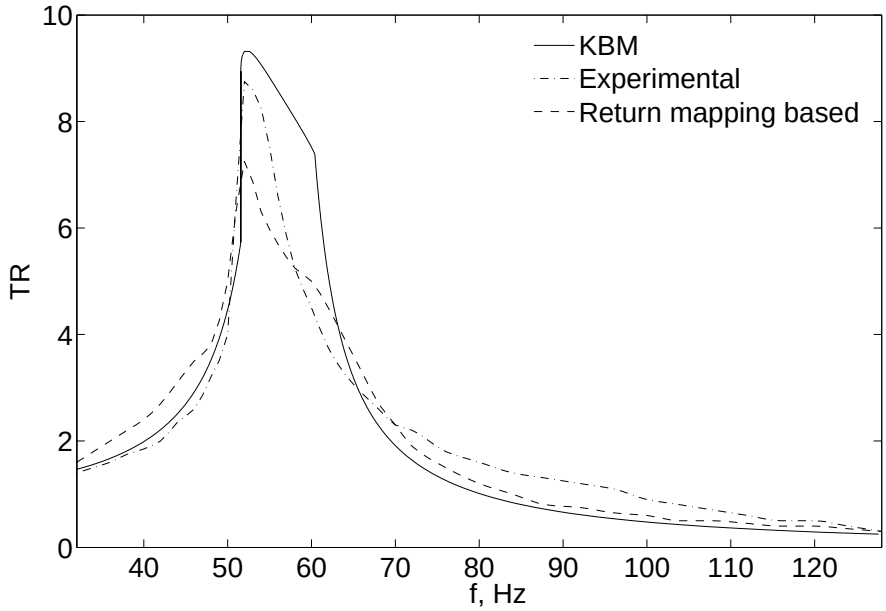

Fig. 88. Comparison of results obtained from the KBM analysis and the return mapping algorithm with the experimental data for $1g$ down sweep.

Table XVIII. Experimental and numerical data for $2g$ sine sweep taken from Ref. [52].

f, Hz	TR_{up}	TR_{dn}	TR_{rm}	f, Hz	TR_{up}	TR_{dn}	TR_{rm}
32.00	1.50	1.30	1.60	68.00	3.00	2.20	1.9
34.00	1.62	1.40	1.70	70.00	2.50	1.90	1.85
36.00	1.75	1.45	1.80	72.00	2.15	1.65	1.75
38.00	1.90	1.50	1.90	76.00	1.70	1.40	1.5
40.00	2.20	1.55	2.10	80.00	1.35	1.25	1.2
42.00	2.50	8.00	2.30	84.00	1.20	1.10	1
44.00	3.00	7.80	6.90	88.00	1.00	1.00	0.8
46.00	3.75	7.50	5.75	92.00	0.80	0.80	0.7
48.00	5.75	7.20	4.20	96.00	0.75	0.75	0.6
50.00	6.20	6.75	3.25	100.00	0.70	0.70	0.55
52.00	6.50	6.50	2.60	104.00	0.65	0.65	0.5
54.00	6.40	6.00	2.25	108.00	0.60	0.60	0.45
56.00	6.25	5.40	2.10	112.00	0.55	0.55	0.4
58.00	6.00	4.75	2.05	116.00	0.50	0.50	0.37
60.00	5.60	4.00	2.05	120.00	0.40	0.40	0.35
62.00	5.00	3.25	2.00	124.00	0.30	0.30	0.3
64.00	4.25	2.75	2.00	128.00	0.25	0.25	0.3
66.00	3.50	2.40	1.95				

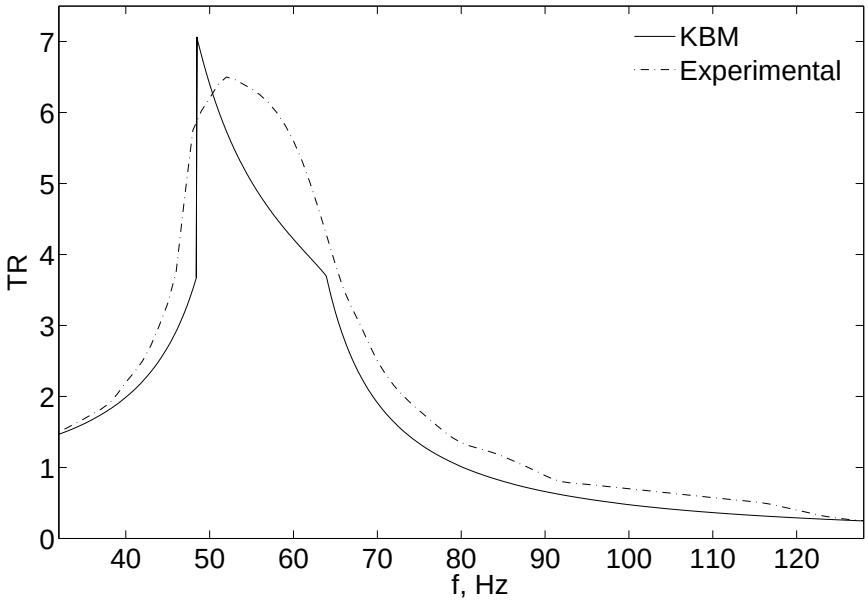

Fig. 89. Comparison of results obtained from the KBM analysis with the experimental data for $2g$ up sweep.

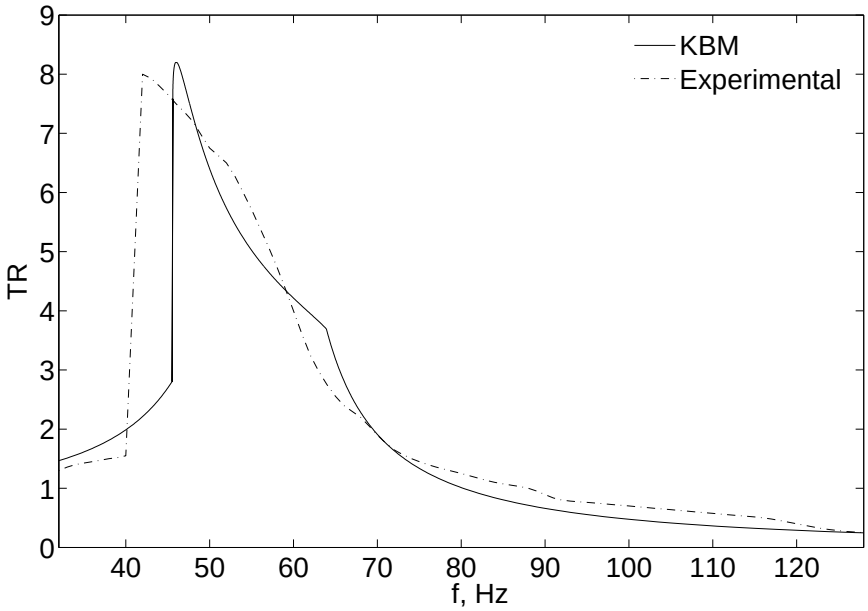

Fig. 90. Comparison of results obtained from the KBM analysis with the experimental data for $2g$ down sweep.

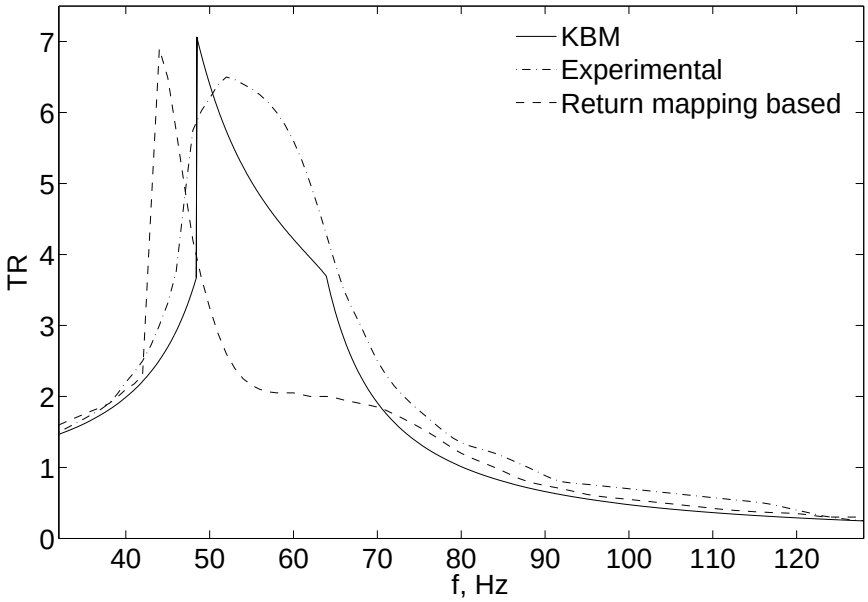

Fig. 91. Comparison of results obtained from the KBM analysis and the return mapping algorithm with the experimental data for $2g$ up sweep.

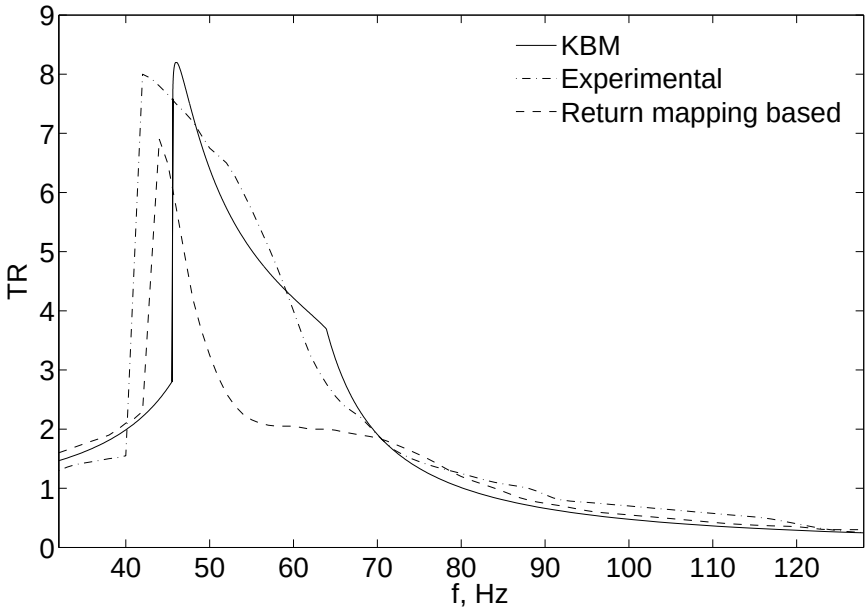

Fig. 92. Comparison of results obtained from the KBM analysis and the return mapping algorithm with the experimental data for $2g$ down sweep.

CHAPTER VII

CONCLUSIONS

The response of an oscillator with hysteretic restoring force and sinusoidal forcing was studied. Hysteresis was modeled using the bilinear and the multilinear model of hysteresis. The steady state response of the system was studied using approximate asymptotic expansions and exact Poincaré maps. The asymptotic expansions were derived using the KBM method. An efficient numerical method was proposed to solve for the response of the system to arbitrary precision. This method was used to calculate and study the Poincaré maps of the system. The damping induced due to hysteresis was evaluated using the KBM solution. A 1-D oscillator with SMA components was analyzed using the KBM method and the results were compared with experimental data. The major findings and contributions of this work are summarized in the following sections.

A. Exact Solution Methodology

An efficient method for obtaining the exact solution of the system was presented in this thesis. To the best of our knowledge this is an original contribution. This method can be readily extended to include any model of hysteresis, provided the hysteresis loop can be approximated by piecewise linear components. This method proceeds by finding the time at which the transition from the present state to the next state of the automaton occurs. The full solution of the system can then be constructed using the analytical solutions for the individual states. It was shown that the problem of finding the transition time boils down to a root finding problem. The algorithm for root finding has guaranteed convergence and $\mathcal{O}(l)$ execution time where l is a measure of the length of the interval to be searched for the roots.

B. Bilinear Hysteresis

The bilinear model of hysteresis was studied. Asymptotic expansions for the response of the system were obtained using the KBM method. It was found that the hysteretic element acts as a 'soft spring', i.e., the resonance frequency of the system decreases due to the presence of hysteresis. It was shown that according to the KBM method the steady state response of the system is unconditionally stable. The dissipation induced by hysteresis can result in bound resonance. An analytical criterion for existence of bound and unbound resonance was derived. Expressions were also derived for the equivalent damping of the system.

Poincaré maps were constructed to analyze the steady state behavior of the system. The study of the Poincaré maps revealed that the true response of the system matches with the approximate expressions derived using the KBM method to a good degree of accuracy. However, for certain cases the KBM method is unable to capture the steady state response of the system adequately. The source of error in the KBM method was discussed. Bifurcation and continuation analysis of the Poincaré maps showed that the steady state is indeed unconditionally stable. The Poincaré did not show any classical bifurcation. The system did not exhibit any complex or chaotic response. However, the sub-harmonic resonances were detected.

C. Multilinear Hysteresis

The multilinear model of hysteresis was proposed and studied. Asymptotic analysis of the system was carried out using the KBM method. As in the case of bilinear hysteresis it was found that the multilinear hysteretic element also acts like a soft spring, thereby lowering the frequency of resonance. Bounded and unbounded resonances were observed in the system and analytical criteria were derived for their existence.

According to the asymptotic analysis the steady state of the system was found to be stable for all parameter values. The equivalent damping properties of the hysteretic system were also studied.

Exact Poincaré maps of the system were constructed to study the steady state response more rigorously. It was found that the results obtained from the asymptotic analysis are indeed a good match for the exact response. However, bifurcation analysis of the Poincaré maps revealed the existence of grazing bifurcations, which in turn resulted in existence of multivalued response in the system. The dominant response of the system was still found to be close to simple periodic orbit predicted using the KBM method. The Poincaré map of the system did not undergo any classical bifurcations and the steady state response of the system was found to be unconditionally stable.

D. Experimental Validation

A 1-D oscillator with SMA elements and harmonic excitation was analyzed using the KBM method. The thermomechanical coupling was not taken into account for the purpose of this analysis. The results were compared with experimental data and one other numerical method available in literature. The SMA components were seen to act like soft springs. However, it was argued that for larger amplitude oscillations the elements would introduce a softening followed by a hardening of the response. The jump phenomena was captured by the KBM analysis.

It was seen that the results of the asymptotic analysis are in agreement with the experimental data. However, there remains scope for improvement in the quality of the results. It was suggested that the results can be bettered by a.) accounting for the thermomechanical coupling, b.) carefully calibrating the experimental setup to measure any damping that might arise due to friction etc. , and c.) improving the

model for SMA material response.

E. Future Work

The research presented in this thesis can be extended in many directions. One avenue for future work would be to obtain better experimental validation for the theoretical results obtained here. One could use the Poincaré maps based analysis to get more accurate results, as compared to the KBM analysis presented in the thesis. The method can also be extended to slightly more complicated systems like two masses connected by SMA components etc.

One feature of the bilinear and the multilinear models of hysteresis studied in this thesis was that the area of hysteresis was unbounded for both cases. In practice, many hysteretic systems exhibit bounded regions of hysteresis. It would be an interesting exercise to approximate the response curves by piecewise linear elements and study some systems with bounded hysteretic regions.

REFERENCES

[1] G. Bertotti and I. Mayergoyz, *The Science of Hysteresis*. Oxford: Elsevier, 2006.

[2] D. Hughes and J. Wen, "Preisach modeling of piezoceramic and shape memory alloy hysteresis," *Smart Materials and Structures*, vol. 6, no. 3, pp. 287–300, 1997.

[3] G. Bertotti, *Hysteresis in Magnetism*. San Diego: Academic Press, 1998.

[4] K. Kohari, T. Saito, and H. Kawakami, "On a hysteresis oscillator including periodic thresholds," *IEICE Transactions on Fundamentals of Electronics, Communications and Computer Sciences*, vol. 76, no. 12, pp. 2102–2107, 1993.

[5] S. Nasuno, A. Kudrolli, and J. Gollub, "Friction in granular layers: Hysteresis and precursors," *Physical Review Letters*, vol. 79, no. 5, pp. 949–952, 1997.

[6] A. Dixit, "Investment and hysteresis," *The Journal of Economic Perspectives*, vol. 6, no. 1, pp. 107–132, 1992.

[7] O. Blanchard and L. Summers, "Hysteresis and the European unemployment problem," *NBER Macroeconomics Annual*, vol. 1, pp. 15–78, 1986.

[8] W. Lacarbonara and F. Vestroni, "Nonclassical responses of oscillators with hysteresis," *Nonlinear Dynamics*, vol. 32, no. 3, pp. 235–258, 2003.

[9] L. Machado and D. Lagoudas, "Nonlinear dynamics of a SMA passive vibration damping device," *in Proc. of SPIE*, vol. 6169, p. 61690X, 2006.

[10] D. Sauter and P. Hagedorn, "On the hysteresis of wire cables in Stockbridge dampers," *International Journal of Non-Linear Mechanics*, vol. 37, no. 8, pp. 1453–1459, 2002.

[11] S. Dyke, B. Spencer Jr, M. Sain, and J. Carlson, "Experimental study of MR dampers for seismic protection," *Smart Materials and Structures*, vol. 7, no. 5, pp. 693–703, 1998.

[12] Z. Chaudhry and C. Rogers, "Bending and shape control of beams using SMA actuators," *Journal of Intelligent Material Systems and Structures*, vol. 2, no. 4, p. 581, 1991.

[13] G. Webb, D. Lagoudas, and A. Kurdila, "Hysteresis modeling of SMA actuators for control applications," *Journal of Intelligent Material Systems and Structures*, vol. 9, no. 6, p. 432, 1998.

[14] M. Brokate and J. Sprekels, *Hysteresis and Phase Transitions*. New York: Springer-Verlag, 1996.

[15] M. Krasnosel'skii and A. Pokrovskii, *Systems with Hysteresis*. New York: Springer-Verlag, 1989.

[16] I. Mayergoyz, *Mathematical Models of Hysteresis and Their Applications*. Oxford: Elsevier, 2003.

[17] A. Visintin, *Differential Models of Hysteresis.* New York: Springer, 1994.

[18] M. Brokate, "Some mathematical properties of the Preisach model for hysteresis," *Magnetics, IEEE Transactions on*, vol. 25, no. 4, pp. 2922–2924, 1989.

[19] M. Krasnosel'skii and A. Pokrovskii, "Hysterant operator," *Soviet Math. Dokl*, vol. 11, pp. 29–33, 1970.

[20] G. Masing, "Eigenspannungen und Verfestigung beim Messing," *in Proc. of the Second International Congress of Applied Mechanics*, pp. 332–335, 1926.

[21] P. Duhem, *The Evolution of Mechanics*. New York: Springer, 1980.

[22] R. Bouc, "Forced vibration of mechanical systems with hysteresis," *in Proc. of the 4th Conference on Nonlinear Oscillations, Prague*, p. 315, 1967.

[23] Y. Wen, "Method for random vibration of hysteretic systems," *Journal of the Engineering Mechanics Division*, vol. 102, no. 2, pp. 249–263, 1976.

[24] T. K. Caughey, "Sinusoidal excitation of a system with bilinear hysteresis," *Journal of Applied Mechanics*, vol. 27, no. 4, pp. 640–643, 1960.

[25] T. Caughey, "Random excitation of a system with bilinear hysteresis," *Journal of Applied Mechanics*, vol. 27, no. 4, pp. 649–652, 1960.

[26] C. Liang and C. Rogers, "One-dimensional thermomechanical constitutive relations for shape memory materials," *Journal of Intelligent Material Systems and Structures*, vol. 1, no. 2, p. 207, 1990.

[27] J. Boyd and D. Lagoudas, "A thermodynamical constitutive model for shape memory materials. Part I. The monolithic shape memory alloy," *International Journal of Plasticity*, vol. 12, no. 6, pp. 805–842, 1996.

[28] B. Raniecki, C. Lexcellent, and K. Tanaka, "Thermodynamic models of pseudoelastic behaviour of shape memory alloys," *Archives Mechanics Archiwum Mechaniki Stosowanej*, vol. 44, pp. 261–284, 1992.

[29] S. Masri, "Forced vibration of the damped bilinear hysteretic oscillator," *The Journal of the Acoustical Society of America*, vol. 57, p. 106, 1975.

[30] D. Capecchi, "Accurate solutions and stability criterion for periodic oscillations in hysteretic systems," *Meccanica*, vol. 25, no. 3, pp. 159–167, 1990.

[31] D. Capecchi, "Periodic response and stability of hysteretic oscillators," *Dynamical Systems*, vol. 6, no. 2, pp. 89–106, 1991.

[32] R. Masiani, D. Capecchi, and F. Vestroni, "Resonant and coupled response of hysteretic two-degree-of-freedom systems using harmonic balance method," *International Journal of Non-Linear Mechanics*, vol. 37, no. 8, pp. 1421–1434, 2002.

[33] D. Capecchi, R. Masiani, and F. Vestroni, "Periodic and non-periodic oscillations of a class of hysteretic two degree of freedom systems," *Nonlinear Dynamics*, vol. 13, no. 4, pp. 309–325, 1997.

[34] R. Pratap and P. Holmes, "Chaos in a mapping describing elastoplastic oscillations," *Nonlinear Dynamics*, vol. 8, no. 1, pp. 111–139, 1995.

[35] J. A. Ewing, "Experimental research in magnetism," *Transaction of the Royal Society of London*, 1895.

[36] F. Preisach, "'Uber die magnetische Nachwirkung," *Z. Physik*, vol. 94, pp. 277–302, 1935.

[37] E. Della Torre, *Magnetic Hysteresis*. New York: IEEE Press, 1999.

[38] J. Takács, *Mathematics of Hysteretic Phenomena: The T(x) Model for the Description of Hysteresis*. Weinheim, Germany: Wiley-VCH, 2003.

[39] M. P. Langevin, "Magnetisme et theorie des electrons," *Ann. Chim. Phys.*, vol. 5, pp. 70–127, 1905.

[40] M. L. Brillouin, "Les moments de rotation et le magnetisme dans la mechanique onodolatoire," *J. Phys. Radium*, vol. 8, pp. 74–84, 1927.

[41] J. Dugdale, *Entropy and Its Physical Meaning*. London, UK: Taylor & Francis, 1996.

[42] K. Otsuka and C. Wayman, *Shape Memory Materials*. Cambridge, UK: Cambridge University Press, 1998.

[43] T. W. Duerig, K. N. Melton, D. Stockel, and C. M. Wayman, *Engineering Aspects of Shape Memory Alloys*. Northants, UK: Butterworth-Heinemann, 1990.

[44] V. Birman, "Review of mechanics of shape memory alloy structures," *Applied Mechanics Reviews*, vol. 50, no. 11, pp. 629–645, 1997.

[45] C. Rogers, C. Liang, and J. Jia, "Behavior of shape memory alloy reinforced composite plates, Part 1: Model formulation and control concepts," *in Proc. AIAA/ASME/ASCE/AHS 30th Structures, Structural Dynamics and Materials Conference*, pp. 2011–2016, 1989.

[46] J. Boyd and D. Lagoudas, "A thermodynamical constitutive model for shape memory materials. Part II. The SMA composite material," *International Journal of Plasticity*, vol. 12, no. 7, pp. 843–873, 1996.

[47] C. Liang and C. Rogers, "The multi-dimensional constitutive relations of shape memory alloys," *Journal of Engineering Mathematics*, vol. 26, no. 5, pp. 429–443, 1992.

[48] D. Lagoudas, Z. Bo, and M. Qidwai, "A unified thermodynamic constitutive model for SMA and finite element analysis of active metal matrix components," *Mechanics of Advanced Materials and Structures*, vol. 3, no. 2, pp. 153–179, 1996.

[49] M. Qidwai and D. Lagoudas, "Numerical implementation of a shape memory alloy thermomechanical constitutive model using return mapping algorithms,"

International Journal for Numerical Methods in Engineering, vol. 47, no. 6, pp. 1123–1168, 2000.

[50] J. Simo and R. Taylor, "A return mapping algorithm for plane stress elastoplasticity," *International Journal for Numerical Methods in Engineering*, vol. 22, no. 3, pp. 649–670, 1986.

[51] M. Ortiz and P. Pinsky, "Global analysis methods for the solution of the elastoplastic and viscoplastic dynamic problems," tech. rep., UCRL-15522, California Univ., Berkeley. Dept. of Civil Engineering, 1982.

[52] D. Lagoudas, L. Machado, and M. Lagoudas, "Nonlinear vibration of a one-degree of freedom shape memory alloy oscillator: A numerical-experimental investigation.," *46 th AIAA/ASME/ASCE/AHS/ASC Structures, Structural Dynamics, and Materials Conference*, pp. 1–18, 2005.

[53] A. Nayfeh, *Perturbation Methods*. New York: Wiley, 1973.

[54] N. Bogoliubov and Y. Mitropolsky, *Asymptotic Methods in the Theory of Non-Linear Oscillations*. Delhi, India: Hindustan Publishing Corporation, 1961.

[55] H. Keller, *Lectures on Numerical Methods in Bifurcation Problems*. New York: Springer, 1987.

[56] E. Doedel, H. Keller, and J. Kernevez, "Numerical analysis and control of bifurcation problems. I. Bifurcation in finite dimensions," *International Journal of Bifurcation and Chaos Applied Sciences Engineering*, vol. 1, no. 3, pp. 493–520, 1991.

[57] E. Allgower and K. Georg, *Introduction to Numerical Continuation Methods*. Philadelphia: Society for Industrial and Applied Mathematics, 2003.

[58] E. Allgower and K. Georg, "Continuation and path following," *Acta Numerica 1993*, pp. 1–64, 1993.

[59] W. Zangwill and C. Garcia, *Pathways to Solutions, Fixed Points, and Equilibria*. NJ, USA: Prentice-Hall, 1981.

[60] E. Doedel, A. Champneys, T. Fairgrieve, Y. Kuznetsov, B. Sandstede, and X. Wang, *AUTO97: Continuation and Bifurcation Software for Ordinary Differential Equations (With HomCont)*. Montreal, Canada: Concordia University, 1998.

[61] A. Dhooge, W. Govaerts, and Y. Kuznetsov, "MATCONT: A MATLAB package for numerical bifurcation analysis of ODEs," *ACM Transactions on Mathematical Software (TOMS)*, vol. 29, no. 2, pp. 141–164, 2003.

[62] A. Back, J. Guckenheimer, M. Myers, F. Wicklin, and P. Worfolk, "DsTool: Computer assisted exploration of dynamical systems," *Notices of the American Mathematical Society*, vol. 39, no. 4, pp. 303–309, 1992.

[63] A. Khibnik, Y. Kuznetsov, V. Levitin, and E. Nikolaev, "LOCBIF," *Interactive LOCal BIFfurcation Analyzer, preprint*, 1992.

[64] Y. Kuznetsov and V. Levitin, "CONTENT: A multiplatform environment for continuation and bifurcation analysis of dynamical systems," *Centrum voor Wiskunde en Informatica, Kruislaan*, vol. 413, p. 1098, 1997.

[65] B. Ermentrout, *Simulating, Analyzing, and Animating Dynamical Systems: A Guide to XPPAUT for Researchers and Students*. Philadelphia: Society for Industrial Mathematics, 2002.

[66] Y. Kuznetsov, *Elements of Applied Bifurcation Theory.* New York: Springer, 2004.

[67] W. Press, *Numerical Recipes in C: The Art of Scientific Computing.* Cambridge, UK: Cambridge University Press, 1992.

APPENDIX A

THE METHOD OF KRYLOV, BOGOLIUBOV AND MITROPOLSKY

In this appendix we present a technique for obtaining asymptotic expansions for analyzing the behavior of nonlinear systems close to linear ones. A nonlinear system is considered to be close to linear one when the system depends on a small parameter ϵ such that for $\epsilon = 0$ the system degenerates into a linear time-invariant system (typically without undergoing a loss in system order). Theories for dealing with such systems were initially developed in celestial mechanics, however, they have been applied to various problems in quantum mechanics, engineering, and pure mathematics. The aim of asymptotic methods is to develop expressions for response of the system in a power-series of the small parameter ϵ. The convergence of such expansions is not evaluated with respect to taking more terms in the series, rather with a small number of terms (typically two) with respect to the limit $\epsilon \to 0$. In other words, the asymptotic expansion should tend to the exact solution uniformly for small ϵ. The reader is refer to Ref. [53] for an excellent introduction to the subject of asymptotic methods. It should be mentioned that an asymptotic expansion is not simply a power series expansion. To bring out this difference consider the following expansion of the exponential

$$\exp(\epsilon t) = 1 + \epsilon t + \frac{\epsilon^2 t^2}{2!} + \dots \tag{A.1}$$

Even though the above expansion is a valid power series, it is not an asymptotic expansion because for every ϵ any finite truncation of the above series will differ substantially from the true value of the exponential for large a enough value of t.

We shall present the technique developed by the Russian mathematicians Nikolai Nikolaevich Bogoliubov, Nikolay Mitrofanovich Krylov, and Yurii Mitropolsky in the

1930's and 40's[1]. This technique is called the KBM technique or the KBM method in the honor of its inventors. The KBM method is sometimes also known as the method of averaging. Note that in the following development we will omit the most rigorous mathematical details of the method. The interested reader is encouraged to read Ref. [54] for getting acquainted with the mathematical foundations of the method.

We consider systems of the form

$$\ddot{x} + \omega_0^2 x = \epsilon f(x, \dot{x}), \tag{A.2}$$

where $f(x, \dot{x})$ is a sufficiently smooth nonlinearity. It is clear that Eq. A.2 reduces to a linear equation for $\epsilon = 0$. Thus, for small values of ϵ it is appropriate to consider it to be close to a linear equation in some sense. Note that if the RHS of Eq. A.2 is not a function of $\dot{x}$ then one can find a constant of motion, and thus the long-term behavior of the system is ascertained without much effort. In such cases the constant of motion can be found as follows

$$\begin{aligned} &\ddot{x} + \omega_0^2 x - \epsilon f(x) = 0 \\ \Rightarrow\ &\dot{x}d\dot{x} + \omega_0^2 x dx - \epsilon f(x)dx = 0 \\ \Rightarrow\ &\frac{\dot{x}^2}{2} + \omega_0^2 \frac{x^2}{2} - \epsilon \int f(x)dx = 0. \end{aligned}$$

However, even in such simple cases the frequency of the nonlinear oscillations cannot be found by using the constant of motion. In the case when the RHS of Eq. A.2 depends on $\dot{x}$ there is little hope of solving the system analytically or even finding a constant of motion (in most cases none exists). In such cases one is left with little choice but to use asymptotic methods. Thankfully, the solutions obtained from these

[1]Bogoliubov was Krylov's student, and Mitropolsky was Bogoliubov's student. The students and the teachers are amongst the most influential figures in Russian mathematical history.

methods are often very insightful and accurate.

When $\epsilon = 0$ the solution of Eq. A.2 is

$$\begin{aligned} x(t) &= a\cos\phi, \\ \dot{a} &= 0, \\ \dot{\phi} &= \omega_0. \end{aligned} \tag{A.3}$$

When ϵ is small it is reasonable to assume that the response of the system will deviate from the ϵ equal to zero case only slightly. Accordingly, we write

$$\begin{aligned} x(t) &= a\cos\phi + \epsilon u_1(a,\phi) + \epsilon^2 u_2(a,\phi) + \ldots, \\ \dot{a} &= \epsilon A_1(a) + \epsilon^2 A_2(a) + \ldots, \\ \dot{\phi} &= \omega_0 + \epsilon B_1(a) + \epsilon^2 B_2(a) + \ldots \end{aligned} \tag{A.4}$$

Note that we have assumed that the time rate of ϕ and a are functions of a alone. The justification for this assumption can be found in Ref. [54]. We are interested in finding the behavior of a, ϕ with time and not in finding higher order correction terms u_i. Even though this might seem incorrect, it is indeed appropriate if the expansion is asymptotic in nature and ϵ is small. Differentiating the first equation of the set A.4 we get

$$\begin{aligned} \dot{x} =& \dot{a}\left(\cos\phi + \epsilon\frac{\partial u_1}{\partial a} + \epsilon^2\frac{\partial u_2}{\partial a} + \ldots\right) + \dot{\phi}\left(-a\sin\phi + \epsilon\frac{\partial u_1}{\partial \phi} + \epsilon^2\frac{\partial u_2}{\partial \phi} + \ldots\right), \\ \ddot{x} =& \ddot{a}\left(\cos\phi + \epsilon\frac{\partial u_1}{\partial a} + \epsilon^2\frac{\partial u_2}{\partial a} + \ldots\right) + \ddot{\phi}\left(-a\sin\phi + \epsilon\frac{\partial u_1}{\partial \phi} + \epsilon^2\frac{\partial u_2}{\partial \phi} + \ldots\right) + \\ &+ \dot{a}^2\left(\epsilon\frac{\partial^2 u_1}{\partial a^2} + \epsilon^2\frac{\partial^2 u_2}{\partial a^2} + \ldots\right) + \dot{\phi}^2\left(-a\cos\phi + \epsilon\frac{\partial^2 u_1}{\partial \phi^2} + \epsilon^2\frac{\partial^2 u_2}{\partial \phi^2} + \ldots\right) + \\ &+ \dot{a}\dot{\phi}\left(\sin\phi + \epsilon\frac{\partial^2 u_1}{\partial a\partial \phi} + \epsilon^2\frac{\partial^2 u_2}{\partial a\partial \phi} + \ldots\right). \end{aligned} \tag{A.5}$$

Using the second and third equations of the set A.4 the following expressions can be

obtained

$$\begin{aligned}
\ddot{a} &= \left(\epsilon\frac{dA_1}{da} + \epsilon^2\frac{dA_2}{da} + \ldots\right)\left(\epsilon A_1 + \epsilon^2 A_2 + \ldots\right) = \epsilon^2 A_1\frac{dA_1}{da} + \ldots, \\
\ddot{\phi} &= \left(\epsilon\frac{dB_1}{da} + \epsilon^2\frac{dB_2}{da} + \ldots\right)\left(\epsilon A_1 + \epsilon^2 A_2 + \ldots\right) = \epsilon^2 A_1\frac{dB_1}{da} + \ldots, \\
\dot{a}^2 &= \left(\epsilon A_1 + \epsilon^2 A_2 + \ldots\right)^2 = \epsilon^2 A_1^2 + \ldots, \\
\dot{\phi}^2 &= \left(\omega_0\epsilon B_1 + \epsilon^2 B_2 + \ldots\right)^2 = \omega_0^2 + \epsilon 2\omega_0 B_1 + \epsilon^2(B_1^2 + 2\omega_0 B_2) + \ldots.
\end{aligned} \tag{A.6}$$

Substituting the set A.6 in the set A.5 and arranging in powers of ϵ we get

$$\begin{aligned}
\dot{x} =& -a\omega_0\sin\phi + \epsilon\left(A_1\cos\phi - aB_1\sin\phi + \omega_0\frac{\partial u_1}{\partial\phi}\right) + \\
&+\epsilon^2\left(A_2\cos\phi - aB_2\sin\phi + A_1\frac{\partial u_1}{\partial a} + B_1\frac{\partial u_1}{\partial\phi} + \omega_0\frac{\partial u_2}{\partial\phi}\right) + \ldots, \\
\ddot{x} =& -a\omega_0^2\cos\phi + \epsilon\left(-2\omega_0 A_1\sin\phi - 2\omega_0 aB_1\cos\phi + \omega_0^2\frac{\partial^2 u_1}{\partial\phi^2}\right) + \\
&+\epsilon^2\left\{\left(A_1\frac{dA_1}{da} - aB_1^2 - 2\omega_0 aB_2\right)\cos\phi - \left(2\omega_0 A_2 + 2A_1B_1 + A_1 a\frac{dB_1}{da}\right)\sin\phi + \right. \\
&\left.+2\omega_0 A_1\frac{\partial^2 u_1}{\partial a\partial\phi} + 2\omega_0 B_1\frac{\partial^2 u_1}{\partial\phi^2} + \omega_0^2\frac{\partial^2 u_2}{\partial\phi^2}\right\} + \ldots.
\end{aligned} \tag{A.7}$$

Thus, the LHS of Eq. A.2 can be written as

$$\begin{aligned}
\ddot{x} + \omega_0 x =& \epsilon\left(-2\omega_0 A_1\sin\phi - 2\omega_0 aB_1\cos\phi + \omega_0^2\frac{\partial^2 u_1}{\partial\phi^2} + \omega_0^2 u_1\right) + \\
&+\epsilon^2\left\{\left(A_1\frac{dA_1}{da} - aB_1^2 - 2\omega_0 aB_2\right)\cos\phi - \left(2\omega_0 A_2 + 2A_1B_1 + A_1 a\frac{dB_1}{da}\right)\sin\phi + \right. \\
&\left.+2\omega_0 A_1\frac{\partial^2 u_1}{\partial a\partial\phi} + 2\omega_0 B_1\frac{\partial^2 u_1}{\partial\phi^2} + \omega_0^2\frac{\partial^2 u_2}{\partial\phi^2} + \omega_0^2 u_2\right\} + \ldots.
\end{aligned} \tag{A.8}$$

The RHS of Eq. A.2 can be expanded in a Taylor series as follows

$$\epsilon f(x,\dot{x}) = \epsilon f_0(a,\phi) + \epsilon^2\left\{u_1 f_x^1(a,\phi) + \left(A_1\cos\phi - aB_1\sin\phi + \omega_0\frac{\partial u_1}{\partial\phi}\right) f_{\dot{x}}^1(a,\phi)\right\} + \ldots, \tag{A.9}$$

where

$$
\begin{aligned}
f_0(a,\phi) &= f(a\cos\phi, -a\omega_0\sin\phi),\\
f_x^1(a,\phi) &= \left.\frac{\partial f}{\partial x}\right|_{x=a\cos\phi,\dot{x}=-a\omega_0\sin\phi},\\
f_{\dot{x}}^1(a,\phi) &= \left.\frac{\partial f}{\partial \dot{x}}\right|_{x=a\cos\phi,\dot{x}=-a\omega_0\sin\phi}.
\end{aligned}
\tag{A.10}
$$

On substituting Eqs. A.8,A.9 into Eq. A.2 and comparing the coefficients of like powers of ϵ we get

$$
\begin{aligned}
\omega_0^2\left(\frac{\partial^2 u_1}{\partial\phi^2}+u_1\right) &= f_0(a,\phi)+2\omega_0 A_1\sin\phi+2\omega_0 aB_1\cos\phi,\\
\omega_0^2\left(\frac{\partial^2 u_2}{\partial\phi^2}+u_2\right) &= f_1(a,\phi)+2\omega_0 A_2\sin\phi+2\omega_0 aB_2\cos\phi,\\
\ldots &= \ldots\\
\omega_0^2\left(\frac{\partial^2 u_i}{\partial\phi^2}+u_i\right) &= f_{i-1}(a,\phi)+2\omega_0 A_i\sin\phi+2\omega_0 aB_i\cos\phi,
\end{aligned}
\tag{A.11}
$$

where

$$
\begin{aligned}
f_0(a,\phi) =& f(a\cos\phi, -a\omega_0\sin\phi),\\
f_1(a,\phi) =& u_1 f_x^1+\left(A_1\cos\phi-aB_1\sin\phi+\omega_0\frac{\partial u_1}{\partial\phi}\right)f_{\dot{x}}^1+\\
&+\left(aB_1^2-A_1\frac{dA_1}{da}\right)\cos\phi+\left(2A_1B_1+A_1a\frac{dB_1}{da}\right)\sin\phi-\\
&-2\omega_0 A_1\frac{\partial^2 u_1}{\partial a\partial\phi}-2\omega_2 B_1\frac{\partial^2 u_1}{\partial\phi^2},\\
\ldots =& \ldots
\end{aligned}
\tag{A.12}
$$

In order to avoid the problem of secular terms in equations of the set A.11 we examine the Fourier series of $f_i(a,\phi)$ and choose A_{i+1}, B_{i+1} such that the secular producing terms cancel out. Since $f_i(a,\phi)$ are periodic in ϕ with period 2π we can obtain the

following Fourier series

$$f_0(a,\phi) = g_0(a) + \sum_{n=1}^{\infty} \left(g_n(a)\cos n\phi + h_n(a)\sin n\phi\right). \tag{A.13}$$

Substituting Eq. A.13 into the RHS of first equation of the set A.11 and setting the secular producing terms to zero we get

$$A_1 = -\frac{1}{2\omega_0}h_1(a) = -\frac{1}{2\pi\omega_0}\int_0^{2\pi} f(a\cos\phi, -a\omega_0\sin\phi)\sin\phi d\phi, \tag{A.14}$$

and

$$B_1 = -\frac{1}{2a\omega_0}h_1(a) = -\frac{1}{2\pi a\omega_0}\int_0^{2\pi} f(a\cos\phi, -a\omega_0\sin\phi)\cos\phi d\phi. \tag{A.15}$$

Thus, we can write the 1-term asymptotic expansion for the solution to Eq. A.2 as

$$\begin{aligned} x &= a\cos\phi, \\ \dot{a} &= \epsilon A_1(a), \\ \dot{\phi} &= \omega_0 + \epsilon B_1(a). \end{aligned} \tag{A.16}$$

Note that we have not obtained and expression for u_1. However, as shown in Ref. [54] the first order correct expansions for $\dot{a}, \dot{\phi}$ can only give a zeroth order correct expansion for x, thus to evaluate the first order correction, u_1, to x one has to find the second order corrections to $\dot{a}, \dot{\phi}$. The derivation for second order corrections can be found in Ref. [54].

The only unanswered question now is about the nomenclature of the method: Why is the KBM method sometimes referred to as the method of averaging? There are two answers to this question. Firstly, the Fourier coefficients are indeed averaged quantities. Secondly, there exist some alternate derivations of the method using explicit averaging. However, in our opinion the development presented here is the most suitable one. In either case the alternate name of the method follows.

Examples

We illustrate the KBM method with two classical examples: the Van-der-Pol equation and the Duffing equation.

Equation of Van-der-Pol

The classical Van-der-Pol equation is as follows

$$\ddot{x} + x = \epsilon(1 - x^2)\dot{x}. \tag{A.17}$$

Using the KBM method we can get the following first approximation for the solution to Eq. A.17

$$\begin{aligned} x &= a\cos\phi, \\ \dot{a} &= \frac{\epsilon a}{2}\left(1 - \frac{a^2}{4}\right), \\ \dot{\phi} &= 1. \end{aligned} \tag{A.18}$$

The above relations suggest that to the first order the frequency of the system is not affected by the nonlinearity. Further, the second equation of the set A.18 has fixed points at $a = 0, 2$. It is clear by inspection that the fixed point at $a = 0$ is unstable (can be confirmed by an eigenvalue analysis) while that at $a = 2$ is stable. Thus, according to the KBM method, the Van-der-Pol equation must have a limit cycle of amplitude 2.

The set A.18 can be solved to get the following expressions for a and x

$$a = \frac{a_0 e^{\epsilon t/2}}{\sqrt{1 + \frac{1}{4}a_0^2(e^{\epsilon t} - 1)}}, \tag{A.19}$$

and

$$x = \frac{a_0 e^{\epsilon t/2}}{\sqrt{1 + \frac{1}{4}a_0^2(e^{\epsilon t} - 1)}} \cos(t + \phi_0), \tag{A.20}$$

where a_0, ϕ_0 are to be found from initial conditions. Again, it is clear from the expression for a that $a \approx 2$ for $e^{\epsilon t} \gg 1$.

Figure 93 shows the comparison of the two-term KBM solution of the Van-der-Pol equation with the results obtained from numerical integration of the equation for two values of ϵ. The results show excellent match for $\epsilon = 0.1$. The numerical solution and the KBM solution can be seen to match fairly well even for $\epsilon = 0.3$, which is not really a 'small value'.

Duffing Equation

The following Duffing equation describes a harmonic oscillator with a cubic nonlinearity

$$\ddot{x} + x = -\epsilon x^3. \tag{A.21}$$

On applying the KBM method for this equation we get the following solution for small ϵ

$$\begin{aligned} x &= a\cos\phi, \\ \dot{a} &= 0, \\ \dot{\phi} &= 1 + \frac{3\epsilon a^2}{8}. \end{aligned} \tag{A.22}$$

We can solve the above equations to get the following expressions for a, ϕ and x

$$\begin{aligned} a &= a_0, \\ \phi &= \phi_0 + \left(1 + \frac{3\epsilon a^2}{8}\right) t, \\ x &= a_0 \cos\left(\phi_0 + \left(1 + \frac{3\epsilon a^2}{8}\right) t\right), \end{aligned} \tag{A.23}$$

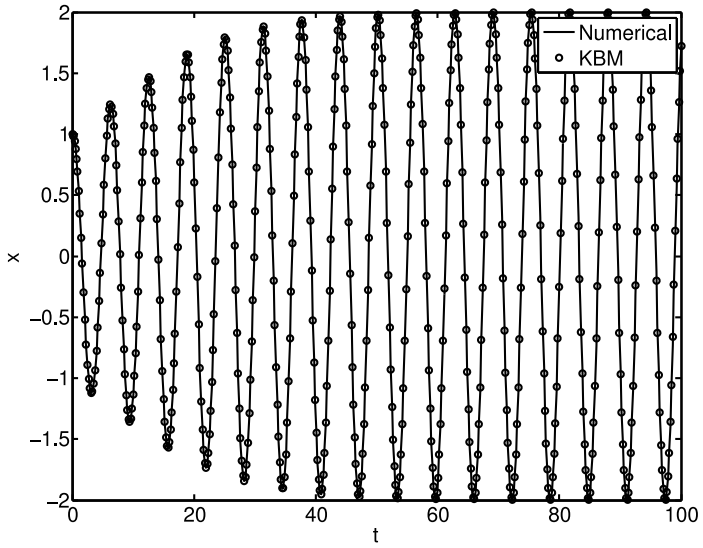

(a) x versus t for $\epsilon = 0.1$

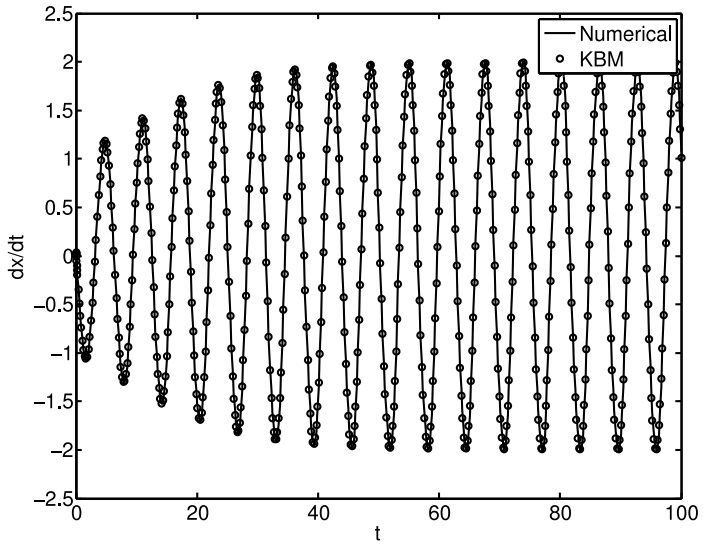

(b) $\dot{x}$ versus t for $\epsilon = 0.1$

Fig. 93. Comparison of KBM method with numerical integration for the Van-der-Pol equation with $\epsilon = 0.1, 0.3$. The initial conditions are $x(0) = 1, \dot{x}(0) = 0$ for all cases.

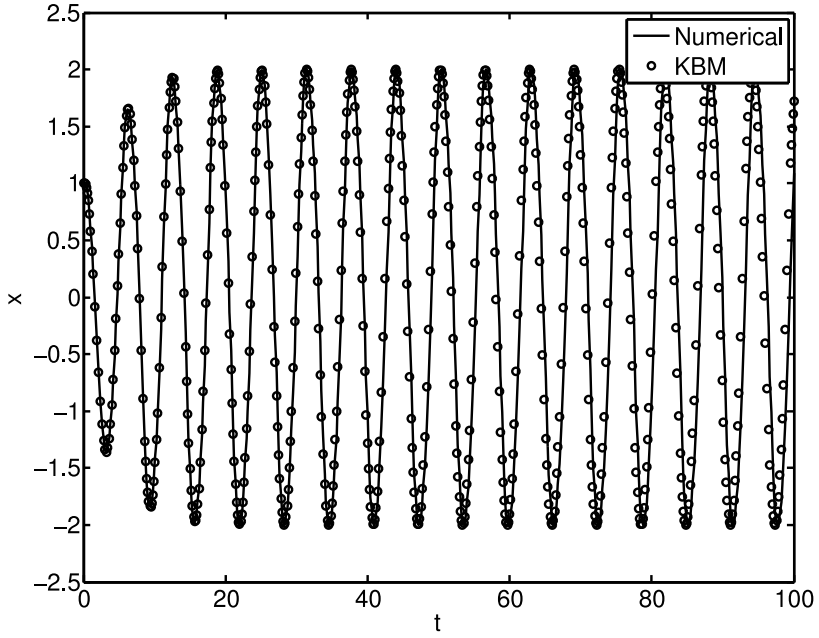

(c) x versus t for $\epsilon = 0.3$

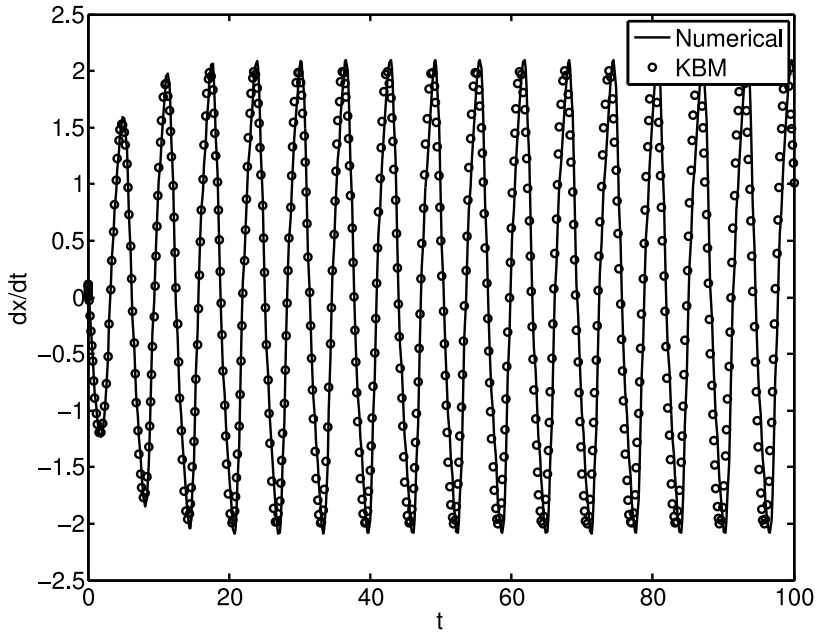

(d) $\dot{x}$ versus t for $\epsilon = 0.3$

Fig. 93. Continued ...

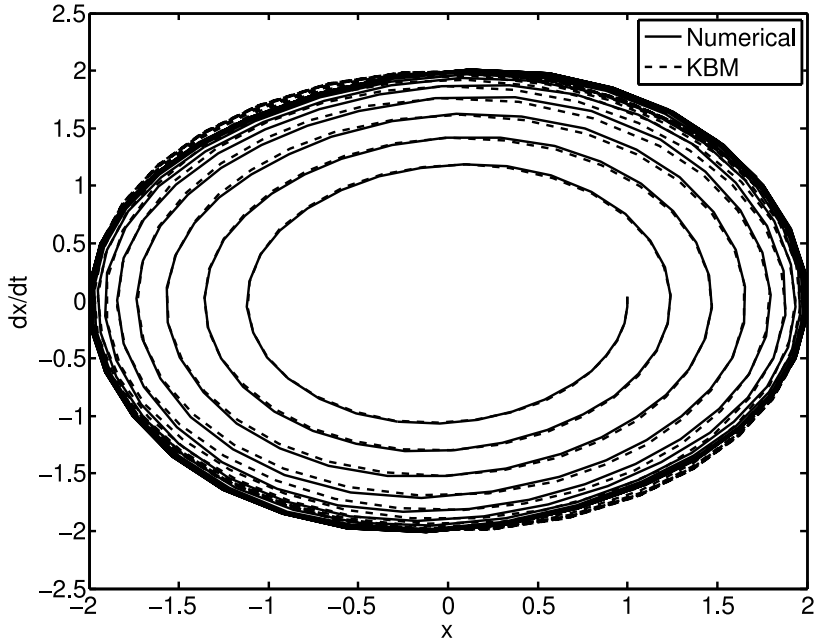

(e) Phase space for $\epsilon = 0.1$

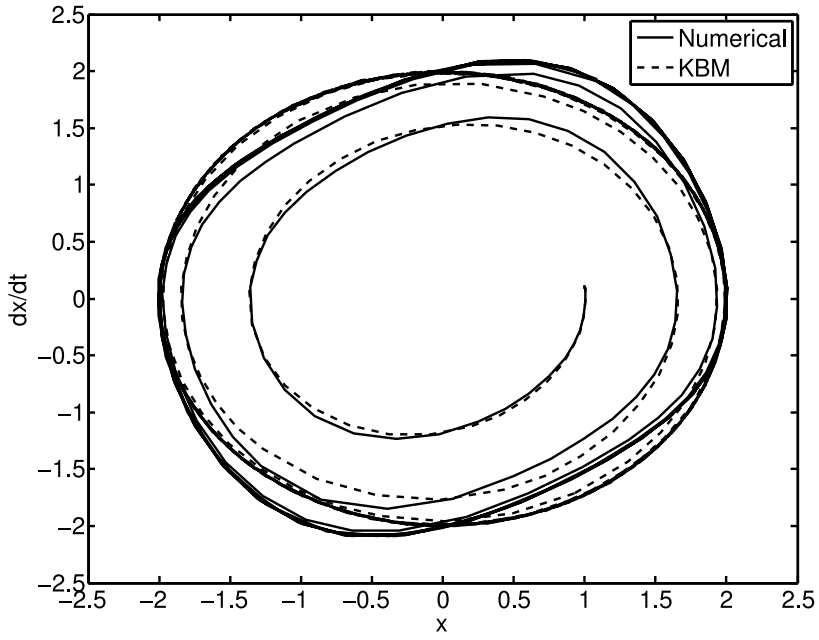

(f) Phase space for $\epsilon = 0.3$

Fig. 93. Continued ...

where a_0, ϕ_0 are to be found from the initial conditions. As expected, the KBM solution indicates the presence of a constant of motion in the form of the constant amplitude, and also indicates an increase in the frequency of oscillations.

Figure 94 shows the comparison of results obtained using the KBM method with those obtained using numerical integration for $\epsilon = 0.1, 0.3$. As before, the results match well even when ϵ is not very small.

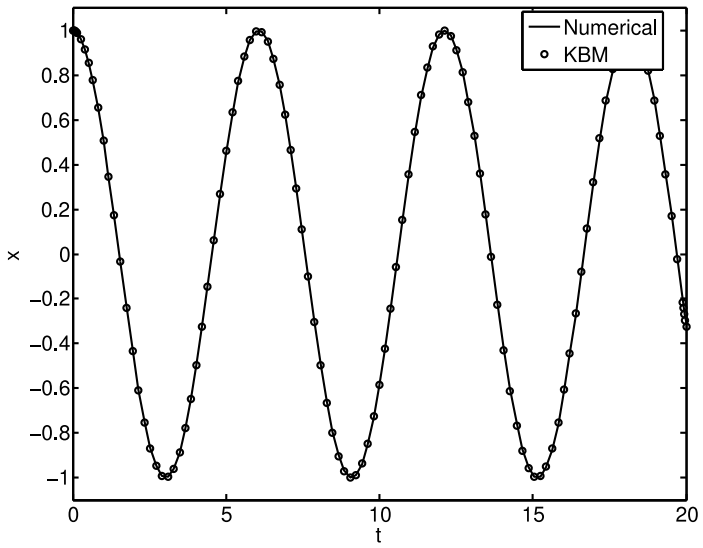

(a) x versus t for $\epsilon = 0.1$

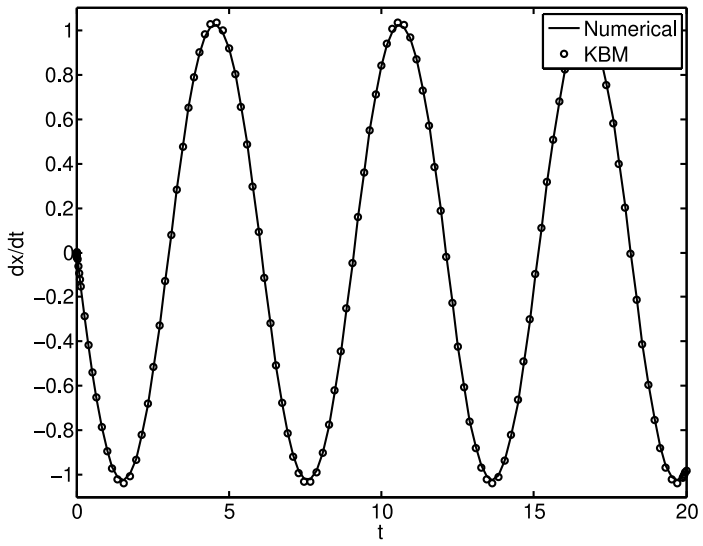

(b) $\dot{x}$ versus t for $\epsilon = 0.1$

Fig. 94. Comparison of KBM method with numerical integration for the Duffing equation with $\epsilon = 0.1, 0.3$. The initial conditions are $x(0) = 1, \dot{x}(0) = 0$ for all cases.

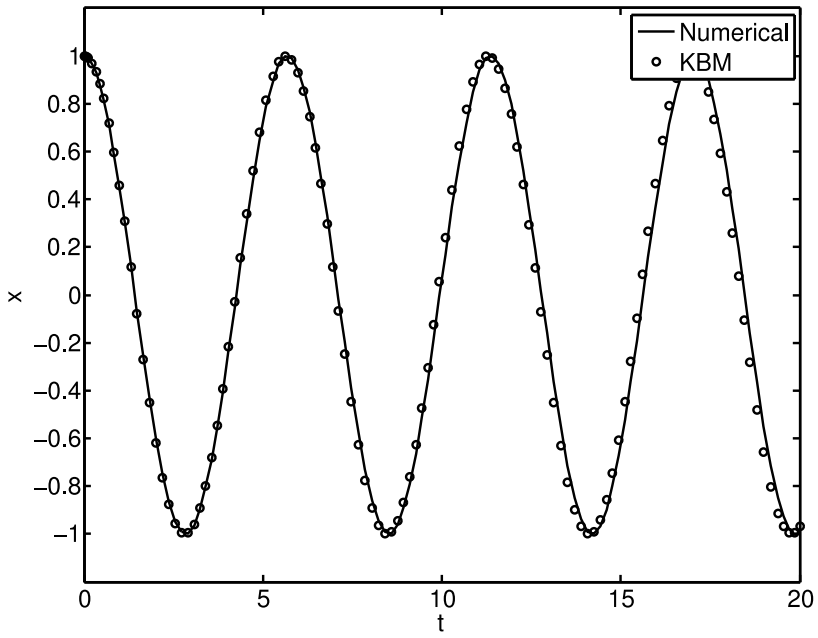

(c) x versus t for $\epsilon = 0.3$

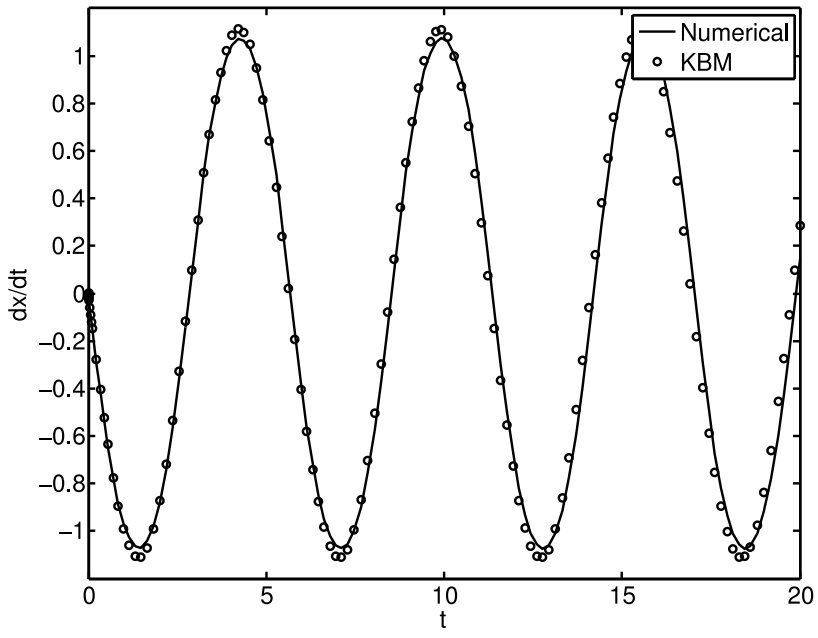

(d) $\dot{x}$ versus t for $\epsilon = 0.3$

Fig. 94. Continued ...

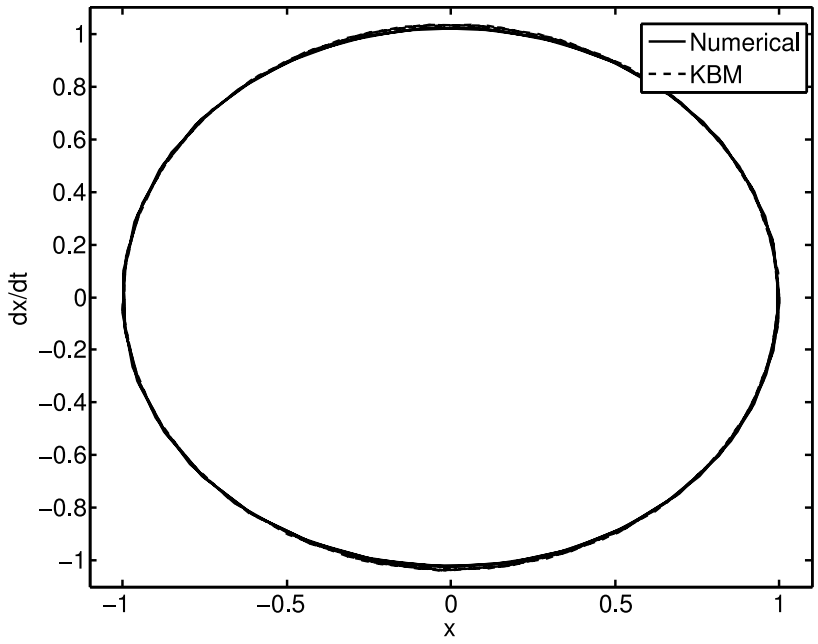

(e) Phase space for $\epsilon = 0.1$

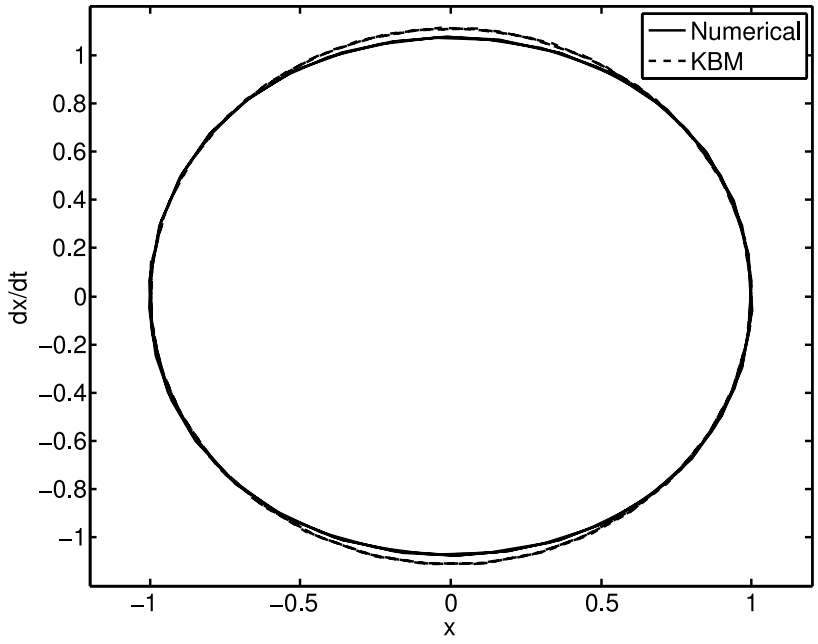

(f) Phase space for $\epsilon = 0.3$

Fig. 94. Continued ...

APPENDIX B

ROOT ISOLATION

In this appendix we consider the problem of isolating the roots of the following equation

$$f(t) = A_1 \sin(\omega_1 t + \Delta_1) + A_2 \sin(\omega_2 t + \Delta_2) = 0. \tag{B.1}$$

By root isolation we mean finding open intervals (t_1, t_2) such that $f(t)$ has at most one zero in interval. Thus, within these intervals the roots do not have any neighboring roots and are 'isolated'. The process of root isolation is an essential step towards finding the roots, which is our ultimate goal. Once the roots are isolated it is a routine matter to find them to any desired accuracy by using the bisection algorithm.

With a change of variables Eq. B.1 can always be to the following equation

$$A_1 \sin(z + \Delta) + A_2 \sin(\omega z) = 0, \tag{B.2}$$

where the new variable z is defined as

$$z = \omega_1 t + \frac{\omega_1}{\omega_2}\Delta_2, \tag{B.3}$$

and

$$\omega = \omega_2/\omega_1, \quad \Delta = (\omega_2\Delta_1 - \omega_1\Delta_2)/\omega_2. \tag{B.4}$$

Thus, the problem of finding zeros of Eq. B.1 is equivalent to solving

$$\sin(z + \Delta) + A \sin(\omega z) = 0, \tag{B.5}$$

where $A = A_2/A_1$. Consider two curves S_1 and S_2 defined as follows

$$S_1 : \sin(z + \Delta), \tag{B.6}$$

$$S_2 : -A \sin(\omega z). \tag{B.7}$$

Eq. B.5 can then be written as

$$S_1 = S_2. \tag{B.8}$$

Note that the structure of Eq. B.5 is invariant under the operation of shifting S_1 and/or S_2 along the z-axis and/or multiplying them by scalars. To show this consider the following transformation

$$\begin{aligned} S_1 &\rightarrow B_1 \sin(z + \Delta + \Delta_3) \\ S_2 &\rightarrow -B_2 \sin(\omega z + \Delta_4). \end{aligned} \tag{B.9}$$

With the above transformation Eq. B.5 becomes

$$B_1 \sin(z + \Delta + \Delta_3) + B_2 \sin(\omega z + \Delta_4) = 0, \tag{B.10}$$

which can easily be put in the following form using a change of variable

$$\sin(u + \Delta') + A' \sin(\omega u) = 0. \tag{B.11}$$

As claimed the above equation has the same structure as Eq. B.5, and the frequencies of the individual components are unchanged as well.

Equation. B.5 can have a root z_1 of multiplicity 2 if

$$\sin(z_1 + \Delta) + A \sin(\omega z_1) = 0, \tag{B.12}$$

$$\cos(z_1 + \Delta) + A\omega \cos(\omega z_1) = 0. \tag{B.13}$$

However, the case with multiplicity of the root equal to greater than 3 is not inter-

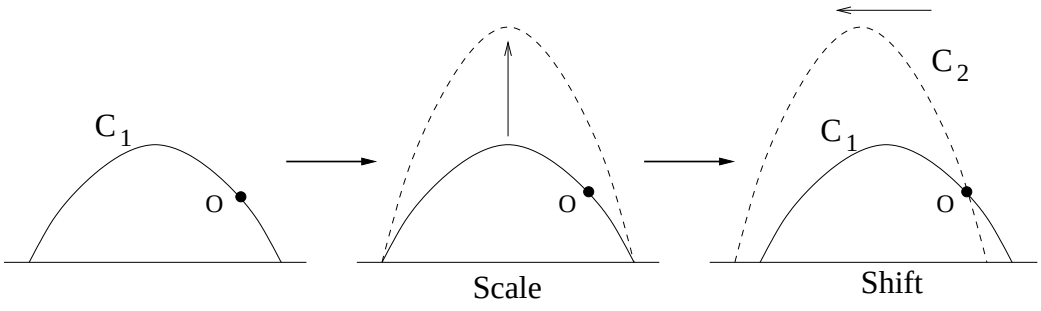

Fig. 95. Construction 1: Scale and shift.

esting since it would demand that the following should hold

$$\begin{aligned} \sin(z_1 + \Delta) + A\sin(\omega z_1) &= 0, \\ \cos(z_1 + \Delta) + A\omega\cos(\omega z_1) &= 0, \\ \sin(z_1 + \Delta) + A\omega^2\sin(\omega z_1) &= 0. \end{aligned} \tag{B.14}$$

The set B.14 admits trivial solutions of the form $z_1 = n\pi/\omega,\ z_1+\Delta = m\pi$ if $|A\omega| = 1$. The necessary conditions for existence of non-trivial solutions can be found to be $\omega = 1, |A| = 1$ (assuming $\omega > 0$). In either case, Eq. B.5 can be solved in closed form, thus the problem of root isolation is resolved. We next look at the more interesting cases were the set B.14 has no solutions.

Claim 1. *If* $\omega > 1$ *then Eq. B.5 has at most two roots between adjacent peaks and zeros of* $\sin(\omega z)$*, if* $\omega < 1$ *then Eq. B.5 has at most two roots between the adjacent peaks and zeros of* $\sin(z + \Delta)$*.*

Proof. As shown in figure 95, given a sinusoidal curve C_1 and a point o on the curve it is always possible to construct another sinusoidal curve C_2 with the same frequency such that the two curves intersect at o and within the quarter period of C_2 that contains o the curve C_2 lies above C_1 on one side of o and below it on the other

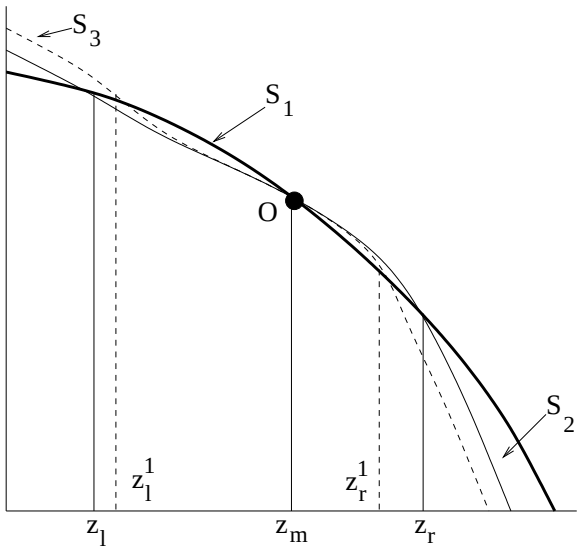

Fig. 96. Construction 2: Moving three roots closer by using the scale and shift construction.

side. The construction shown in figure 95 is be referred to as the scale and shift construction. We will use this construction to prove the claim using a contradiction.

Suppose $\omega > 1$ (the case with $\omega < 1$ can he handled similarly). Since $\omega > 1$ we shall refer to S_2 as the 'faster' curve. Let if possible S_1 and S_2 intersect three times between an adjacent peak and zero of S_2 (see figure 96). Then one can use the scale and shift construction to construct another curve S_3 such that S_1 and S_3 intersect three times between an adjacent peak and zero of S_3 and the intersections are closer to each other as compared to the intersections of S_1 and S_2. By continuing this construction the intersections can be made to come arbitrarily close to each other, thus creating a root of Eq. B.5 with multiplicity 3, which is a contradiction since the construction of scaling and shifting does not alter the structure of Eq. B.5. These arguments can be put in rigorous terms as follows.

Let z_l, z_m, z_r be the three intersections of S_1 and S_2. Since S_2 is monotonic in the

considered interval, without the loss of generality we can assumed it to be decreasing. It follows that if $z_l < z_m < z_r$ then $S_2(z_l) < S_2(z_m) < S_2(z_r)$. By construction S_3 satisfies the following

$$\begin{aligned} S_3(z_l) &> S_2(z_l), \\ S_3(z_m) &= S_2(z_m), \\ S_3(z_r) &< S_2(z_r). \end{aligned} \tag{B.15}$$

Since the deformation of S_2 into S_3 can be continuous, it follows that S_3 can be chosen to be such that S_3 and S_2 are on the same side of S_1 in a sufficiently small interval around z_m. Then, by continuity S_3 and S_1 should have at least one intersection between z_m and z_l, and at least one intersection between z_m and z_r. Finally, since it is possible to construct S_3 such that there are no intersections other than z_m (by choosing a large enough scaling factor), therefore, by continuity, there should exist a scaling at which the intersections are arbitrarily close (after which two of them collide and annihilate each other). This, however, leads us to a contradiction, and hence the claim must be true.

Note: Similar arguments can be made for other types of intersections of curves. See figure 97 for example. In this case S_1 is scaled and shifted. □

Using the claim 1 it is possible to isolate roots of Eq. B.5 in pairs of two. Even though it is an enormous simplification, methods like bisection can be used only if the individual roots can be isolated. A methodology for isolating the individual roots is presented next.

Note that if there are two intersections of the curves S_1 and S_2 in a quarter period of the faster curve then these intersections can be made to come arbitrarily close to each other by shifting one of the curves. This construction, called the shift construction, is depicted in figure 98. Thus, if there are two intersections of the

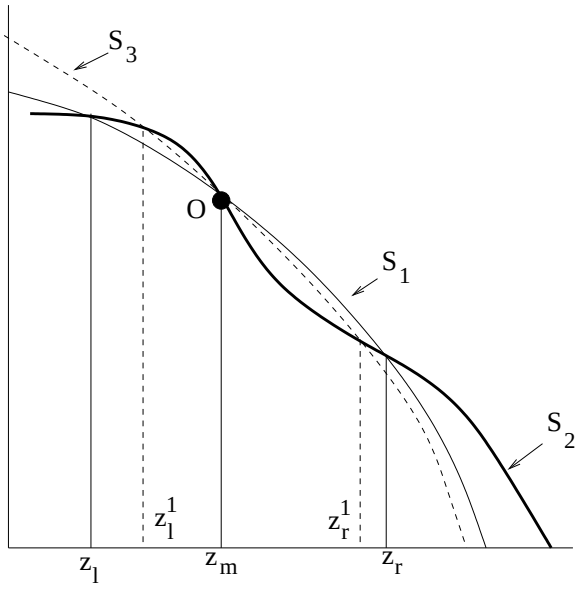

Fig. 97. Scale and shift construction for other type of intersections.

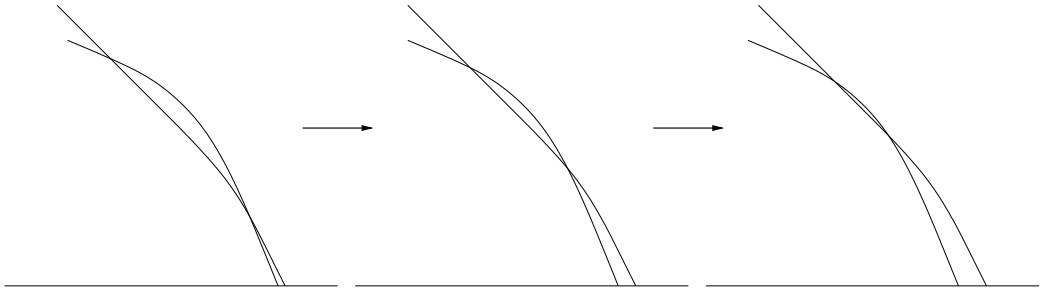

Fig. 98. Construction 3: Moving two roots closer by shifts.

curves between an adjacent zero and peak of the faster curve then there exists some shift Δ for which Eq. B.5 has a root of multiplicity 2. Therefore, there can be two roots of Eq. B.5 in the quarter period of the faster curve only if Eq. B.5 has a root of multiplicity 2 for some Δ. It is easy to show that the following are necessary conditions for existence of a root of multiplicity 2 of Eq. B.5

$$\begin{aligned} A^2 > 1, \quad 1 > A^2\omega^2; \quad \text{for } \omega < 1, \\ A^2 < 1, \quad 1 < A^2\omega^2; \quad \text{for } \omega > 1. \end{aligned} \tag{B.16}$$

If the conditions B.16 are not satisfied then the roots of Eq. B.5 can be isolated using claim 1. In that case the following intervals contain unique roots of Eq. B.5

$$\begin{aligned} I_n = (z_n, z_{i-n}), \quad z_n = -\Delta + \frac{n}{2}\pi; \quad \text{for } \omega < 1, \\ I_n = (z_n, z_{i-n}), \quad z_n = \frac{n\pi}{2\omega}; \quad \text{for } \omega > 1. \end{aligned} \tag{B.17}$$

The intervals B.17 shall be referred to as the relevant intervals. If the conditions B.16 are indeed satisfied then claim 1 needs to be strengthened. Note that the derivative of Eq. B.5 vanishes when

$$\cos(z + \Delta) + A\omega\cos(\omega z) = 0. \tag{B.18}$$

Equation B.18 has the same structure as Eq. B.5 and thus it zeros can be isolated (at least in pairs) using the same arguments. Note that the relevant intervals are the same for Eqs. B.5 and B.18. Further, it is easy to show that the following are necessary conditions for existence of a root of multiplicity 2 of Eq. B.18

$$\begin{aligned} A^2\omega^2 > 1, \quad 1 > A^2\omega^4; \quad \text{for } \omega < 1, \\ A^2\omega^2 < 1, \quad 1 < A^2\omega^4; \quad \text{for } \omega > 1. \end{aligned} \tag{B.19}$$

It is obvious to see that conditions B.16 and B.19 cannot hold simultaneously. Thus, if there exist two roots of Eq. B.5 in the relevant intervals, the Eq. B.18 has a unique

root in those intervals. Finally, since the roots of Eq. B.5 are necessarily separated by roots of Eq. B.18, therefore the individual roots of Eq. B.5 can be isolated by using claim 1 and the above stated arguments.

We conclude this appendix with some examples showing the application of the developed results. Figure 99 shows the graph of the function $f(z) = \sin(z + \Delta) + A\sin(\omega z)$ for some values of $A,\ \omega$ and Δ. The first root of the function $f(z)$ is calculated by using the bisection algorithm on the intervals found using the proposed method and is shown in the graphs. For some of the graphs the values of the parameters $A,\ \omega$ and Δ are deliberately chosen such that the conditions for existence of roots of multiplicity two are satisfied and that the first root is a root of multiplicity two. These cases are of relevance because for these cases the roots are discontinuous functions of the parameters.

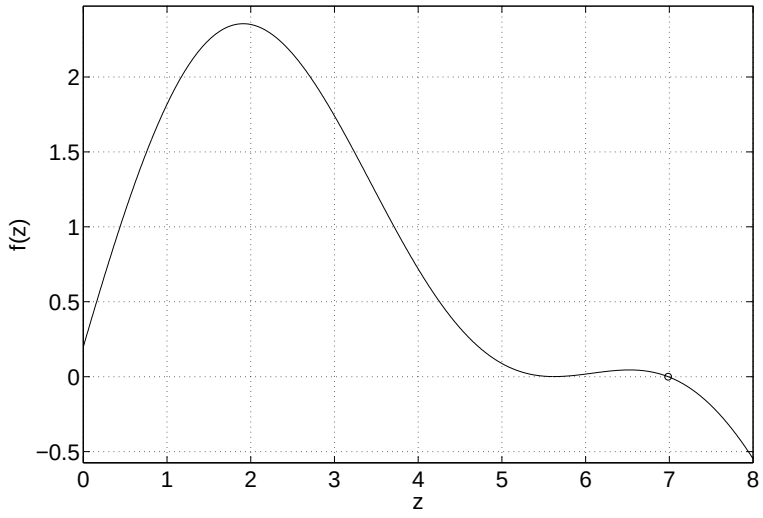

(a) $f(z)$ versus z with $A = 1.8,\ \omega = 0.5143,\ \Delta = 0.2$. The first root, $z = 6.99$, is shown by the circle.

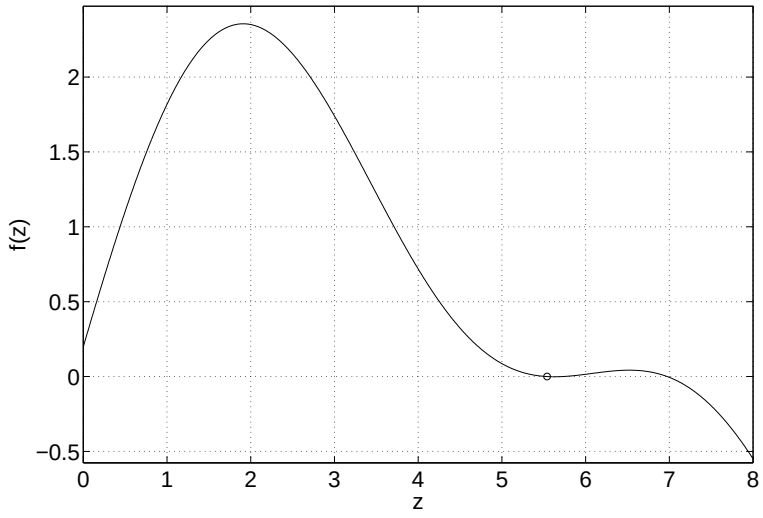

(b) $f(z)$ versus z with $A = 1.8,\ \omega = 0.5145,\ \Delta = 0.2$. The first root, $z = 5.54$, is shown by the circle.

Fig. 99. First root of the function $f(z) = \sin(z + \Delta) + A\sin(\omega z)$ for different cases. Note the roots multiplicity two.

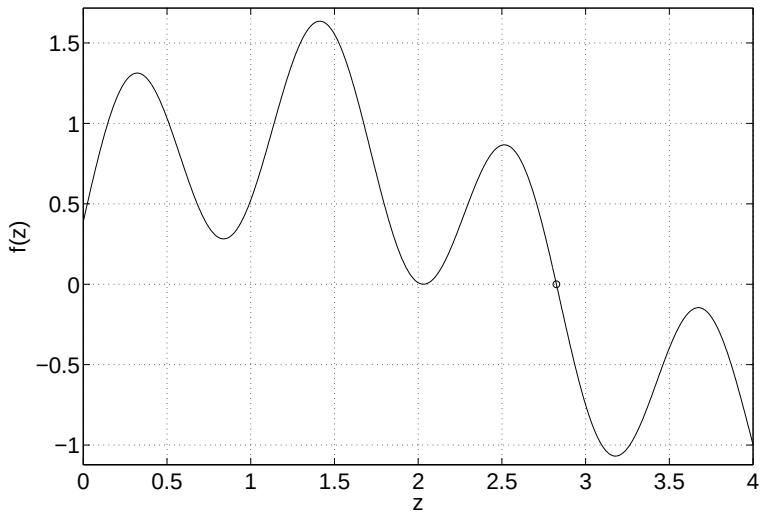

(c) $f(z)$ versus z with $A = 0.666,\ \omega = 5.1,\ \Delta = 0.4$. The first root, $z = 2.82$, is shown by the circle.

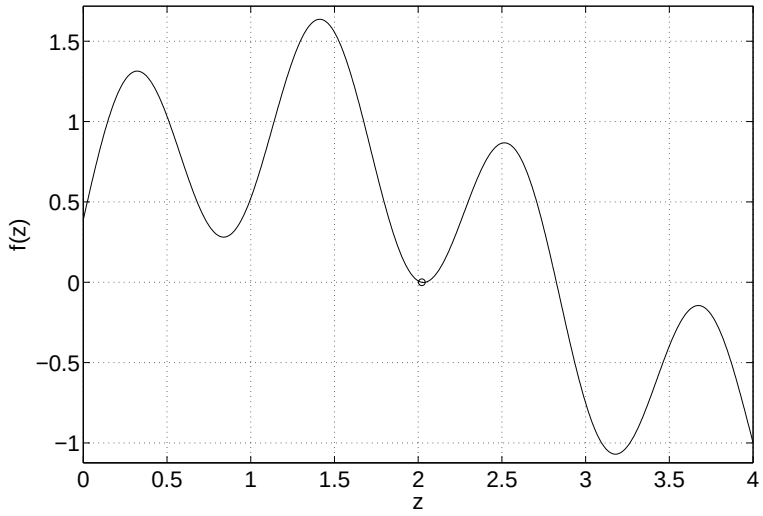

(d) $f(z)$ versus z with $A = 0.667,\ \omega = 5.1,\ \Delta = 0.4$. The first root, $z = 2.02$, is shown by the circle.

Fig. 99. Continued ...

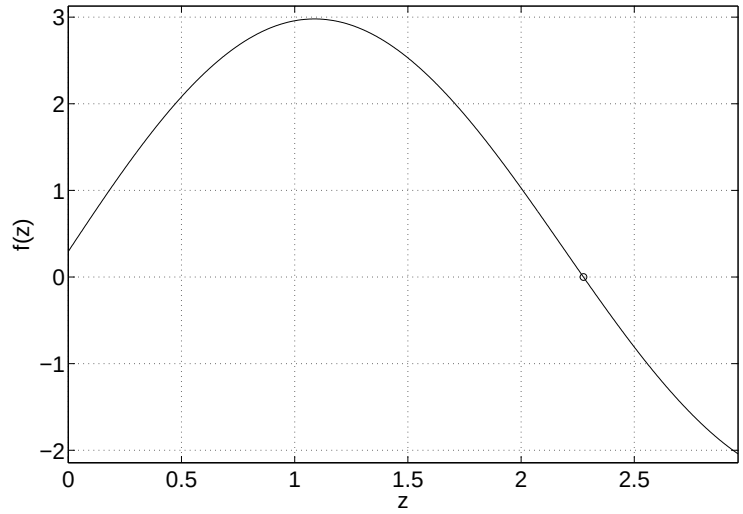

(e) $f(z)$ versus z with $A = 2.0,\ \omega = 1.5,\ \Delta = 0.3$. The first root, $z = 2.27$, is shown by the circle.

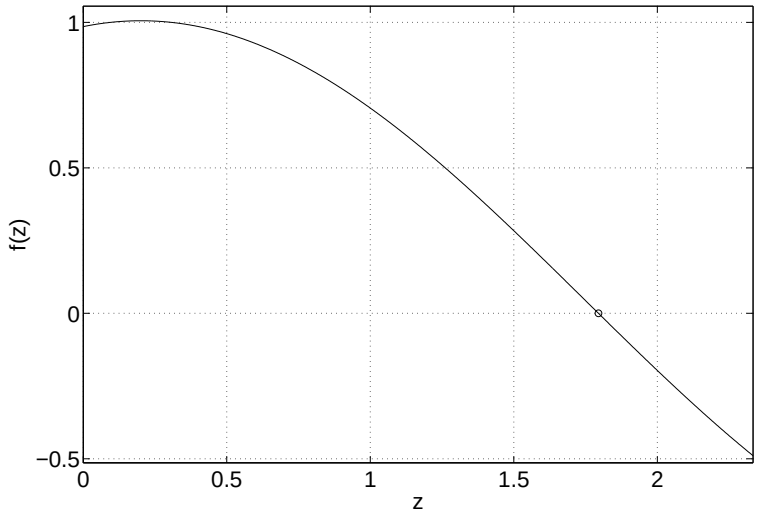

(f) $f(z)$ versus z with $A = 0.2,\ \omega = 0.15,\ \Delta = 1.4$. The first root, $z = 1.79$, is shown by the circle.

Fig. 99. Continued ...

APPENDIX C

CONTINUATION AND BIFURCATION ALGORITHMS

In this appendix we present a discussion of tools and techniques used for carrying out bifurcation and continuation analysis of discrete maps. Continuation analysis was originally developed for solving tough nonlinear problems via methods of homotopy. However, over the years this method has been applied to a very diverse set of problems, both in engineering and in pure sciences. Good introductions to this subject can be found in the works of Keller [55], Doedel [56], Allgower [57, 58] and Gracia [59] among others.

We consider general one parameter discrete dynamical systems of the form

$$x \mapsto f(x, \lambda), \tag{C.1}$$

where $x \in \mathbb{R}^n$, $\lambda \in \mathbb{R}^1$ and $f(x, \lambda) : \mathbb{R}^{n+1} \mapsto \mathbb{R}^n$ is sufficiently smooth. Generally x represents the discrete dynamic variables of interest and is also known as the state vector. On the other hand λ represents a parameter in the system, like the damping or stiffness, and is called the parameter (or the parameter vector, if there are more than one parameters). The fixed points or the equilibria of the system (C.1) are given by

$$x - f(x, \lambda) = 0. \tag{C.2}$$

Equation C.2 defines an implicit curve in $\mathbb{R}^n$. Under certain technical hypothesis, the existence of the implicit curve is ascertained by the Implicit Function Theorem. The goal of continuation algorithms is to trace out such a curve starting from one known point on the curve. The task of continuing a curve of equilibria emanating from one equilibrium is usually accomplished by the use of *predictor-corrector* algorithms. The

essence of such algorithms is to first guess or predict the next point on the curve and then refine or correct the predicted point to desired accuracy. Tangent prediction and Newton correction are amongst the most popular prediction-correction algorithms.

Before moving on to the more technical aspects of continuation and bifurcation algorithms we illustrate the important aspects of typical continuation problems by the means of an example. Consider the classic 1-D normal form of the discrete pitch-fork bifurcation

$$x \mapsto (1+\lambda)x - x^3. \tag{C.3}$$

This example illustrates many important aspects of continuation algorithms. The fixed points of Eq. C.3 are given by

$$\lambda x - x^3 = 0. \tag{C.4}$$

The solutions to Eq. C.4 are $(0, \lambda)$, and $(\pm\sqrt{\lambda}, \lambda)$. The corresponding multipliers are $1+\lambda$ and $1-2\lambda$, respectively. In a small neighborhood of $\lambda = 0$, there are 1 or 3 fixed points depending on the sign of λ. For $\lambda < 0$ the only fixed point is $x = 0$ and it is stable. For $\lambda > 0$ the fixed point $x = 0$ looses its stability and two other stable fixed points given by $x = \pm\sqrt{\lambda}$ are born. The bifurcation diagram in a sufficiently small neighborhood of $\lambda = 0$ is shown in figure 100. In this simple example we were able to take the analysis to a good length without restoring to numerics, however, this might not be the case in more complicated and/or higher dimensional systems. We next discuss how this analysis could have been carried out numerically.

Suppose we somehow know that $(x, \lambda) = (0, -0.5)$ is a fixed point of the map C.3. The aim of a continuation algorithm is then to start at this point and trace the entire family of solutions of Eq. C.4 emanating from it, thereby generating the bifurcation diagram (perhaps without the stability information). Note that in figure 100 two

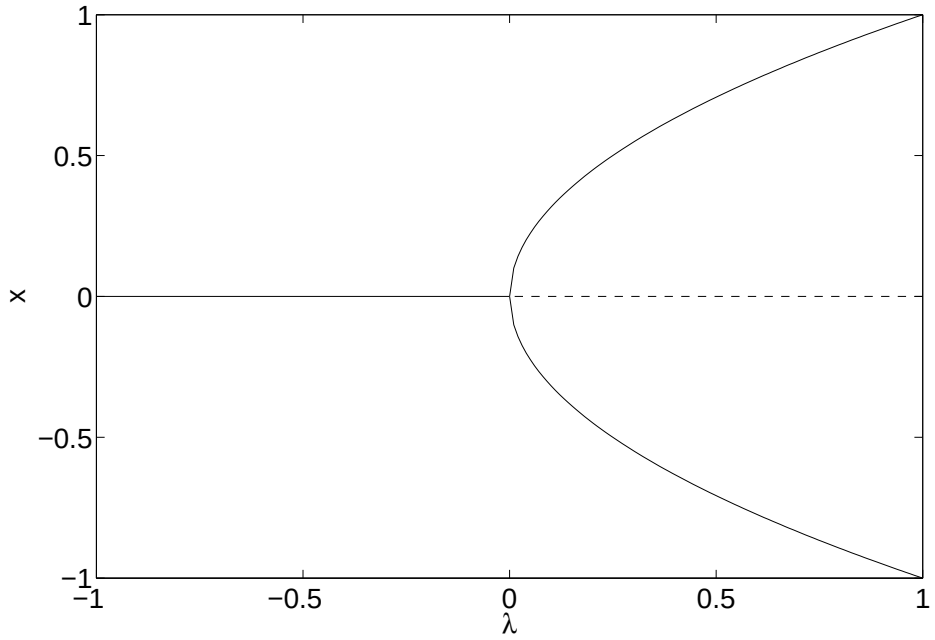

Fig. 100. Bifurcation diagram showing a supercritical pitchfork bifurcation.

fixed point curves intersect at the point $(0, 0)$. Such points are called branch points. Another task of a continuation algorithm is to identify such points and to be able to continue all branches emanating from a branch point, if needed. Further, notice that the curved branch folds (has an extremum with respect to the parameter λ) at the point $(0, 0)$. Such points are called fold points. The straight branch changes stability as it passes through the point $(0, 0)$. Such points are called bifurcation points. Fold points are necessarily bifurcation points as well. It is the job a continuation algorithm to keep track of such points. Once the family of equilibria is known, a bifurcation analysis can be used to calculate the stability of the equilibria. Detecting phenomena like birth of limit cycles, change of stability etc. are in the realm of bifurcation analysis. Usually the bifurcation analysis is local in nature and cannot provide information about the non-local bifurcations of the system. Thus, a continuation and a bifurcation algorithm working together can provide valuable information about the asymptotic behavior of a system.

There are several codes that can be used for continuation and bifurcation analysis. Prominent amongst these are AUTO [60], MATCONT [61], DSTOOL [62], LOCBIF [63], CONTENT [64], XPPAUT [65], and PyCont. In this thesis we used CL_MATCONT_for_maps (a command line tool in the MATCONT family) for carrying out the bifurcation analysis of the bilinear and the multilinear hysteretic oscillators. MATCONT was chosen because of its enhanced capabilities and because it runs on MATLAB, thereby enabling the user to use all the features of MATLAB. Table XIX[2] presents a comparative summary of the codes mentioned above.

The stability of points on an equilibria curve can be found by carrying out a local eigenvalue analysis. The well known Gorbman Hartman theorem states that if all

[2]taken almost verbatim from Dr. Kuznetsov's webpage http://www.math.uu.nl/people/kuznet/res.html

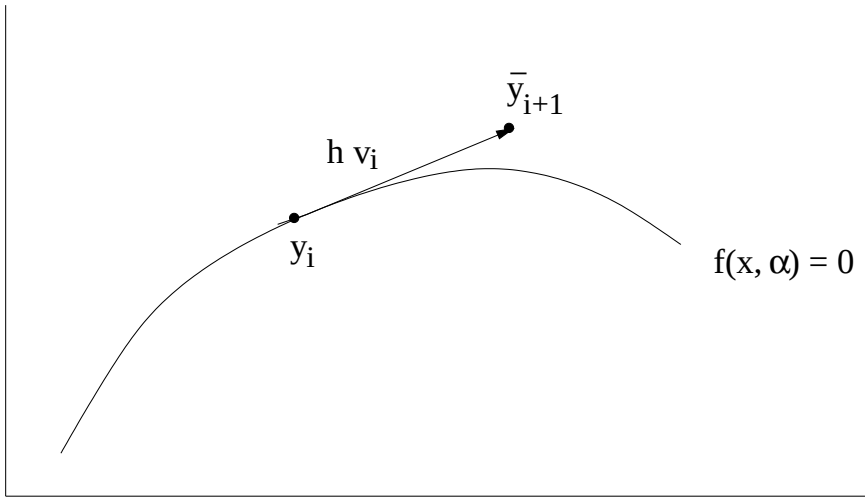

Fig. 101. Tangent prediction.

eigenvalues of the Jacobian matrix at a fixed point are in the open left half complex plain then the equilibrium is locally asymptotically stable. This result is used to characterize the stability of the fixed point curve. Bifurcations (or changes in stability) along the curve can be detected by observing the eigenvalues. A computationally efficient way of finding bifurcation points is by the use of so-called *test functions*. Test functions for a bifurcation are functions that have a regular zero at the bifurcation point. For example, the determinant of the Jacobian matrix has a regular zero at a generic fold point, and can thus serve as a test function for a fold bifurcation.

Prediction and Correction

Suppose that we are interested in continuing the implicit curve

$$g(x, \lambda) \equiv x - f(x, \lambda) = 0, \tag{C.5}$$

Table XIX. Capabilities of standard bifurcation analysis tools. A=Auto, C=CONTENT, M=MATCONT, P=PyCont.

Capability	A	C	M	P
time-integration		+	+	+
Poincaré maps			+	
continuation of equilibria	+	+	+	+
detection of branch points and codim 1 bifurcations of equilibria	+	+	+	+
computation of normal forms for codim 1 bifurcations of equilibria		+	+	+
continuation of codim 1 bifurcations of equilibria	+	+	+	+
detection of codim 2 equilibrium bifurcations (cusp, Bogdanov-Takens, fold-Hopf, generalized and double Hopf)		+	+	+
continuation of limit cycles	+	+	+	+
detection of branch points and codim 1 bifurcations (limit points, flip and N-S) of cycles	+	+	+	+
continuation of codim 1 bifurcations of cycles	+		+	+
branch switching at equilibrium and cycle bifurcations continuation of branching points of equilibria and cycles	+ +	+	+ +	+ +
computation of normal forms for codim 1 bifurcations of cycles			+	+
detection of codim 2 bifurcations of cycles			+	
continuation of orbits homoclinic to equilibria	+			

from a regular point y_i, where y_i is the augmented vector $[x_i, \lambda_i]$. Let v be the tangent vector to the fixed point curve at a point $y = (x, \lambda)$. Then

$$J(y)v = 0, \tag{C.6}$$

where

$$J \equiv \begin{bmatrix} \frac{\partial g}{\partial x} \\ \\ \frac{\partial g}{\partial \lambda} \end{bmatrix}, \tag{C.7}$$

and

$$v \equiv \begin{bmatrix} \dot{x} \\ \\ \dot{\lambda} \end{bmatrix}; \quad ||v|| = 1. \tag{C.8}$$

It is clear from Eq. C.6 that

$$v \in N(J), \tag{C.9}$$

where $N(J)$ is the null-space of J. The vector v is unique up to a sign if the space $N(J)$ is one dimensional. According to the tangent prediction method, the predicted point $\bar{y}_{i+1}$ is

$$\bar{y}_{i+1} = hv_i + y_i, \tag{C.10}$$

where h is the step-size and v_i is the unit tangent vector to the implicit curve $g(y) = 0$ at the point y_i (see figure 101). At a generic point Eqs. C.6, C.8 define the vector v up to a $\pm$ sign. The sign is fixed using the continuity of vector v along the curve

$$v_i \cdot v_{i-1} > 0, \tag{C.11}$$

where $(\cdot)$ is the standard vector inner product.

After finding a predicted point $\bar{y}_{i+1}$ it is necessary to correct the point to the required precision. This correction is achieved using Newton-Ralphson iteration like methods. Notice that $g(y) = 0$ gives only n equations where n is the dimensionality

of the state vector. The vector y is $n+1$ dimensional, thus one needs to specify one more condition before applying Newton-Ralphson like methods to the system. There are many ways to impose this additional condition. The pseudo-arclenght condition given by

$$k(y_{i+1}) \equiv (y_{i+1} - y_i) \cdot v_i - h_i = 0 \tag{C.12}$$

is one of the widely used additional conditions. Thus, the augmented system iterated by the Newton-Ralphson like method is

$$\begin{aligned} g(y_{i+1}) &= 0, \\ k(y_{i+1}) &= 0. \end{aligned} \tag{C.13}$$

This prediction-correction scheme is often called the pseudo-arclength continuation and is shown graphically in figure 102. Using the prediction-correction method one can keep advancing along an equilibrium curve till one hits a branch point, where the tangent vector v is no longer unique. In the next section we show how to take care of such points.

Branch Point Detection

A regular point of the equilibrium curve is defined as a point for with the null-space of J is one-dimensional. It is obvious that the null space of J is of dimension at least 2 at a branch point. Thus, the following can be used to characterize and identify branch points

$$\text{Rank}(N(J)) > 1. \tag{C.14}$$

Further, the null vectors at a branch point can be used to locally characterize and follow the various branches of equilibria emanating from the point. The appearance of a branch point along the continued curve is indicated by an increase in dimension

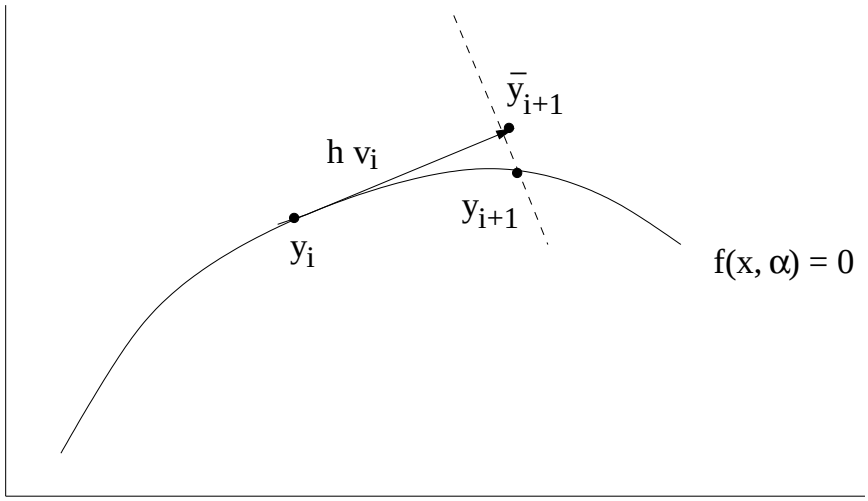

Fig. 102. Pseudo-arclength correction.

of the null-space of the Jacobian matrix $J(y)$. Once the dimension of the null-space is ascertained, the vectors spanning the null space can be found. The different branches of equilibria emanating from the branch point can then be traced by using each of these vectors as tangent vectors in the tangent prediction method described in the previous section.

Bifurcation Detection

At each point on the fixed point curve one can evaluate certain *test functions* and associated degeneracy conditions and conclude about the presence of bifurcations at the point. Test functions have a regular zero at the bifurcation points. The test functions and degeneracy conditions for the classical codim-1 bifurcations of discrete systems are discussed next. A more complete discussion of these topics can be found in Ref. [66].

Fold Points

Since the matrix

$$J' = \left.\frac{\partial f}{\partial x}\right|_{y=y_i} \tag{C.15}$$

has a single eigenvalue equal to 1 at a generic fold point, so the following function can be used as a test function for fold point detection

$$\xi_t(y_i) = \det\left(J' - I_n\right), \tag{C.16}$$

where I_n is the $n \times n$ identity matrix. For a generic fold bifurcation the existence of a simple zero of the said test function is a necessary but not a sufficient condition. The following conditions, sometimes also known as the non-degeneracy conditions, together with the test function are the necessary and sufficient conditions for the bifurcation to occur

$$\begin{aligned} f_{xx}(y_i) &\neq 0, \\ f_{\lambda}(y_i) &\neq 0. \end{aligned} \tag{C.17}$$

Flip Bifurcation

The flip bifurcation is characterized by the presence of a single multiplier equal to -1. Thus, the following can be used as a test function for locating a flip bifurcation

$$\xi_f(y_i) = \det\left(J' + I_n\right). \tag{C.18}$$

The associated non-degeneracy conditions are

$$\begin{aligned} &\frac{1}{2}(f_{xx}(y_i))^2 + \frac{1}{3}f_{xxx}(y_i) \neq 0, \\ &f_{x\lambda}(y_i) \neq 0. \end{aligned} \tag{C.19}$$

Neimark-Sacker Bifurcation

At a Neimark-Sacker point the Jacobian matrix has a single complex eigenvalue pair on the unit circle. A suitable test function for this bifurcation can be found by invoking Stéphanos theorem. It is mentioned here that the following function can serve as a test function for the Neimark-Sacker bifurcation

$$\xi_{NS}(y_i) = \det\left(J' \bullet J' - I_m\right), \tag{C.20}$$

where $(\bullet)$ is the bialternate product and $m = n(n-1)/2$. The non-degeneracy conditions associated with the Neimark-Sacker bifurcation are quite technical and are not discussed here. The interested reader is referred to Ref. [66] for a better treatment of the subject.

Stability Analysis

An eigenvalue analysis can be used to characterize the stability at desired points on the fixed point curve. A point y_i is a stable equilibrium if the matrix

$$J' = \left.\frac{\partial f}{\partial x}\right|_{y=y_i} \tag{C.21}$$

has eigenvalues inside the unit circle in the complex plane, and unstable if it has any eigenvalue outside the unit circle. The points were the eigenvalues are on the unit circle correspond to bifurcation points and are dealt accordingly. Algorithms for finding eigenvalues of general matrices can be found in Ref. [67].

We end this appendix with bifurcation diagrams for the generic codim-1 bifurcations of smooth maps. Note that the Neimark-Sacker bifurcation is possible only in 2 or more dimensions.

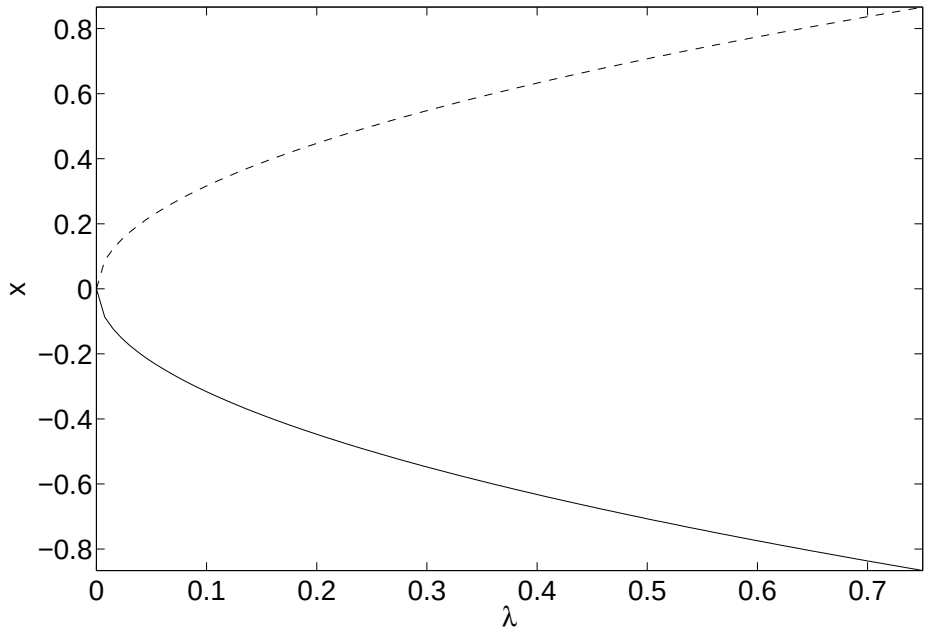

Fig. 103. Typical fold bifurcation. Normal form: $x \mapsto x + \lambda - x^2$.

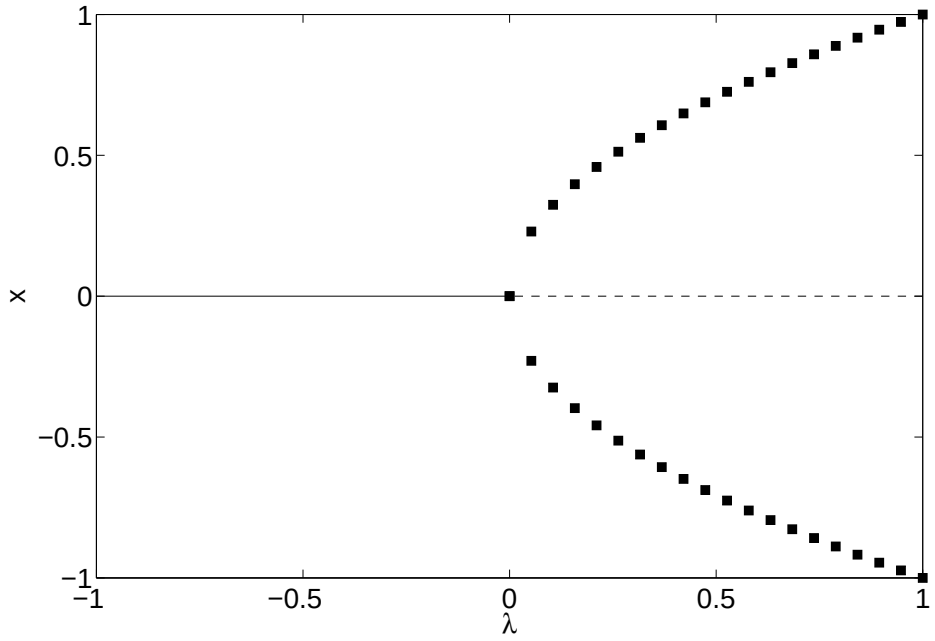

Fig. 104. Typical flip bifurcation. Normal form: $x \mapsto -(1+\lambda)x + x^3$. Filled squares denote stable (two period) orbit.

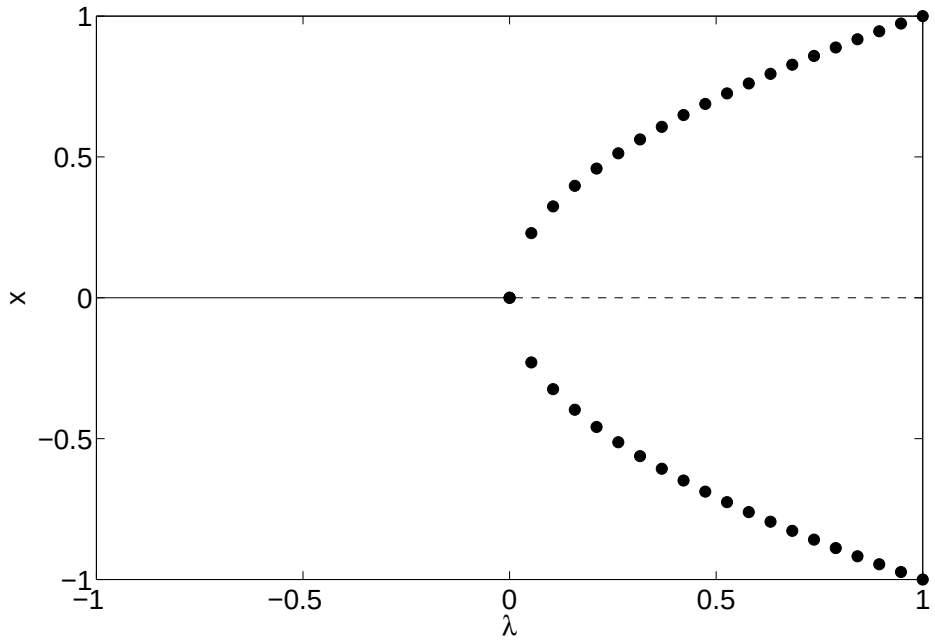

Fig. 105. Typical Neimark-Sacker bifurcation. See Ref. [66] for normal form. Filled circles denote stable limit cycle.

VITA

Ashivni Shekhawat received his B. Tech. in aerospace engineering from the Indian Institute of Technology Kanpur in 2004. He joined Texas A&M University to pursue graduate studies in aerospace engineering in the Dwight Look College of Engineering in the year 2006 and received his M.S. degree in 2008. He has a broad interest in the field of applied mathematics with focus on nonlinear dynamics, bifurcation theory and dynamical systems. He may be contacted by e-mail at shekhawat.ashivni@gmail.com. His postal address is

Texas A&M University

Department of Aerospace Engineering

H.R. Bright Building

3141 TAMU College Station, TX 77843-3141.

The typist for this thesis was Ashivni Shekhawat.